Simulation of the Resonance Raman Spectra For Uracil and its Derivatives

by

Shuai Sun

A thesis submitted in partial fulfillment of the requirements for the degree of

Doctor of Philosophy

Department of Chemistry

University of Alberta

Abstract

In this thesis, we simulated the resonance Raman spectra of uracil and its derivatives, including 5-halogenated (F, Cl, Br) uracils and thymine, using the Herzberg-Teller short-time dynamics formalism. The electronic structure calculations are carried out using density functional theory (DFT) for ground states and time-dependent density functional theory (TD-DFT) for excited states. As the resonance Raman spectra are governed by the ground state normal modes and the excited state Cartesian gradient, the resulting spectra are examined in terms of these two factors.

In the simulation of the resonance Raman spectrum for uracil, the performance of different functionals is investigated. The ground state geometry is optimized at the levels of PBE0/aug-cc-pVTZ and B3LYP/aug-cc-pVTZ, respectively. The gradient of the bright excited state is computed using Time Dependent Density Functional Theory (TD-DFT) and Spin Flip Time Dependent Density Functional Theory (SF-TD-DFT). The excited state calculations are carried out in both the gas phase and implicit water using the conductor-like Polarizable Continuum (C-PCM) Model. The ground state equilibrium structure is found to impact the resulting resonance Raman spectrum significantly. The simulated resonance Raman spectrum using the long range corrected functionals, i.e., CAMB3LYP and LC-BLYP, and based on the PBE0/aug-cc-pVTZ optimized ground state structure shows better agreement with the experimental spectrum than using standard hybrid functionals, i.e., PBE0 and B3LYP. The solvation effect leads to a change in the energetic order of the $n \rightarrow \pi^*$

and $\pi \rightarrow \pi^*$ excited states, and it improves the agreement with the experimental spectrum, especially with regard to the relative intensities of the peaks with frequencies greater than 1600 cm^{-1}.

The resonance Raman spectra of the 5-halogenated (F, Cl, and Br) uracils are simulated, and the effects of halogen substitution are investigated through the comparison between the spectra of the three 5-halogenated uracils. The gradient of the S_1 excited state is computed at the CAMB3LYP/aug-cc-pVTZ level of theory in implicit water (C-PCM), based on the equilibrium geometry determined using PBE0/aug-cc-pVTZ in implicit water (C-PCM). The simulated resonance Raman spectra show good agreement with the experimental spectra both in terms of peak positions and intensities. The differences in the normal mode eigenvectors and excited state Cartesian gradients between 5-fluorouracil and 5-chlorouracil are used to interpret the dissimilarity between their resonance Raman spectra. Meanwhile, the similarity between the spectra of 5-chlorouracil and 5-bromouracil is explained by the correspondence between their normal modes and excited state gradients.

The effects of explicit hydrogen bonding with H_2O on the resonance Raman spectra of uracil and thymine are also investigated computationally. The three bonding sites in uracil and thymine that form lowest energy uracil-H_2O and thymine-H_2O complexes are examined. The ground state structures of the three uracil-H_2O and corresponding thymine-H_2O complexes are optimized at the PBE0/aug-cc-pVTZ level of theory in H_2O (C-PCM), and the gradients of the bright excited state (S_1) are computed at the TD-CAMB3LYP/aug-cc-pVTZ level of theory in H_2O (C-PCM). Explicit hydrogen bonding to water is found to cause significant changes in the resonance Raman spectra of uracil and thymine when compared to the isolated molecules. The effect of hydrogen boding is primarily on the ground state normal mode character, especially for the high frequency modes (> 1600 cm^{-1}), rather than on the excited

state Cartesian gradients. Different hydrogen bonding sites are found to have different contributions in the resulting resonance Raman spectra, and inclusion of explicit hydrogen bonding on the carbonyl bond opposite to the ring nitrogen is necessary to obtain good agreement between the simulated and experimental resonance Raman spectra of uracil and thymine.

While accomplishing the research in this thesis, an interface of the resonance Raman computer code in ORCA (orca_asa) to GAMESS-US and Gaussian09 was developed. The resulting software can be used as a general tool for computing resonance Raman spectra. Therefore, in principle any electronic structure method that can determine a (numerical or analytical) Hessian can be used to compute the ground state. Meanwhile, a variety of methods could be used to determine the excited state gradients either analytically, or, in a much more computationally expensive fashion, numerically. Where available, solvation effects can be accounted for via polarizable continuum models (PCM) or, if specific solute-solvent interactions are important, with explicit solvent + PCM.

Preface

The research work in Chapter 2 was accomplished by Shuai Sun and Alex Brown, and was published in the *Journal of Physical Chemistry A*, **2014**, *118*, 9228.
The work in Chapters 3 and 4 was carried out by Shuai Sun and Alex Brown, and these chapters are in preparation for submission to peer-reviewed scientific journals.

Acknowledgements

I would like to express my sincere gratitude to Dr. Alex Brown. As my research supervisor, he helped me in all the time of research and writing of this thesis. I could not have imagined having a better advisor and mentor for my Ph.D study.

I also want to thank my family, my friends and my co-workers who supported and helped me during my Ph.D study.

We thank Dr. Glen Loppnow (University of Alberta) for providing the experimental resonance Raman spectra for uracil, 5-halogenated uracils and thymine.

Table of Contents

List of Tables

List of Figures

List of Abbreviations and Acronyms

aug-cc-pVTZ	*Dunning's augmented, correlation-consistent valence triple-ζ basis set with polarization functions*
B3LYP	*Becke, three-parameter, Lee-Yang-Parr hybrid functional*
BHHLYP	*Becke, Lee-Yang-Parr half-and-half functional*
BO	*Born Oppenheimer*
BLYP	*Becke, Lee-Yang-Parr hybrid functional*
CAMB3LYP	*Coulomb-attenuating method, Becke, three-parameter, Lee-Yang-Parr hybrid functional*
C-PCM	*conductor-like polarizable continuum model*
DFT	*density functional theory*
DNA	*deoxyribonucleic acid*
EFP	*effective fragment potential*
FC	*Frank Condon*
FWHM	*full width at half maximum*
HT	*Herzberg-Teller*
IMDHO	*independent mode displaced harmonic oscillator*
KHD	*Kramer-Heisenberg-Dirac*
KK	*Kramers-Kronig*
LC	*long range corrected*
LLCT	*ligand-to-ligand charge transfer transitions*
LMCT	*ligand-to-metal charge transfer transitions*

LR	*long range corrected functionals*
MLCT	*metal-to-ligand charge transfer transitions*
MMCT	*metal-to-metal (intervalence) charge transfer transitions*
NLR	*non long range corrected functionals*
PBE0	*Perdew-Burke-Ernzerhof, zero-parameter, hybrid functional*
PCM	*polarizable continuum models*
PED	*potential energy distribution*
PES	*potential energy surface*
PGA	*poly-L-glutamic*
QM/MM	*quantum mechanics/molecular mechanics*
RNA	*ribonucleic acid*
RWA	*rotating wave approximation*
SF-TD-DFT	*spin flip time-dependent density functional theory*
T-jump	*temperature jump*
TD-DFT	*time-dependent density functional theory*
TDPT	*time-dependent perturbation theory*
UV	*ultraviolet*
VPT2	*vibrational second-order level of perturbation theory*

List of Symbols

$\sigma_A(\omega)$	*absorption cross section*
Å	*angstrom*
θ	*bond angle*
P	*Cauchy principal value integral*
e	*charge of electron*
r	*coordinate of electron, or bond length*
$\mathfrak{S}$	*cosine similarity between a pair of normal modes*
$\mathbf{\Lambda}$	*diagonal matrix of eigenvalues of the mass weighted Hessian*
$\mathbf{M}$	*diagonal matrix of the atomic masses*
ϕ	*dihedral angle*
Δ_k	*dimensionless displacements*
μ	*dipole moment operator*
$\|e\rangle$, ψ_e	*electronic wavefunction for the excited state*
$\mathbf{T}$	*eigenvector of the mass weighted Hessian*
E	*electric field*
μ_{ge}	*electronic transition dipole moment*
$\|g\rangle$, ψ_g	*electronic wavefunction for the ground state*
$\mathbf{V_X}$	*energy gradient of the excited state in Cartesian coordinates*
$\|f\rangle$	*final vibronic states*
$\langle J\|K\rangle$	*Frank Condon factor between vibrational states J and K*

ω_{jk}	*frequency between states j and k*
ω	*frequency of the incident radiation,*
	or frequency of the peak in resonance Raman spectra
ω_s	*frequency of the scattered photon*
μ_{fi}^{ind}	*induced transition dipole moment*
$\|i\rangle$	*initial vibronic states*
$\|n\rangle$	*intermediate vibronic states*
v_k^1	*kth normal mode of the first molecule in the computation*
	of cosine similarity
Γ	*linewidth parameter*
m_e	*mass of electron (in atomic unit)*
V_{ni}	*matrix element of the perturbation*
$\mathbf{\Delta_Q}$	*matrix of ground state normal mode displacements*
$\mathbf{D^{(m)}}$	*matrix of mass weighted differences in the Cartesian coordinates*
v_m^2	*mth normal mode of the second molecule in the computation*
	of cosine similarity
Q	*normal mode coordinate*
S_n	*nth singlet excited state*
f	*oscillator strength*
μ_{fi}^{perm}	*permanent transition dipole moment*
$\hbar$	*reduced planck constant*
$\sigma(\omega)$	*resonance Raman excitation profile*
c	*speed of light*
$\mathbf{L}$	*transformation matrix between mass-weighted Cartesian*
	and normal coordinates

$\alpha_{i\to f}$	*transition polarizability between the ith and fth states*
H	*(vibrational) Hamiltonian operator*
E_{v}	*vertical excitation enenrgy*
$\|F\rangle$, χ_F	*vibrational wavefunction for the fth state*
$\|I\rangle$, χ_I	*vibrational wavefunction for the ith state*
$\|N\rangle$, χ_N	*vibrational wavefunction for the nth state*

Chapter 1

Introduction

Raman spectroscopy is an experimental measurement of the Raman scattering phenomenon that occurs when a molecule interacts with an incident electromagnetic field of an appropriate wavelength.[1] In the Raman scattering process, the molecule is promoted to a higher vibrational state (or demoted to a lower one) after the molecule interacts with the incident light, see Figure 1.1(a). Thus, the frequency of the emitted photon is different from the incident light. In other words, Raman scattering is an inelastic process. When the energy of the incident light is very close to an electronic transition energy of the molecule, the intensities of Raman spectra are significantly enhanced; the resulting spectrum is referred as resonance Raman spectrum. In Figure 1.1, we compare the resonance and the (off-resonance) Raman scattering processes. In (off-resonance) Raman spectroscopy, the information obtained is only about the ground state properties of the molecule. However, resonance Raman spectroscopy can provide information about the electronically excited state properties of the molecule.[2]

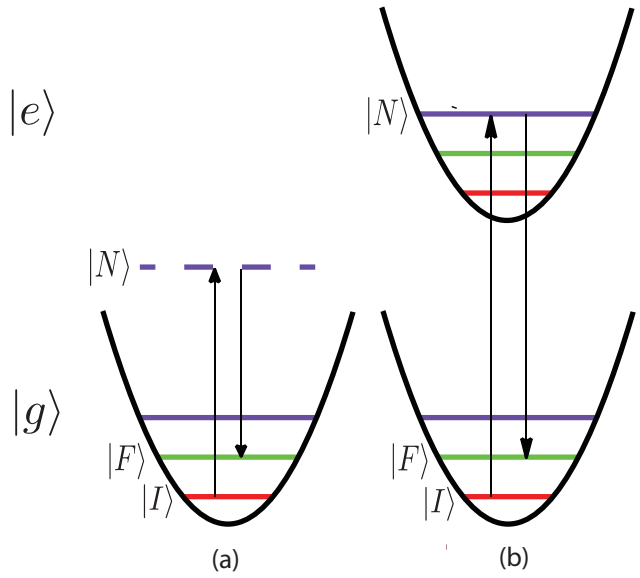

Figure 1.1: *Comparison between the (a) (off-resonance) Raman scattering and (b) resonance Raman scattering.* $|g\rangle$ *and* $|e\rangle$ *stand for electronic ground and excited states, respectively.* $|I\rangle$, $|N\rangle$ *and* $|F\rangle$ *are the initial, intermediate and final vibrational states, respectively. The dashed line represents the virtual intermediate state.*

In this chapter, the theoretical background of resonance Raman spectroscopy is reviewed, and three commonly used methods for simulating resonance Raman spectra are introduced. Second, the applications of resonance Raman spectroscopy will be introduced, where the focus is on both biological molecules, e.g., nucleic acids and proteins, and inorganic molecules, e.g., transition metal complexes. Finally, the methods developed and research carried out as part of this thesis in the area of computational simulations of resonance Raman spectroscopy will be outlined.

1.1 Theoretical Background

1.1.1 Kramer-Heisenberg-Dirac equation

In Raman and resonance Raman spectra, the spectral intensity, corresponding to the transition $i \rightarrow f$, is proportional to the square of the modulus of the transition polarizability, $|\alpha_{i\rightarrow f}|^2$. Although there are a plethora of methods used to compute

the transition polarizability, most of them begin with the Kramer-Heisenberg-Dirac (KHD) equation,[3–5]

$$\alpha_{i\to f} = \frac{1}{\hbar}\sum_n \left[\frac{\langle f|\mu|n\rangle\langle n|\mu|i\rangle}{\omega_{nf}+\omega} + \frac{\langle f|\mu|n\rangle\langle n|\mu|i\rangle}{\omega_{ni}-\omega}\right], \tag{1.1}$$

where $|i\rangle$, $|n\rangle$ and $|f\rangle$ are the initial, intermediate and final vibronic states, respectively, ω_{jk} is the frequency corresponding to the energy differences between states j and k, and ω is the frequency of the incident radiation. The KHD equation is developed and, thus, named after three scientists, Kramer, Heisenberg[3,4] and Dirac.[5] Although the derivation of KHD equation has been presented in many standard textbooks,[1,6,7] for the completeness of understanding, its derivation is outlined in this introduction.

To derive Equation 1.1, we start with evaluating the transition dipole moment, $\langle\psi_f(t)|\mu|\psi_i(t)\rangle$, using the time-dependent wavefunction. The following derivation is in the framework of first-order time-dependent perturbation theory (TDPT). In TDPT, the wavefunction of the vibronic state i can be expressed as a combination of unperturbed states,

$$|\psi_i(t)\rangle = \sum_n c_n^i(t)e^{-\mathrm{i}E_n t/\hbar}|n\rangle. \tag{1.2}$$

The time dependent coefficients, $c_n^i(t)$, are given by

$$c_n^i(t) = \delta_{ni} - \frac{\mathrm{i}}{\hbar}\int_0^t \mathrm{d}t' e^{\mathrm{i}\omega_{ni}t'}V_{ni}(t'), \tag{1.3}$$

where V_{ni} is the matrix element of the perturbation.

The perturbation is defined as $V = \mu E$, where μ is the dipole moment operator and $E = \frac{E_0}{2}(e^{-\mathrm{i}\omega t} + e^{\mathrm{i}\omega t})$ is the electric field. Therefore, the matrix element of the perturbation, V_{ni}, is given as

$$\begin{aligned} V_{ni}(t) &= \frac{-1}{2}\langle n|\mu E_0|i\rangle(e^{\mathrm{i}\omega t} + e^{-\mathrm{i}\omega t}) \\ &= \frac{-1}{2}\langle n|\mu|i\rangle(e^{\mathrm{i}\omega t} + e^{-\mathrm{i}\omega t})E_0 \\ &= -\frac{\mu_{ni}E_0}{2}(e^{\mathrm{i}\omega t} + e^{-\mathrm{i}\omega t}). \end{aligned} \tag{1.4}$$

After substituting V_{ni} into Eq (1.3), the coefficients are given as

$$\begin{aligned} c_n^i(t) &= \delta_{ni} + \frac{i\mu_{ni}E_0}{2\hbar}\int_0^t \mathrm{d}t' e^{\mathrm{i}\omega_{ni}t'}(e^{\mathrm{i}\omega t'} + e^{-\mathrm{i}\omega t'}) \\ &= \delta_{ni} + \frac{\mu_{ni}E_0}{2\hbar}\left[\frac{e^{\mathrm{i}(\omega+\omega_{ni})t}-1}{\omega+\omega_{ni}} - \frac{e^{-\mathrm{i}(\omega-\omega_{ni})t}-1}{\omega-\omega_{ni}}\right]. \end{aligned} \tag{1.5}$$

Therefore, Eq 1.2 can be written as

$$\begin{aligned} |\psi_i(t)\rangle &= e^{-\mathrm{i}E_i t/\hbar}|i\rangle + \sum_n \frac{\mu_{ni}E_0}{2\hbar}\left[\frac{e^{\mathrm{i}(\omega+\omega_{ni})t}-1}{\omega+\omega_{ni}} - \frac{e^{-\mathrm{i}(\omega-\omega_{ni})t}-1}{\omega-\omega_{ni}}\right] e^{-\mathrm{i}E_n t/\hbar}|n\rangle \\ &= e^{-\mathrm{i}E_i t/\hbar}\left\{|i\rangle + \sum_n \frac{\mu_{ni}E_0}{2\hbar}\left[\frac{e^{\mathrm{i}\omega t}-e^{-\mathrm{i}\omega_{ni}t}}{\omega+\omega_{ni}} - \frac{e^{-\mathrm{i}\omega t}-e^{-\mathrm{i}\omega_{ni}t}}{\omega-\omega_{ni}}\right]|n\rangle\right\}. \end{aligned} \tag{1.6}$$

Under the rotating wave approximation (RWA), we can drop the $e^{-\mathrm{i}\omega_{ni}t}$ term. Therefore, the resulting wavefunction becomes

$$|\psi_i(t)\rangle = e^{-\mathrm{i}E_i t/\hbar}\left\{|i\rangle + \sum_n \frac{\mu_{ni}E_0}{2\hbar}\left[\frac{e^{\mathrm{i}\omega t}}{\omega+\omega_{ni}} - \frac{e^{-\mathrm{i}\omega t}}{\omega-\omega_{ni}}\right]|n\rangle\right\}. \tag{1.7}$$

Similarly, the wavefunction for final state f, can be written as

$$\langle\psi_f(t)| = e^{\mathrm{i}E_f t/\hbar}\left\{\langle f| + \sum_n \frac{\mu_{fn}E_0}{2\hbar}\left[\frac{e^{-\mathrm{i}\omega t}}{\omega+\omega_{nf}} - \frac{e^{\mathrm{i}\omega t}}{\omega-\omega_{nf}}\right]\langle n|\right\}. \tag{1.8}$$

If the time-dependent wavefunction, $|\psi_i(t)\rangle$ and $\langle\psi_f(t)|$ (Eqs 1.7 and 1.8) are substituted into the expression for transition dipole moment, $\langle\psi_f(t)|\mu|\psi_i(t)\rangle$, we obtain

$$\begin{aligned} \langle\psi_f(t)|\mu|\psi_i(t)\rangle &= e^{\mathrm{i}\omega_{fi}t}\Bigg\{\langle f|\mu|i\rangle \\ &\quad + \frac{E_0}{2\hbar}\sum_n \mu_{fn}\mu_{ni}\left[\frac{e^{\mathrm{i}\omega t}}{\omega+\omega_{ni}} - \frac{e^{-\mathrm{i}\omega t}}{\omega-\omega_{ni}}\right] + \frac{E_0}{2\hbar}\sum_n \mu_{ni}\mu_{fn}\left[\frac{e^{-\mathrm{i}\omega t}}{\omega+\omega_{nf}} - \frac{e^{\mathrm{i}\omega t}}{\omega-\omega_{nf}}\right]\Bigg\} \\ &= e^{\mathrm{i}\omega_{fi}t}\Bigg\{\mu_{fi}^{\mathrm{perm}} \\ &\quad + \frac{1}{2}\sum_n\left[\frac{1}{\hbar}\left(\frac{\mu_{fn}\mu_{ni}}{\omega+\omega_{ni}} - \frac{\mu_{ni}\mu_{fn}}{\omega-\omega_{nf}}\right)e^{\mathrm{i}\omega t} + \frac{1}{\hbar}\left(\frac{\mu_{ni}\mu_{fn}}{\omega+\omega_{nf}} - \frac{\mu_{fn}\mu_{ni}}{\omega-\omega_{ni}}\right)e^{-\mathrm{i}\omega t}\right]E_0\Bigg\} \\ &= e^{\mathrm{i}\omega_{fi}t}\left(\mu_{fi}^{\mathrm{perm}} + \mu_{fi}^{\mathrm{ind}}\right). \end{aligned} \tag{1.9}$$

The leading term in the curly brace of Eq 1.9 gives the transition matrix element of the permanent transition dipole moment between the initial state i and final state f, $\mu_{fi}^{\text{perm}} = \langle f|\mu|i\rangle$, and the second term gives the induced transition dipole moment. Therefore,

$$\begin{aligned}\mu_{fi}^{\text{ind}} &= \frac{1}{2}\sum_n \left[\frac{1}{\hbar}\left(\frac{\mu_{fn}\mu_{ni}}{\omega+\omega_{ni}} - \frac{\mu_{ni}\mu_{fn}}{\omega-\omega_{nf}}\right)e^{\mathrm{i}\omega t} + \frac{1}{\hbar}\left(\frac{\mu_{ni}\mu_{fn}}{\omega+\omega_{nf}} - \frac{\mu_{fn}\mu_{ni}}{\omega-\omega_{ni}}\right)e^{-\mathrm{i}\omega t}\right]E_0 \\ &= \frac{1}{2}\sum_n \left[\frac{1}{\hbar}\left(\frac{\mu_{ni}\mu_{fn}}{\omega_{nf}+\omega} + \frac{\mu_{fn}\mu_{ni}}{\omega_{ni}-\omega}\right)e^{-\mathrm{i}\omega t} + \frac{1}{\hbar}\left(\frac{\mu_{fn}\mu_{ni}}{\omega_{ni}+\omega} + \frac{\mu_{ni}\mu_{fn}}{\omega_{nf}-\omega}\right)e^{\mathrm{i}\omega t}\right]E_0.\end{aligned} \tag{1.10}$$

If we define the first term in the square bracket as $\alpha_{i\to f}$

$$\alpha_{i\to f} = \frac{1}{\hbar}\sum_n \left(\frac{\mu_{ni}\mu_{fn}}{\omega_{nf}+\omega} + \frac{\mu_{fn}\mu_{ni}}{\omega_{ni}-\omega}\right), \tag{1.11}$$

and utilize the relationship that $\alpha_{i\to f} = \alpha_{f\to i}^*$ (Hermitian), Eq 1.10 becomes

$$\begin{aligned}\mu_{fi}^{\text{ind}} &= \frac{1}{2}\left[\alpha_{i\to f}e^{-\mathrm{i}\omega t} + \alpha_{f\to i}^* e^{\mathrm{i}\omega t}\right]E_0 \\ &= \alpha_{i\to f}\frac{E_0}{2}(e^{-\mathrm{i}\omega t} + e^{\mathrm{i}\omega t}) \\ &= \alpha_{i\to f}E.\end{aligned} \tag{1.12}$$

Hence, we confirmed the quantity we defined previously, $\alpha_{i\to f}$, is the transition polarizability, and the quantity defined by Eq 1.11 is the KHD equation.

1.1.2 Approximations and further simplifications

To utilize the KHD equation in practical computations, Eq 1.11 must be simplified further using several approximations. These approximations include the Born Oppenheimer (BO) approximation, the Condon approximation and the resonance condition.

Since $|i\rangle, |n\rangle$ and $|f\rangle$ in Eq 1.11 are all vibronic wavefunctions, according to the BO approximation, these wavefunctions can be separated into electronic and nuclear contributions, and the overall vibronic wavefunction can be written as the product of these two parts. Therefore, we have

$$\begin{aligned}|i\rangle &= |\psi_g(r;Q)\rangle|\chi_I^g(Q)\rangle \equiv |g\rangle|I\rangle \\ |n\rangle &= |\psi_e(r;Q)\rangle|\chi_N^e(Q)\rangle \equiv |e\rangle|N\rangle \\ |f\rangle &= |\psi_g(r;Q)\rangle|\chi_F^g(Q)\rangle \equiv |g\rangle|F\rangle,\end{aligned} \tag{1.13}$$

where $|g\rangle$ and $|e\rangle$ are the electronic wavefunctions for the ground and excited states, respectively; $|I\rangle$, $|N\rangle$ and $|F\rangle$ are the vibrational wavefunctions for the ith, nth, and fth state.

Accordingly, the transition dipole moments in Eq 1.11 can be evaluated under the BO approximation as

$$\begin{aligned} \mu_{fn} &= \langle f|\mu|n\rangle = \langle Fg|\mu|eN\rangle = \langle F|\langle g|\mu|e\rangle|N\rangle = \langle F|\mu_{ge}|N\rangle \\ \mu_{ni} &= \langle N|\mu_{ge}|I\rangle, \end{aligned} \tag{1.14}$$

where μ_{ge} is the transition dipole moment evaluated with respect to the electronic wavefunction.

Since μ_{ge} parametrically depends on the normal mode coordinate Q, it can be expanded in a Taylor series along the normal mode coordinate,

$$\mu_{ge}(Q) = \mu_{ge}^0 + \sum_{k=1}^{3N-6} \left(\frac{\partial \mu_{ge}}{\partial Q_k}\right)_0 Q_k + \cdots, \tag{1.15}$$

where the subscript 0 indicates the equilibrium position.

Invoking the Condon approximation, only the leading term in Eq 1.15 is kept and the rest of the terms are neglected. Therefore, the transition dipole moments in Eq 1.14 are further reduced to

$$\begin{aligned} \mu_{fn} &= \mu_{ge}^0 \langle F|N\rangle \\ \mu_{ni} &= \mu_{ge}^0 \langle N|I\rangle, \end{aligned} \tag{1.16}$$

where the overlaps between the vibrational wavefunctions, i.e., $\langle F|N\rangle$ and $\langle N|I\rangle$ are known as Frank Condon (FC) Factors.

In the resonance Raman process, the energy of the incident photon is very close to the electronic transition energy, $\omega_{ni} \approx \omega$, so the second term in the brace of Eq 1.11 becomes the dominant term. Based on this resonance condition, the second term is kept and the first can be neglected. After these three approximations are applied, the KHD equation can be written as

$$\alpha_{i\to f} = \frac{(\mu_{ge}^0)^2}{\hbar} \sum_N \left(\frac{\langle F|N\rangle\langle N|I\rangle}{\omega_{ni} - \omega}\right). \tag{1.17}$$

Finally, rewriting ω_{ni} as $\omega_{ge} + \omega_n - \omega_i$, and adding a damping term $-\mathrm{i}\Gamma$ in the denominator of 1.17, the polarizability in resonance Raman spectroscopy can be written

as

$$\alpha_{i\to f} = \frac{(\mu_{ge}^0)^2}{\hbar} \sum_N \left(\frac{\langle F|N\rangle\langle N|I\rangle}{\omega_{ge} + \omega_n - \omega_i - \omega - \mathrm{i}\Gamma} \right), \tag{1.18}$$

where Γ is the linewidth parameter characterizing homogeneous and inhomogenous broadening. Equation 1.18 is also referred to as the Albrecht A term in the literature.[8,9]

The resonance Raman spectrum can be simulated directly by computing each term in the KHD equation (Eq 1.11) or in its simplified version, i.e. Eq 1.18. Since in this formalism, one needs to sum over each of the intermediate vibrational states and determine the overlap between them, this approach is often called the "sum-over-states approach."[2] The resonance Raman excitation profile, $\sigma(\omega)$, can be defined as

$$\sigma(\omega) = \frac{8\pi e^4 \omega_s^3 \omega}{9c^4} |\alpha_{i\to f}|^2, \tag{1.19}$$

where ω_s is the frequency of the scattered photon, e is the charge of electron and c is the speed of light.

1.1.3 Time-dependent wave packet approach

Since the sum-over-states (time-independent) approach can be computationally expensive to implement in practice, one may wish to simulate resonance Raman spectra in the time domain. This alternative approach, based on the time-dependent wave packets, was initially developed by Heller,[10] and applied to resonance Raman spectroscopy simulations by Lee and Heller.[10,11] In this approach, the KHD equation is converted from the frequency domain into the time domain, and the resonance Raman spectra are simulated by determining wave packet dynamics on the electronically excited state.

To derive the time dependent formalism, we first need to recognize the following half-Fourier relationship,

$$\frac{1}{\mathrm{i}(\omega - \mathrm{i}\Gamma)} = \int_0^\infty e^{-\mathrm{i}(\omega - \mathrm{i}\Gamma)t} \mathrm{d}t. \tag{1.20}$$

Using the half-Fourier relationship, Eq 1.18 can be rewritten as

$$\alpha_{i\to f} = \mathrm{i}\frac{(\mu^0_{ge})^2}{\hbar}\int_0^\infty \mathrm{d}t \sum_N \langle F|N\rangle\langle N|I\rangle \exp\left[-\mathrm{i}(\omega_{ge}+\omega_n-\omega_i-\omega-\mathrm{i}\Gamma)t\right]. \quad (1.21)$$

Since

$$\langle N|\exp\left[-\mathrm{i}(\omega_{ge}+\omega_n)t\right] = \langle N|\exp\left[-\frac{\mathrm{i}(E_{ge}+E_n)t}{\hbar}\right] = \langle N|\exp\left[-\frac{\mathrm{i}Ht}{\hbar}\right], \quad (1.22)$$

where H is the excited state vibrational Hamiltonian, and $\exp\left[-\frac{\mathrm{i}Ht}{\hbar}\right]$ is a time propagator (with a phase factor $\exp\left[-\frac{\mathrm{i}(E_{ge})t}{\hbar}\right]$), we can rewrite Eq 1.21 as

$$\alpha_{i\to f} = \mathrm{i}\frac{(\mu^0_{ge})^2}{\hbar}\int_0^\infty \mathrm{d}t \sum_N \langle F|N\rangle\langle N|e^{-\mathrm{i}Ht/\hbar}|I\rangle \exp\left[\mathrm{i}(\omega_i+\omega+\mathrm{i}\Gamma)t\right]. \quad (1.23)$$

If we consider the propagator $e^{-\mathrm{i}Ht/\hbar}$ to act on the right hand side, then $\alpha_{i\to f}$ can be determined in the time domain as

$$\alpha_{i\to f} = \mathrm{i}\frac{(\mu^0_{ge})^2}{\hbar}\int_0^\infty \mathrm{d}t\langle F|I(t)\rangle \exp\left[\mathrm{i}(\omega_i+\omega)t\right]\exp(-\Gamma t), \quad (1.24)$$

where $|I(t)\rangle \equiv e^{-\mathrm{i}Ht/\hbar}|I\rangle$ is a time dependent vibrational wave packet that evolves on the excited state.

1.1.4 Transformation theory

Transformation theory simulates resonance Raman spectroscopy by exploiting the relationship between the optical absorption spectrum and the resonance Raman spectrum. This approach was developed independently by the groups of Blazej and Peticolas,[12] and Tonks and Page.[13,14] Transformation theory is based on the facts that (1) the cross section of the optical absorption spectrum is proportional to the imaginary part of the Rayleigh scattering amplitude, (2) the polarizability of the Raman scattering process can be written in terms of real and imaginary parts of the Rayleigh scattering amplitude, and (3) the real and imaginary parts of the Rayleigh scattering amplitude are related by the Kramers-Kronig (KK) transformation. Therefore,

if the KK transform is applied to information in the optical absorption spectrum, the resulting mathematical relationship would be an expression that connects the polarizability and the absorption cross section.

The polarizability determined using transformation theory is given as

$$\alpha_{0\to1} = \mu_{ge}^2 \frac{\Delta_1}{\sqrt{2}} \left[\Phi(\omega) - \Phi(\omega - \omega_1)\right], \tag{1.25}$$

where ω_1 is the vibrational frequency of the (Raman active) normal mode, and Δ_1 is the dimensionless displacement of this mode (for the definition see Section 1.1.5). The function Φ is defined as

$$\Phi(\omega) = \mathrm{i}\pi \frac{\sigma_A(\omega)}{\omega} + P\left(\int_0^\infty \frac{\sigma_A(\omega')}{\omega'(\omega' - \omega)} \mathrm{d}\omega'\right), \tag{1.26}$$

where $\sigma_A(\omega)$ is the absorption cross section at the incident frequency ω and P denotes the Cauchy principal value integral.

The three main approaches introduced in this chapter (sum-over-states, time dependent, and transformation theory) are related to each other. The relationship is clarified and illustrated by Myer et al., see Figure 2 in Ref 2. To the best of our knowledge, among the three approaches, only the time dependent approach has been coded in (commercial or freely) available software packages including ORCA,[15,16] NWCHEM,[17,18] and ADF,[19–22] while the codes for the other two approaches have not been made available for public use. More detailed discussions of the three approaches can be found in Refs 2 and 23.

Besides the three common approaches for simulating resonance Raman spectra, there are also other methods, such as the Shorygin method[23] and Savin's Equation.[23–26] Combining the polarizability theory and the dispersion equation, Shorygin developed a semiclassical approach for computing the resonance Raman intensities via the vibrational frequencies and normal mode displacements (for the definition see Section 1.1.5). Savin developed equations for simulating the resonance Raman intensities in the pre-resonance region ($\omega \lesssim \omega_{ge}$). Due to the limitation of their accuracies in the simulations of resonance Raman spectra, these two methods will not be

elaborated further. More detailed discussions about these two methods can be found in Ref 23.

1.1.5 Independent mode displaced harmonic oscillator model

From the discussions above, the use of the sum-over-states approach requires computing FC factors, i.e., $\langle F|N\rangle$ and $\langle N|I\rangle$. Meanwhile, the time dependent formalism also relies on the determination of the FC factor, $\langle F|I(t)\rangle$, which describes the wave packet propagation. Since the vibrational wavefunctions in these overlaps are multi-dimensional functions in terms of $3N-6$ normal mode coordinates, evaluating these overlaps could be computationally costly. To solve this problem, the FC factors can be evaluated via the independent mode displaced harmonic oscillator (IMDHO) model. This model is also used in the derivation of transformation theory.

Here the use of the IMDHO model is only shown within the time dependent formalism, and its use in the sum-over-states approach and transformation theory can be found in Refs 2, 27 and 28, respectively. Using the IMDHO model, the overlap with $3N-6$ variables, $\langle F|I(t)\rangle$, can be written as products of $3N-6$ independent one dimensional overlaps,

$$\langle F|I(t)\rangle = \prod_{k=1}^{3N-6} \langle F_k|I_k(t)\rangle. \tag{1.27}$$

If we assume the vibrational modes have no frequency shifts upon electronic excitation, then each overlap integral between two one dimensional harmonic oscillators in Eq 1.27 can be readily evaluated to give[29]

$$\langle F|I(t)\rangle = \prod_{k=1}^{3N-6} \left\{ \frac{(-1)^{m_k}\Delta_k^{m_k}}{\sqrt{2^{m_k}m_k!}}(1-e^{-\mathrm{i}\omega_k t})^{m_k} \right\} e^{-\sum_k \frac{\Delta_k^2}{2}(1-e^{-\mathrm{i}\omega_k t})} e^{-\mathrm{i}\omega_i t - \mathrm{i}\omega_{ge} t}, \tag{1.28}$$

where Δ_k is the the displacement between ground and excited-state potential minima in dimensionless normal coordinates of the kth mode, and m_k is the excitation number of the kth mode in the vibrational state $|F\rangle$.

Applying the expression above to Eq 1.24, we obtain the final expression of the

transitional polarizability in the time-dependent approach,

$$\begin{aligned}\alpha_{i\to f} =& \frac{\mathrm{i}}{\hbar}(\mu_{ge}^{0})^{2}\prod_{k=1}^{3N-6}\left\{\frac{(-1)^{m_k}\Delta_k^{m_k}}{\sqrt{2^{m_k}m_k!}}\right\}\times \\ & \int_0^{\infty}\mathrm{d}t\prod_{k=1}^{3N-6}\left\{(1-e^{-\mathrm{i}\omega_k t})^{m_k}\right\}e^{-\sum_k\frac{\Delta_k^2}{2}(1-e^{-\mathrm{i}\omega_k t})+\mathrm{i}(\omega-\omega_{ge})t-\Gamma t}.\end{aligned} \tag{1.29}$$

1.1.6 Determination of dimensionless normal mode displacements

Since Δ represents the shift in origin (equilibrium position) between the ground and excited electronic states along the normal modes, the values of Δ along each normal coordinate can be determined via electronic structure calculations. In the following, we introduce three approaches to compute the values of Δ.

(1) The first method is to determine the normal mode displacements by comparing the ground and excited state optimized geometries. The structure of the molecule needs to be optimized in both ground and excited electronic states, and the differences between these two optimized structures are determined in Cartesian coordinates. These differences can then be projected onto the normal mode coordinates via a transformation matrix,

$$\mathbf{\Delta_Q} = \mathbf{L}^{\intercal}\mathbf{D}^{(\mathbf{m})}, \tag{1.30}$$

where $\mathbf{D}^{(\mathbf{m})}$ is the vector that contains the mass weighted differences in the Cartesian coordinates, and $\mathbf{L}$ is the transformation matrix between mass-weighted Cartesian and normal coordinates. Therefore, the displacement along normal modes can be determined and stored in matrix $\mathbf{\Delta_Q}$.

(2) The second method is to compute the normal mode displacement via the Cartesian excited state gradients at the vertical excitation geometry, i.e., ground state equilibrium geometry. In this method, it is assumed that the shift of the molecule from the vertical excitation geometry to the excited state minimum is accomplished by one single Newton-Raphson step. Therefore, the shift between the

ground and excited state minima is governed solely by the gradient at the vertical excitation geometry. If the normal modes are assumed to be parallel and the frequencies are the same for ground and excited states, the excited state gradients and the normal mode displacements can be related by

$$\mathbf{\Delta_Q} = \mathbf{\Lambda^{-1} T^{\intercal} M^{-1/2} V_X}. \tag{1.31}$$

Here $\mathbf{\Delta_Q}$ is the matrix of ground state normal mode displacements, $\mathbf{\Lambda}$ is the diagonal matrix of eigenvalues of the mass weighted Hessian, $\mathbf{T}$ is the matrix of eigenvectors of the mass weighted Hessian, $\mathbf{M}$ is the diagonal matrix of the atomic masses, and $\mathbf{V_X}$ is the energy gradient of the excited state in Cartesian coordinates. The excited state gradients can be determined directly from a variety of electronic structure theory approaches. Note that since the normal mode coordinates are assumed to remain the same for the ground and excited state, we neglected the possible mixing or rotation of normal modes coordinates upon excitation, as known as the Duschinsky effect.

(3) The third method is to evaluate the excited state potential energy surface along each normal mode and then determine the displacement based on the structure of the surface.

Method (1) requires excited state geometry optimizations, which can be computationally expensive, and also can lead to reordering of the relative energies of the excited states involved in the transitions as one moves away from the FC region. Scanning the excited state PES in method (3) is also computationally expensive. In contrast, method (2) only requires the computation of gradients in the excited state. Therefore, we chose method (2) over (1) and (3) for the simulation of the resonance Raman spectra in this thesis.

1.2 Applications of Resonance Raman Spectroscopy

Resonance Raman spectroscopy has been applied in many different fields, because of the structural and dynamical information that it can provide.[25,30–34] In this section,

two classes of molecules for which resonance Raman spectroscopy has been extensively applied are briefly discussed: (i) biological molecules, such as nucleic acids and proteins, and (ii) inorganic compounds such as transition metal complexes. Through the brief introduction to previous applications, the power and utility of resonance Raman spectroscopy will be highlighted.

1.2.1 Biological molecules

Nucleic acids

Nucleic acids are of pivotal importance in chemical and biological processes, because of their roles as carriers of genetic information. Due to the short excited state life times of nucleic acids, resonance Raman spectroscopy which probes short-time dynamics plays a complementary role to other time-resolved spectroscopies, e.g. pump probe spectroscopy and UV-vis absorption spectroscopy, in investigating the excited state structure and dynamics of nucleic acids. The applications of resonance Raman spectroscopy for nucleic acids range from small molecules, such as individual nucleobases, nucleosides, and nucleotides (see Figures 1.2 and 1.3 for the relevant structures) to biological macromolecule such as DNA and RNA.

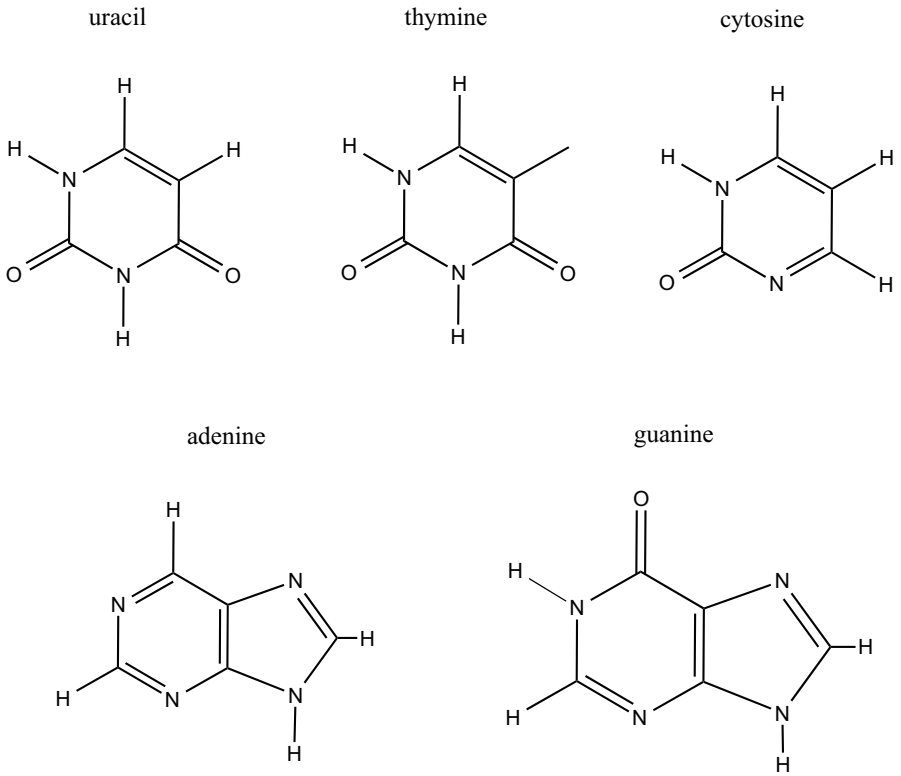

Figure 1.2: *Chemical structures of the nucleobases.*

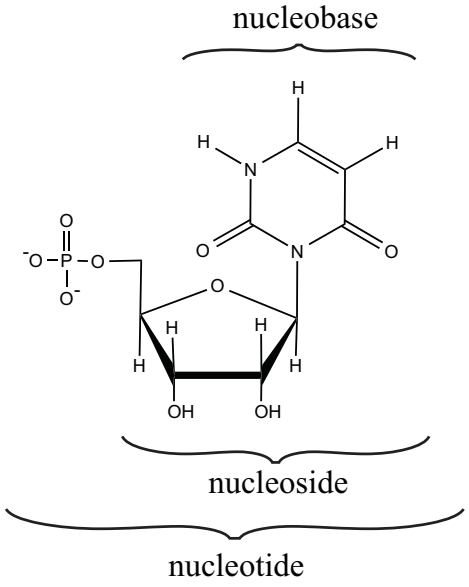

Figure 1.3: *Relationship between the chemical structures of nucleobase, nucleoside and nucleotide, using uracil as an example.*

The experimental resonance Raman spectra of all the isolated nucleobases (uracil, thymine, cytosine, adenine, and guanine) have been measured by various groups.[35–43] Peticolas and co-workers measured the experimental resonance Raman spectra of uracil[36] and thymine.[37] These were compared to simulated spectra computed using transformation theory. The Loppnow group extracted the excited state normal mode displacements from the experimentally measured spectra of uracil,[43] thymine[44] and cytosine[45] via fitting procedures based on the time-dependent formalism. The research groups of Loppnow[38–40] and Zheng[46] also independently investigated the effects of site-specific deuteration and methylation on the resonance Raman spectra of deuterated/methylated uracil and thymine. In the nucleosides and nucleotides, the role of sugar and phosphate, and the corresponding vibrational coupling, have been examined. The research groups of Peticolas,[47,48] Nishimura[49] and Spiro[50,51] studied the resonance Raman spectra and excitation profiles of adenine monophosphate, uridine, cytidine and guanidine. More recently, Zhu et al.[52] measured and compared the resonance Raman spectra of thymine and thymidine, and found that the total

reorganization energy of thymidine is smaller than thymine. They attributed this difference to the shift of the excited state potential energy surface of thymidine.

Resonance Raman spectroscopy is also used to study the structures and dynamics of DNAs and RNAs. Using both Raman and resonance Raman spectroscopy, Thomas and co-workers determined the secondary structure polymorphism of Oxytricha telomeric DNA sequence, and probed the concentration dependence of the transition between different DNA conformations.[31,53] The interaction between DNA and small molecules such as drugs, e.g., andriamycin,[54] distamycin[55] and hypercin,[56] have also been studied using resonance Raman spectroscopy. A more detailed review about the applications of resonance Raman spectroscopy to nucleic acids can be found in Ref. 31.

Peptides and proteins

Resonance Raman spectroscopy can also be utilized to investigate the secondary structure and folding mechanism(s) of peptides and proteins.[32] The mechanism of protein folding is one of the most important biological problems. As a key step in protein folding, the formation of protein secondary structures can not only provide insight into the biological function, but also give guidance for the potential applications of peptides and proteins in drug design or medical treatment.[57,58]

Several groups showed that resonance Raman spectra are sensitive to the conformations of proteins and peptides, and there are close correlations between spectral features and protein secondary structures.[59–63] For example, Asher and co-workers studied the structure of α-helical poly-L-glutamic (PGA) during the unfolding process when temperature was increased.[59] They found that Amide I, II, III, and C bands in PGA changed spectral features, i.e., peak positions, intensities and broadenings, as the temperature increased.[59–61] They also studied the correlation between Amide III frequencies and the Ramachandran angle, and use this to determine a quantitative relationship between the Ramachandran angle and temperature.[59,62]

The combination of resonance Raman spectroscopy with Temperature jump (T-jump) kinetic studies can also serve as a powerful tool to examine the protein fold-

ing/unfolding process.[64–66] Lednev, Karnoup and Asher et al. combined resonance Raman spectra and the T-jump kinetic study to examine the unfolding conformational change of the AP peptide.[64,65] Spiro and co-workers investigated the unfolding of apomyoglobin using 197 nm and 229 nm excitations for resonance Raman spectroscopy combined with a kinetic T-jump study.[66]

Recently, resonance Raman spectroscopy has been used to explore and understand the interactions between drugs and proteins. For example, Hashimoto et al.[67] studied the interactions between human serum albumin and drugs such as warfarin, ibuprofen and palmitate. Couling et al.[68] studied three drug-protein systems, dihydrofolate reductase with its inhibitor trimethoprim, gyrase with novobiocin, and catechol O-methyltransferase with dinitrocatechol.

Although resonance Raman spectroscopy has been shown to be a powerful tool for the experimental study of the structure and dynamics of biological molecules, most of the computational simulations have been restricted to small molecules such as nucleobases and nucleosides,[27,36,37,50,69,70] rather than large molecule such as DNA, RNA or proteins, due to the high computational cost for large biological molecules. Recently, the research group of Mukamel developed a QM/MM approach that can be utilized in simulating resonance Raman spectra of larger biological molecules. The spectra of a series of peptides (and proteins), such as β-sheet amyloid fibrils,[71] trp-cage peptide[72] and photoactive yellow protein,[73] have been benchmarked using this method. This provides a very promising method to simulate the resonance Raman spectra of large (biological) molecules.

1.2.2 Transition metal complexes

For transition metal complexes, resonance Raman spectroscopy is commonly used for investigating their charge transfer processes.[25] These charge transfer transitions include metal-to-ligand charge transfer transitions (MLCT), ligand-to-metal charge transfer transitions (LMCT), ligand-to-ligand charge transfer transitions (LLCT), and metal-to-metal (intervalence) charge transfer transitions (MMCT).

Here we select a few examples of studies on the charge transfer transitions in

metal complexes to highlight the utility of resonance Raman spectroscopy for underlining the photophysical behaviour in these systems. More detailed and thorough reviews can found in Refs 25 and 23. Spiro et al.[74] studied the MLCT in a bis(pyridine)iron(II) heme. Although this complex has weak features in its absorption spectrum, strong Raman transitions are observed on the pyridine ligand as well as the iron-pyridine stretch, and a Fe(II)→pyridine charge-transfer band can be assigned. Loppnow and coworkers[75] measured the resonance Raman excitation profile of the blue copper protein plastocyanin. The Cys→Cu LMCT process was investigated using a fitting procedure that extracted the reorganization energy from the experimental resonance Raman spectrum. Wootton and Zink[76] reported the LLCT bands in the resonance Raman spectra of two metal diimine dithiolate complexes. They calculated the distortions in the ligands using experimental absorption spectroscopy in conjunction with experimental resonance Raman spectroscopy, and assigned the electronic transitions to LLCT. Lubitz et al.[77] obtained the resonance Raman spectra of (dppe)Ni(μ−pdt)Fe(CO)$_3$ and [(dppe)Ni(μ−pdt)(μ−H)Fe(CO)$_3$][BF$_4$], which revealed the vibrational modes of the [NiFe] hydrogenase active site. Comparing with the theoretical spectra, the dominant electronic transitions in the visible wavelengths were identified as MMCT and MLCT.

The computational resonance Raman spectra for transition metal complexes have been simulated using sum-over-state and time-dependent approaches. For example, Barone et al.[78] simulated the resonance Raman spectrum of [Ru(bpy)$_3$]$^{2+}$, see Figure 1.4 for the corresponding structre, via the sum-over-state formalism, and Jensen et al.[79] studied the spectrum of the same complex using the time-dependent approach.

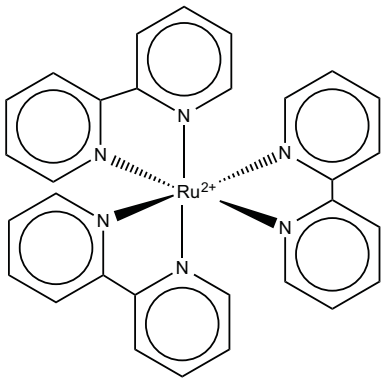

Figure 1.4: *Chemical structure of [Ru(bpy)$_3$]$^{2+}$.*

1.3 Outline of the Following Chapters

Although resonance Raman spectroscopy has been used as a powerful tool in studying the structure and dynamics of molecules, extracting the structural and dynamical information requires assistance from quantum chemical computations. The experimental resonance Raman spectra for uracil,[35,43] 5-halogenated uracils,[80] and thymine[44,52] have been measured by several groups, but there are only a few computational studies on the resonance Raman spectra of these compounds. None of these studies have used the time-dependent approach; one of them used the sum-over-state approach and the others used transformation theory. In this thesis, we focus on the computational study of the resonance Raman spectra of uracil and its derivatives using the time dependent formalism, see Eq 1.29, based upon the quantum chemical computations. The electronic structure calculations are carried out using density functional theory (DFT) and time-dependent density functional theory (TD-DFT). DFT is used for the ground state optimization and determination of the normal modes, see Eq 1.31. TD-DFT is used for computing the Cartesian gradients in the excited state.

We developed an interface of the resonance Raman computer code (orca_asa[15,16]) in ORCA[81] to GAMESS-US[82,83] and Gaussian,[84] which can be used as a general tool for computing resonance Raman spectra. Therefore, in principle any electronic struc-

ture method that can determine a (numerical or analytical) Hessian can be used to compute the ground state. Similarly, a variety of methods could be used to determine the excited state gradients either analytically, or, in a much more computationally expensive fashion, numerically. Where available, solvation effects can be accounted for via polarizable continuum models (PCM).

In Chapter 2, we investigated the performance of different functionals for the simulation of the resonance Raman spectrum of uracil. Two different functionals, PBE0 and B3LYP, were used to optimize the ground-state equilibrium structure of uracil, and determine the corresponding vibrational frequencies and normal modes. Five functionals, including long range corrected functionals (CAMB3LYP and LC-BLYP), hybrid functionals (B3LYP and PBE0), and Spin Flip-TD-DFT (SF-TD-DFT) with BHHLYP, are used to compute the excited state Cartesian gradients. The resulting resonance Raman spectra are compared with experiment, and the performance of different functionals are evaluated.

In Chapter 3, we studied the 5-halogenated (F, Cl, and Br) uracils and their corresponding simulated resonance Raman spectra. The simulated spectra are compared with the experimental measurements, and the differences between the resonance Raman spectra of the three 5-halogenated uracils, caused by the effect of halogen substitution, are examined in terms of ground state normal mode eigenvectors and excited state Cartesian gradients.

In Chapter 4, we examined the effect of solvation on the resonance Raman spectra of uracil and thymine. Three possible hydrogen bonding sites on uracil and thymine are chosen and non-covalently bonded with one single explicit water. As the resonance Raman spectrum is governed by the ground state normal modes and the excited state Cartesian gradient, we examined how these two factors are changed in different mono water configurations and investigated the correlation to the differences between the spectra.

Chapter 2

Simulation of the Resonance Raman Spectrum For Uracil*

2.1 Introduction

The study of the interaction between ultraviolet (UV) light and the DNA and RNA nucleobases is of great fundamental and applied interest.[85–88] UV light is known to cause photodamage of DNA, and eventually the loss of genomic information.[89–91] The UV-induced damage to DNA has been found to cause health problems known as photocarcinogenesis.[92]

When UV radiation interacts with DNA and RNA bases, they are promoted to electronically excited states. This is the starting point for a series of photochemical and photophysical processes that may lead to further photodamage. Due to the fast non-radiative transitions in the nucleobases that have been studied extensively,[85,88,93] the nucleobases are well-protected from photodamage.

The initial excited state structural dynamics of the nucleobases are also of great interest since they initiate the long-time photodynamics. Experimentally the initial dynamics for the nucleobases on the excited electronic state can be probed by resonance Raman spectroscopy.[30,38,40,41,44,45,80,94–96] By tuning the incident excitation wavelength to be resonant with the electronic transition of the nucleobase studied, the intensity of the Raman spectrum is strongly enhanced. The frequencies and in-

*A version of this chapter was published in the *Journal of Physical Chemistry A*, **2014**, *118*, 9228.

tensities of the peaks in the resonance Raman spectrum provide crucial information on how the normal modes of the nucleobases are driven by the potential of the electronically excited state. However, extracting this information requires assistance from quantum chemical computations. By performing accurate electronic structure computations on the ground state potential energy surface (PES), using, e.g., Density Functional Theory (DFT), and for the excited state, using methods such as Time Dependent Density Functional Theory (TD-DFT), one can determine all the required data needed to compute the resonance Raman spectra of the nuleobases.[16] Importantly, the comparison between the theoretical and experimental spectra provide a more stringent test for the computational method used for the excited electronic state since the agreement is most sensitive to the gradient of the PES rather than simply the vertical excitation energy. In this paper, we focus on uracil in part due to the challenges associated with the computational determination of the states involved in its UV-vis absorption, e.g., reordering of the $\pi \rightarrow \pi^*$ and $n \rightarrow \pi^*$excited states due to solvation.[85,88,97–105] TD-DFT is used to simulate the resonance Raman spectrum of uracil, and to assist in the interpretation of its experimental spectrum.[43] The chemical structure and the atomic indices of uracil are shown in Figure 2.1. Historically there are two methods used to simulate resonance Raman spectra in general, and, more specifically, for uracil. One method is based on the Kramers-Kronig transformation (KK) which gives the relationship between the polarizability and the optical absorption.[27,36,37] The other method is based on the Herzberg-Teller formalism (HT)[16,106] which relies on the short time dynamics of the molecule in the excited electronic state. Both methods require knowledge of the normal mode displacements to the excited state minimum from the ground state minimum. There are two (commonly used) approaches that can determine the normal mode displacements. One is to locate the excited state minimum in order to find out these displacements, and the other approach is to determine the displacements from the gradient of the excited state at the vertical excitation point, when assuming such displacements are due to very "short time" dynamics of nuclei on the excited state. Since the second approach asks for only the excited-state gradient instead of requiring a geometry optimization in the

excited state, it is computationally much more convenient than the first approach. In this paper, we use the excited-state gradients to simulate the resonance Raman spectrum of uracil.

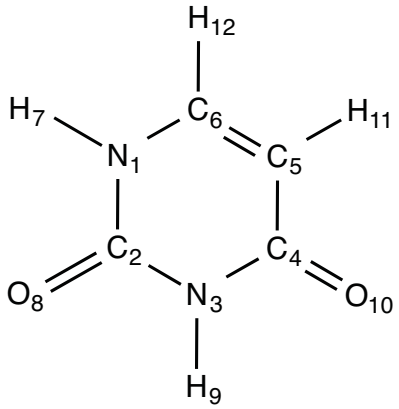

Figure 2.1: *Chemical structure of uracil with atomic numbering used.*

Excited state electronic structure computations of uracil have been carried out utilizing many different levels of theory including both TD-DFT[107,108] and wave-function based methods such as CIS,[109] CASPT2,[110,111] EOM-CCSD,[112] CR-EOM-CCSD(T),[113] CC2[114] and MRCI.[115] Most of these studies focused on the benchmarking of vertical excitation energies[112] or investigating the lifetime and conical intersections of the excited states.[85,93] Only a few simulated the resonance Raman spectrum of uracil.[27,36,37] In 1995, Peticolas and Rush[36,37] simulated the resonance Raman spectrum using the KK transformation, with the ground and excited state properties obtained at the HF/6-31G* and CIS/6-31G* levels of theory, respectively. In 2004, Neugebauer and Hess[27] compared the resonance Raman spectrum using the KK transformation to the spectrum computed by the Savin's equation,[24–26] and they found the spectra by the two methods to be in qualitative agreement. Within the Savin's equation, they determined the excited state gradient at the CIS/6-31G*, MR-MP2/6-31G*, B3LYP/TZVP, and BP86/TZVP levels of theory. They concluded that the results based on CIS agreed with experiment best, and that TD-DFT calculations are problematic because the peak intensity of the C-O stretching at 1754

cm^{-1} is much higher than that measured in the experimental spectrum. However, CIS showed the bright transition for uracil is from S_0 to S_1, whereas this result is inconsistent with most other (gas phase) computations that determine the bright transition to be $S_0 \rightarrow S_2$.[107,108,110,115,116]

The solvent effects on uracil and its excited state properties have been studied using implicit models[97–99,101] and explicit solvent treatments via uracil-water complexes,[101,102,105,117,118] QM/MM,[100] the effective fragment potential water model,[104] and also the fragment molecular orbital method.[103] However, the effect of solvent on the resonance Raman spectrum of uracil has not yet been investigated.

In this paper, we simulated the resonance Raman spectrum of uracil in both the gas phase and implicit water using different functionals via TD-DFT. In particular, we have explored the differences arising in the simulated spectrum due to the use of hybrid (PBE0 and B3LYP) versus long range corrected (CAMB3LYP and LC-BLYP) functionals as well as spin flip TD-DFT.

2.2 Computational Methods

The ground state equilibrium structure of uracil is obtained by geometrical optimization using DFT. The computations were performed via two functionals, PBE0[119,120] and B3LYP,[121–123] with the aug-cc-pVTZ basis set.[124,125] The Hessians of these equilibrium structures were then determined, and the vibrational frequencies and corresponding normal modes were extracted. The potential energy distribution (PED) of the normal modes is analyzed based on PBE0/aug-cc-pVTZ and B3LYP/aug-cc-pVTZ optimized structures, respectively.

TD-DFT computations were carried out using the optimized structures, and the vertical excitation energies and corresponding oscillator strengths of the first three excited states were determined. These excited state calculations are performed using the PBE0, B3LYP, CAMB3LYP[126] and LC-BLYP[127] functionals with the aug-cc-pVTZ basis set. Recent research showed that using spin flip TD-DFT (SF-TD-DFT),[128,129] the conical intersection of uracil can be computed with accuracy competitive with

wavefunction based approaches.[118] Thus, we also performed a computation at the SF-TD-DFT/BHHLYP/aug-cc-pVTZ level of theory and compared results with TD-DFT ones using the functionals listed previously. SF-TD-DFT/BHHLYP/aug-cc-pVTZ is carried out using ROHF[130–135] and the Tamm Dancoff approximation. Since the transition dipole moments are not available for SF-TD-DFT, the dipole moment for computing its resonance Raman spectrum is taken from corresponding value determined with the PBE0 functional.

To determine the resonance Raman spectrum, the energy gradient for the excited electronic state is required. The energy gradient in Cartesian coordinate space is extracted from the TD-DFT calculations.[127,136] The TD-DFT excited state gradients are determined analytically while the SF-TD-DFT gradients must be computed by numerical differentiation. The gradients are computed both in the gas phase and implicit water using the conductor-like Polarizable Continuum Model (C-PCM).[137–140] The gradients are then converted into dimensionless displacement via the following equation:

$$\mathbf{\Delta_Q} = \mathbf{\Lambda^{-1} T^{\intercal} M^{-1/2} V_X}. \tag{2.1}$$

Here $\mathbf{\Delta_Q}$ is the matrix of ground state normal mode displacements, $\mathbf{\Lambda}$ is the diagonal matrix of eigenvalues of the mass weighted Hessian, $\mathbf{T}$ is the eigenvector of the mass weighted Hessian, $\mathbf{M}$ is the diagonal matrix of the atomic masses, and $\mathbf{V_X}$ is the energy gradient of the excited state in Cartesian coordinates from TD-DFT calculations. The normal mode displacements were then converted into dimensionless displacements using

$$\Delta_k = \left(\frac{\Lambda_k}{m_e}\right)^{\frac{1}{4}} \Delta_{Qk}. \tag{2.2}$$

Using data from the electronic structure equations above, the independent harmonic oscillator (IMDHO) model within the Herzberg-Teller short-time dynamics formalism[106] is then applied and the resonance Raman spectrum is simulated under the first order approximation. The incident photon energy is chosen as 266 nm and the fwhm in the simulation is set as 30 cm^{-1}, which is selected to be equal to the fwhm of the single peak in the experimental resonance Raman spectra.[43]

The DFT and TD-DFT computations are carried out using electronic structure calculation software packages ORCA (v.3.0)[81] and GAMESS-US (1May2013),[82,83] respectively. GAMESS-US was used for the TD-DFT computations due to the availability of analytic gradients for all functionals considered. The resonance Raman spectra are determined via the program orca_asa.[15,16] Further details of the theoretical background for the resonance Raman simulation can be found in Ref. 16 and 15. The PED analysis used the VEDA4 software package[141,142] and the Hessians for the PED analysis are computed using Gaussian (G09).[84]

2.3 Results and Discussion

2.3.1 Equilibrium geometry, vibrational frequencies and normal modes

The equilibrium structure and vibrational frequencies of uracil have been the subjects of numerous previous theoretical and experimental studies.[43,143–158] However, to computationally determine the resonance Raman spectrum, the vibrational frequencies, and, more importantly, the corresponding eigenvectors are required, see Eq. 2.1. Computational studies have investigated the roles of explicit and implicit solvation,[149–151,155,158,159] as well as anharmonicity[152,153] on the vibrations. However, while these treatments lead to frequency shifts, Peng et al.[149] suggest that the inclusion of explicit water does not significantly change the vibrational eigenvectors. Hence, we consider gas-phase optimization and determination of Hessians with appropriate scaling of the resulting vibrational frequencies.[160,161]

The equilibrium structure of uracil in the gas phase is determined at the PBE0/aug-cc-pVTZ and B3LYP/aug-cc-pVTZ levels of theory, and the corresponding geometries are given in Table A1 along with the experimental structure;[143,162,163] the Cartesian coordinates of the optimized structures are provided in Tables A2 and A3. Comparing the bond lengths and bond angles, the computed geometries are, not surprisingly, close to experimental data with minor discrepancies. The equilibrium structures are very similar between these two functionals.

The vibrational frequencies of uracil computed based on the geometries above are given in Table 2.1. Note that only the modes required for understanding the experimental resonance Raman spectrum are presented here; data for all modes is available in Table A4 and Table A5 of the Appendix A. The computed frequencies are $\sim 4\%$ higher compared to the experimental frequencies. After applying appropriate scaling factors[160,161] for each functional (the values of the scaling factors are given in Table 2.1), the differences between the scaled frequencies and the experimental results are reduced to $\sim 2\%$. Since the vibrational frequencies in this study are all computed using the harmonic approximation, this could be one of sources of inaccuracies when comparing the theoretical and experimental resonance Raman spectra. A recent study[152] confirmed that although harmonic frequency calculations at the DFT level give overall good accuracy for uracil, e.g. the B3LYP/aug-cc-pVTZ level of theory gives 11 cm^{-1} in mean absolute error compared to experimental values, including anharmonic corrections can further improve the accuracy.

Table 2.1: *Potential Energy Distribution Analysis and Scaled Vibrational Frequencies (ω/cm^{-1}) of Ground State Normal Modes of Uracil. Each Mode is Computed by PBE0/aug-cc-pVTZ (First Line in Each Row) and B3LYP/aug-cc-pVTZ (Second Line in Each Row)*

mode	ω(scaled)[a,b]	PED
7	551	-stretch(N_3-C_4)[10%]+bend(O_8-C_2-N_3)[10%]+bend(O_{10}-C_4-C_5)[23%]+bend(N_3-C_2-N_1)[35%]
	553	-stretch(N_3-C_4)[10%]+bend(O_8-C_2-N_3)[11%]+bend(O_{10}-C_4-C_5)[22%]+bend(N_3-C_2-N_1)[36%]
11	764	out-of-plane(O_8-N_1-N_3-C_2)[79%] [c]
	761	stretch(N_3-C_2)[11%]+stretch(N_1-C_2)[32%]+bend(C_6-N_1-C_2)[22%]
12	765	stretch(N_3-C_2)[10%]+stretch(N_1-C_2)[30%]+bend(C_6-N_1-C_2)[23%]
	762	out-of-plane(O_8-N_1-N_3-C_2)[77%] [c]
18	1159	-stretch(N_1-C_6)[10%]+stretch(N_3-C_2)[14%]-bend(H_7-N_1-C_6)[22%]+bend(H_{12}-C_6-C_5)[30%]
	1153	-stretch(N_3-C_2)[29%]+stretch(N_3-C_4)[22%]+bend(H_7-N_1-C_6)[11%]-bend(H_12-C_6-C_5)[12%]
19	1189	-stretch(N_3-C_2)[16%]+stretch(N_3-C_4)[21%]-bend(H_{11}-C_5-C_4)[27%]
	1187	stretch(N_1-C_6)[15%]+bend(H_{11}-C_5-C_4)[36%]-bend(H_{12}-C_6-C_5)[17%]
20	1331	-bend(H_7-N_1-C_6)[11%]+bend(H_9-N_3-C_4)[33%]-bend(H_{12}-C_6-C_5)[17%]
	1336	-stretch(N_1-C_2)[12%]+bend(H_9-N_3-C_4)[30%]-bend(H_{11}-C_5-C_4)[13%]-bend(H_{12}-C_6-C_5)[11%]
21	1358	bend(H_9-N_3-C_4)[28%]+bend(H_{11}-C_5-C_4)[13%]+bend(H_{12}-C_6-C_5)[19%]
	1359	stretch(N_1-C_2)[15%]-stretch(N_3-C_4)[13%]+bend(C_4-N_3-C_2)[14%]+bend(H_9-N_3-C_4)[19%]+bend(O_8-C_2-N_3)[14%]
22	1370	-stretch(N_1-C_2)[14%]-bend(C_4-N_3-C_2)[18%]+bend(H_7-N_1-C_6)[17%]
	1375	bend(H_7-N_1-C_6)[10%]+bend(H_9-N_3-C_4)[18%]+bend(H_{11}-C_5-C_4)[11%]+bend(H_{12}-C_6-C_5)[31%]
23	1452	-stretch(N_1-C_6)[19%]+stretch(N_1-C_2)[11%]+bend(H_7-N_1-C_6)[30%]+bend(C_5-C_6-N_1)[11%]
	1448	-stretch(N_1-C_6)[18%]+bend(H_7-N_1-C_6)[39%]+bend(C_5-C_6-N_1)[10%]
24	1662	stretch(C_5-C_6)[61%]-bend(H_{12}-C_6-C_5)[10%]
	1616	stretch(C_5-C_6)[60%]-bend(H_{12}-C_6-C_5)[12%]
25	1721	stretch(O_{10}-C_4)[72%]
	1702	stretch(O_{10}-C_4)[70%]
26	1752	stretch(O_8-C_2)[73%]
	1733	stretch(O_8-C_2)[72%]

[a] For normal modes computed using PBE0/aug-cc-pVTZ optimized geometry, vibrational frequencies lower than 1000 cm^{-1} are scaled by 0.9776, and higher than 1000 cm^{-1} are scaled by 0.9676. See Ref. 160.

[b] For normal modes computed using B3LYP/aug-cc-pVTZ optimized geometry, vibrational frequencies lower than 1000 cm^{-1} are scaled by 0.9891, and higher than 1000 cm^{-1} are scaled by 0.9568. See Ref. 161.

[c] out-of-plane(O_8-N_1-N_3-C_2) refers to the angle between the O_8-C_2 vector and the N_1-N_3-C_2 plane.

The normal modes analyzed with their potential energy distributions (PED) are given in Table 2.1. Here we chose a set of internal coordinates (stretch, bend, and out-of-plane) as basic components, which decompose each normal mode. This decomposition allows us to compare normal modes determined at the PBE0/aug-cc-pVTZ and B3LYP/aug-cc-pVTZ levels of theory. The results are discussed using the following five general classes: "same modes", "same with extra modes", "exchanged modes", "partially exchanged modes" and "redistributed modes".

In the "same modes" class, the normal modes given by PBE0 and B3LYP are almost identical, and thus, they are described by the same set of internal coordinates with only a 1-2% difference in contributions. Modes 7, 24, 25, and 26 fall into this category.

The normal modes described as "same with extra modes" have almost the same internal coordinate contributions but there are additional contributions for one of the functionals. For example, mode 23 is similar for both PBE0 and B3LYP but there is an additional stretch(N_1-C_2) component in the PBE0 ground state.

The "exchanged modes" in this study are modes 11 and 12. According to the PED analysis based on the PBE0, mode 11 is out-of-plane(O_8-N_1-N_3-C_2), and it has a lower vibrational frequency compared to mode 12 (stretch(N_3-C_2)+stretch(N_1-C_2)+bend(C_6-N_1-C_2));however, these two modes are switched for B3LYP, which gives a higher frequency to the out-of-plane(O_8-N_1-N_3-C_2) mode as compared to the other mode.

There are also cases where two modes are not totally exchanged but only have a part of them switched, and this situation is referred as "partially exchanged modes". This type includes modes 18 and 19. Stretch(N_1-C_6) is in mode 18 of PBE0, but it is assigned as mode 19 of B3LYP; meanwhile, stretch(N_3-C_4) changed from mode 19 of PBE0 to mode 18 of B3LYP. Besides these two switched components, there are also some components in modes 18 and 19 that are unchanged, e.g., bend(H_7-N_1-C_6) and bend(H_{11}-C_5-C_4). Meanwhile, bend(H_{12}-C_6-C_5) has 30% contribution in mode 18 of PBE0, but it is redistributed in B3LYP as 12% in mode 18 and 17% in mode 19. Similarly, stretch(N_3-C_2) is redistributed from 29% in mode 18 of B3LYP into 14%

and 16% in mode 18 and 19 of PBE0.

If the vibrational energy is redistributed among multiple normal modes for different functionals, it is termed as "redistributed modes". The modes discussed here are modes 20, 21, and 22. These three modes in PBE0 contain one stretch component (stretch(N_1-C_2)) and five bend components (bend(H_7-N_1-C_6), bend(H_9-N_3-C_4), bend(H_{12}-C_6-C_5), bend(H_{11}-C_5-C_4), bend(C_4-N_3-C_2)), and these components are reshuffled in modes 20, 21, 22 of B3LYP. There are also two extra components added in mode 21 of B3LYP: stretch(N_3-C_4) and bend(O_8-C_2-N_3).

Within the HT approach, the normal modes are assumed to remain the same as in the ground electronic state at the moment the molecule is excited. Since the PED analysis shows that both frequencies and normal modes determined by PBE0 and B3LYP are not identical, we expect the computationally determined resonance Raman spectrum of uracil will exhibit features that depend on the choice of method for determining the ground state optimized geometry and the corresponding normal modes.

2.3.2 Vertical excitation energies and oscillator strengths

The vertical excitation energies and oscillator strengths of uracil have been investigated extensively in previous experimental[43,164] and computational[97–105,107,108,110–112,114,116–118] studies. The vertical excitation energy of uracil has been measured experimentally in both the gas phase and aqueous phase using UV-vis absorption spectroscopy and determined to be 5.1 eV in the gas phase[164] and 4.7 eV in the aqueous phase.[43] Solvation effects on the vertical excitation energies of uracil have been studied computationally with both implicit[97–99,101] and explicit models[100–105,117,118] in the solution phase. Here, the excited state properties (energies and gradients) have been evaluated in the gas phase and with implicit water solvation.

The vertical excitation energies from the PBE0 and B3LYP optimized ground state geometries to the lowest three singlet excited states of uracil are determined by TD-DFT (PBE0, B3LYP, CAMB3LYP, and LC-BLYP) and SF-TD-DFT (BHHLYP) in both the gas phase and implicit water using C-PCM, see Table 2.2 and Table 2.3,

respectively. While the vertical excitation energies do not play a crucial role in the determination of the resonance Raman spectrum, they are reported for completeness as well as for discussion of the use of vertical excitation energies for assessing different computational approaches for resonance Raman spectra.

Table 2.2: *Vertical Excitation Energies (E_V/eV), Oscillator Strengths (f) and Λ Parameters[165] for the Three Lowest Singlet Excited States of Uracil in the Gas Phase for Different Functionals at the PBE0/aug-cc-pVTZ and B3LYP/aug-cc-pVTZ Optimized Geometries. All the TD-DFT Computations use the aug-cc-pVTZ Basis Set.*

		S_1 $n \rightarrow \pi^*$			S_2 $\pi \rightarrow \pi^*$			S_3 Rydberg		
ground state	excited state	E_V	f	Λ[c]	E_V	f	Λ	E_V	f	Λ
PBE0	PBE0	4.806	0.000	0.402	5.288	0.137	0.722	5.903	0.002	0.247
	B3LYP	4.684	0.000	0.401	5.175	0.124	0.718	5.609	0.002	0.256
	CAMB3LYP	5.086	0.000	0.379	5.417	0.174	0.711	6.029	0.003	0.210
	LC-BLYP	5.069	0.000	0.377	5.390	0.175	0.696	6.097	0.004	0.184
	BHHLYP[a]	5.620	-	-	5.836	-	-	6.120	-	-
B3LYP	PBE0	4.781	0.000	0.404	5.255	0.135	0.721	5.913	0.002	0.249
	B3LYP	4.660	0.000	0.404	5.143	0.123	0.716	5.620	0.002	0.258
	CAMB3LYP	5.057	0.000	0.386	5.387	0.173	0.710	6.039	0.003	0.211
	LC-BLYP	5.040	0.000	0.381	5.361	0.174	0.697	6.106	0.003	0.185
	BHHLYP[a]	5.609	-	-	5.813	-	-	6.133	-	-
experiment[b]		-	-	-	5.1	-	-	-	-	-

[a] Determined by SF-TD-DFT using the Tamm Dancoff approximation.

[b] Ref.164

[c] $\Lambda = \frac{\sum_{i,a} \kappa_{ia}^2 \langle|\phi_i|||\phi_a|\rangle}{\sum_{i,a} \kappa_{ia}^2}$. ϕ_i and ϕ_a are occupied and virtual orbitals, respectively.

Table 2.3: *Vertical Excitation Energies (E_V/eV), Oscillator Strengths (f) and Λ Parameters[165] for the Three Lowest Singlet Excited States of Uracil in the Implicit Water for Different Functionals at the PBE0/aug-cc-pVTZ and B3LYP/aug-cc-pVTZ Optimized Geometries. All the TD-DFT Computations use the aug-cc-pVTZ Basis Set.*

		S_1 $\pi \rightarrow \pi^*$			S_2 $n \rightarrow \pi^*$			S_3 Rydberg		
ground state	excited state	E_V	f	Λ[c]	E_V	f	Λ	E_V	f	Λ
PBE0	PBE0	5.127	0.312	0.727	5.180	0.000	0.406	6.238	0.010	0.264
	B3LYP	5.031	0.295	0.726	5.072	0.000	0.405	5.948	0.009	0.272
	CAMB3LYP	5.206	0.366	0.719	5.440	0.000	0.395	6.347	0.013	0.222
	LC-BLYP	5.165	0.368	0.700	5.393	0.000	0.387	6.386	0.014	0.196
	BHHLYP[a]	5.781	-	-	6.010	-	-	6.403	-	-
B3LYP	PBE0	5.099	0.309	0.726	5.154	0.000	0.408	6.246	0.006	0.343
	B3LYP	5.002	0.291	0.725	5.047	0.000	0.408	5.961	0.008	0.275
	CAMB3LYP	5.180	0.363	0.719	5.410	0.000	0.397	6.361	0.012	0.224
	LC-BLYP	5.138	0.365	0.700	5.363	0.000	0.390	6.400	0.013	0.198
	BHHLYP[a]	5.748	-	-	5.981	-	-	6.424	-	-
experiment[b]		4.7	-	-	-	-	-	-	-	-

[a] Determined by SF-TD-DFT using the Tamm Dancoff approximation.
[b] Ref.43, according to the UV-vis absorption spectrum.
[c] $\Lambda = \frac{\sum_{i,a} \kappa_{ia}^2 \langle|\phi_i|||\phi_a|\rangle}{\sum_{i,a} \kappa_{ia}^2}$. ϕ_i and ϕ_a are occupied and virtual orbitals, respectively.

In the gas phase, the $n \rightarrow \pi^*$ state is at lower energy than the $\pi \rightarrow \pi^*$ state, independent of the functional chosen, see Table 2.2. However, in the implicit water, the $n \rightarrow \pi^*$ state is strongly perturbed and blue shifted by 0.3 - 0.4 eV, whereas the $\pi \rightarrow \pi^*$ state is mildly red shifted by 0.1 - 0.2 eV. The solvation effect leads to a change in the energetic order of the excited states and the sensitivity of the relative energies of $n \rightarrow \pi^*$ and $\pi \rightarrow \pi^*$ for uracil has been reported previously for implicit and explicit water[97–105] .

Since the trends with respect to the choice of functional for the vertical excitation energies are similar in the gas phase and C-PCM in Tables 2.2 and 2.3, the following discussion pertains to both phases. For the two different ground state geometries, the vertical excitation energy for a given functional does not differ by more than 0.03 eV, e.g., for the S_2 state, the excitation energies for CAMB3LYP are 5.440 eV and 5.410 eV for the PBE0 and B3LYP ground state geometries, respectively, see Table 2.3. However, the difference in excitation energies between functionals for a given

ground state geometry can be more than 0.4 eV, e.g, for the PBE0 ground state geometry, the excitation energy to the S_2 state is 5.072 eV for B3LYP and 5.440 eV for CAMB3LYP; the difference between standard TDDFT and SF-TD-DFT can be even larger. For the functionals considered, the vertical excitation energies for PBE0 and B3LYP (non long range corrected functionals, NLR) are the lowest, with CAMB3LYP and LC-BLYP (long range corrected functionals, LR) the energies are $\sim$ 0.1-0.3 eV higher, and SF-TD-DFT using BHHLYP gives the highest energies. The TD-DFT results give good agreement with the experimental measurement, although the hybrid functionals (B3LYP and PBE0) gives slightly superior performance to the long range corrected functionals; the SF-TD-DFT with BHHLYP result is too high by $\sim$ 0.7 - 1.0 eV in agreement with the value reported by Zhang and Herbert.[118]

We also computed the oscillator strength of uracil for transitions to the first three excited states. In the gas phase, the transitions of $S_0 \rightarrow S_1$ and $S_0 \rightarrow S_3$ have zero oscillator strength, and for the $S_0 \rightarrow S_2$ transition the oscillator strength is above 0.1 for all functionals. These results clearly showed that S_2 is a bright state and the other two states are dark in the gas phase. In implicit solution, due to the change of the state order, S_1 becomes a bright state, where its oscillator strengths is $\sim$ 0.3 for all functionals, but S_2 and S_3 are dark states.

The Λ parameter[165] for each excited state is given in Table 2.2 and 2.3. The Λ parameter of S_3 is much lower than 0.4 which confirms S_3 is a Rydberg state in both the gas phase and implicit water. This agrees with the observation in Ref. 107.

2.3.3 Resonance Raman spectra

The gradients of the bright electronically excited state are computed at the ground state equilibrium geometry, and these gradients are then converted into the dimensionless displacements, see Eq. 2.1. The computations of gradients are carried out in both the gas phase and implicit water using C-PCM. The resulting dimensionless displacements of the vibrational modes of interest ($|\Delta| > 0.5$ and also including modes 21, 22, and 23) are given in Tables 2.4 and 2.5 (gas phase), and Tables 2.6 and 2.7 (implicit solution). The data for all modes within the frequency range of the

experimental spectrum can be found in Tables A4, A5, A6, and A7 of the Appendix A. The resonance Raman spectrum of uracil is simulated using the dimensionless displacements above. The spectra using the PBE0 and B3LYP optimized ground state are shown in Figures 2.2 and 2.3, respectively, for the gas phase, and in Figures 2.4 and 2.5 for implicit water. As can be seen, the resonance Raman spectra, for a given optimized ground state, do not change significantly upon including solvent effects. Thus, in general, the discussions following refer to spectra in both the gas phase and implicit water.

Table 2.4: *Vibrational Frequencies (ω/cm^{-1}) Lower Than 1000 cm^{-1} and Dimensionless Displacements ($|\Delta|$)of Uracil in the Gas Phase for the S_2 Excited State. All Computations use the aug-cc-pVTZ Basis Set.*

modes	7	11	12
ω(PBE0)	563	781	782
ω(scaled by 0.9776)[b]	551	764	765
$\|\Delta\|$(PBE0)	0.935	0.000	0.811
$\|\Delta\|$(B3LYP)	0.799	0.000	1.102
$\|\Delta\|$(CAMB3LYP)	0.960	0.000	0.784
$\|\Delta\|$(LC-BLYP)	0.967	0.000	0.766
$\|\Delta\|$(BHHLYP)[a]	1.345	0.000	0.371
ω(B3LYP)	560	767	771
ω(scaled by 0.9891)[c]	553	761	762
$\|\Delta\|$(PBE0)	1.013	0.505	0.040
$\|\Delta\|$(B3LYP)	0.865	0.809	0.066
$\|\Delta\|$(CAMB3LYP)	1.039	0.481	0.037
$\|\Delta\|$(LC-BLYP)	1.046	0.462	0.036
$\|\Delta\|$(BHHLYP)[a]	1.438	0.056	0.001
ω(experiment, IR)[d]	551	757	759
ω(experiment, rR)[e]	579	789	
$\|\Delta\|$(experiment)[e]	0.46	0.48	

[a] Determined by SF-TD-DFT using the Tamm Dancoff approximation and numerical gradients.
[b] Ref. 160
[c] Ref. 161
[d] Ref. 156, Ref. 157
[e] Ref. 43

Table 2.5: *Vibrational Frequencies (ω/cm^{-1}) Higher Than 1000 cm^{-1} and Dimensionless Displacements ($|\Delta|$)of Uracil in the Gas Phase for the S_2 Excited State. All Computations use the aug-cc-pVTZ Basis Set.*

modes	18	19	20	21	22	23	24	25	26
ω(PBE0)	1211	1243	1391	1420	1432	1518	1696	1798	1831
ω(scaled by 0.9568)[b]	1159	1189	1331	1358	1370	1452	1622	1721	1752
$\|\Delta\|$(PBE0)	0.335	0.707	0.548	0.104	0.248	0.401	0.767	0.494	0.527
$\|\Delta\|$(B3LYP)	0.372	0.684	0.523	0.083	0.290	0.441	0.687	0.506	0.627
$\|\Delta\|$(CAMB3LYP)	0.278	0.788	0.623	0.137	0.200	0.353	0.898	0.546	0.329
$\|\Delta\|$(LC-BLYP)	0.275	0.833	0.656	0.146	0.189	0.295	0.910	0.586	0.323
$\|\Delta\|$(BHHLYP)[a]	0.314	1.116	0.793	0.168	0.108	0.362	1.076	0.560	0.151
ω(B3LYP)	1191	1227	1381	1404	1421	1497	1670	1759	1791
ω(scaled by 0.9676)[c]	1153	1187	1336	1359	1375	1448	1616	1702	1733
$\|\Delta\|$(PBE0)	0.735	0.539	0.341	0.318	0.330	0.322	0.771	0.467	0.498
$\|\Delta\|$(B3LYP)	0.759	0.499	0.295	0.354	0.340	0.358	0.689	0.479	0.602
$\|\Delta\|$(CAMB3LYP)	0.728	0.647	0.434	0.284	0.328	0.280	0.909	0.525	0.294
$\|\Delta\|$(LC-BLYP)	0.7490	0.691	0.471	0.275	0.329	0.223	0.921	0.567	0.287
$\|\Delta\|$(BHHLYP)[a]	0.944	0.918	0.599	0.257	0.311	0.300	1.086	0.543	0.115
ω(experiment, IR)[d]	1185	1217	1359	1389	1400	1472	1643	1706	1764
ω(experiment, rR)[e]	1235			1388			1623	1664	
$\|\Delta\|$(experiment)[e]	0.74			0.45			0.30	0.60	

[a] Determined by SF-TD-DFT using the Tamm Dancoff approximation and numerical gradients.
[b] Ref. 160
[c] Ref. 161
[d] Ref. 156, Ref. 157
[e] Ref. 43

Table 2.6: *Vibrational Frequencies (ω/cm^{-1}) Lower Than 1000 cm^{-1} and Dimensionless Displacements ($|\Delta|$)of Uracil in the Implicit Water for the S_1 Excited State. All Computations use the aug-cc-pVTZ Basis Set.*

modes	7	11	12
ω(PBE0)	563	781	782
ω(scaled by 0.9776)[b]	551	764	765
$\|\Delta\|$(PBE0)	0.914	0.018	0.764
$\|\Delta\|$(B3LYP)	0.784	0.021	1.060
$\|\Delta\|$(CAMB3LYP)	0.920	0.020	0.707
$\|\Delta\|$(LC-BLYP)	0.924	0.020	0.674
$\|\Delta\|$(BHHLYP)[a]	1.327	0.022	0.383
ω(B3LYP)	560	767	771
ω(scaled by 0.9891)[c]	553	761	762
$\|\Delta\|$(PBE0)	1.018	0.450	0.050
$\|\Delta\|$(B3LYP)	0.877	0.759	0.079
$\|\Delta\|$(CAMB3LYP)	1.023	0.392	0.050
$\|\Delta\|$(LC-BLYP)	1.028	0.357	0.046
$\|\Delta\|$(BHHLYP)[a]	1.445	0.066	0.012
ω(experiment, IR)[d]	551	757	759
ω(experiment, rR)[e]	579	789	
$\|\Delta\|$(experiment)[e]	0.46	0.48	

[a] Determined by SF-TD-DFT using the Tamm Dancoff approximation and numerical gradients.
[b] Ref. 160
[c] Ref. 161
[d] Ref. 156, Ref. 157
[e] Ref. 43

Table 2.7: *Vibrational Frequencies (ω/cm^{-1}) Higher Than 1000 cm^{-1} and Dimensionless Displacements ($|\Delta|$)of Uracil in the Implicit Water for the S_1 Excited State. All Computations use the aug-cc-pVTZ Basis Set.*

modes	18	19	20	21	22	23	24	25	26
ω(PBE0)	1211	1243	1391	1420	1432	1518	1696	1798	1831
ω(scaled by 0.9568)[b]	1159	1189	1331	1358	1370	1452	1622	1721	1752
$\|\Delta\|$(PBE0)	0.174	0.738	0.579	0.091	0.193	0.354	0.869	0.785	0.516
$\|\Delta\|$(B3LYP)	0.197	0.707	0.553	0.074	0.224	0.380	0.799	0.807	0.593
$\|\Delta\|$(CAMB3LYP)	0.155	0.845	0.656	0.108	0.174	0.338	0.969	0.836	0.413
$\|\Delta\|$(LC-BLYP)	0.158	0.902	0.693	0.116	0.170	0.290	0.977	0.884	0.428
$\|\Delta\|$(BHHLYP)[a]	0.196	1.046	0.739	0.104	0.050	0.341	0.975	0.801	0.264
ω(B3LYP)	1191	1227	1381	1404	1421	1497	1670	1759	1791
ω(scaled by 0.9676)[c]	1153	1187	1336	1359	1375	1448	1616	1702	1733
$\|\Delta\|$(PBE0)	0.625	0.639	0.387	0.306	0.264	0.243	0.868	0.777	0.487
$\|\Delta\|$(B3LYP)	0.630	0.599	0.347	0.330	0.269	0.265	0.795	0.799	0.567
$\|\Delta\|$(CAMB3LYP)	0.673	0.749	0.459	0.307	0.269	0.224	0.973	0.833	0.381
$\|\Delta\|$(LC-BLYP)	0.707	0.801	0.495	0.307	0.276	0.175	0.980	0.884	0.397
$\|\Delta\|$(BHHLYP)[a]	0.809	0.893	0.562	0.249	0.196	0.247	0.980	0.794	0.229
ω(experiment, IR)[d]	1185	1217	1359	1389	1400	1472	1643	1706	1764
ω(experiment, rR)[e]	1235			1388			1623	1664	
$\|\Delta\|$(experiment)[e]	0.74			0.45			0.30	0.60	

[a] Determined by SF-TD-DFT using the Tamm Dancoff approximation and numerical gradients.
[b] Ref. 160
[c] Ref. 161
[d] Ref. 156, Ref. 157
[e] Ref. 43

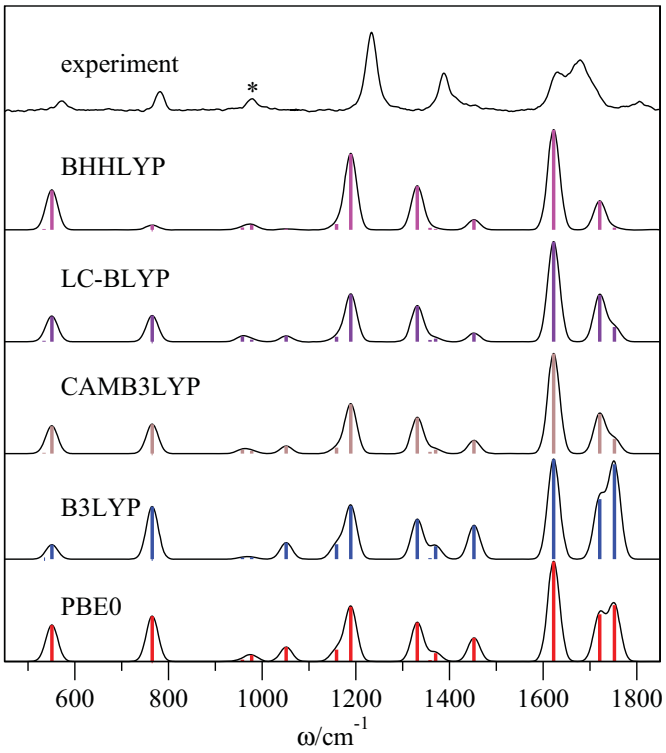

Figure 2.2: *Resonance Raman spectra of uracil in the gas phase. Frequency (ω/cm^{-1}) for PBE0 ground state is scaled by 0.9776 (frequencies lower than 1000 cm^{-1}) and 0.9568 (frequencies higher than 1000 cm^{-1}). fwhm used in the simulation is 30 cm^{-1}. The experimental spectrum is measured in water and taken from Ref 43. The asterisk in the experimental spectrum[43] indicates the internal standard peak by ca. 0.4 M sulfate.*

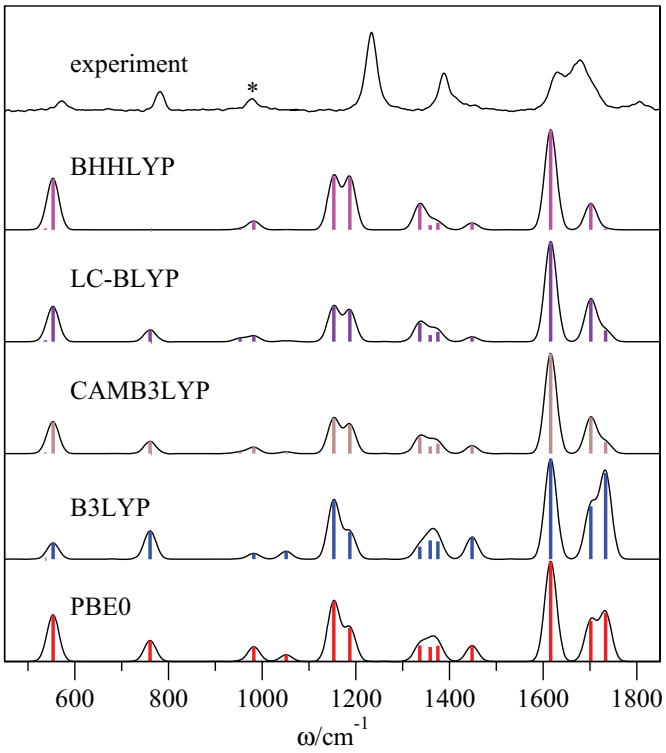

Figure 2.3: *Resonance Raman spectra of uracil in the gas phase. Frequency (ω/cm^{-1}) for B3LYP ground state is scaled by 0.9891(frequencies lower than 1000 cm^{-1}) and 0.9676 (frequencies higher than 1000 cm^{-1}). fwhm used in the simulation is 30 cm^{-1}. The experimental spectrum is measured in water and taken from Ref 43. The asterisk in the experimental spectrum[43] indicates the internal standard peak by ca. 0.4 M sulfate.*

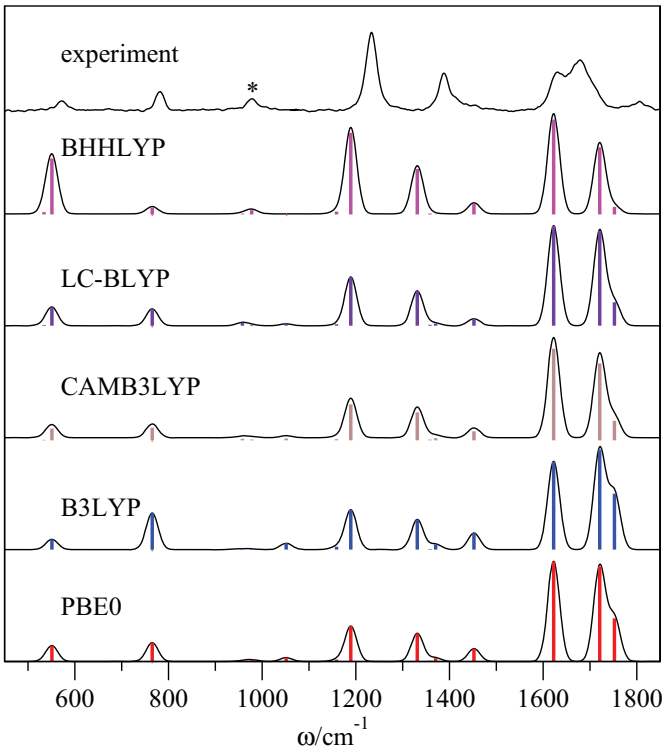

Figure 2.4: *Resonance Raman spectra of uracil in implicit water. Frequency (ω/cm^{-1}) for PBE0 ground state is scaled by 0.9776 (frequencies lower than 1000 cm-1) and 0.9568 (frequencies higher than 1000 cm-1). fwhm used in the simulation is 30 cm-1. The experimental spectrum is measured in water and taken from Ref 43. The asterisk in the experimental spectrum[43] indicates the internal standard peak by ca. 0.4 M sulfate.*

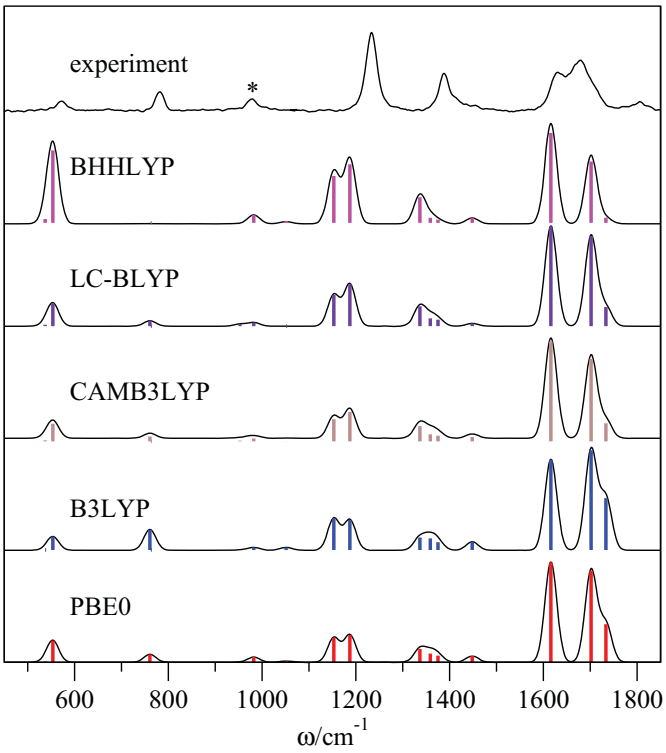

Figure 2.5: *Resonance Raman spectra of uracil in implicit water. Frequency (ω/cm^{-1}) for B3LYP ground state is scaled by 0.9891(frequencies lower than 1000 cm^{-1}) and 0.9676 (frequencies higher than 1000 cm^{-1}). fwhm used in the simulation is 30 cm^{-1}. The experimental spectrum is measured in water and taken from Ref 43. The asterisk in the experimental spectrum[43] indicates the internal standard peak by ca. 0.4 M sulfate.*

The peaks belonging to "exchange modes", "partial exchange modes" and "redistributed modes" in the PED analysis exhibit large changes for the different ground state functionals, see Table 2.4 - 2.7. We discuss each of these classes of modes in turn.

According to the PED, the vibrational assignments for modes 11 and 12 at $\sim$ 760 cm^{-1} are exchanged from PBE0 to B3LYP, and therefore their dimensionless displacements are also exchanged. This is reflected in the corresponding peak inten-

sities; mode 11 and mode 12 intensities are zero (observable) and observable (close to zero) for PBE0 (B3LYP) ground state, respectively; compare Figures 2.2 and 2.3 for a given choice of functional for the excited state. Different functionals for the excited state have little impact on the peak patterns of modes 11 and 12. The only exception is for SF-TD-DFT with BHHLYP, where both modes have zero intensity, which does not agree with the experimental spectrum. The computationally determined Δ values are in reasonable agreement with the value ($\Delta = 0.48$) obtained by fitting the experimental spectrum.[43] However, the present PED analysis provides a slightly different assignment for this strongly mixed mode.

For modes 18 and 19, i.e. "partially exchanged modes", at $\sim$ 1150 -1190 cm^{-1}, the ratio between the corresponding peak intensities, I(mode 18)/I(mode 19), is impacted by the choice of the ground state optimized geometry and its corresponding Hessian. For the PBE0 ground state, this ratio I(mode 18)/I(mode 19) is much less than 1 for all functionals for the excited state, see Figures 2.2 and 2.4. For the B3LYP optimized ground state, the ratio depends on the method used for the excited state, i.e., for NLR functionals I(mode 18)/I(mode 19) ≈ 2 while for LR it is ≈ 1.7. B3LYP/BHHLYP further increases the height of mode 19, and thus the ratio is reduced to ≈ 1. Because of the solvation effect, this ratio in Figure 2.5 changes to $\sim$ 0.9 - 1 for all functionals. Compared to the experimental spectrum for modes 18 and 19, using PBE0 to compute ground state normal modes gives better agreement than using B3LYP. The computationally determined Δ values are in reasonable agreement with those from the previous fit[43] and the PED analysis, see Table 2.1, confirms the assignment as ring stretch coupled to hydrogen bend.

For the "redistributed modes" 20-22 between 1300-1400 cm^{-1}, the change in the peak patterns is more complicated. For the PBE0 optimized ground state, the major peak is from mode 20, see Figures 2.2 and 2.4, and the agreement between the computationally determined Δ values and the experimental fit is reasonable, see Tables 2.5 and 2.7. For the B3LYP ground state, the three peaks have almost equal contributions using TD-PBE0 and TD-B3LYP for the excited state. For CAMB3LYP, LC-BLYP and SF-TD-DFT with BHHLYP, the peak patterns are similar to Figure

2.2, but the intensity of mode 20 is reduced. For the PBE0 optimized ground state, the present PED analysis for mode 20 suggests that this mode is primarily H_9-N_3-C_4 bend, which is in moderate agreement with the previous assignment.[43] Moreover, the present results suggest that the shoulder on this peak observed experimentally is due to the minor contributions of mode 21 and mode 22.

Modes 7, 23, 24, 25 and 26 belong to "same modes" and "same and extra modes" groups, and, thus, their peak intensities do not depend significantly on the choices of functional for the ground state optimization.

The peak corresponding to mode 26 at 1750 cm^{-1}, i.e., the peak for stretch(O_8-C_2) at the highest energy, exhibits a strong dependence on the choice of functional for determining the excited state. For computations using TD-PBE0 and TD-B3LYP (NLR functional), this peak is anomalously high compared to the experimental spectrum. This observation agrees with Ref. 27, which found that the intensity of the O_8-C_2 stretching mode is overestimated by B3LYP/TZVP. However, by using CAMB3LYP and LC-BLYP (LR functional), this overestimated peak is reduced to less than one fourth of its previous intensity. It is further reduced to almost zero intensity when SF-TD-DFT with BHHLYP is used. It is possible that this mode corresponds to the small unassigned peak at $\sim$1800 cm^{-1} in the experimental spectrum. Similar to mode 26, the peak intensity of mode 23 at $\sim$ 1450 cm^{-1} determined with NLR functionals is higher than in the experimental spectrum, and this peak is also reduced by using LR and BHHLYP. No distinct peak is observed in the experimental spectrum at 1450 cm^{-1}; however, there is a long tail, to high energy, for the peak at 1370 cm^{-1} that could encompass a low intensity peak. The gradient change due to the choice of functional for modes 23 and 26 does not depend upon whether the computation is in the gas phase or in implicit water using C-PCM.

To understand the change in peak intensity with the choice of functional, we investigated the gradient of the S_2 excited state energy surface along mode 26. Since the ground states optimized by PBE0 and B3LYP are very similar along mode 26, the discussions are based around the PBE0/aug-cc-pVTZ equilibrium structure, and the relative energies are computed in the gas phase. The relative energies of the

S_2 excited state are defined as $\Delta E_{\mathrm{V}}(S_2) = E_{\mathrm{V}}(S_2, r) - E_{\mathrm{V}}(S_2, r_e)$, where $E_{\mathrm{V}}(S_2, r)$ is the vertical excitation energy of the second excited state along the bond O_8-C_2, and $E_{\mathrm{V}}(S_2, r_e)$ is the vertical excitation energy of this state at the equilibrium bond length, i.e., $r_e = 1.208501$Å. The bond length of O_8-C_2 is varied from 1.158501 Å to 1.298501 Å, where atom O_8 is the translating atom and C_2 is the fixed atom. The relative energies of $\Delta E_{\mathrm{V}}(S_2)$ using five different functionals for determining the excited states are plotted in Figure A1. All computations determine negative gradients at the equilibrium bond length of O_8-C_2 ($r_e = 1.208501$Å), but there are some noticeable differences between the gradients computed by NLR functionals (PBE0 and B3LYP) and by the other three functionals (CAMB3LYP, LC-BLYP and SF-TD-DFT with BHHLYP). The trend of magnitudes of the gradients of $\Delta E_{\mathrm{V}}(S_2)$ is B3LYP>PBE0>CAMB3LYP>LC-BLYP>BHHLYP, which agrees with the trend of dimensionless displacements of mode 26, see Table 2.5.

The peak intensities of modes 7, 24 and 25 exhibit little difference on the choice of the functional used for computing the excited state. In both the gas phase and implicit water, the peak intensity of mode 24 is overestimated compared to the experimental spectrum. Mode 25 demonstrates significant changes from the gas phase to implicit water, where the peak intensity is ~ 2 times higher in implicit water than in the gas phase. Mode 25 is also slightly too intense when compared with the experimental spectrum.

Modes 24-26 between 1600-1800 cm^{-1} represent the major difference between the computed and experimental spectra, where the relative peak positions of these three modes in the experiment are closer together than for any of the computations and their relative intensity compared to mode 19 (at 1200 cm−1) is too large. These differences are (most likely) due to the impact of explicit hydrogen bonding between water and the carbonyl groups corresponding to modes 25 and 26. For example, the frequencies of both carbonyl modes (modes 25 and 26) are red shifted when more explicit waters are included in a simulation, while the frequency of mode 24 is only modestly affected.[154] The relative peak intensities between the two carbonyl modes is well captured by using the long range corrected functionals rather than the standard

hybrid functionals, but the relative intensity between these modes and mode 19 is not captured within the current model.

Overall the simulated resonance Raman spectrum shows good agreement with the experimental measurement if the PBE0/aug-cc-pVTZ optimized ground state is used along with CAMB3LYP or LC-BLYP for the excited state gradients. The use of implicit solvation improves the agreement with the experimental spectrum, especially with regard to the relative intensities of the peaks with frequencies greater than 1600 cm^{-1}. The dimensionless displacements for most of the modes and, hence, the resonance Raman spectra computed using different functionals exhibit only subtle differences for a given ground state, see for example Table 2.6, Table 2.7, and Figure 2.4. Therefore, for uracil, all of the functionals considered would be suitable for interpreting the general features of the experimentally measured Resonance Raman spectrum and the excited state dynamics in the short time limit; although the detailed features are better reproduced by CAMB3LYP, LC-BLYP and SF-TD-DFT with BHHLYP. However, for longer time dynamics probed via alternate spectroscopies such as pump-probe, these subtle differences would be manifest into more significant discrepancies between functionals.

One question that may arise is the source of the differences between the various spectra shown in Figures 2.2 and 2.3, respectively, for the gas phase, or correspondingly for Figures 2.4 and 2.5 with implicit solvation. According to Eq.2.1, the initial short time dynamics of the molecule in the excited state, indicated by the the dimensionless displacements Δ_Q, is governed by both the excited state Cartesian gradients V_X and the normal mode vectors T at the ground state equilibrium geometry. In Figure 2.6, both the magnitude and the direction of the Cartesian gradient for each atom of uracil in the S2 state (in the gas-phase) are provided for (i) different ground state geometries (PBE0 vs. B3LYP) with the same method and basis set (CAM-B3LYP/aug-cc-pVTZ) for the excited state gradients and (ii) the same ground state geometry (PBE0) with different functionals (CAMB3LYP vs. B3LYP) used to determine the excited state gradient. It is clear that, using the same functional CAMB3LYP, the Cartesian gradients are almost identical between the PBE0

and B3LYP optimized geometries (except for the minor differences on atoms O_8 and O_{10}). Therefore, for the excited state determined using a given functional, the dimensionless displacement is most strongly impacted by the projection onto different normal modes rather than a significant change in the excited state gradients due to a (small) change in geometry. On the other hand, comparing the Cartesian gradients determined using CAMB3LYP and B3LYP at the same (PBE0) equilibrium geometry, a discernible difference is observed for atoms N_1, C_2, C_6, and O_8. Therefore, the dimensional displacement is very sensitive to the choice of the functional used to determine the excited state.

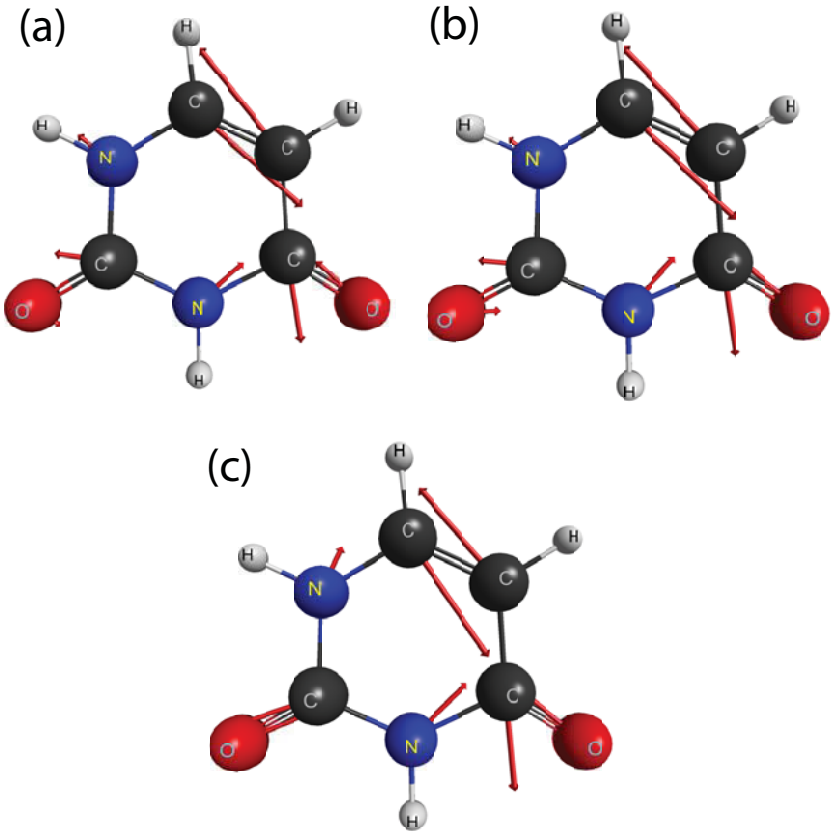

Figure 2.6: *Vectors illustrating the Cartesian gradients for each atom of uracil in the gas phase for the S_2 excited state. The gradient is computed at the B3LYP/aug-cc-PVTZ ground state geometry with the excited state at (a) CAMB3LYP/aug-cc-pVTZ and at the PBE0/aug-cc-pVTZ ground state geometry with the excited state determined using (b) CAMB3LYP/aug-cc-pVTZ and (c) B3LYP/aug-cc-pVTZ levels of theory.*

2.4 Conclusions

In this study, we simulated the resonance Raman spectrum of uracil using TD-DFT, and investigated the performance of different functionals. Two different functionals, PBE0 and B3LYP were used, to optimize the ground state equilibrium structure and determine the vibrational frequencies and normal modes of uracil. The PED analysis showed different normal mode characters for ground states optimized by PBE0 and

B3LYP. Therefore, the description of the ground state can have a notable impact on the computationally determined resonance Raman spectrum of uracil.

The excited state computations are carried out in both the gas phase and implicit water using C-PCM. We determined the vertical excitation energies of the lowest three singlet excited states and found that the hybrid functionals gave the best good agreement with the experimental value, the long range corrected functionals modestly overestimated the energies while SF-TD-DFT with BHHLYP overestimates more significantly, see Tables 2.2 and 2.3. The comparison of the results from the gas phase and implicit water confirms the $n \rightarrow \pi^*$ state is blue shifted and the $\pi \rightarrow \pi^*$ state is slightly red shifted in water.

We also computed the dimensionless displacements of the bright excited state of uracil and see that resulting resonance Raman spectra using CAMB3LYP, LC-BLYP and SF-TD-DFT with BHHLYP have better agreement with experiment than the spectra determined using hybrid functionals (B3LYP and PBE0). The agreement is very good within the IMDHO model even without invoking other effects, e.g. explicit hydrogen bonding, Duschinsky rotation. Interestingly, the resulting resonance Raman spectra in the two phases do not show significant differences except the peak of mode 25.

In this work, it is evident that a functional that provides accurate vertical excitation energies does not necessarily give an equally good performance for the excited state energy gradients. The accuracy of the gradient is readily assessed through comparison of the simulated resonance Raman spectrum with the experimental one. As such, this test of different functionals for short time dynamics provides a useful initial screening of methods for long time excited state dynamics.

Chapter 3

Simulation of the Resonance Raman Spectra For 5-Halogenated (F, Cl, and Br) Uracils

3.1 Introduction

For the purposes of both fundamental understanding and practical applications, the interaction between 5-halogenated uracils and ultra-violet (UV) light has received much attention from chemists and biologists in the past decades.[30,80,166–173] By forming a series of DNA analogues which replace thymine, 5-halogenated uracils are able to provide enhanced photosensitivity to UV radiation while retaining the identical in vivo activity.[166–169] 5-fluorouracil has also been introduced as a radiosensitizer to improve the treatment of cancers.[174,175] Moreover, the photoreaction of DNA containing 5-bromouracil is used to investigate local DNA conformations.[170–172] Hence, the 5-halogenated uracils find a diversity of uses.

The initial excited state structural dynamics of the 5-halogenated uracils are of pivotal importance, as they are the starting point in a series of photochemical and photophysical processes, after the molecule interacts with the UV light. Experimentally, the initial structural dynamics on the excited state of uracil, its isotopomers and derivatives, including 5-halogenated uracils, can be probed by resonance Raman spectroscopy.[30,35,38–40,44,46,52,80,173] In 2006, Billinghurst et al. measured the resonance Raman spectra of 5-fluorouracil, 5-chlorouracil, and 5-bromouracil in water.[80]

In 2009, the resonance spectrum of 5-chlorouracil in methanol was measured by Weng et al.[173] Since in resonance Raman spectroscopy, the incident photon energy is very close to the vertical excitation energy of molecule, the intensity of the spectrum is significantly enhanced. Assisted by quantum chemistry computations, one is able to simulate the resonance Raman spectrum and extract information regarding the initial excited state structural dynamics, i.e. the normal mode displacement of the molecule on the excited-state potential energy surface. Since, to the best of our knowledge, no experimental resonance Raman spectrum of 5-iodouracil has been reported, the computational study of the resonance Raman spectra in this paper only focuses on 5-fluoro-, 5-chloro, and 5-bromouracil.

Although computational studies on the 5-halogenated uracils examined many of their excited state properties, e.g. vertical excitation energies, deactivation mechanism, population transfer, and excited state life-time,[97,176–183] there is only a single paper reporting the computational determination of the resonance Raman spectra of 5-fluorouracil and 5-chlorouracil. In 2006, Ten, Burova and Baranov computed the relative intensities of the lines in the resonance Raman spectra of 5-fluorouracil and 5-chlorouracil via the quantum mechanical sum-over-state approach.[184] They did not aim to match the relative intensities of the computed lines to the experiment, but rather focused on showing qualitatively the presence of the most intense bands. However, to the best our knowledge, the ab initio simulation of the resonance Raman spectra of the 5-halogenated uracils have neither been compared to the experimental spectra in detail nor interpreted in terms of the roles of the ground state normal modes and the excited state gradients.

The resonance Raman spectra in this study are determined using the Herzberg-Teller short-time dynamics formalism (HT)[16,106] with the independent harmonic oscillator (IMDHO) model. In this approach, the vibrational wavefunction on the excited electronic state behaves like a wavepacket, and the overlap between the initial and final vibrational wavefunctions can be computed via the normal mode displacements of the molecule on the potential energy surface of the excited electronic state. The displacements can be determined by projecting the gradient of the excited state at

the vertical excitation point onto the normal modes of molecule at ground state equilibrium geometry. The spectrum is then simulated using the normal mode displacements and the transition dipole moment (within the Condon approximation) from the ground to excited electronic state.

In this paper, we simulated the resonance Raman spectra of three 5-halogenated uracils (5-fluorouracil, 5-chlorouracil and 5-bromouracil) in implicit water, and studied the reasons for their spectral differences by examining both their ground and excited state properties. The chemical structure and the atomic indices of the 5-halogenated uracils are given in Figure 3.1. The ground state properties of 5-halogenated uracils are studied using density functional theory (DFT), and the excited gradient is computed using time dependent density functional theory (TD-DFT). Through this comparison, the effect of halogen substitution in electronic structure can be clarified.

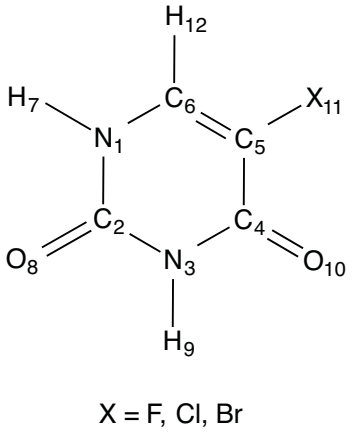

Figure 3.1: *Chemical structure of the 5-halogenated uracils with atomic numbering used in this work.*

3.2 Computational Methods

The equilibrium structures of the three 5-halogenated uracils, i.e., 5-fluorouracil, 5-chlorouracil and 5-bromouracil, are determined at the PBE0/aug-cc-pVTZ level of theory[119,120,125] in implicit water via the conductor-like Polarizable Continuum Model (C-PCM).[137,138] Cartesian coordinates of all optimized structures are available in Table B1 in Appendix B. The ground state vibrational frequencies and the corresponding normal modes are determined by diagonalizing the Hessian matrix computed at the optimized geometry. The TD-DFT computations are carried out at the CAMB3LYP/aug-cc-pVTZ level of theory[126] using these equilibrium structures. The vertical excitation energies and the corresponding oscillator strengths of the first three singlet excited states were determined. The computations were carried out using the same functionals and basis set for the ground and excited states, as well as choice of PCM model, as in our recent study of uracil.[69]

To obtain the resonance Raman spectrum, the energy gradient of the S_1 excited state in Cartesian coordinates space was also computed;[185–187] for all the 5-halogenated uracils, S_1 is the lowest energy bright state at the CAMB3LYP/aug-cc-pVTZ level of theory in C-PCM (H_2O). The Cartesian gradient is converted into normal mode displacements via

$$\mathbf{\Delta_Q} = \mathbf{\Lambda^{-1} T^{\intercal} M^{-1/2} V_X}. \tag{3.1}$$

In Eq (3.1), $\mathbf{\Delta_Q}$ is the matrix of ground state normal mode displacements, $\mathbf{\Lambda}$ is the diagonal matrix of eigenvalues of the mass weighted Hessian, $\mathbf{T}$ is the eigenvector of the mass weighted Hessian, $\mathbf{M}$ is the diagonal matrix of the atomic masses, and $\mathbf{V_X}$ is the energy gradient of the excited state in Cartesian coordinates. The dimensionless displacements required to compute the resonance Raman are determined as

$$\Delta_k = \left(\frac{\Lambda_k}{m_e}\right)^{\frac{1}{4}} \Delta_{Qk}, \tag{3.2}$$

where m_e is the mass of the electron.

The resonance Raman spectrum is determined via the Herzberg-Teller short-time dynamics formalism[106] utilizing the independent harmonic oscillator (IMDHO)

model. The simulation is performed under the first order approximation, and the fwhm of the spectrum is chosen as 30 cm^{-1}, in order to match the width of a single peak in the experimental resonance Raman spectra.[80] The incident photon energy is chosen as 275 nm, which is equal to the energy of the incident light in the experiment.[80]

The DFT and TD-DFT computations are performed using Gaussian (G09),[84] and the resonance Raman spectra are simulated via the program orca_asa.[15,16] The potential energy distribution (PED) is analyzed using the VEDA4 software package,[141,142] and the Λ parameters[165] are determined using the Gabedit software package.[188] More theoretical details for the simulation of the resonance Raman spectra can be found in Refs. 16 and 15.

Table 3.1: *Potential Energy Distribution Analysis and Vibrational Frequencies (ω/cm^{-1}) of Ground State Normal Modes of 5-Halogenated Uracils at the PBE0/aug-cc-pVTZ level of theory in H_2O (C-PCM).*

	mode	ω	PED
5-fluorouracil	8	545	+bend($O_{10}C_4N_3$)[25%]-bend($N_3C_2N_1$)[22%]-bend($C_6N_1C_2$)[16%]
	10	637	+bend($F_{11}C_5C_4$)[28%]-bend($O_8C_2N_3$)[27%]+bend($O_{10}C_4N_3$)[15%]-bend($C_4N_3C_2$)[12%]
	12	762	+bend($N_3C_2N_1$)[22%]+stretch(N_1C_2)[17%]-bend($C_4N_3C_2$)[12%]-bend($C_5C_6N_1$)[10%]+stretch($F_{11}C_5$)[7%]
	15	826	+bend($C_5C_6N_1$)[25%]+stretch($F_{11}C_5$)[19%]-bend($C_4N_3C_2$)[11%]
	18	1185	-stretch(N_1C_6)[26%]-bend($H_7N_1C_6$)[23%]+bend($H_{12}C_6C_5$)[13%]+bend($C_5C_6N_1$)[10%]
	19	1227	+stretch(N_3C_4)[34%]-bend($H_{12}C_6C_5$)[18%]-stretch(N_3C_2)[18%]+bend($H_9N_3C_4$)[11%]
	20	1278	+stretch($F_{11}C_5$)[39%]-stretch(N_1C_6)[27%]
	21	1370	+bend($H_{12}C_6C_5$)[39%]+stretch(C_5C_6)[16%]
	22	1415	+bend($H_9N_3C_4$)[59%]
	23	1454	+bend($H_7N_1C_6$)[25%]-stretch(N_1C_2)[12%]+stretch(N_3C_2)[10%]
	24	1533	-bend($H_7N_1C_6$)[23%]-stretch(N_1C_2)[18%]-bend($C_5C_6N_1$)[15%]
	25	1730	+stretch(C_5C_6)[47%]+stretch($O_{10}C_4$)[15%]
	26	1740	+stretch($O_{10}C_4$)[40%]-stretch(C_5C_6)[18%]-stretch(O_8C_2)[16%]
	27	1782	+stretch(O_8C_2)[49%]+stretch($O_{10}C_4$)[22%]
	8	549	+bend($O_{10}C_4N_3$)[28%]-bend($C_6N_1C_2$)[17%]+stretch(N_3C_4)[14%]+stretch(N_3C_2)[12%]
	10	613	+bend($O_8C_2N_3$)[27%]-bend($O_{10}C_4N_3$)[17%]-bend($Cl_{11}C_5C_4$)[16%]+bend($C_4N_3C_2$)[13%]

	12	676	+bend($N_3C_2N_1$)[33%]+stretch($Cl_{11}C_5$)[27%]-bend($C_4N_3C_2$)[10%]
	15	797	+stretch(N_1C_2)[24%]+bend($C_6N_1C_2$)[19%]-bend($N_3C_2N_1$)[14%]+stretch(N_3C_2)[12%]
	18	1102	+bend($C_5C_6N_1$)[38%]-stretch($Cl_{11}C_5$)[23%]+bend($N_3C_2N_1$)[11%]
	19	1207	+stretch(N_1C_6)[51%]+bend($H_7N_1C_6$)[24%]
	20	1233	+stretch(N_3C_4)[35%]-stretch(N_3C_2)[25%]-bend($H_{12}C_6C_5$)[19%]
5-chlorouracil	21	1360	+bend($H_{12}C_6C_5$)[44%]+stretch(C_5C_6)[23%]-stretch(N_3C_2)[10%]
	22	1419	+bend($H_9N_3C_4$)[62%]
	23	1442	+stretch(N_1C_2)[19%]-bend($H_7N_1C_6$)[15%]-stretch(N_3C_2)[12%]
	24	1522	+bend($H_7N_1C_6$)[36%]-stretch(N_1C_6)[15%]+bend($C_5C_6N_1$)[13%]+stretch(N_1C_2)[12%]
	25	1688	+stretch(C_5C_6)[64%]-bend($H_{12}C_6C_5$)[13%]
	26	1738	+stretch($O_{10}C_4$)[65%]-stretch(O_8C_2)[13%]
	27	1782	+stretch(O_8C_2)[60%]+stretch($O_{10}C_4$)[16%]
	8	547	+bend($O_{10}C_4N_3$)[28%]- bend($C_6N_1C_2$)[17%]+stretch(N_3C_2)[13%]+bend($C_4N_3C_2$)[13%]+stretch(N_3C_4)[11%]
	9	605	-bend($O_8C_2N_3$)[25%]+bend($O_{10}C_4N_3$)[16%]-bend($N_3C_2N_1$)[18%]+bend($Br_{11}C_5C_4$)[13%]
	11	639	+bend($N_3C_2N_1$)[31%]+stretch($Br_{11}C_5$)[24%]-bend($O_8C_2N_3$)[10%]
5-bromouracil	15	794	+stretch(N_1C_2)[25%]+bend($C_6N_1C_2$)[21%]-bend($N_3C_2N_1$)[12%]+stretch(N_3C_2)[12%]
	18	1074	+bend($C_5C_6N_1$)[40%]-stretch($Br_{11}C_5$)[16%]+bend($N_3C_2N_1$)[13%]-bend($C_6N_1C_2$)[10%]
	19	1204	+stretch(N_1C_6)[51%]+bend($H_7N_1C_6$)[21%]-stretch(N_3C_4)[10%]
	20	1235	+stretch(N_3C_4)[29%]-stretch(N_3C_2)[26%]-bend($H_{12}C_6C_5$)[20%]

	21	1361	+bend($H_{12}C_6C_5$)[47%]+stretch(C_5C_6)[24%]-stretch(N_3C_2)[10%]
	22	1418	+bend($H_9N_3C_4$)[61%]
	23	1438	-stretch(N_1C_2)[19%]+bend($H_7N_1C_6$)[14%]+stretch(N_3C_2)[12%]-bend($C_4N_3C_2$)[10%]
5-bromouracil	24	1518	+bend($H_7N_1C_6$)[37%]-stretch(N_1C_6)[16%]+stretch(N_1C_2)[12%]+bend($C_5C_6N_1$)[11%]
	25	1681	+stretch(C_5C_6)[63%]-bend($H_{12}C_6C_5$)[13%]
	26	1736	+stretch($O_{10}C_4$)[68%]-stretch(O_8C_2)[10%]
	27	1782	+stretch(O_8C_2)[62%]+stretch($O_{10}C_4$)[14%]

3.3 Results and Discussion

3.3.1 Equilibrium geometry, vibrational frequencies and normal modes

The optimized geometrical parameters of the three halogenated uracils are given in Table B2 in the Appendix B. All bond lengths and bond angles (save those involving halogen) do not show substantial changes upon modifying the halogen substituent, i.e. the differences are < 0.0064 Å in bond length and $< 1.3°$ in bond angle, see Table B2. However, as expected, the C_5-X_{11} (X=F, Cl, Br) bond lengths increase significantly with the increasing mass of X_{11}, i.e., C_5-Cl_{11} is 0.38 Å longer than C_5-F_{11}, and C_5-Br_{11} is 0.54 Å longer than C_5-F_{11}.

Experimentally, the vibrational frequencies of the 5-halogenated uracils have been measured using IR[146,147,189–194] and Raman spectroscopy,[146,189,191–193] and the normal modes corresponding to the peaks in the spectra can be assigned using electronic structure calculations.[195] In our previous study on the simulation of the resonance Raman spectrum of uracil,[69] we found that the choice of functional for the ground state optimization and subsequent Hessian determination significantly affects the relative peak intensities. The spectrum based on the optimized geometry and vibrational frequencies determined using PBE0/aug-cc-pVTZ lead to better agreement with the experiment compared to using B3LYP/aug-cc-pVTZ. Therefore, in this study we compute the ground state structure of the 5-halogenated uracils and their corresponding Hessian matrices at the PBE0/aug-cc-pVTZ level of theory, and all the computations are carried out in implicit water using C-PCM. As there is no vibrational frequency scaling factor available when using C-PCM, we reported the unscaled frequencies for the 5-halogenated uracils.

The (unscaled) vibrational frequencies and corresponding normal modes via PED analysis of the 5-halogenated uracils are provided in Table 3.1 for those normal modes that are required for understanding the experimental resonance Raman spectra, see Section 3.3.3. The normal modes are numbered from 1 to 30 for each halogenated uracil derivative, and modes 8 to 27 presents in the frequency range of the experi-

mental spectra (500 - 1800 cm^{-1}). For analysis of all normal modes between 500 - 1800 cm^{-1}, see Tables B3, B4 and B5 in the Appendix B. The frequency shift caused by the substitution of the halogen atom at X_{11} is determined by comparing the vibrational frequencies of each normal mode in the halogenated uracil derivatives, see Table 3.2 and Figure B1. Modes that are compared directly are based upon their cosine similarity to 5-fluorouracil, see Figure 3.2. The experimental frequencies are given in Table 3.2. The difference between the simulated and experimental frequencies are less than 30 cm^{-1} for modes <1600 cm^{-1}, and $\sim$ 35 - 56 cm^{-1} for modes $>$ 1600 cm^{-1}. The difference is likely due to anharmonicity and the explicit solvent effect.

Table 3.2: *Vibrational Frequencies (ω/cm^{-1}) Shift of 5-Halogenated Uracils in H_2O (C-PCM).*

	mode	8	10	12	15	18	19	21	22	23	24	25	26	27
5-fluorouracil	ω (simulation)	545	637	762	826	1185	1227	1370	1415	1454	1533	1730	1740	1782
	ω (experiment)[a]	553	639	760	820	1183	1223	1349	1431	1431	-	1689	1705	-
	mode	8	10	12	15	19	20	21	22	23	24	25	26	27
5-chlorouracil	ω (simulation)	549	613	676	797	1207	1233	1360	1419	1442	1522	1688	1738	1782
	ω (experiment)[b]	551	610	-	785	1190	1229	1337	1432	1432	-	1634	1682	-
	$\Delta\omega$[c]	4	-24	-87	-29	22	6	-10	4	-12	-11	-41	-2	0
	mode	8	9	11	15	19	20	21	22	23	24	25	26	27
5-bromouracil	ω (simulation)	547	605	639	794	1204	1235	1361	1418	1438	1518	1681	1736	1782
	ω (experiment)[b]	-	613	-	791	1181	1232	1338	1447	2447	-	1631	1680	-
	$\Delta\omega$[d]	-2	-8	-37	-3	-3	2	1	-1	-4	-4	-8	-2	0

[a] Ref.80.
[b] Ref.80, frequencies determined at the maximum intensity of each peak in the resonance Raman spectra.
[c] $\Delta\omega = \omega$(5-chlorouracil, simulation) $- \omega$(5-fluorouracil, simulation).
[d] $\Delta\omega = \omega$(5-bromouracil, simulation) $- \omega$(5-chlorouracil, simulation).

As the normal modes play a crucial role in the determination of the resonance Raman spectrum, see Eq.3.1, it is worthwhile to define a criterion that quantifies the similarity/dissimilarity of the normal modes for the three 5-substituted uracils. Therefore, the cosine similarity between every pair of normal modes from the different 5-halogenated uracils is also determined as

$$\mathfrak{S}(v_k^1, v_m^2) = \frac{\left|\sum_{i=1}^{n} v_{k,i}^1 v_{m,i}^2\right|}{\sqrt{\sum_{i=1}^{n} \left(v_{k,i}^1\right)^2}\sqrt{\sum_{i=1}^{n} \left(v_{m,i}^2\right)^2}}. \tag{3.3}$$

Here v_k^1 and v_m^2 are the kth and mth normal modes from the first and second molecule,

respectively, and $v^1_{k,i}$ and $v^2_{m,i}$ are the ith components of the normal modes in Cartesian coordinate space. The possible value of $\mathfrak{S}(v^1_k, v^2_m)$ ranges from 0 to 1, where 0 means the two normal modes are completely independent and 1 means these two modes are identical.

The cosine similarity between the normal modes of 5-fluorouracil and uracil presents high dissimilarity (few modes with $\mathfrak{S} > 0.85$), see Figure B2, so we chose the normal modes of 5-fluorouracil, rather than uracil, as the reference to study the similarity between the 5-halogenated uracils. The cosine similarity between the normal modes important for interpreting the resonance Raman spectra of each species are shown in Figure 3.2 for (a) 5-fluorouracil and 5-chlorouracil, (b) 5-fluororouracil and 5-bromouracil, and (c) 5-chlorouracil and 5-bromouracil. (The complete data for all normal modes between 500 - 1800 cm^{-1} can be found in Figures B3, B4 and B5 of the Appendix B.)

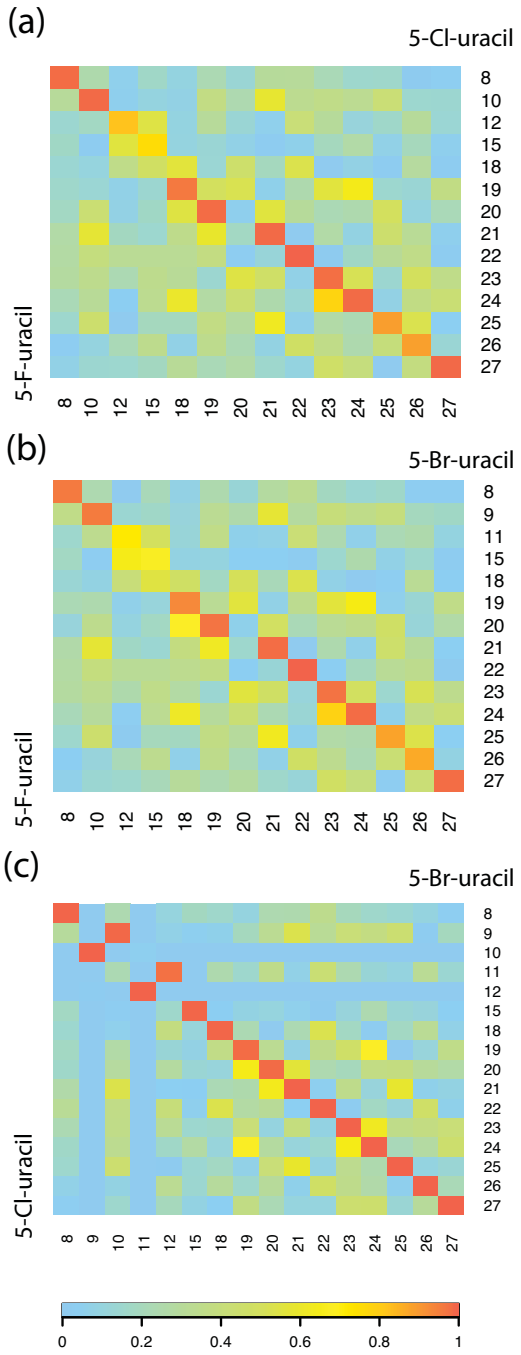

Figure 3.2: *The cosine similarity for the normal modes of (a) 5-fluorouracil vs. 5-chlorouracil, (b) 5-fluorouracil vs. 5-bromouracil and (c) 5-chlorouracil vs. 5-bromouracil, see main text for further details. x- and y-axes correspond to vibrational mode numbering, see Table 3.1.*

In Figure 3.2(a), we see that the cosine similarity of many modes in 5-fluorouracil is greater than 0.9 for at least one corresponding mode in 5-chlorouracil. These modes (numbered for 5-fluorouracil) include 8, 10, 18 (19 in 5-chlorouracil), 19 (20 in 5-chlorouracil), 20-24, and 27. The large cosine similarity indicates that these modes do not change significantly when fluorine is substituted with chlorine in 5-chlorouracil. The vibrational frequencies for the majority of these modes shift less than 12 cm^{-1} in going from 5-fluorouracil to 5-chlorouracil, see Table 3.2. The only exceptions are modes 10 and 18 that shift -24 cm^{-1} and 22 cm^{-1}, respectively. The large shift of mode 10 is due to the ($F_{11}C_5C_4$) bend in 5-fluorouracil changing to ($Cl_{11}C_5C_4$) bend in 5-chlororuracil. The shift of mode 19 can be attributed to the increment of (N_1C_6) stretch in 5-chlorouracil.

Some modes have moderate similarity in 5-fluorouracil versus 5-chlorouracil, i.e., modes 12, 15, 25, and 26. For the low-frequency modes, the value of $\mathfrak{S}(v_{12}^{\mathrm{F}}, v_{12}^{\mathrm{Cl}})$ is 0.81, and $\mathfrak{S}(v_{15}^{\mathrm{F}}, v_{15}^{\mathrm{Cl}})$ is only 0.75, see Figure 3.2(a). The PED, see Table 3.1, shows that the internal coordinates of modes 12 and 15 of 5-fluorouracil are quite different from 5-chlorouracil. Some components in modes 12 and 15 of 5-chlorouracil are significantly reduced compared to 5-fluorouracil. For example, the ($C_5C_6N_1$) bend contributes 10% in mode 12 and 25% in mode 15 of 5-fluorouracil, but in 5-chlorouracil this component is less than 6% in both modes 12 and 15. On the other hand, some other components increases significantly. For instance, the ($C_6N_1C_2$) bend is less than 5% in mode 12 of 5-fluorouracil, but in 5-chlorouracil contributes 7% and 19% in modes 12 and 15, respectively. The vibrational energy of other components, e.g., ($C_4N_3C_2$) bend and ($N_3C_2N_1$) bend, is also redistributed significantly between modes 12 and 15. It is notable that ($F_{11}C_5$) stretch contributes 7% in mode 12 and 19% in mode 15 of 5-fluorouracil, but in 5-chlorouracil mode 12 has 27% from ($Cl_{11}C_5$) stretch and mode 15 has no contribution from ($Cl_{11}C_5$) stretch. In Table 3.2, the shift of the vibrational frequency of modes 12 and 15 are -87 and -29 cm^{-1} from 5-fluorouacil to 5-chlorouracil. It is self-evident that the difference of mass between fluorine and chlorine atoms is the reason for the redistribution of the vibrational energy in modes 12 and 15.

For the high-frequency modes with moderate similarity, the value of $\mathfrak{S}(v_{25}^{\mathrm{F}}, v_{25}^{\mathrm{Cl}})$ and $\mathfrak{S}(v_{26}^{\mathrm{F}}, v_{26}^{\mathrm{Cl}})$ are both 0.88. This lowering of similarity is due to the vibrational energy redistribution between modes 25 and 26. In 5-fluorouracil, the (C_5C_6) stretch is 47% in mode 25 and 16% in mode 26. However, in 5-chlorouracil the contribution of this stretching component increases to 63% in mode 25 but reduces to 0% in mode 26. Similarly, ($O_{10}C_4$) stretch contributes only in mode 25 but not in mode 26 of 5-chlorouracil, but in 5-fluorouracil both modes 25 and 26 have contributions from ($O_{10}C_4$) stretch. The vibrational frequency comparison shows mode 25 shifts -25 cm^{-1} and mode 26 shifts -2 cm^{-1} from 5-fluorouracil to 5-chlorouracil.

It is notable that mode 20 of 5-fluorouracil has high dissimilarity to all the modes of 5-chlorouracil ($\mathfrak{S}(v_{20}^{\mathrm{F}}, v_N^{\mathrm{Cl}}) \leq 0.52$, $8 \leq N \leq 27$), see Figure 3.2(a). Similarly, $\mathfrak{S}(v_{18}^{\mathrm{Cl}}, v_N^{\mathrm{F}}) \leq 0.56$, $8 \leq N \leq 27$, see Figure 3.2(a), hence mode 18 of 5-chlorouracil does not correspond to a single mode but to many components in multiple modes in 5-fluorouracil. Since both mode 20 in 5-fluorouracil and mode 18 in 5-chlorouracil contain the ($X_{11}C_5$) stretch (39% ($F_{11}C_5$) stretch in mode 20 and 23% in ($Cl_{11}C_5$) stretch in mode 18), the dissimilarity is likely to be caused by the substitution of the halogen atom.

The discussion of the cosine similarity of 5-fluorouracil versus 5-bromouracil is analogous to 5-fluorouracil versus 5-chlorouracil. Comparing Figure 3.2 (a) and (b), 5-chlorouracil and 5-bromouracil have very similar normal mode character, save for re-ordering of some low-energy modes. The cosine similarity of 5-chlorouracil versus 5-bromouracil is also demonstrated in Figure 3.2(c). In Table 3.2 and Figure B1 it indicates that the difference of the vibrational frequencies between 5-chlorouracil and 5-bromouracil is no more than 10 cm^{-1}, except for mode 12 of 5-chlorouracil. It is interesting to point out that modes 10 and 12 in 5-chlorouracil correspond to modes 9 and 11 in 5-bromouracil.

3.3.2 Vertical excitation energies and oscillator strengths

The vertical excitation energy of 5-fluorouracil has been studied extensively with electronic structure calculations previously. The values have been determined at

various levels of theory, including EOM-CCSD,[183] CASPT2,[176,177] CIS,[196] and TD-DFT.[97,178,180,181] The excitation energies have been computed in both the gas phase[97,176,177,196] and in solution.[97,178,180,181,183] To the best of our knowledge, there is only one paper that has reported the theoretical vertical excitation energy of 5-chlorouracil, which are computed at the TD-B3LYP/6-311+G(d,p) level of theory in the gas phase;[173] and there has been only one paper regarding exploration of the excited state potential energy surface, including the vertical excitation energies, of 5-bromouracil, at the CASPT2//CASSCF(16,12)/6-311G* level of theory in the gas phase.[182] However, no value has been reported regarding the vertical excitation energies of 5-chlorouracil and 5-bromouracil in water.

The vertical excitation energies of the 5-halogenated uracils at corresponding equilibrium geometries were determined at the TD-CAMB3LYP/aug-cc-pVTZ level of theory in implicit water using C-PCM. These values along with the corresponding oscillator strengths and Λ- parameters[165] are reported in Table 3.3. The vertical excitation energies do not play a crucial role in the determination of the resonance Raman spectrum but it is useful to compare the present results to experiment, and worth reporting the excitation energies of 5-chlorouracil and 5-bromouracil in water, see Table 3.3.

Table 3.3: *Vertical Excitation Energies (E_V/eV), Oscillator Strengths (f) and Λ Parameters[165] for the Three Lowest Singlet Excited States of 5-Halogenated Uracils at the CAMB3LYP/aug-cc-pVTZ level of theory in H_2O (C-PCM). Experimental Values are Included for Comparison.*

	S_1 $\pi \rightarrow \pi^*$			S_2 $n \rightarrow \pi^*$			S_3 Rydberg		
	E_V	f	Λ[d]	E_V	f	Λ	E_V	f	Λ
5-fluorouracil	4.940	0.3267	0.760	5.374	0.0000	0.478	6.285	0.0068	0.224
experiment	4.68[a], 4.66[b], 4.67[c]	-	-	-	-	-	-	-	-
5-chlorouracil	4.820	0.3368	0.769	5.395	0.0000	0.441	6.091	0.0003	0.272
experiment	4.54[b], 4.52[c]	-	-	-	-	-	-	-	-
5-bromouracil	4.783	0.3337	0.755	5.386	0.0000	0.475	5.463	0.0004	0.373
experiment	4.47[c]	-	-	-	-	-	-	-	-

[a] Ref.196, measured in water.
[b] Ref.97, measured in water.
[c] Ref.197, measured in water.
[d] $\Lambda = \frac{\sum_{i,a} \kappa_{ia}^2 \langle |\phi_i| | |\phi_a| \rangle}{\sum_{i,a} \kappa_{ia}^2}$. ϕ_i and ϕ_a are occupied and virtual orbitals, respectively.

It is interesting to compare the vertical excitation energies for the 5-halogenated uracils. The value of the vertical excitation energy to S_1 decreases by approximately 0.12 eV from 5-fluorouracil to 5-chlorouracil and 0.04 eV from 5-chlorouracil to 5-bromouracil. The red shift of the vertical excitation energy to S_1 upon changing the halogen substituent has been observed experimentaly,[97,197] see Table 3.3 for corresponding experimental shifts. The vertical excitation energy to S_2 shows little difference as the halogen is changed. The oscillator strength shows that in implicit water S_1 is bright state but S_2 is dark. The energy of excitation to S_3 decreases even more than S_1. From 5-fluorouracil to 5-chlorouracil it drops 0.2 eV and from 5-chlorouracil to 5-bromouracil it is reduced a further 0.6 eV. The Λ- parameter indicates that S_3 is a Rydberg state with strong charge transfer character, which is also similar to what is found in uracil.[69]

Compared to the experiment,[97,196,197] the computed vertical excitation energies of the 5-halogenated uracils are overestimated ~ 0.3 eV. We observed a similar discrepancy between the computational and experimental vertical excitation energies for uracil determined at the CAMB3LYP/aug-cc-pVTZ level of theory.[69]

Comparing to the theoretical vertical excitation energies of the 5-fluorouracil,[97,176,177,196] 5-chlorouracil[173] and 5-bromouracil[182] in the gas phase, our computations show that, for the 5-halogenated uracils in the C-PCM, $\pi \rightarrow \pi^*$ transition is red shifted and $n \rightarrow \pi^*$ transition is blue shifted, which is due to the solvation effect, see Table 3.3. The re-ordering the energetics of excited state has been previously reported for 5-fluorouracil,[97,178,180,181,183] and also has been observed in our previous study on the vertical excitation energy of uracil,[69] the parent molecule of 5-halogenated uracils.

3.3.3 Resonance Raman spectra

The Cartesian gradients on the S_1 excited state for the three 5-halogenated uracils are determined and the resonance Raman spectra are simulated by projecting these gradients onto the normal mode coordinates. Previously,[69] we found that, if using TD-DFT, the excited state gradient is very sensitive to the functional chosen, and a long range corrected functional (CAMB3LYP) provided better agreement than standard

hybrid functionals with the experimentally measured resonance Raman spectrum for uracil. Hence, for the 5-halogenated uracils considered here, the excited state gradients are determined at the CAMB3LYP/aug-cc-pVTZ level of theory. In the following discussion, we compare the resulting simulated resonance Raman spectra of the three halogenated uracils with experimental measurements,[80] see Figure 3.3. The differences between the spectra for the three species are investigated via analysis of the ground and excited states, i.e., normal modes and Cartesian gradients, respectively.

By fitting the experimental resonance Raman spectra, with input of peak positions and well-justified assumptions on line broadening, the displacements $|\Delta|$ can be determined. To the best of our knowledge, the experimental fitting displacements of 5-fluorouracil in water[80] and 5-chlorouracil in methanol[173] have been determined, but the displacements of 5-chlorouracil and 5-bromouracil in water have not been investigated experimentally.

Table 3.4: *Vibrational Frequencies (ω/cm^{-1}) and Dimensionless Displacements ($|\Delta|$) for the S_1 Excited State of 5-Halogenated Uracils at the CAMB3LYP/aug-cc-pVTZ level of theory with PBE0/aug-cc-pVTZ ground state in H_2O (C-PCM). Also Reported are the Experimental Measurement from the Resonance Raman Spectra.*

	modes	8	10	12	15	18	19	20	21	22	23	24	25	26	27
5-fluorouracil	ω	545	637	762	826	1185	1227	1278	1370	1415	1454	1533	1730	1740	1782
	$\|\Delta\|$	0.7051	0.3025	0.6311	0.5241	0.0253	0.5852	0.5348	0.9796	0.2126	0.0775	0.3863	1.1035	0.1935	0.2688
	ω(experiment)[a]	553	639	760	820	1183	1223	1253	1349	1431			1689	1705	
	$\|\Delta\|$(experiment)[a]	0.11	0.15	0.21	0.19	0.20	0.47	0.29	0.75	0.26			0.85	0.33	
	modes	8	10	12	15	18	19	20	21	22	23	24	25	26	27
5-chlorouracil	ω	549	613	676	797	1102	1207	1233	1360	1419	1442	1522	1688	1738	1782
	$\|\Delta\|$	0.5591	0.4572	0.2412	0.8020	0.0312	0.0216	0.6093	0.9867	0.2054	0.1840	0.3436	1.0617	0.2603	0.2945
	ω(experiment)[b]	551	610		785		1190	1229	1337	1432			1634	1682	
	modes	8	9	11	15	18	19	20	21	22	23	24	25	26	27
5-bromouracil	ω	547	605	639	794	1074	1204	1235	1361	1418	1438	1518	1681	1736	1782
	$\|\Delta\|$	0.4571	0.4802	0.1282	0.8029	0.0243	0.0202	0.6261	0.9782	0.1603	0.1928	0.3367	1.0354	0.2775	0.2893
	ω(experiment)[b]		613		791		1181	1232	1338	1447			1631	1680	

[a] Ref.80.

[b] Ref.80, frequencies determined at the maximum intensity of each peak in the resonance Raman spectra.

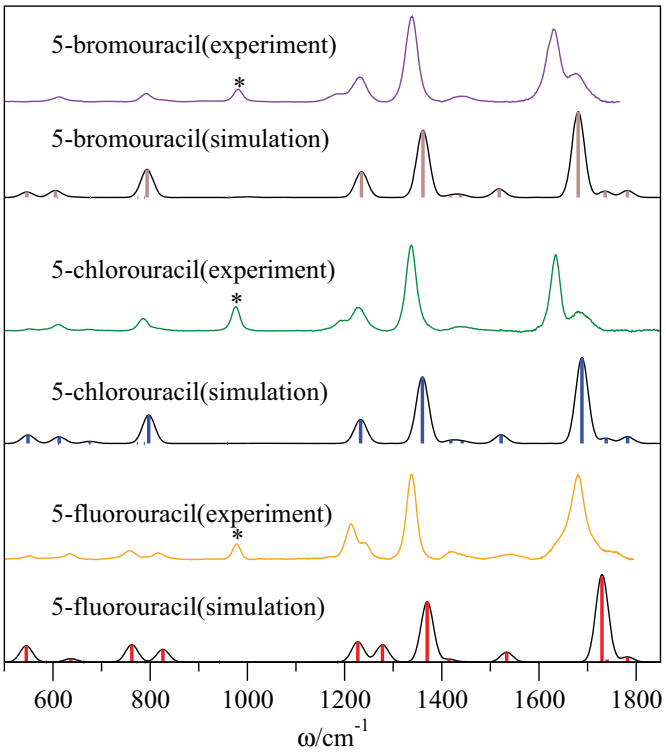

Figure 3.3: *Resonance Raman spectra of 5-halogenated uracils. Simulations performed in H_2O (C-PCM) using PBE0/aug-cc-pVTZ ground state geometries and TD-CAMB3LYP/aug-cc-pVTZ for the excited state. fwhm used in the simulations is 30 cm^{-1}. The experimental spectra are taken from Ref 80. The asterisk in the experimental spectra[80] indicates the internal standard peak of ca. 0.3 M sulfate.*

5-fluorouracil

In the simulated spectrum of 5-fluorouracil, the majority of the peaks observed experimentally between 500 cm^{-1} and 1800 cm^{-1} are well determined, see Figure 3.3. The relative agreement and assignment are discussed from low to high frequency; unless indicated otherwise, the frequency in the text refer to the experimental values. The positions (even without frequency scaling) of the four low intensity peaks between 500 cm^{-1} and 900 cm^{-1} are captured very well. However, the intensities of some of these

low frequency peaks, i.e., modes 8, 12 and 15, and their corresponding dimensionless displacements, are slightly overestimated compared to those in the experimental spectrum and as determined by the fit values of the displacements,[80] see Figure 3.3 and Table 3.4.

According to the simulation, mode 19, related to (N_3C_4) stretch, corresponds to the peak at 1223 cm^{-1} and mode 20, related to ($F_{11}C_5$) stretch, is the shoulder peak at slightly higher frequency. In the simulation, the ratio of $I(\text{mode } 20)/[I(\text{mode } 19) + I(\text{mode } 18)]$ is approximately 0.85, which is much larger than the value of 0.32 observed in the experiment. The discrepancy is caused both by an underestimation of the intensity for mode 19 (and/or mode 18) and overestimation for mode 20. In the experimental fitting,[80] these peaks were assigned including modes 18, 19 and 20, while the simulation suggests that mode 18 plays no role in the resonance Raman spectrum. Thus, the underestimation of the intensity of mode 18 may be the reason for the high ratio of peak intensities determined computationally, or it may simply be from the underestimation of mode 19. In the experiment the peaks corresponding to mode 21 (1349 cm^{-1}) and mode 25 (1689 cm^{-1}) have almost equal intensity, but in the simulation the peak intensity of mode 21 is slightly too low.

5-chlorouracil and 5-bromouracil

The experimental (and, hence, simulated) resonance Raman spectra of 5-chlorouracil and 5-bromouracil are very similar, see Figure 3.3. Therefore, the analysis of the spectrum of 5-bromouracil is analogous to that for 5-chlorouracil, and, only the latter is discussed in detail here.

As expected, the relative peak positions for 5-chlorouracil agree well with the experimental measurement, except for the usual modest shift to higher frequency for peaks > 1000 cm^{-1}. The peak intensities of the low frequency modes 10 and 12, at 610 cm^{-1} and 676 cm^{-1} (computational values provided), respectively, have good agreement with the experimental spectrum, but the intensities of modes 8 (551 cm^{-1}) and mode 15 (785 cm^{-1}) are moderately overestimated. Compared to the spectrum of 5-fluorouracil, the relative peak intensity of mode 12 in 5-chlorouracil is lower and

the intensity of mode 15 is higher. Since the PED assignments show a redistribution between mode 12 and mode 15, as discussed with respect to the cosine similarity, the intensity of these two modes switches as well.

The shoulder peak at 1190 cm^{-1} in the experimental spectrum is significantly underestimated in its intensity in the simulated spectrum. The peak intensities of modes 18 (1102 cm^{-1}, computational value) and mode 19 (1190 cm^{-1}) are only 0.2% and 0.1% of mode 20 (1229 cm^{-1}), respectively, but in experiment the peak at 1190 cm^{-1} is approximately 50% of the peak at 1229 cm^{-1}. As expected from their low intensities, the displacements of modes 18 and 19 also have small $|\Delta|$ values, see Table 3.4. From the comparison of the peak intensities, it cannot be determined whether the shoulder peak observed experimentally corresponds to mode 18 or mode 19. The similarity analysis shows mode 19 of 5-fluorouracil (peak at 1223 cm^{-1}) is very similar to mode 20 of 5-chlorouracil (peak at 1229 cm^{-1}), see Figure 3.2(a), and the PED analysis shows its primary contributions are (N_3C_4) stretch, (N_3C_2) stretch and ($H_{12}C_6C_5$) bend, see Table 3.1. The shoulder peak 1253 cm^{-1} in 5-fluorouracil, corresponding to mode 20, is significantly reduced in the spectrum of 5-chlorouracil, because mode 20 of 5-fluorouracil is dissimilar to all the modes of 5-chlorouracil, see Figure 3.2(a). Mode 19 of 5-chlorouracil is composed of (N_1C_6) stretch and ($H_7N_1C_6$) bend. Therefore, the PED analysis and cosine similarity analysis is unable to assign the shoulder peak at 1190 cm^{-1} to either mode 18 or mode 19. Since in experiment the peak at 1229 cm^{-1} is 39 cm^{-1} higher than its shoulder peak, this shoulder peak is more likely to correspond to mode 19 (26 cm^{-1} lower than mode 20) than mode 18 (131 cm^{-1} lower than mode 20).

In the spectrum of 5-chlorouracil, the broad, low intensity peak at 1432 cm^{-1} most likely comprises at least two modes, 22 and 23, and mode 24 may also contribute in the higher energy region.

Another peak's intensity that is underestimated in the simulation is mode 26 (1682 cm^{-1}), which corresponds to the shoulder peak observed in the experiment at 1682 cm^{-1}; on the other hand its position relative to mode 25 (peak at 1688 cm^{-1}), i.e., 50 cm^{-1} higher frequency, is correctly predicted compared to experiment, i.e., 48 cm^{-1}

splitting between these two peaks. Comparing the spectra of 5-chlorouracil and 5-fluorouracil, the peaks above 1600 cm^{-1} are very different. In 5-fluorouracil, there is a broad peak at 1689 cm^{-1} with a small (experimentally) unassigned peak at 1747 cm^{-1}. Based on the simulation, this broad peak is composed of two modes, 25 and 26 (albeit with one much more intense than the other), and the small unassigned peak is mode 27. However, in the experimental spectrum for 5-chlorouracil, there are two peaks that are separated by 48 cm^{-1}. The peak at 1634 cm^{-1} is assigned with only one mode, mode 25, and the shoulder peak at 1682 cm^{-1} contains two modes, modes 26 and 27, albeit the simulated intensities are too low. As discussed above, the cosine similarity shows the normal mode characters of modes 25 and 26 are moderately different, which is caused by the vibrational energy redistribution of (C_5C_6) stretch and ($O_{10}C_4$) stretch between 5-fluorouracil and 5-chlorouracil, see Table 3.1.

Role of exited state Cartesian gradients

According to Eq (3.1), the differences between the spectra for 5-fluorouracil, 5-chlorouracil and 5- bromouracil can be attributed to two factors: the ground state eigenvectors of the Hessian matrix $\mathbf{T}$ and the Cartesian gradient on the excited electronic state $\mathbf{V_x}$. The Cartesian gradients for the S_1 state as determined at the TD-CAMB3LYP/aug-cc-pVTZ level of theory in H_2O (C-PCM) of the 5-halogenated uracils are illustrated as vectors for each atom in Figure 3.4. The Cartesian gradients for the S_1 state of uracil are also determined at the same level of theory and solvent model. Comparing the excited state Cartesian gradients of 5-fluorouracil to 5-chlorouracil, the gradient on N_3, C_5, C_6, and O_{10} are almost identical, but the gradient on N_1, C_2, C_4 and X_{11} are different. For the gradients that are different, the vectors in 5-chlorouracil are much more aligned along the N_1-C_6, C_2-N_3, C_4-C_5 and C_5-X_{11} bonds than in 5-fluorouracil. Furthermore, there is a very small gradient on O_8 for 5-fluorouracil but a negligible gradient on this atom in 5-chlorouracil. Most of the gradients on the atoms of 5-bromouracil are similar to 5-chlorouracil, except that the vectors on C_2 and X_{11} more strongly align along the C_2-N_3 and C_5-X_{11} bonds than in 5-chlorouracil. Comparing the Cartesian gradients of 5-halogenated uracils

and uracil, the difference is mainly between the magnitude of the gradients on X_{11} in 5-halogenated uracils and the corresponding hydrogen atom in uracil (H_{11}). While all the 5-halogenated uracils have some moderate gradients on X_{11}, the gradient on H_{11} for uracil is negligible, see Figure B6.

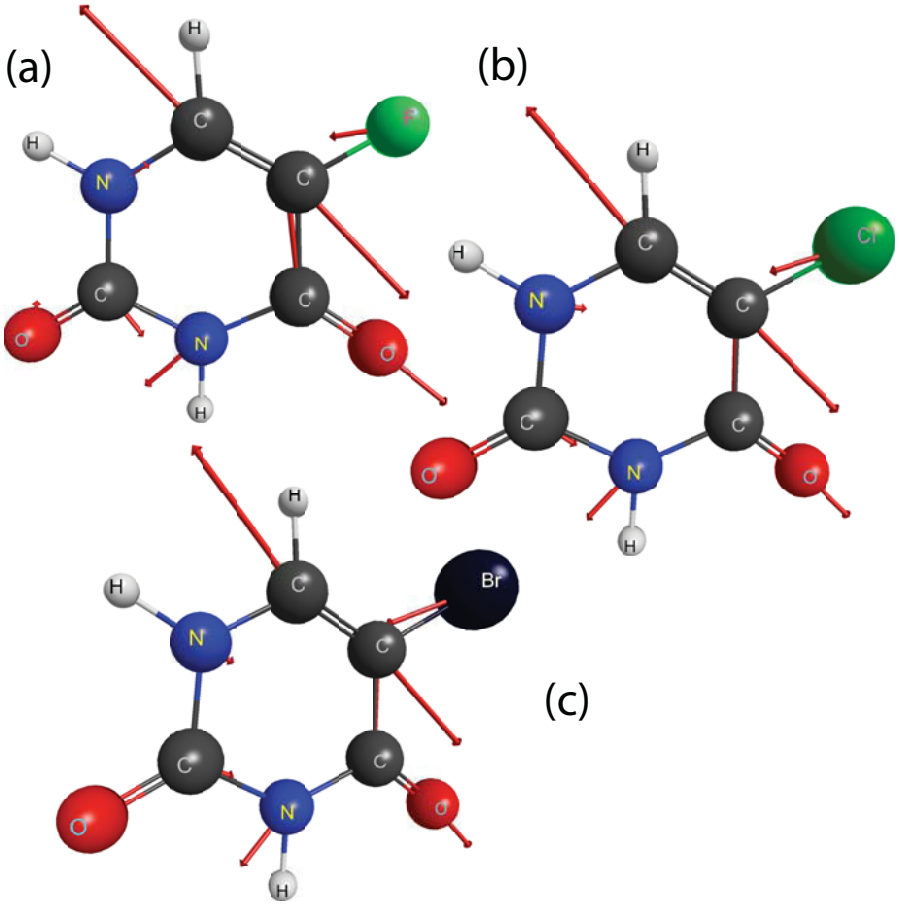

Figure 3.4: *Vectors illustrating the Cartesian gradients for each atom of (a) 5-fluorouracil (b) 5-chlorouracil and (c) 5-bromouracil determined using TD-CAMB3LYP/aug-cc-pVTZ in H_2O (C-PCM) for the S_1 excited state.*

To understand, how the difference between the Cartesian gradients for the excited state contributes to the differences in the resonance Raman spectra, we computed two resonance Raman spectra whose normal mode eigenvectors are both taken from 5-chlorouracil, but using different excited state gradients, see Figure 3.5(a). One of

the excited state gradients is from the S_1 state of 5-fluorouracil (F_e) and the other one is from the S_1 state of 5-chlorouracil (Cl_e). Both spectra are simulated using the vertical excitation energy and transition dipole moments based on Cl_e. We also determined the (normalized) differences between these two spectra by subtracting the intensity of F_e from Cl_e for each mode, see Figure 3.5(b).

In Figure 3.5(b), we see the differences of the spectra caused by different excited gradients are less than 15% of the maximum intensity of the spectrum. For the modes lower than 1000 cm^{-1}, the contribution of Cl_e is to increase the peak intensity; for the modes higher than 1000 cm^{-1}, Cl_e reduces the peak intensity (except for modes 22, 23 and 24, that exhibit very small increases). The largest changes occurred for modes 15 and 21, in which each mode increases (or decreases) by approximately 15% of the spectrum maximum intensity, while modes 8, 10, 20 and 26 changed by $\sim$ 5%. Therefore, while the difference in excited state gradients plays a moderate role, the strong difference between the resonance Raman spectra for 5-fluorouracil and 5-chlorouracil arises from the major changes in the ground state normal modes, see discussion of cosine similarity and Figure 3.2.

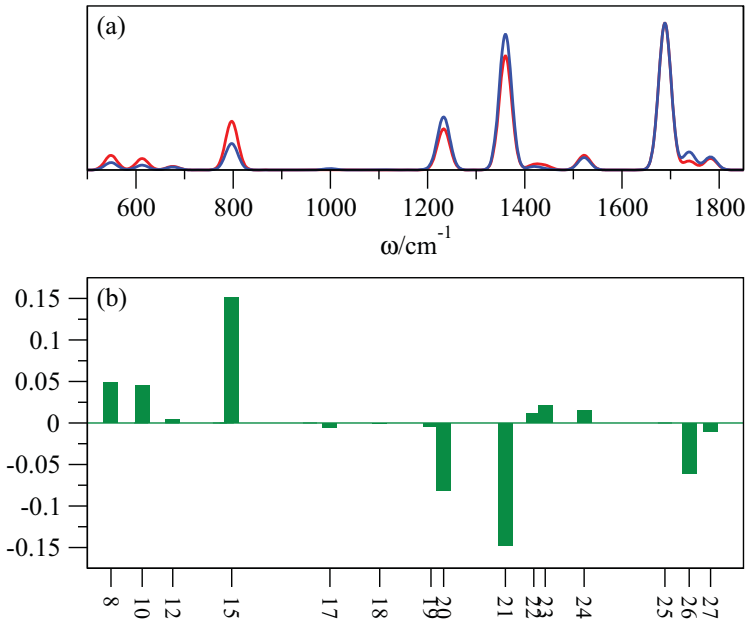

Figure 3.5: *(a) Resonance Raman spectra of Cl_e (red) and F_e (blue), see main text for computational details. fwhm used in the simulation is 30 cm^{-1}. (b) The intensity difference of the (normalized) resonance Raman spectra of Cl_e and F_e.*

We simulated the resonance Raman spectrum using excited state gradients from the S_1 state of 5-bromouracil (Br_e) and normal mode eigenvectors from 5-chlorouracil, see Figure 3.6(a). The (normalized) differences between the spectra, Br_e and Cl_e, are determined via subtracting the intensity of the former from the later for each mode, see Figure 3.6(b). The largest differences is $\sim$ 9%, which is smaller than the largest difference between Cl_e and F_e, which is 15%. The major changes include 9% in mode 21, 5% in mode 15 and 3% in mode 10. The changes in the rest of the modes are less than 2%. Since the normal mode characters of 5-chlorouracil and 5-bromouracil also share high cosine similarity, see Figure 3.2(c), both the experimental and simulated

resonance Raman spectra of these two uracil derivatives are very similar to each other.

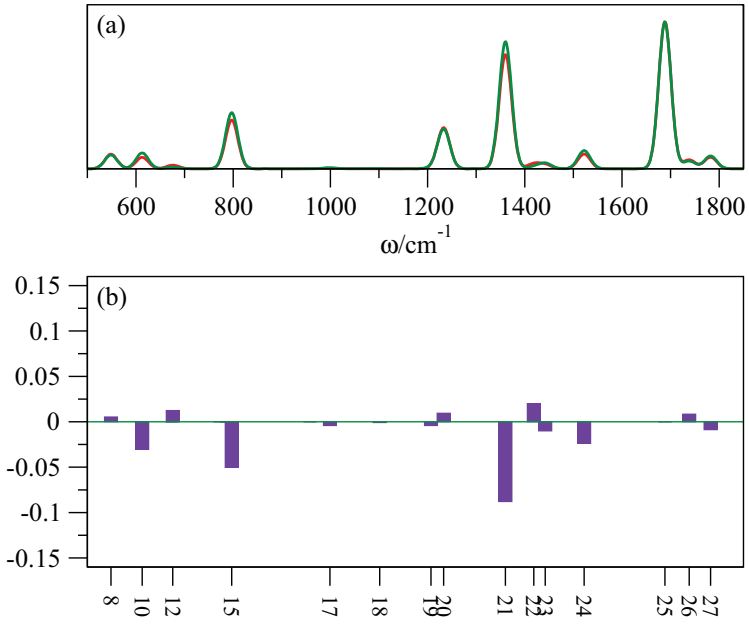

Figure 3.6: *(a) Resonance Raman spectra of Cl_e (red) and Br_e (green), see main text for computational details. fwhm used in the simulation is 30 cm^{-1}. (b) The intensity difference of the (normalized) resonance Raman spectra of Cl_e and Br_e.*

3.4 Conclusions

In this study, the resonance Raman spectra of the 5-halogenated (F, Cl, and Br) uracils are simulated via DFT (for the ground state), TD-DFT (for the excited state) and the HT formalism. The resulting peak positions and their intensities are compared with experimental measurements,[80] and for most of the peaks, there is reasonable agreement. To the best of our knowledge, although the relative intensi-

ties of the lines in the resonance Raman spectra of 5-fluorouracil and 5-chlorouracil have been computed via the sum-over-state approach previously,[184] the spectrum of 5-bromouracil has not been simulated and analyzed before. We also reported the vertical excitation energies of the three 5-halogenated uracils, in which the values for 5-chlorouracil and 5-bromouracil have not been reported before. The red shift of the vertical excitation energy to S_1 upon changing the halogen substituent observed in experiment[97,197] is confirmed by our computation using CAMB3LYP/aug-cc-pVTZ, see Table 3.3.

We investigated the substituent effect on the resonance Raman spectra of the three 5-halogenated uracils. Between the experimental spectra of 5-fluorouracil and 5-chlorouracil, there are a few dissimilar peaks being observed, see Figure 3.3. The dual-peak at 800cm^{-1} in 5-fluorouracil corresponds to one single peak in 5-chlorouracil; the shoulder peak at 1250 cm^{-1} in 5-fluorouracil is "shifted" to 1190 cm^{-1} in 5-chlorouracil; and the single peak at 1700 cm^{-1} in 5-fluorouracil corresponds to two peaks in 5-chlorouracil in the region with same frequency. The cause of these differences are examined systematically in terms of their ground state vibrational frequencies, normal modes eigenvectors and excited state Cartesian gradients. The PED analysis and cosine similarity show that, although most of the normal modes between 5-fluorouracil and 5-chlorouracil are similar, some modes in the low (modes 12 and 15) and high frequency region (modes 25 and 26) have moderate dissimilarity, see Table 3.1 and Figure 3.2(a). On the other hand, the difference contributed by the excited Cartesian gradients are between 5 $\sim$ 15% as determined in the comparison between the resonance Raman spectra of F_e and Cl_e, see Figure 3.5. Since the shoulder peak at 1190 cm^{-1} in 5-chlorouracil is underestimated in the simulation, the dual peak structure is not reproduced in the simulation. From the discussion above, we can conclude that cause of the differences between the spectra of 5-fluorouracil and 5-chlorouracil are due to both the ground state normal mode eigenvectors and excited state gradients.

Since the experimental spectra of 5-chlorouracil and 5-bromouracil are very similar, according to Eq 3.1, we expect the normal mode eigenvector, $\mathbf{T}$ and the excited

state Cartesian gradient, $\mathbf{V_X}$, between the two halogenated uracil derivatives to have high similarity. This is confirmed by the cosine similarity between 5-chlorouracil and 5-bromouracil, see Figure 3.2(c), and the resonance Raman spectra determined using Br_e and Cl_e, see Figure 3.6.

As the number of electrons and the mass of the halogen atom increase in the 5-halogenated uracils, not only the normal mode but also the excited state gradient varies with different halogen substituent. Therefore, as the consequence of these two factors combined, the resulting resonance Raman spectra of the 5-halogenated uracils are different.

Chapter 4

Effects of Hydrogen Bonding with H_2O on the Resonance Raman Spectra of Uracil and Thymine

4.1 Introduction

Resonance Raman spectroscopy has been used to probe the initial electronically excited state dynamics of uracil, thymine and their derivatives.[30,38–40,43,44,46,52,80,96,173] During the measurement of the spectrum, the energy of the incident excitation light is (near-)resonant with the transition energy to the electronic state of the nucleobase. Therefore, the frequencies and intensities of the peaks in the resonance Raman spectrum provide crucial information on the initial dynamics of the molecule on its electronically excited state potential. The experimental resonance Raman spectra of uracil and thymine have been measured and interpreted by various research groups.[43,44,52] In 2007 and 2009, Yarasi et al. measured the resonance Raman spectra of uracil and thymine in water,[43,44] as well as their corresponding resonance Raman excitation profiles. In 2008, Xin-Ming Zhu et al. investigated the resonance Raman spectrum of thymidine and compared the results with the spectrum of thymine.[52]

Assisted by quantum chemical computations, information regarding the initial excited state dynamics can be extracted by simulating the resonance Raman spectrum. The spectrum can be determined by performing accurate electronic structure computations on the ground state potential energy surface (PES) using, e.g., Density

Functional Theory (DFT), and for the excited state, using methods such as Time Dependent Density Functional Theory (TD-DFT).[16] The resonance Raman spectra of uracil and thymine have been studied computationally via electronic structure calculations.[27,36,37,69] These simulations have been carried out based on two methods: the Kramers-Kronig transformation (KK)[12,27] and the Herzberg-Teller formalism (HT).[16,106] The KK method relies on the relationship between the polarizability and the optical absorption.[27,36,37] In 1995, Peticolas and Rush[36] simulated the resonance Raman spectrum of uracil using the KK transformation, where the ground and excited state properties were obtained at the HF/6-31G* and CIS/6-31G* levels of theory, respectively. They also simulated the resonance Raman spectrum of thymine[37] via the same procedure, and compared the result with uracil. In 2004, Neugebauer and Hess[27] simulated the resonance Raman spectrum of uracil using an improved formalism of the KK transformation. They also determined the excited state gradient of uracil at different levels of theory, simulated the resonance Raman spectrum of uracil using Savin's equation[24–26] for preresonant Raman scattering, and compared the resulting spectrum to that computed by the KK formalism. They found the spectra by the two methods give qualitative agreement to each other. On the other hand, the HT method is based on the short time dynamics of the molecule in the excited electronic state. In 2014, Sun and Brown simulated the resonance Raman spectra of uracil using TD-DFT.[69] It was found that excited state gradients determined with long range corrected functionals, e.g. CAMB3LYP, combined with a PBE0/aug-cc-pVTZ optimized ground state structure, exhibit better agreement with the experimental spectrum than using standard hybrid functionals such as PBE0 and B3LYP for the excited states.

Although there have been extensive studies on the effect of solvation on the excited state properties of uracil and thymine, they have focused primarily on the vertical excitation energies, the excited state relaxation pathways and the corresponding lifetimes.[97–105,117,118,179,180,198,199] To the best of our knowledge, there is only one study that investigated the effect of solvation on the resonance Raman spectrum of uracil,[69] and no analogous study for thymine. Sun and Brown[69] compared excited state Carte-

sian gradients for uracil, and the resulting resonance Raman spectra, determined in both implicit water and the gas phase. They found that including implicit water, when determining the excited state gradients, improved the agreement with the experiment for the peak intensities, especially for peaks with frequencies greater than 1600 cm^{-1}. However, the impact of explicit water and the hydrogen bonds that are formed with the solute have yet to be studied thoroughly for the resonance Raman spectrum of uracil.

In this paper, we focus on studying the effects of explicit hydrogen bonding with water on the resonance Raman spectra of uracil and thymine. The chemical structures and the atomic indices utilized for uracil and thymine are shown in Figure 4.1. The excited state gradients for uracil and thymine complexed with one (or two) explicit water(s) are determined via TD-DFT and the resonance Raman spectra of these mono- (and di-) water configurations are simulated using the HT method. As the resonance Raman spectrum is governed by the ground state normal modes and the excited state Cartesian gradient, we examined how these two factors are changed in different mono water configurations and investigated the corresponding differences between spectra.

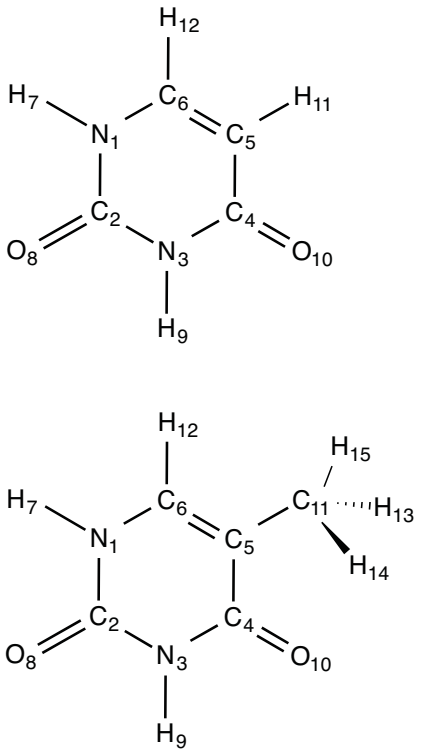

Figure 4.1: *Chemical structures of uracil and thymine with atomic numbering used throughout the manuscript.*

4.2 Computational Methods

We chose the three bonding sites in uracil and thymine that are most likely to form hydrogen bonds in water, and added a single explicit water, see Figures 4.2 and 4.3. The choice of the hydrogen bond sites is accordance with complexes that have lowest relative energies in previous uracil-H_2O and thymine-H_2O studies.[150,155,159,200–203] The ground state structures of the three uracil-H_2O and corresponding thymine-H_2O complexes, (A), (B), and (C), see Figures 4.2 and 4.3, are optimized at the PBE0/aug-cc-pVTZ level of theory[119,120,124,125] embedded in implicit water using the conductor-like Polarizable Continuum Model (C-PCM).[137,138] The convergence criteria for the maximum of force and displacement are 1.5×10^{-5} and 6.0×10^{-5} in atomic

units, respectively; the convergence criteria for the RMS of force and displacement are 1.0×10^{-5} and 4.0×10^{-5} in atomic units, respectively; and the ultrafine integration grid (pruned 99 radial shells, 590 angular points) is used. The Hessian matrix for each configuration is computed, and the corresponding vibrational frequencies and normal modes determined. To further investigate the impact of the hydrogen bonds, we analyzed the potential energy distribution (PED) and the cosine similarity (see Eq 4.3 below) of the normal modes in each of the uracil- and thymine-H_2O complexes.

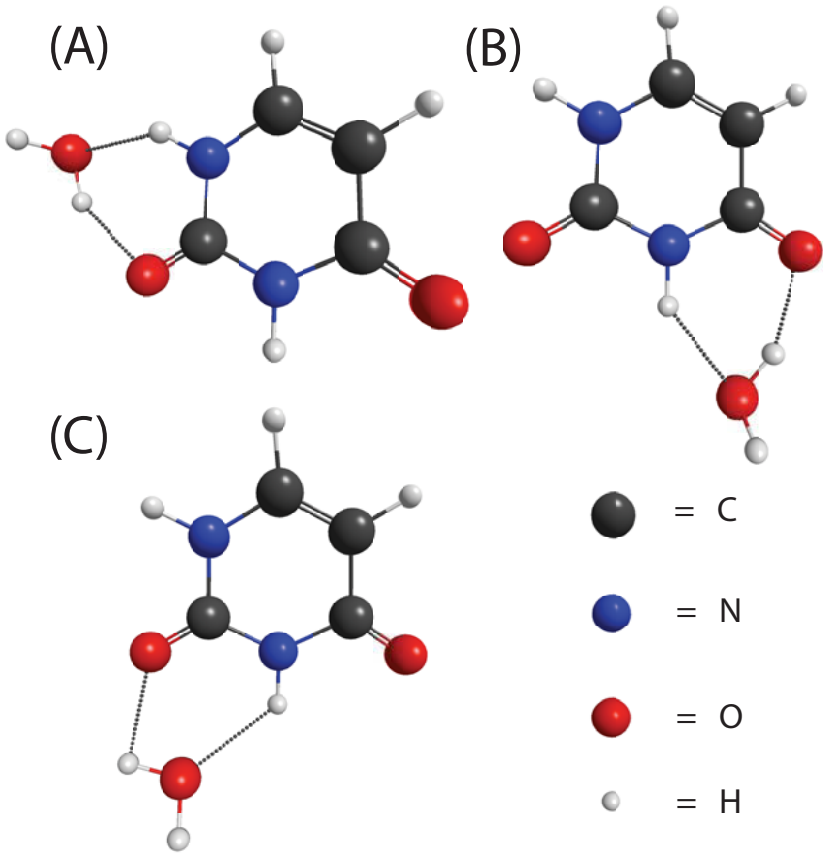

Figure 4.2: *The geometries of uracil-H_2O complexes (A), (B), and (C), as determined at the PBE0/aug-cc-pVTZ level of theory in C-PCM (H_2O).*

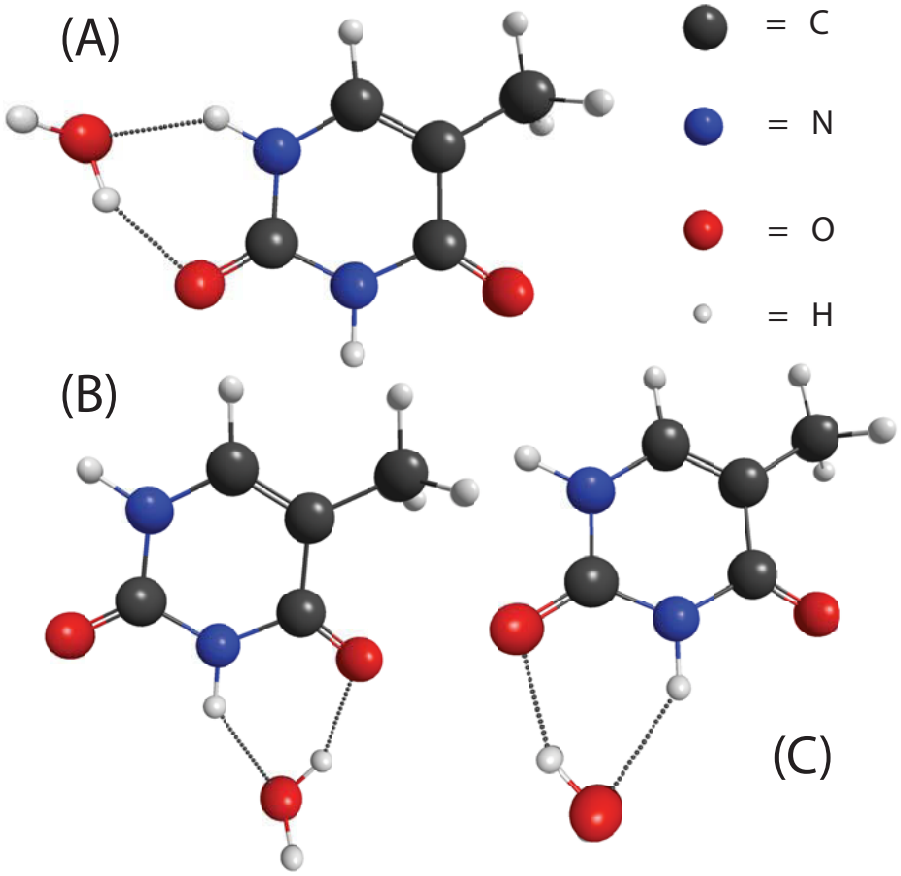

Figure 4.3: *The geometries of thymine-H_2O complexes (A), (B), and (C), as determined at the PBE0/aug-cc-pVTZ level of theory in C-PCM (H_2O).*

The vertical excitation energies and corresponding oscillator strengths of the first three excited states were determined at the CAMB3LYP/aug-cc-pVTZ level of theory[124–126] via TD-DFT. The excited state gradients of the bright state (S_1) were determined in Cartesian coordinates, as required for the computation of the resonance Raman spectrum, see below. All the excited state computations, including the vertical excitation energies and excited state gradients, are performed using C-PCM with default parameters for water to mimic the effects of bulk solvation.

To simulate the resonance Raman spectrum, one needs to compute the dimen-

sionless displacements via

$$\mathbf{\Delta_Q} = \mathbf{\Lambda^{-1} T^{\intercal} M^{-1/2} V_X}. \tag{4.1}$$

Here $\mathbf{\Delta_Q}$ is the matrix of ground state normal mode displacements, $\mathbf{\Lambda}$ is the diagonal matrix of eigenvalues of the mass weighted Hessian, $\mathbf{T}$ contains the eigenvectors of the mass weighted Hessian, $\mathbf{M}$ is the diagonal matrix of the atomic masses, and $\mathbf{V_X}$ is the energy gradients of the excited state in Cartesian coordinates. The energy gradients ($\mathbf{V_X}$) are determined analytically using TD-DFT, and the eigenvectors of the mass weighted Hessian ($\mathbf{T}$) are extracted from the ground state DFT computation. The normal mode displacements were converted into dimensionless displacements using

$$\Delta_k = \left(\frac{\Lambda_k}{m_e}\right)^{\frac{1}{4}} \Delta_{Qk}. \tag{4.2}$$

We simulated the resonance Raman spectrum under the first order approximation using the independent harmonic oscillator (IMDHO) model within the Herzberg-Teller short-time dynamics formalism.[106] The incident photon energy is chosen as 266 nm and the fwhm in the simulation is 30 cm^{-1}, in order to match the fwhm of well-defined single peaks in the experimental resonance Raman spectra.[43,44]

The DFT and TD-DFT computations are performed using Gaussian (G09),[84] and the resonance Raman spectra are simulated via the program orca_asa.[15,16] The PEDs of the normal modes are analyzed via the VEDA4 software package,[141,142] and the Λ parameters[165] are determined using the Gabedit software package.[188] More details of the theoretical derivations for the resonance Raman simulation can be found in Refs. 16 and 15.

4.3 Results and Discussion

4.3.1 Equilibrium geometry, vibrational frequencies and normal modes

The effect of solvation on the optimized geometries and vibrational frequencies of uracil and thymine have been presented previously in numerous experimental and

computational studies.[69,101,149–151,154,155,157–159,200–210] In the computational studies, the water solvation environment has been simulated using both implicit[69,101,151] and explicit water.[101,149,150,154,155,158,159,203,209,210] In the present work focused on the resonance Raman spectra, the primary interest is in the vibrational frequencies (that impact peak positions) and eigenvectors (that strongly effect peak intensities).

The ground state structures of three uracil-H_2O and three thymine-H_2O complexes are optimized at the PBE0/aug-cc-pVTZ level of theory in the gas phase and in implicit water using C-PCM. The optimized structures are shown in Figures 4.2 and 4.3, and the relative total energy of each configuration is given in Table 4.1. For uracil-H_2O (thymine-H_2O) in the gas phase, (A) is the most stable configuration, while (B) and (C) are 1.42 kcal/mol (1.54 kcal/mol) and 2.15 kcal/mol (1.97 kcal/mol) higher in energy than (A). The relative energy ordering of these complexes in the gas phase agrees with that reported previously.[150,155,159,200–203] Embedded in implicit water, the relative energy order of the complexes is changed. The relative energy difference is significantly reduced from $\sim$ 1-2 kcal/mol (in the gas phase) to $<$ 0.5 kcal/mol (in implicit water); (B) is now most stable, but (A) and (B) are essentially isoenergetic.

Table 4.1: *Relative Energies of Uracil-H_2O and Thymine-H_2O complexes as Determined using the PBE0/aug-cc-pVTZ Level of Theory in the Gas Phase and with Implicit Water Solvation (C-PCM).*

	ΔE/kcalmol^{-1}			
	uracil		thymine	
	gas phase	water (C-PCM)	gas phase	water (C-PCM)
(A)	0.00	0.08	0.00	0.01
(B)	1.42	0.00	1.54	0.00
(C)	2.15	0.44	1.97	0.30

The bond lengths in uracil and thymine in the gas phase, implicit water, and the water complexes (plus implicit water) are given in Table 4.2. The complete geometrical parameters are given in Tables C1, C2 and C3 in the Electronic Supplementary Information (ESI). The geometries of uracil (and thymine) with explicit water in different bonding sites show only small differences ($<$ 0.02 Åchange in any bond length)

between each other, see Tables C1, C2 in the ESI. When water is complexed with uracil (thymine), one of the H-O bonds of water forms a six membered ring with the C-O, N-H, and C-N bonds in uracil (thymine), see Figures 4.2 and 4.3. Thus, compared to the gas phase bond lengths, the bond lengths of C-O and N-H in the ring increase, while the bond length of C-N gets shortened, see the numbers highlighted (in italics) in Table 4.2. On the other hand, the bond lengths in water complexes exhibit almost no difference from the corresponding bond lengths in implicit water ($< 9 \times 10^{-3}$Å).

Table 4.2: *Equilibrium Bond Lengths in Uracil and Thymine Both as Isolated Molecules and Complexed 1:1 with Water. Results Determined using PBE0/aug-cc-pVTZ in the Gas Phase or H_2O (C-PCM).*[a]

	uracil					thymine				
bond length/Å	gas	H_2O(C-PCM)	(A)	(B)	(C)	gas	H_2O(C-PCM)	(A)	(B)	(C)
$r(C_2\text{-}O_8)$	1.2085	1.2162	*1.2252*	*1.2159*	1.2251	1.2097	1.2181	*1.2275*	*1.2178*	1.2273
$r(C_4\text{-}O_{10})$	1.2109	1.2213	1.2209	1.2308	*1.2212*	1.2127	1.2219	1.2214	1.2314	*1.2217*
$r(N_1\text{-}H_7)$	1.0054	1.0073	*1.0194*	1.0076	1.0074	1.0053	1.0069	*1.0182*	1.0072	1.0073
$r(N_3\text{-}H_9)$	1.0093	1.0100	1.0102	*1.0197*	*1.0196*	1.0093	1.0099	1.0101	*1.0194*	*1.0191*
$r(N_1\text{-}C_2)$	1.3825	1.3726	*1.3667*	1.3740	1.3672	1.3770	1.3672	*1.3614*	1.3686	1.3616
$r(C_2\text{-}N_3)$	1.3728	1.3713	1.3661	*1.3706*	1.3653	1.3740	1.3712	1.3658	*1.3706*	1.3653
$r(N_3\text{-}C_4)$	1.3993	1.3921	1.3940	1.3847	*1.3914*	1.3944	1.3890	1.3910	1.3820	*1.3885*

[a] Bonds involved in the six membered ring between water and uracil (or thymine), see main text for definition, are italicised.

As required by the HT formalism for the resonance Raman simulation, we need to determine computationally the ground state vibrational frequencies and normal modes for the uracil- and thymine-H_2O complexes, see Equation 4.1. The vibrational frequencies of the uracil- and thymine-H_2O complexes have been computed, see Tables 4.3 and 4.4, and their relative frequency shifts determined, see Tables C4 and C5 in the ESI; only frequencies relevant to the experimental resonance Raman spectra are provided. The potential energy distribution (PED) is used to analyze the vibrational energy distribution of normal modes in each configuration for both uracil-H_2O and thymine-H_2O, see Tables 4.3 and 4.4. In the PED analysis, a set of internal coordinates, i.e., stretch, bend, torsion, out-of-plane, is chosen to decompose each normal mode described by the eigenvector of the Hessian matrix. Thus it allows us to compare the vibrational energy distribution of the normal modes in different uracil and thymine configurations. Note that only the modes required for understanding the resonance Raman spectrum and the hydrogen bonding effect are presented here; PED analysis for all modes can be found in Tables C6 - C11 in the ESI. The relationship between the normal modes are examined by computing their corresponding cosine similarity. The cosine similarity between two arbitrary normal modes is defined as

$$\mathfrak{S}(v_k^1, v_m^2) = \frac{\left|\sum_{i=1}^{n} v_{k,i}^1 v_{m,i}^2\right|}{\sqrt{\sum_{i=1}^{n} \left(v_{k,i}^1\right)^2}\sqrt{\sum_{i=1}^{n} \left(v_{m,i}^2\right)^2}}. \tag{4.3}$$

Here v_k^1 and v_m^2 are the kth and mth normal modes from the first and second structures, respectively, and $v_{k,i}^1$ and $v_{m,i}^2$ are the ith components of the normal modes in Cartesian coordinate space. The value of $\mathfrak{S}(v_k^1, v_m^2)$ ranges from 0 to 1, where 0 means the two normal modes are completely independent and 1 indicates that the two modes are identical. The vibrational frequencies and normal modes of uracil- and thymine-H_2O complexes have also been compared to the isolated molecules in implicit water, see Table C4 and Figure C3 in the ESI.

4.3.2 Uracil-H_2O

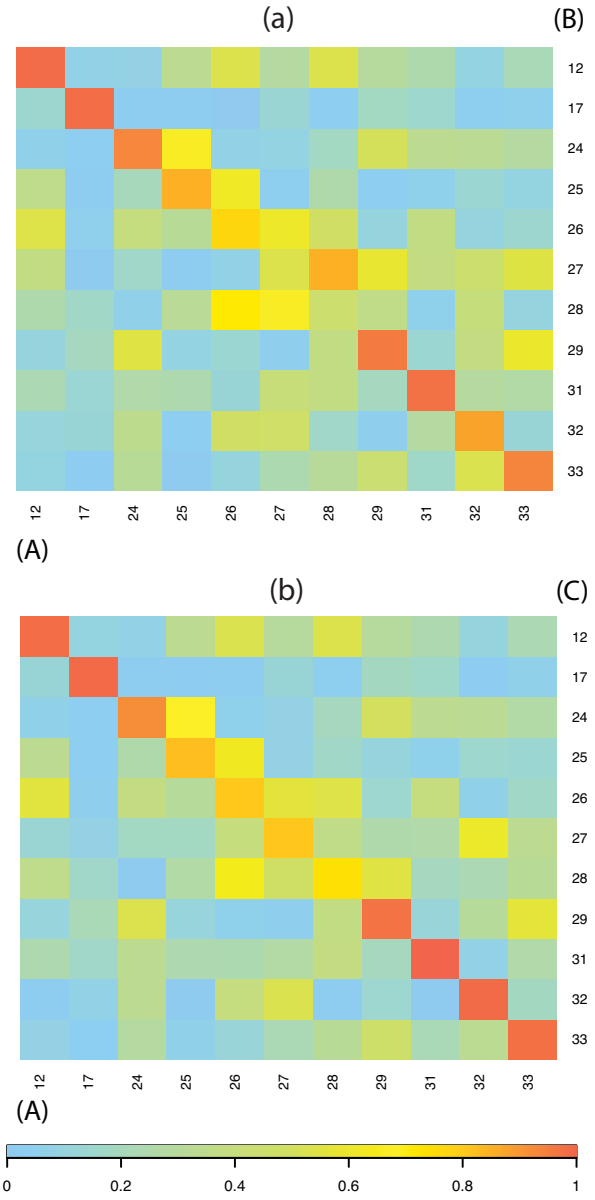

Figure 4.4: *Cosine similarity of (a) complexes (A) vs. (B) and (b) complexes (A) vs. (C) for uracil-H_2O. For the definition of the cosine similarity, see Eq 4.3.*

Table 4.3: *Potential Energy Distribution Analysis and Vibrational Frequencies (ω/cm^{-1}) of Ground State Normal Modes of Uracil-H_2O as Determined Using PBE0/aug-cc-pVTZ in H_2O (C-PCM). Values Correspond to Complexes A, B, and C, Respectively.*

mode	ω	PED
	579	-stretch(N_3C_4)[9%]+bend($C_5C_4O_{10}$)[24%]+bend($N_3C_2O_8$)[13%]+bend($N_1C_2N_3$)[30%]
12	574	+bend($N_3C_2O_8$)[15%]+bend($C_5C_4O_{10}$)[30%]+bend($N_1C_2N_3$)[30%]
	574	+bend($C_5C_4O_{10}$)[29%]+bend($N_3C_2O_8$)[20%]+bend($N_1C_2N_3$)[24%]
	794	+stretch(N_1C_2)[25%]+stretch(C_2N_3)[11%]-bend($N_1C_6C_5$)[9%]+bend($C_2N_1C_6$)[23%]
17	798	+stretch(N_1C_2)[28%]+stretch(C_2N_3)[10%]+bend($C_2N_1C_6$)[25%]
	795	+stretch(N_1C_6)[8%]+stretch(N_1C_2)[26%]+stretch(C_2N_3)[11%]+bend($C_2N_1C_6$)[22%]
	1243	-stretch(N_1C_6)[10%]+stretch(C_2N_3)[19%]-stretch(N_3C_4)[11%]-bend($C_6N_1H_7$)[13%]+bend($C_5C_6H_{12}$)[28%]
24	1230	+stretch(N_1C_6)[18%]+bend($C_6N_1H_7$)[23%]-bend($C_5C_6H_{12}$)[31%]+bend($C_4C_5H_{11}$)[10%]
	1224	-stretch(N_1C_6)[16%]-bend($C_6N_1H_7$)[24%]+bend($C_5C_6H_{12}$)[31%]-bend($C_4C_5H_{11}$)[12%]
	1254	-stretch(N_1C_6)[17%]-stretch(C_2N_3)[9%]+stretch(N_3C_4)[21%]-bend($C_4C_5H_{11}$)[25%]
25	1265	-stretch(C_2N_3)[27%]+stretch(N_3C_4)[32%]-bend($C_4C_5H_{11}$)[14%]
	1261	-stretch(C_2N_3)[22%]+stretch(N_3C_4)[31%]-bend($C_4C_5H_{11}$)[17%]
	1404	+stretch(C_2N_3)[11%]+bend($C_4N_3H_9$)[42%]-bend($C_4C_5H_{11}$)[9%]
26	1407	+stretch(C_5C_6)[9%]+bend($C_6N_1H_7$)[9%]+bend($C_5C_6H_{12}$)[32%]+bend($C_4C_5H_{11}$)[24%]
	1414	+stretch(C_5C_6)[10%]+bend($C_6N_1H_7$)[11%]+bend($C_5C_6H_{12}$)[32%]+bend($C_4C_5H_{11}$)[21%]
	1424	-stretch(C_4O_{10})[9%]+stretch(C_2O_8)[8%]+bend($C_4N_3H_9$)[21%]+bend($C_5C_6H_{12}$)[28%]+bend($C_4C_5H_{11}$)[16%]
27	1447	-stretch(N_1C_2)[15%]+bend($C_6N_1H_7$)[15%]-bend($C_2N_3C_4$)[15%]
	1445	-stretch(C_4O_{10})[10%]+stretch(C_2O_8)[13%]+bend($C_4N_3H_9$)[33%]+bend($C_5C_6H_{12}$)[8%]

	1462	-stretch(N_1C_2)[23%]+stretch(N_3C_4)[10%]+bend($C_6N_1H_7$)[12%]-bend($N_3C_2O_8$)[9%]-bend($C_2N_3C_4$)[16%]
28	1450	-stretch(C_4O_{10})[13%]+bend($C_4N_3H_9$)[52%]
	1458	-stretch(N_1C_2)[12%]+stretch(N_3C_4)[10%]+bend($C_6N_1H_7$)[15%]-bend($C_4N_3H_9$)[23%]-bend($N_3C_2O_8$)[11%]-bend($C_2N_3C_4$)[12%]
	1542	+stretch(C_2O_8)[15%]-stretch(N_1C_6)[17%]+bend($C_6N_1H_7$)[43%]+bend($N_1C_6C_5$)[8%]
29	1532	+stretch(C_2O_8)[9%]-stretch(N_1C_6)[16%]+stretch(N_1C_2)[12%]-stretch(N_3C_4)[10%]+bend($N_1C_6C_5$)[10%]+bend($C_6N_1H_7$)[27%]
	1523	+stretch(C_2O_8)[12%]-stretch(N_1C_6)[17%]+stretch(N_1C_2)[11%]-stretch(N_3C_4)[9%]+bend($N_1C_6C_5$)[10%]+bend($C_6N_1H_7$)[26%]
	1685	+stretch(C_5C_6)[58%]-stretch(N_1C_6)[8%]-bend($C_5C_6H_{12}$)[12%]
31	1683	-stretch(C_4O_{10})[13%]+stretch(C_5C_6)[52%]-stretch(N_1C_6)[8%]-bend($C_5C_6H_{12}$)[13%]
	1690	+stretch(C_5C_6)[58%]-bend($C_5C_6H_{12}$)[11%]
	1723	+stretch(C_4O_{10})[51%]-stretch(C_2O_8)[16%]+bend($C_4N_3H_9$)[11%]
32	1711	+stretch(C_4O_{10})[47%]+stretch(C_5C_6)[8%]+bend($C_4N_3H_9$)[14%]
	1724	+stretch(C_4O_{10})[50%]-stretch(C_2O_8)[14%]+bend($C_4N_3H_9$)[14%]
	1763	+stretch(C_4O_{10})[21%]+stretch(C_2O_8)[40%]-bend($C_6N_1H_7$)[8%]
33	1772	+stretch(C_2O_8)[69%]
	1758	+stretch(C_4O_{10})[21%]+stretch(C_2O_8)[44%]

Hydrogen-bonding with explicit water not only shifts the vibrational frequencies but also alters the characters of normal modes. Using complex (A) as the reference, the cosine similarities of (A) vs. (B) and (A) vs. (C) were computed. The normal mode character of complex (A) is more similar to complex (C) rather than (B), see Figure 4.4, where the cosine similarity for all modes is > 0.74, for (A) and (C), but for (A) vs. (B) the lowest cosine similarity is 0.66. In the following, the frequency shifts and changes between mode character are highlighted as these differences will manifest themselves in the resonance Raman spectra.

Between complex (A) and complex (C), modes 12 and 17 have similarity higher than 0.98 and modes 24 - 28 have lower, but still significant, similarities of 0.74 - 0.91, see Figure 4.4(b). According to the PED analysis, modes 24-28 in complex (A) are composed of four stretching components (stretch(N_1C_2), stretch(C_2N_3), stretch(N_3C_4), and stretch(N_1C_6)) and five bending components (bend($C_2N_3C_4$), bend($C_4N_3H_9$), bend($C_4C_5H_{11}$), bend($C_5C_6H_{12}$), and bend($C_6N_1H_7$)). When changing the explicit water from site A to C, the vibrational energy of these modes is redistributed. Mode 29 has a slightly lower similarity of 0.96 between complexes (A) and (C). The contribution of bend($C_6N_1H_7$) to mode 29 in (C) is smaller than in (A), and the contributions of stretch(N_3C_4) and stretch(N_3C_4) are increased. Compared to complex (A), the vibrational frequencies of modes 24, 27 and 29 of complex (C) are shifted -19, +20 and -19 cm^{-1}, respectively, see Table C4.

Similar to (A) vs. (C), in complexes (A) and (B), modes 12 and 17 have similarity higher than 0.98, and modes 24 - 28 have similarities of 0.66 - 0.93, which is due to the vibrational energy redistribution of these modes. Notably, mode 28 of complex (A) corresponds to mode 27 of complex (B) ($\mathfrak{S}(v_{28}^{A}, v_{27}^{B}) = 0.84$), and both of these modes are dominated by stretch(N_1C_2), bend($C_6N_1H_7$) and bend($C_2N_3C_4$). The frequency shift between mode 28 in (A) and mode 27 in (B) is -15 cm^{-1}, see Table C4.

Comparing modes 31, 32 and 33 in the three complexes, modes 32 and 33 in complexes (A) and (C) are dominated by the mixture of stretch(C_4O_{10}) and stretch(C_2O_8), while stretch(C_5C_6) comprises primarily mode 31. However, in complex (B), stretch(C_5C_6) and stretch(C_4O_{10}) are mixed between modes 31 and 32, and mode 33 is dominated

by stretch(C_2O_8) only. It is important that the cosine similarity of mode 32 between complex (A) and (B) ($\mathfrak{S}(v_{32}^{\mathrm{A}}, v_{32}^{\mathrm{B}}) = 0.87$) is much lower than the similarity between (A) and (C) ($\mathfrak{S}(v_{32}^{\mathrm{A}}, v_{32}^{\mathrm{C}}) = 0.98$). PED analysis shows mode 32 in both complex (A) and (C) is composed with stretch(C_4O_{10}) (50-51%), stretch(C_2O_8) (14-16%) and bend($C_4N_3H_9$) (11-14%). However, mode 32 of complex (B) is dominated by 47% of stretch(C_4O_{10}), 8% of stretch(C_5C_6) and 14% of bend($C_4N_3H_9$), whereas stretch(C_2O_8) is lower than 5%. This indicates that the stretching of the O_2-C_8 and O_4-C_{10} bonds are sensitive to the hydrogen bonding environment; a result that is qualitatively not surprising.

The cosine similarity between complex (A) and isolated uracil in implicit water (C-PCM) is computed as well, see Figure C3. Since the cosine similarity between all the modes (that are relevant to the experimental resonance Raman spectra) are $>$ 0.94, it indicates that the normal mode character in complex (A) (and, thus complex (C)) are very similar to isolated uracil in H_2O (C-PCM).

4.3.3 Thymine-H_2O

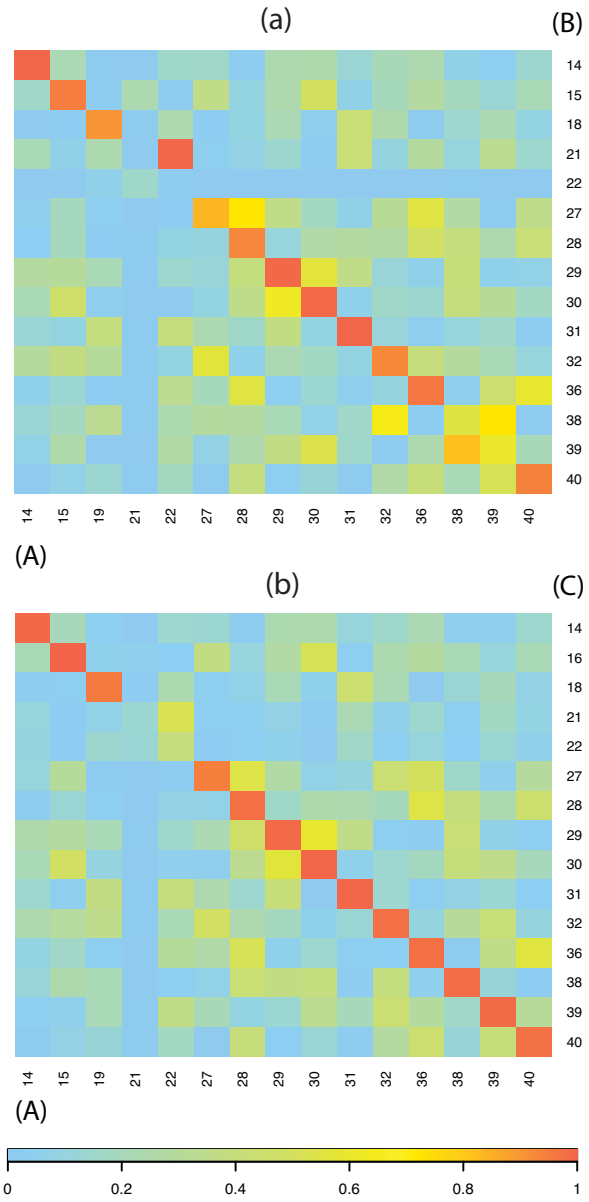

Figure 4.5: *Cosine similarity of (a) complexes (A) vs. (B) and (b) complexes (A) vs. (C) for thymine-H_2O. For the definition of the cosine similarity, see Eq 4.3.*

Table 4.4: *Potential Energy Distribution Analysis and Vibrational Frequencies (ω/cm^{-1}) of Ground State Normal Modes of Thymine-H_2O as Determined Using PBE0/aug-cc-pVTZ in H_2O (C-PCM).Values Correspond to Complexes A, B, and C, Respectively.*

mode	ω	PED
	562	-stretch(N_3C_4)[12%]-bend($N_3C_4O_{10}$)[24%]+bend($C_2N_1C_6$)[15%]+bend($N_1C_2N_3$)[11%]
14	559	+stretch(C_2N_3)[10%]+stretch(N_3C_4)[13%]+bend($N_3C_4O_{10}$)[27%]-bend($C_2N_1C_6$)[17%]-bend($N_1C_2N_3$)[15%]
	561	+stretch(C_2N_3)[9%]+stretch(N_3C_4)[13%]+bend($N_3C_4O_{10}$)[25%]-bend($C_2N_1C_6$)[19%]-bend($N_1C_2N_3$)[12%]
15	618	-bend($N_3C_4O_{10}$)[17%]-bend($N_1C_2O_8$)[33%]+bend($C_2N_3C_4$)[15%]-bend($C_4C_5C_{11}$)[14%]
15	621	+bend($N_1C_2O_8$)[15%]+bend($N_3C_4O_{10}$)[9%]-bend($C_2N_3C_4$)[9%]-torsion($C_5C_6N_1H_7$)[45%]
16	618	-bend($N_3C_4O_{10}$)[16%]-bend($N_1C_2O_8$)[33%]+bend($C_2N_3C_4$)[15%]-bend($C_4C_5C_{11}$)[14%]
19	757	+stretch(N_1C_2)[13%]+stretch(C_5C_{11})[12%]-bend($N_1C_6C_5$)[9%]+bend($N_1C_2N_3$)[27%]-bend($C_2N_3C_4$)[14%]
18	764	-stretch(N_1C_2)[13%]-stretch(C_5C_{11})[11%]+bend($N_1C_6C_5$)[9%]-bend($N_1C_2N_3$)[28%]+bend($C_2N_3C_4$)[12%]
18	760	+stretch(N_1C_2)[12%]+stretch(C_5C_{11})[12%]-bend($N_1C_6C_5$)[10%]+bend($N_1C_2N_3$)[28%]-bend($C_2N_3C_4$)[13%]
	798	+torsion($N_1H_7O_{16}H_{17}$)[9%]-torsion($C_5C_6N_1H_7$)[8%]-out-of-plane($C_4C_5N_3O_{10}$)[55%]
21	821	+stretch(N_1C_2)[11%]-stretch(C_5C_{11})[16%]-bend($N_1C_6C_5$)[14%]+bend($C_2N_1C_6$)[11%]-bend($N_1C_2N_3$)[9%]+bend($C_2N_3C_4$)[10%]
	819	-stretch(C_5C_{11})[8%]+torsion($C_5C_4N_3H_9$)[25%]+out-of-plane($C_4C_5N_3O_{10}$)[9%]
	818	+stretch(N_1C_2)[12%]-stretch(C_5C_{11})[15%]-bend($N_1C_6C_5$)[14%]+bend($C_2N_1C_6$)[11%]-bend($N_1C_2N_3$)[8%]+bend($C_2N_3C_4$)[10%]
22	827	+torsion($N_3H_9O_{16}H_{17}$)[33%]+torsion($C_5C_4N_3H_9$)[14%]-out-of-plane($C_2N_1N_3O_8$)[9%]+out-of-plane($C_4C_5N_3O_{10}$)[10%]
	821	+torsion($C_5C_4N_3H_9$)[32%]+out-of-plane($C_4C_5N_3O_{10}$)[10%]
	1188	+stretch(N_3C_4)[29%]-stretch(C_5C_{11})[14%]+bend($N_1C_6C_5$)[9%]-bend($N_3C_4O_{10}$)[8%]

27	1190	-stretch(N_1C_6)[18%]+stretch(N_3C_4)[10%]+bend($N_1C_6C_5$)[9%]-bend($C_6N_1H_7$)[17%]-bend($N_1C_6H_{12}$)[16%]
	1185	-stretch(N_1C_6)[14%]+stretch(N_3C_4)[19%]-stretch(C_5C_{11})[8%]+bend($N_1C_6C_5$)[9%]-bend($C_6N_1H_7$)[11%]-bend($N_1C_6H_{12}$)[9%]
	1238	+stretch(N_1C_6)[29%]-stretch(C_2N_3)[11%]+bend($C_6N_1H_7$)[17%]+bend($N_1C_6H_{12}$)[18%]
28	1238	-stretch(N_1C_6)[18%]+stretch(C_2N_3)[9%]-stretch(N_3C_4)[18%]+stretch(C_5C_{11})[19%]-bend($C_6N_1H_7$)[12%]
	1232	+stretch(N_1C_6)[25%]-stretch(C_2N_3)[10%]+stretch(N_3C_4)[13%]-stretch(C_5C_{11})[15%]+bend($C_6N_1H_7$)[18%]+bend($N_1C_6H_{12}$)[9%]
	1266	-stretch(N_1C_6)[20%]-stretch(C_2N_3)[14%]+stretch(N_3C_4)[11%]+stretch(C_5C_{11})[20%]-bend($N_1C_6C_5$)[8%]+bend($N_1C_6H_{12}$)[15%]
29	1266	+stretch(N_1C_6)[20%]+stretch(C_2N_3)[21%]-stretch(N_3C_4)[18%]-stretch(C_5C_{11})[13%]-bend($N_1C_6H_{12}$)[13%]
	1269	-stretch(N_1C_6)[16%]-stretch(C_2N_3)[17%]+stretch(N_3C_4)[15%]+stretch(C_5C_{11})[16%]+bend($N_1C_6H_{12}$)[18%]
	1387	-stretch(C_5C_6)[17%]+stretch(C_2N_3)[9%]+bend($N_1C_6H_{12}$)[34%]
30	1385	-stretch(C_5C_6)[17%]+bend($N_1C_6H_{12}$)[38%]
	1390	-stretch(C_5C_6)[17%]+bend($N_1C_6H_{12}$)[40%]
	1410	+bend($H_{13}C_{11}H_{15}$)[25%]+bend($H_{13}C_{11}H_{14}$)[35%]+bend($H_{14}C_{11}H_{15}$)[25%]
31	1410	+stretch(C_5C_{11})[8%]+bend($H_{13}C_{11}H_{15}$)[24%]+bend($H_{13}C_{11}H_{14}$)[37%]+bend($H_{14}C_{11}H_{15}$)[25%]
	1409	+stretch(C_5C_{11})[8%]+bend($H_{14}C_{11}H_{15}$)[26%]+bend($H_{13}C_{11}H_{14}$)[36%]+bend($H_{13}C_{11}H_{15}$)[26%]
	1413	-stretch(C_4O_{10})[9%]+stretch(C_2O_8)[12%]+bend($C_4N_3H_9$)[58%]
32	1448	-stretch(C_4O_{10})[11%]-bend($C_6N_1H_7$)[13%]+bend($C_4N_3H_9$)[53%]
	1446	-stretch(C_4O_{10})[10%]+stretch(C_2O_8)[14%]+bend($C_4N_3H_9$)[62%]
	1538	+stretch(C_2O_8)[13%]-stretch(N_1C_6)[8%]+stretch(N_1C_2)[10%]+bend($N_1C_6C_5$)[13%]+bend($C_6N_1H_7$)[37%]
36	1533	+stretch(C_2O_8)[8%]+stretch(N_1C_2)[16%]-stretch(N_3C_4)[12%]+bend($N_1C_6C_5$)[18%]+bend($C_6N_1H_7$)[23%]
	1526	+stretch(C_2O_8)[9%]+stretch(N_1C_2)[18%]-stretch(N_3C_4)[10%]+bend($N_1C_6C_5$)[18%]+bend($C_6N_1H_7$)[22%]

	1711	+stretch(C_4O_{10})[11%]+stretch(C_5C_6)[46%]+bend($N_1C_6H_{12}$)[8%]
38	1701	+stretch(C_4O_{10})[60%]-bend($H_{17}O_{16}H_{18}$)[8%]+bend($C_4N_3H_9$)[17%]
	1715	+stretch(C_4O_{10})[20%]+stretch(C_5C_6)[37%]+bend($C_4N_3H_9$)[9%]
	1719	+stretch(C_4O_{10})[47%]-stretch(C_5C_6)[17%]
39	1713	+stretch(C_5C_6)[63%]+bend($N_1C_6H_{12}$)[14%]
	1720	+stretch(C_4O_{10})[39%]-stretch(C_5C_6)[27%]
	1755	+stretch(C_4O_{10})[19%]+stretch(C_2O_8)[42%]-stretch(N_1C_2)[8%]-bend($C_6N_1H_7$)[9%]
40	1767	+stretch(C_2O_8)[69%]
	1752	+stretch(C_4O_{10})[18%]+stretch(C_2O_8)[47%]-stretch(N_1C_2)[8%]

The cosine similarities of complexes (A) vs. (B) and (A) vs. (C) for thymine are determined and shown in Figure 4.5, respectively. As with uracil-H_2O, the normal modes between (A) and (C) are very similar; their cosine similarity is higher than 0.95, except for modes 21 ad 22, see Figure 4.5(b). On the other hand, the normal modes between (A) and (B) have more dissimilarity in modes 27, 38 and 39, see Figure 4.5(a). Modes 21 and 22 of complex (C) are both comprised of torsion($C_5C_4N_3H_9$) ($\sim$ 30%) and out-of-plane($C_4C_5N_3O_{10}$) ($\sim$ 10%). However, mode 21 in complex (A) is dominated by out-of-plane($C_4C_5N_3O_{10}$) and mode 22 is the combination of stretch(N_1C_2), stretch(C_5C_{11}), bend($N_1C_6C_5$), and bend($C_2N_1C_6$), see Table 4.4. In contrast with (A) vs. (C), mode 21 of complex (B) vs. mode 22 of complex (A) has high similarity ($\mathfrak{S}(v_{22}^{\mathrm{A}}, v_{21}^{\mathrm{B}}) = 0.99$).

$\mathfrak{S}(v_{27}^{\mathrm{A}}, v_{27}^{\mathrm{B}})$ is equal to 0.83 and $\mathfrak{S}(v_{28}^{\mathrm{A}}, v_{27}^{\mathrm{B}})$ is equal to 0.71, and they are lower than the corresponding mode in (C) ($\mathfrak{S}(v_{27}^{\mathrm{A}}, v_{27}^{\mathrm{C}}) = 0.94$). This is caused by the vibrational energy being redistributed between mode 27 and mode 28, that is, stretch(N_1C_6) increased from 6% in (A) to 18% in (B), and bend($C_6N_1H_7$) increased from 3% to 17%.

Another major difference from (A) vs. (C) is that in (A) vs. (B) modes 38, 39 and 40 do not maintain the one-to-one correlation, see Figure 4.5(a), ($\mathfrak{S}(v_{38}^{\mathrm{A}}, v_{39}^{\mathrm{B}}) =$ 0.82 and $\mathfrak{S}(v_{39}^{\mathrm{A}}, v_{38}^{\mathrm{B}}) = 0.73$). PED analysis shows that in complexes (A) and (C), modes 38, 39 and 40 are the combination of stretch(C_4O_{10}), stretch(C_5C_6) and stretch(C_2O_8). Mode 38 is assigned with the combination between stretch(C_5C_6) ($\sim$ 40%) and stretch(C_4O_{10}) ($\sim$ 15%); mode 39 is stretch(C_4O_{10}) ($\sim$ 43%) combined with stretch(C_5C_6) ($\sim$22%); mode 40 is the combination of stretch(C_4O_{10})($\sim$ 18%) and stretch(C_2O_8) ($\sim$ 45%). However, mode 38 of complex (B) is dominated by 60% of stretch(C_4O_{10}) (and 17% of bend($C_4N_3H_9$)); mode 39 has contribution from 63% of stretch(C_5C_6) (and 14% of bend($N_1C_6H_{12}$)); mode 40 is mainly contributed by stretch(C_2O_8). Therefore, the different bonding sites of the explicit water on thymine can significantly change the normal mode character of its high frequency modes ($>$ 1700 cm^{-1}) and this should be manifest in the corresponding resonance Raman spectra.

Although there are some changes in the normal mode character, the vibrational frequencies in different complexes are not significantly shifted. Most of the frequency shifts are less than 10 cm^{-1}, except that mode 32 is shifted 30 cm^{-1} from (A) to (B) and (C), see Table C5.

The vibrational frequency shift of isolated thymine in implicit water (C-PCM) and its cosine similarity to complex (A) are determined, see Table C5 and Figure C9. According to Figure C9, as with uracil-H_2O, the normal modes in thymine-H_2O have high similarity between complex (A) (and, thus (C)) and isolated thymine in implicit water (C-PCM).

4.3.4 Vertical excitation energies and oscillator strengths

The effect of solvation on the vertical excitation energies of uracil and thymine has been studied extensively via TD-DFT and wavefunction-based method using both implicit[97–99,101,180] and explicit water.[100–105,117,118,180,199] In computing the excited state gradients, we have also determined the vertical excitation energies, oscillator strengths and Λ parameter for the three lowest excited singlet states of uracil and thymine in the gas phase, implicit water (C-PCM), and with one explicit water plus C-PCM at the CAMB3LYP/aug-cc-pVTZ level of theory; the optimized geometries are from Section 4.3.1 as determined using PBE0/aug-cc-pVTZ.

Extensive studies[97–105,117,118,180,199] for both uracil and thymine showed the energy of the $n \rightarrow \pi^*$ state in water is strongly blue shifted, and the $\pi \rightarrow \pi^*$ is moderately red shifted compared to the energy in the gas phase. This trend is also observed in our study as well, see Table 4.5.

The difference in the vertical excitation energies is less than 0.15 eV in uracil-H_2O complexes and less than 0.18 eV in thymine-H_2O complexes; the differences in the vertical excitation energies between uracil (thymine) in implicit water (C-PCM) and uracil-H_2O (thymine-H_2O) are less than 0.16 eV (0.16 eV), see Table 4.5. The oscillator strengths and Λ parameters of uracil-H_2O and thymine-H_2O do not change significantly either. In other words, the vertical excitation energies, oscillator strengths and Λ parameter of uracil- and thymine-H_2O are not very sensitive to the

presence of a single explicit solvent molecule.

Table 4.5: *Vertical Excitation Energies (E_V/eV), Oscillator Strengths (f) and Λ Parameters[165] for the Three Lowest Singlet Excited States of Uracil and Thymine in the Gas Phase, in Implicit Water (C-PCM) and with One Explicit Water Plus (C-PCM).*

	S_1 $\pi \rightarrow \pi^*$			S_2 $n \rightarrow \pi^*$			S_3 Rydberg		
uracil	E_V	f	Λ[e]	E_V	f	Λ	E_V	f	Λ
gas[a,b]	5.086	0.0000	0.379	5.417	0.1740	0.711	6.029	0.0030	0.210
H_2O(C-PCM)	5.173	0.3653	0.727	5.344	0.0000	0.384	6.344	0.0142	0.221
(A)	5.163	0.3808	0.724	5.359	0.0000	0.368	6.402	0.0331	0.194
(B)	5.140	0.3523	0.720	5.506	0.0001	0.358	6.403	0.0151	0.198
(C)	5.217	0.3596	0.870	5.325	0.0000	0.485	6.409	0.0150	0.228
experiment[c]	4.7	-	-	-	-	-	-	-	-
thymine	E_V	f	Λ	E_V	f	Λ	E_V	f	Λ
gas[b]	5.128	0.0000	0.395	5.229	0.1775	0.789	5.779	0.0005	0.235
H_2O(C-PCM)	5.003	0.3628	0.719	5.350	0.0000	0.369	6.077	0.0020	0.218
(A)	5.004	0.3811	0.719	5.362	0.0000	0.363	6.132	0.0025	0.215
(B)	4.961	0.3452	0.713	5.511	0.0000	0.350	6.129	0.0022	0.191
(C)	5.052	0.3621	0.820	5.332	0.0000	0.455	6.143	0.0021	0.227
experiment[d]	4.7	0.1342	-	-	-	-	-	-	-

[a] Ref.69

[b] in the gas phase, S_1 is $n \rightarrow \pi^*$, and S_2 is $\pi \rightarrow \pi^*$.

[c] Ref.43, according to the UV-vis absorption spectrum.

[d] Ref.52.

[e] $\Lambda = \frac{\sum_{i,a} \kappa_{ia}^2 \langle|\phi_i|||\phi_a|\rangle}{\sum_{i,a} \kappa_{ia}^2}$. ϕ_i and ϕ_a are occupied and virtual orbitals, respectively.

4.3.5 Resonance Raman spectra

The Cartesian gradients of the bright excited state in each uracil and thymine configuration are determined via TD-DFT at the CAMB3LYP/aug-cc-pVTZ level of theory. The dimensionless normal mode displacements are computed based on the corresponding optimized ground state structures, and the resonance Raman spectra are simulated and compared with the experimental results.

Uracil-H_2O

The resonance Raman spectra for the uracil-H_2O complexes (A), (B) and (C) along with the implicit water simulation and experimental measurements[43] for comparison are illustrated in Figure 4.6; the corresponding comparison including gas-phase

simulations are shown for comparison, see Figure C4(a); as discussed previously,[69] agreement with experiment is improved by including implicit solvation. The peak positions, $|\Delta|$ values for the three complexes and the experimentally determined $|\Delta|$ values are given in Table 4.6.

The peak positions and intensities in the resonance Raman spectra of complexes (A) and (C) are very similar, while the spectrum of complex (B) exhibits a different pattern of intensities for the peaks with frequencies between 800 and 1600 cm^{-1}, and more significant differences in the peaks with frequencies higher than 1600 cm^{-1}. The frequency shifts of the peak positions between the complexes are less than ± 30 cm^{-1}, see Table 4.3.

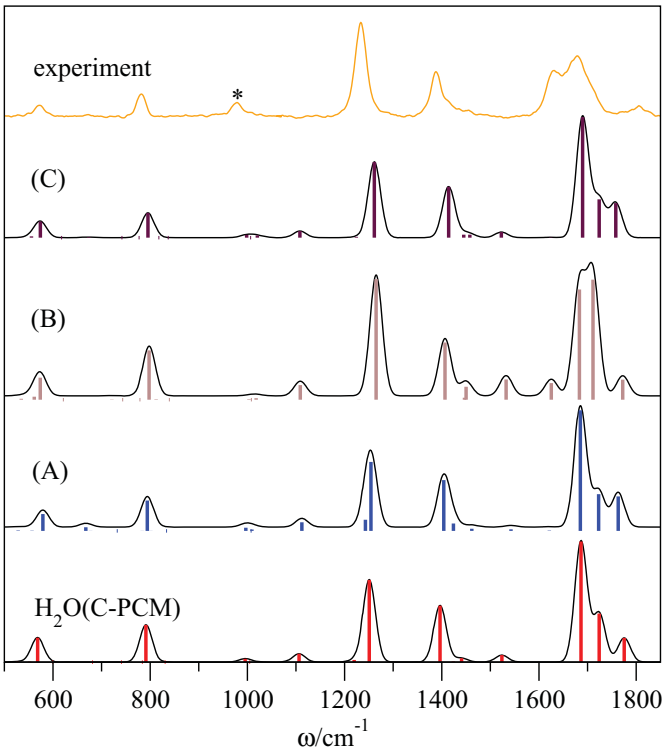

Figure 4.6: *Resonance Raman spectra of uracil in implicit water and with one explicit water plus C-PCM. Ground and excited states determined at the PBE0/aug-cc-pVTZ and TD-CAMB3LYP/aug-cc-pVTZ levels of theory, respectively. fwhm used in the simulation is 30 cm^{-1}. The experimental spectrum is measured in water and taken from Ref 43. The asterisk in the experimental spectrum[43] indicates the internal standard peak by ca. 0.4 M sulfate.*

Table 4.6: *Vibrational Frequencies (ω/cm^{-1}) for the Ground State and Dimensionless Displacements ($|\Delta|$) for S_1 State of Uracil-H_2O Complexes as Compared to the Experimentally Determined Values.*

H_2O(C-PCM)	modes	7	12	18	19	20	21	22	23	24	25	26
	ω[a]	568	791	1220	1251	1396	1424	1441	1524	1686	1724	1775
	$\lvert\Delta\rvert$[b]	0.8935	0.8168	0.1458	0.8846	0.6841	0.0728	0.1747	0.2312	0.9235	0.5791	0.4008
(A)	modes	12	17	24	25	26	27	28	29	31	32	33
	ω[a]	579	794	1243	1254	1404	1424	1462	1542	1685	1723	1763
	$\lvert\Delta\rvert$[b]	0.8510	0.8286	0.3376	0.8329	0.6589	0.2494	0.1325	0.1099	0.9030	0.4914	0.4692
(B)	modes	12	17	24	25	26	27	28	29	31	32	33
	ω[a]	574	798	1230	1265	1407	1447	1450	1532	1683	1711	1772
	$\lvert\Delta\rvert$[b]	0.8765	0.9226	0.0385	0.9123	0.5734	0.1034	0.2661	0.3193	0.6984	0.7207	0.2875
(C)	modes	12	17	24	25	26	27	28	29	31	32	33
	ω[a]	574	795	1224	1261	1414	1445	1458	1523	1690	1724	1758
	$\lvert\Delta\rvert$[b]	0.8975	0.7962	0.0992	0.9143	0.6843	0.1612	0.1625	0.2155	0.9404	0.5237	0.4912
experiment[c]	ω	579	789	1235		1388				1623	1664	
	$\lvert\Delta\rvert$	0.46	0.48	0.74		0.45				0.30	0.60	

[a] Determined using PBE0/aug-cc-pVTZ in implicit water (C-PCM).
[b] Determined using TD-CAMB3LYP/aug-cc-pVTZ in implicit water (C-PCM).
[c] Ref.43.

For the three complexes, the peaks corresponding to modes 12 ($\sim$ 580 cm^{-1}) and 17 ($\sim$ 800 cm^{-1}) are almost identical, since their normal mode characters are similar, see Figure 4.4; the intensity of mode 17 is slightly enhanced for complex (B). On the other hand, due to the vibrational energy redistribution between modes 24 - 29, the resonance Raman spectra show different relative peak intensities between complexes (A), (B) and (C). The peak intensity ratio $I(\text{mode 24})/I(\text{mode 25}) = 0.15$ in complex (A), but this ratio is ≤ 0.01 in complex (B) and (C). The $|\Delta|$ value of mode 24 in (A) (1243 cm^{-1}) is ten times larger than (B) (1230 cm^{-1}) and four times larger than (C) (1224 cm^{-1}), see Table 4.6. The peak intensity of mode 26 ($\sim$ 1410 cm^{-1}) exhibits almost no difference between the three complexes, while the peak intensities of mode 27 and mode 28 have large differences. In complex (A), the peak intensity corresponding to mode 27 (1424 cm^{-1}) is higher than mode 28 (1462 cm^{-1}); in complex (B) the intensities of these two modes (1447 and 1450 cm^{-1}) are reversed due to the exchange of the normal mode characters; in complex (C), the peak intensities of these two modes (1445 and 1458 cm^{-1}) are almost equal. As expected, the dimensionless displacements of modes 26, 27 and 28 show the same trend as observed for the peak intensities, see Table 4.6. The displacement of mode 29 ($\sim$ 1530 cm^{-1}) in the three complexes is (B) > (A) > (C). The same trend can also be observed in the corresponding peak intensities. Compared to the experimental spectrum, the displacements of mode 29 in complex (B) and (C) are slightly overestimated.

The peak patterns in the high frequency region (>1600cm^{-1}) are similar between complexes (A) and (C), because the normal mode character of modes 31, 32 and 33, as discussed in Section 4.3.1, is similar. In (A) and (C), $I(\text{mode 31})/I(\text{mode 32}) = 3.2$, and it is much larger than 1. In contrast, the relative peak intensity of mode 32 in complex (B) is significantly changed, and $I(\text{mode 31})/I(\text{mode 32}) = 0.92$, which is smaller than 1. The dramatic change of the peak ratio can be observed in the displacements of modes 31 and 32 in (B), where $|\Delta|$(mode 31) reduces and $|\Delta|$(mode 32) increases. Compared to the experimental spectrum whose peak ratio is 0.76, complex (B) gives better agreement than the other two complexes in terms of the high frequency peak.

The peak intensity ratio $I(\text{mode } 25)/I(\text{mode } 31) = 1.09$ (slightly larger than 1) in complex (B), which is higher than the corresponding peak intensity ratio in complex (A) (0.57) and complex (C) (0.63) (both are < 1). Since in the experimental spectrum this peak intensity ratio is equal to 2.26, which is much larger than 1, the explicit hydrogen bonding to site (B) improves the relative peak intensity of mode 25.

PED analysis shows the three modes belonging to the high frequency region in the three complexes are mainly composed of stretching components, i.e., stretch(C_5C_6), stretch(C_4O_{10}), and stretch(C_2O_8). In complex (A) and (C), mode 31 is dominated by stretch(C_5C_6), but modes 32 and 33 are mainly mixed between stretch(C_4O_{10}) ($\sim$ 50% in mode 32, $\sim$ 21% in mode 33) and stretch(C_2O_8) ($\sim$ 15% in mode 32, $\sim$ 40% in mode 33). However, in complex (B) modes 31 and 32 are combined between stretch(C_5C_6) ($\sim$ 52% in mode 31, $\sim$ 8% in mode 32) and stretch(C_4O_{10}) ($\sim$ 13% in mode 31, $\sim$ 47% in mode 32), while mode 33 is dominated by the single component stretch(C_2O_8) ($\sim$ 69%), see Table 4.3.

Since the dimensionless displacement depends on both the normal mode eigenvector and the Cartesian gradient in the excited state, we also compared Cartesian gradients of the bright state for (A), (B) and (C), see Figure 4.7. It is clear that there are no significant differences between their excited state Cartesian gradients (except the minor differences on atoms N_1 and C_4 between (B) and (A)/(C)), hence their initial excited state dynamics. Therefore, the differences of the peak ratio between modes 31 and 32 in (A), (B) and (C) are primarily governed by the differences in their ground state normal modes. It also indicates that the dual peak pattern at 1700 cm^{-1} in the experimental resonance Raman spectrum requires explicit hydrogen bonding to site (B), especially to bond C_4O_{10}.

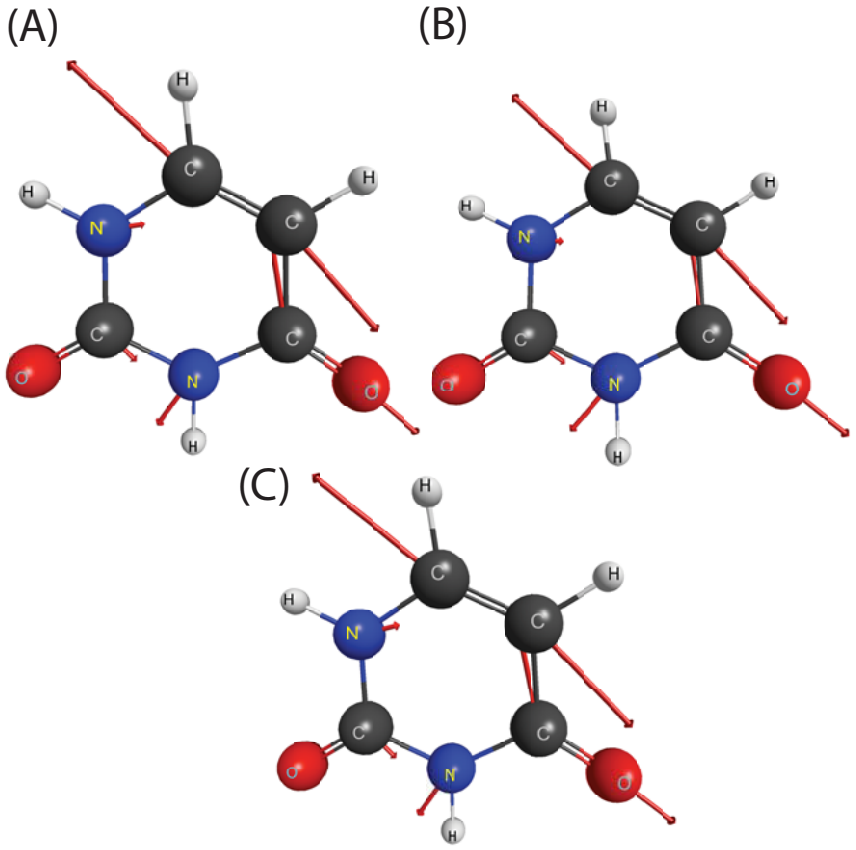

Figure 4.7: *Vectors illustrating the Cartesian gradients for each atom of (A), (B) and (C) uracil-H_2O complexes in implicit water for the S_1 excited state as determined at the TD-CAMB3LYP/aug-cc-pVTZ level of theory. For clarity, the explicit water is not illustrated.*

The excited state Cartesian gradients of isolated uracil in H_2O (C-PCM) are illustrated in Figure C5(a) in the ESI, and do not show significant differences from the gradients of the uracil-H_2O complexes. As the eigenvectors of normal modes on the ground state are very similar between isolated uracil (in implicit water) and complex (A), see Figure C3, the spectra for these two compounds resemble each other strongly, see Figure 4.6.

We further studied the hydrogen-bonding effect on bond C_4O_{10} by simulating the resonance Raman spectra of a selective set of uracil-$(H_2O)_2$ complexes. In these

complexes, complex (B) (using one explicit water) was the initial structure, and a second water was added at site A, B or C. These water complexes are referred to as (AB), (BB), and (BC) hereafter. The equilibrium geometries and relative energies of the uracil-$(H_2O)_2$ complexes are shown in Figure C6. The relative energies of (AB), (BB) and (BC) are 2.32, 0.00, and 3.75 kcal/mol, respectively. For the high frequency peaks (modes 38 and 39, > 1600 cm^{-1}), only (AB) shows the dual peak structure as seen in the experimental spectrum, while (BB) and (BC) have only a single peak at 1700 cm^{-1}, see Figure 4.8. This is because in (BB) and (BC) the peak position of modes 38 and 39 are too close to each other, so that the two peaks do not get resolved (for the simulated 30 cm^{-1} fwhm) but merged into one peak. However, the ratio of the peak intensity I(mode 38)/I(mode 39) still get improved significantly in these three complexes as in (B). I(mode 38)/I(mode 39) is equal to 1.05 in (AB), 0.82 in (BB), and 1.16 in (BC), which are all much closer to the experimental ratio of 0.75. The displacements of mode 38 are smaller than mode 31 in mono water complexes, while mode 39 has larger displacements than mode 32 in mono-water complexes, see Table 4.6. Compared to complexes (A) and (C), whose I(mode 31)/I(mode 32) = 3.2, complexes with hydrogen-bonding to bond C_4O_{10} give better agreement with the experiment for the peaks above 1600 cm^{-1}.

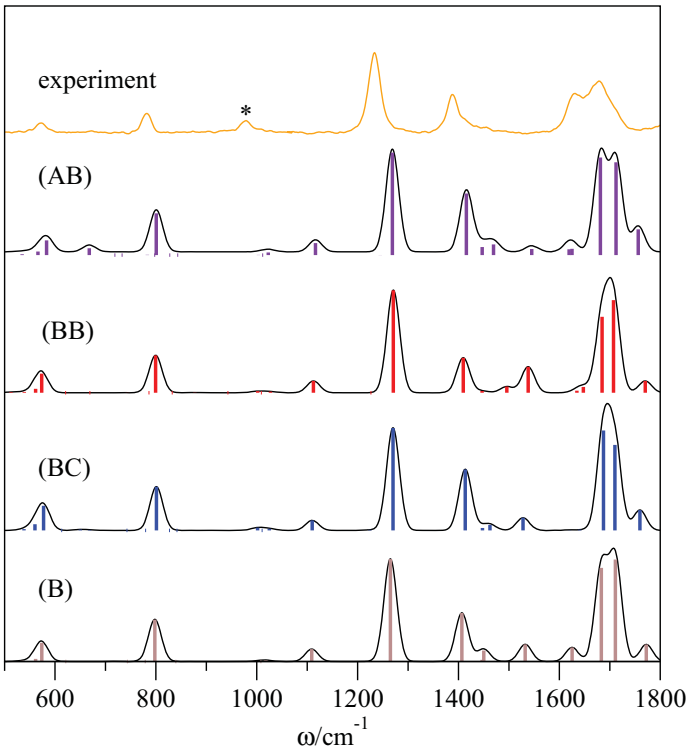

Figure 4.8: *Resonance Raman spectra of uracil computed including two explicit waters plus C-PCM. Ground and excited state determined at the PBE0/aug-cc-pVTZ and TD-CAMB3LYP/aug-cc-pVTZ levels of theory, respectively. fwhm used in the simulation is 30 cm^{-1}. The experimental spectrum is measured in water and taken from Ref 43. The asterisk in the experimental spectrum[43] indicates the internal standard peak by ca. 0.4 M sulfate.*

Thymine-H_2O

The resonance Raman spectra for thymine-H_2O complexes (A), (B), and (C) and implicit water simulation along with the experimental measurement[44] are shown in Figure 4.9; for a comparison to the gas-phase simulation, see Figure C4(b).

The peaks with frequencies lower than 1000 cm^{-1} (modes 14, 15, 19, 21,and 22) have similar patterns between complexes (A), (B), and (C), since their normal

modes are similar, see Figure 4.5. Mode 21 (818 cm^{-1}) in (A) and mode 22 (821 cm^{-1}) in (B) correspond to the same normal mode character, that is stretch(N_1C_2), stretch(C_5C_{11}), bend($N_1C_6C_5$), and bend($C_2N_1C_6$) in the PED, see Table 4.4; and their cosine similarity, $\mathfrak{S}(v_{22}^{A}, v_{21}^{B}) = 0.99$. The peak at 819-820 cm^{-1} in (C) is the combination of modes 21 and 22, which are both assigned as torsion($C_5C_4N_3H_9$), see Table 4.4. The displacement of mode 22 in complex (A) is much higher than mode 21; in complex (B), mode 21 has a larger displacement than mode 22. However, in complex (C), the displacements of modes 21 and 22 are almost equal, see Table 4.6.

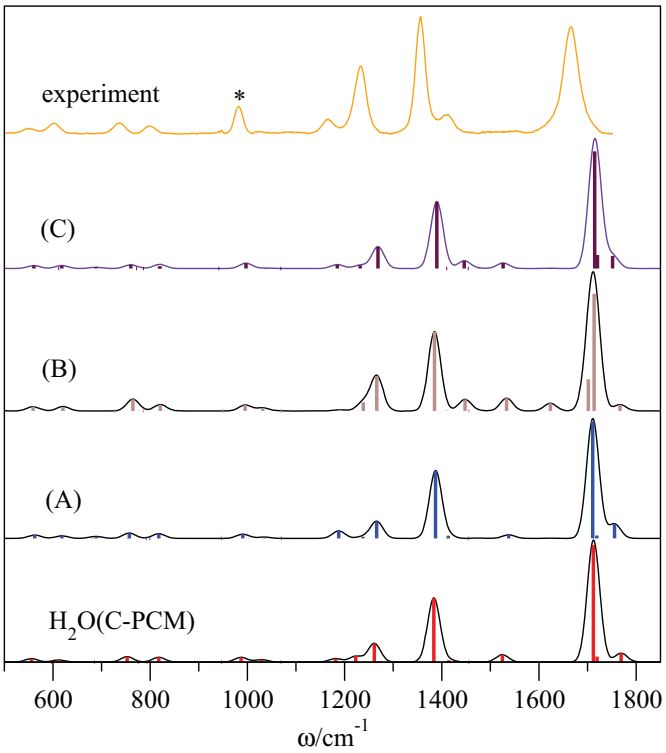

Figure 4.9: *Resonance Raman spectra of thymine in implicit water and with one explicit water plus C-PCM. Ground and excited state determined at the PBE0/aug-cc-pVTZ and TD-CAMB3LYP/aug-cc-pVTZ levels of theory, respectively. fwhm used in the simulation is 30 cm^{-1}. The experimental spectrum is measured in water and taken from Ref 44. The asterisk in the experimental spectrum[44] indicates the internal standard peak by ca. 0.4 M sulfate.*

Table 4.7: *Vibrational Frequencies (ω/cm^{-1}) for the Ground State and Dimensionless Displacements ($|\Delta|$) for S_1 State of Thymine-H_2O Complexes as Compared to the Experimentally Determined Values..*

H_2O(C-PCM)	modes	9	11	13	16		21	22	23	24	25	26	30	31	32	33
	ω	556	612	753	818		1182	1223	1261	1384	1409	1414	1525	1712	1719	1769
	$\|\Delta\|$	0.6292	0.4427	0.5643	0.4864		0.2748	0.3424	0.5878	0.9806	0.0463	0.1630	0.3012	1.0710	0.2310	0.2867
	modes	14	15	19	21	22	27	28	29	30	31	32	36	38	39	40
(A)	ω^a	562	618	757	798	818	1188	1238	1266	1387	1410	1413	1538	1711	1719	1755
	$\|\Delta\|^b$	0.6096	0.4768	0.5389	0.0029	0.4785	0.3965	0.1812	0.5576	1.0026	0.0506	0.1965	0.2068	1.0723	0.1694	0.3671
	modes	14	15	18	21	22	27	28	29	30	31	32	36	38	39	40
(B)	ω^a	559	621	764	821	827	1190	1238	1266	1385	1410	1448	1533	1701	1713	1767
	$\|\Delta\|^b$	0.5768	0.5022	0.6897	0.4701	0.0868	0.1342	0.3514	0.6907	0.9355	0.0626	0.3386	0.3335	0.4660	0.8895	0.1996
	modes	14	16	18	21	22	27	28	29	30	31	32	36	38	39	40
(C)	ω^a	561	618	760	819	821	1185	1232	1269	1390	1409	1446	1526	1715	1720	1752
	$\|\Delta\|^b$	0.5664	0.5199	0.4699	0.3318	0.3140	0.2951	0.2579	0.6385	1.0068	0.0207	0.3255	0.2598	1.0589	0.3588	0.3407
experiment[c]	ω	571	617	757	820		1176		1242	1368	1421			1670		
	$\|\Delta\|$	0.46	0.49	0.54	0.43		0.56		0.73	0.82	0.43			0.85		

[a] Determined using PBE0/aug-cc-pVTZ in implicit water (C-PCM).
[b] Determined using TD-CAMB3LYP/aug-cc-pVTZ in implicit water (C-PCM).
[c] Ref.52.

Mode 27 in (A) and (C) (1188 and 1185 cm^{-1}) has larger displacements, hence higher peak intensity, than in (B) (1190 cm^{-1}) . This is because of the vibrational energy redistribution between modes 27 and 28, see Figure 4.5. The peaks between 1200 cm^{-1} and 1600 cm^{-1} have good consistency between (A), (B), and (C).

In contrast with uracil, the spectrum above 1600 cm^{-1} in thymine only has a single peak instead of a dual peak. Our simulation shows this single peak at 1700 cm^{-1} is actually composed by two vibrational modes 38 and 39. However, because the frequency difference between the two modes is less than 12 cm^{-1}, the two corresponding peaks are not resolved. This frequency difference is much smaller than for the corresponding modes in uracil (modes 31 and 32), where the difference is $\sim$ 28 - 38 cm^{-1}. Due to the merger of the two peaks in thymine, it is difficult to determine which spectrum for a given complex has better agreement with the experiment by simply comparing the peak intensity. On the other hand, similar to uracil, there is significant difference in the peak intensity ratio of modes 38 and 39 in the thymine-H_2O complexes (corresponding modes are 31 and 32 in uracil-H_2O complexes) between (A), (B), and (C); $I(\text{mode } 38)/I(\text{mode } 39) = 40$ in (A) and 8.69 in (C), but only 0.27 for (B), see Figure 4.9.

As shown in Figure 4.10, the excited state gradients of (A), (B), and (C) for thymine-H_2O are almost identical, so the differences between their resonance Raman spectra are solely due to their different normal mode characters. Despite the small gradient vector on the methyl group of thymine, the rest of the excited gradient of thymine is, not surprisingly, similar with uracil (slight difference on atom N_1 and O_8), because of the resemblance in their molecular structure, see Figure 4.1.

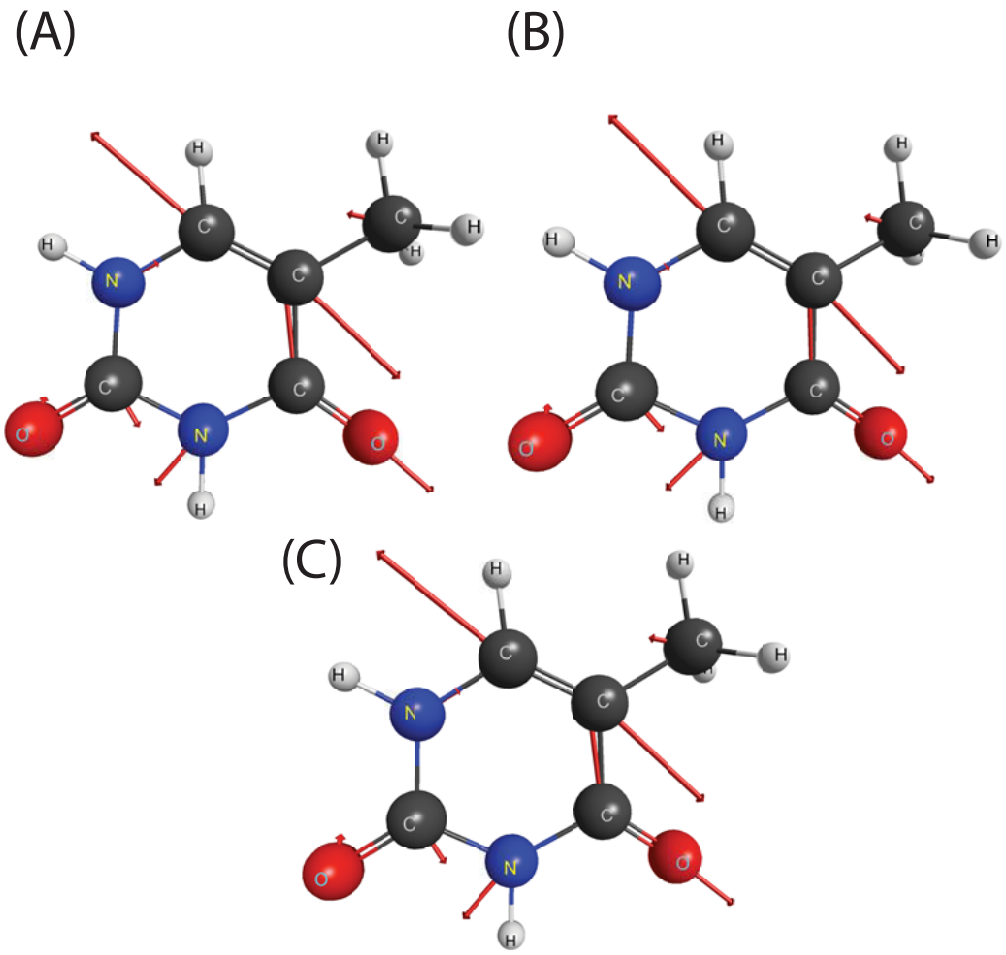

Figure 4.10: *Vectors illustrating the Cartesian gradients for each atom of (A), (B) and (C) thymine-H_2O complexes in implicit water for the S_1 excited state as determined at the TD-CAMB3LYP/aug-cc-pVTZ level of theory. For clarity, the explicit water is not illustrated.*

Since uracil and thymine have almost the same excited state gradients, and similar changes in the ratio of high frequency peaks intensity when bonding to C_4O_{10}, the structure of the high frequency peaks in thymine should be analogous to the peaks in uracil. Therefore, the single peak at 1700 cm^{-1} is composed by two modes and their

intensity ratio, $I(\text{mode } 38)/I(\text{mode } 39)$, should be less than 1 as in uracil.

We simulated the resonance Raman spectra of the thymine-$(H_2O)_2$ complexes (AB), (BB) and (BC), see Figure 4.11. The equilibrium geometries and relative energies of the thymine-$(H_2O)_2$ complexes are shown in Figure C10. The relative energies of (AB), (BB) and (BC) are 3.71, 0.00, and 3.53 kcal/mol, respectively. Similar to (B), for peaks with frequencies > 1600 cm^{-1}, the ratio of the peak intensity in thymine-$(H_2O)_2$ complexes, $I(\text{mode } 45)/I(\text{mode } 46)$, is much less than 1 as well (0.12 in (AB), 0.19 in (BB) and 0.49 in (BC)). Therefore, we can conclude that the high frequency peak pattern in the experimental spectrum of thymine is the consequence of the explicit hydrogen bonding to the bond C_4O_{10}.

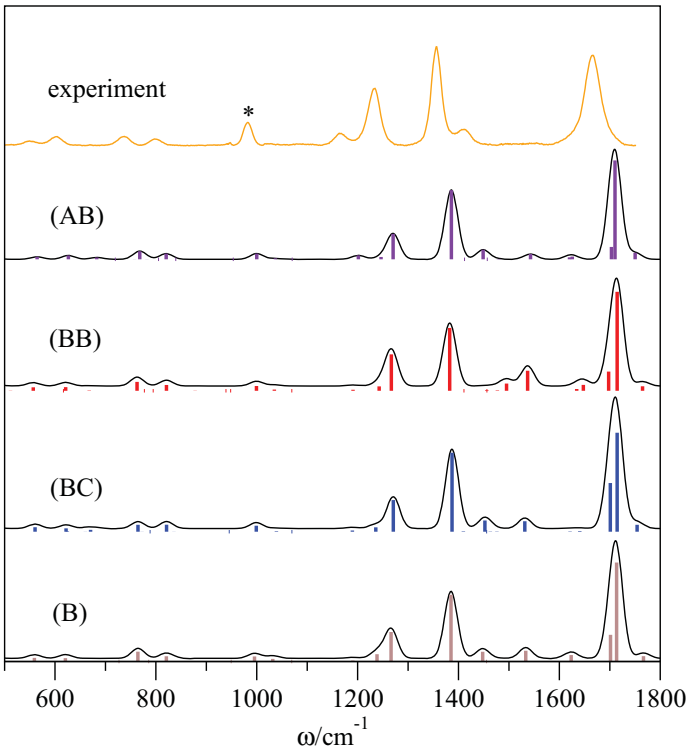

Figure 4.11: *Resonance Raman spectra of thymine computed including two explicit waters plus C-PCM. Ground and excited state determined at the PBE0/aug-cc-pVTZ and TD-CAMB3LYP/aug-cc-pVTZ levels of theory, respectively. fwhm used in the simulation is 30 cm^{-1}. The experimental spectrum is measured in water and taken from Ref 44. The asterisk in the experimental spectrum[44] indicates the internal standard peak by ca. 0.4 M sulfate.*

For isolated thymine in implicit water, because both its excited state gradient (of S_1 state) and normal mode characters on the ground state are almost identical to complex (A), see Figure C9 and C5(b), the resulting resonance Raman spectrum of the isolated thymine in implicit water is similar to (A) as well, see Figure 4.9.

4.4 Conclusions

In this study, we simulated the resonance Raman spectra of three uracil-H_2O and three thymine-H_2O complexes. The equilibrium structures, vibrational frequencies, and normal modes on the ground state electronic state are determined at the PBE0/aug-cc-pVTZ level of theory in implicit water (C-PCM). The vertical excitation energies, oscillator strengths, and Cartesian gradients on the excited electronic state are computed at the TD-CAMB3LYP/aug-cc-pVTZ level of theory in implicit water (C-PCM). In each uracil-H_2O (thymine-H_2O) complex, the water molecule is hydrogen bonded to different hydrogen bonding site. Therefore, by comparing the corresponding resonance Raman spectra, the effects of hydrogen boding in different uracil-H_2O (thymine-H_2O) complexes can be revealed. Since the resonance Raman spectra are simulated based on the ground state normal modes and the excited state Cartesian gradient, the comparisons between spectra are analyzed in terms of these two factors.

The eigenvector of the normal modes on the ground state of the uracil- and thymine-H_2O complexes are examined using PED analysis and cosine similarity. For uracil-H_2O complexes, the cosine similarity showed that the low frequency modes (mode 12 and mode 17) between complex (A), (B) and (C) have high similarity (> 0.98), but modes 24 - 28 have lower similarity (0.66 - 0.93), which is due to the vibrational energy redistribution, see the PED analysis in Table 4.3. The PED analysis also showed that the internal components in the high frequency modes (modes 31-33) are different between the three complexes. While mode 31 has high similarity between the three complexes, modes 32 and 33 have higher similarity in complexes (A) vs. (C) than (A) vs. (B). Similar to uracil-H_2O, the normal modes between (A) and (C) of thymine-H_2O are very similar ($\mathfrak{S} > 0.95$), except for modes 21 ad 22, see Figure 4.5(b), while the normal modes between (A) and (B) have more dissimilarity in modes 27, 38 and 39, see Figure 4.5(a). For the high frequency modes (modes 38-40), modes 38 and 39 have high similarity between (A) and (C), but are dissimilar between (A) and (B); mode 40 is similar in complexes (A), (B) and (C). The dissimilarity of the high frequency modes of uracil- and thymine-H_2O is a result of

the sensitivity of the O-C bonds of uracil (and thymine) to their hydrogen bonding environment. Meanwhile, the excited state Cartesian gradients of the bright state for uracil-H_2O complexes do not show significant differences, nor do the gradients for thymine-H_2O complexes, see Figure 4.7 and 4.10.

The resonance Raman spectra of uracil-H_2O complexes are simulated and compared to the experimental measurement.[43] The two peaks at high frequency ($\sim$ 1685 and 1715 cm^{-1}) in complex (B) have better peak intensity ratio than the corresponding peaks in complex (A) and (C). The relative peak intensity of mode 25 in complex (B) (1685 cm^{-1}) is closer to the experimental measurement than the corresponding peak in (A) and (C). Therefore, the spectrum of complex (B) has better agreement to the experimental spectrum than the other two complexes (A) and (C). Since the excited state Cartesian gradients are similar in the three complexes, the differences between the peak intensities discussed above, are the manifestation of the different normal mode eigenvectors on the ground state that are altered by different bonding sites of the explicit water.

The similar comparison is made between the resonance Raman spectra of the three thymine-H_2O complexes. Although the spectra above 1700 cm^{-1} in thymine only have a single peak instead of a dual peak, in the three simulated resonance Raman spectra of thymine-H_2O complexes, significant differences are observed in the peak intensity ratio of modes 38 and 39 ($\sim$ 1710 and 1720 cm^{-1}) in the three complexes, where the ratio in (B) is much smaller than in (A) and (C). The reason for this difference is, again, the changing of the normal mode eigenvectors impacted by the explicit hydrogen boding to water.

The unique role of site B in the resonance Raman spectra of uracil and thymine is further investigated by simulating the resonance Raman spectra of a selective set of uracil- and thymine-$(H_2O)_2$ complexes. In these complexes, complex (B) (using one explicit water) was the initial structure, and a second water was added at site A, B or C. The peak patterns in the high frequency region ($>$ 1600 cm^{-1}) in uracil- and thymine-H_2O complexes resembled those in the same spectral region for uracil- and thymine-$(H_2O)_2$ complexes. This confirms the necessary inclusion of explicit

hydrogen bonding on site B on uracil and thymine.

In summary, the explicit hydrogen bonding to water can significantly change the resonance Raman spectra of uracil and thymine. The effect of hydrogen bonding is primarily on the normal mode character, especially for the high frequency modes ($>$ 1600 cm^{-1}), but has little impact on the excited state Cartesian gradients of uracil and thymine. Different hydrogen bonding sites are found to have different contributions in the resulting resonance Raman spectra, and inclusion of explicit hydrogen bonding on site B (C_4O_{10}) is necessary to obtain good agreement between the simulated and experimental resonance Raman spectra of uracil and thymine.

Chapter 5

Conclusions and Future Work

5.1 Summary of Thesis Research

In this thesis, we developed an interface of the resonance Raman computer code (orca_asa) in ORCA (v 3.0) to the GAMESS-US (1May2013) and Gaussian (G09) software packages; currently implemented and tested for DFT ground states and TD-DFT excited states both in the gas phase and for PCM treatment of solvation. The present implementation can be used as a general tool for computing resonance Raman spectra to assist with the interpretation and understanding of experimental measurements. Using this tool, we simulated the resonance Raman spectra of uracil and its derivatives, including 5-halogenated (F, Cl, Br) uracils and thymine, and examined the spectra in terms of ground state normal mode eigenvectors and excited state Cartesian gradients.

We studied the performance of different functionals for both the ground and excited states in the simulation of the resonance Raman spectra of uracil, see Chapter 2. The ground state was optimized using PBE0/aug-cc-pVTZ and B3LYP/aug-cc-pVTZ, and the corresponding vibrational frequencies and eigenvectors of the normal modes were determined at the same level of theory, see Table 2.1. The excited state gradients in Cartesian space were computed using time-dependent density functional theory (TD-DFT) with four different functionals, including CAMB3LYP, LC-BLYP, B3LYP, PBE0 as well as spin flip TD-DFT (SF-TD-DFT) with BHHLYP, see Figure 2.6. All excited state computations are carried out using the aug-cc-pVTZ basis set.

The excited state calculations were undertaken in both the gas phase and implicit water using the conductor-like Polarizable Continuum (C-PCM) Model. The ground state equilibrium structure was found to impact the resulting resonance Raman spectrum significantly through differences in the corresponding normal mode eigenvectors, see Figures 2.2 and 2.3. Results based on the PBE0/aug-cc-pVTZ ground state exhibited better agreement with experiment than those from the B3LYP/aug-cc-pVTZ ground state. The simulated resonance Raman spectra using the long range corrected functionals, i.e., CAMB3LYP and LC-BLYP, showed better agreement with the experimental spectrum than using standard hybrid functionals, i.e., PBE0 and B3LYP, for the excited state gradients, see Figure 2.2. The solvation effect leads to a change in the energetic order of the (dark) $n \rightarrow \pi^*$ and (bright) $\pi \rightarrow \pi^*$ excited states, as observed previously,[97–105] see Table 2.3. Incorporating solvent effects via PCM improves the agreement with the experimental spectrum, especially with regard to the relative intensities of the peaks with frequencies greater than 1600 cm^{-1}, see Figures 2.2 and 2.4.

For the simulation of resonance Raman spectra of the 5-halogenated uracils, i.e., 5-fluorouracil, 5-chlorouracil and 5-bromouracil, we computed the equilibrium structures, corresponding vibrational frequencies and normal modes, at the PBE0/aug-cc-pVTZ level of theory in implicit water using C-PCM. The excited state gradients were determined at the TD-CAMB3LYP/aug-cc-pVTZ level of theory in C-PCM, see Chapter 3. The functionals and basis set for the ground and excited states, as well as choice of PCM model, used in the computations are chosen based on the conclusions of Chapter 2. The resulting spectra were examined in terms of ground state normal mode eigenvectors and excited state Cartesian gradients. Using PED analysis and cosine similarity, we showed that although most of the normal modes between 5-fluorouracil and 5-chlorouracil are similar, some modes in the low (modes 12 and 15) and high frequency region (modes 25 and 26) have moderate dissimilarity, see Figure 3.2(a). Meanwhile, the contribution by the excited Cartesian gradients to the differences between the spectra are between $5 \sim 15\%$, see Figure 3.5. We concluded that the differences between the spectra of 5-fluorouracil and 5-chlorouracil are due

to both the ground state normal mode eigenvectors and excited state gradients, see Figure 3.3. The ground state normal mode eigenvectors between 5-chlorouracil and 5-bromouracil have high similarity, see Figure 3.2(b), so do their excited state gradients, see Figure 3.4. Therefore, this explains the reason why the experimental resonance Raman spectra of these two molecules are very similar, see Figure 3.3.

As we see in Chapter 2, the effect of implicit water not only significantly impacts the vertical excitation energies, but also plays a remarkable role in the resonance Raman spectra. To further study the effect of solvation, we directed our attention to studying the effect of explicit water on the resonance Raman spectra of uracil and thymine, see Chapter 4. We chose the three bonding sites in uracil and thymine that are most likely to form hydrogen bonds in water, and added a single explicit water, see Figures 4.2 and 4.3. The resonance Raman spectra of the three uracil-H_2O complexes and three corresponding thymine-H_2O complexes were simulated, see Figures 4.6 and 4.9. The ground state structures were optimized at the PBE0/aug-cc-pVTZ level of theory. The vertical excitation energies, corresponding oscillator strengths of the first three excited states, and the excited state gradients of the bright state (S_1) were determined at the CAMB3LYP/aug-cc-pVTZ level of theory, see Table 4.5. All the ground and excited state computations were performed using H_2O (C-PCM) in addition to the explicit water. The effects of hydrogen boding in different uracil-H_2O and thymine-H_2O complexes are revealed in the comparison between the corresponding resonance Raman spectra, see Figures 4.6 and 4.9. In the spectra of uracil-H_2O, the two peaks in high frequency region ($\sim$ 1685 and 1715 cm^{-1}) have better peak intensity ratio in complex (B) than in complex (A) and (C); the peak intensity of mode 25 in complex (B) (1685 cm^{-1}) is closer to the experimental measurement than the corresponding peak in (A) and (C). Therefore, for uracil-H_2O complexes, the spectrum of complex (B) have better agreement to the experimental spectrum than the other two complexes (A) and (C), see Figure 4.6. The similar comparison is made between the resonance Raman spectra of the three thymine-H_2O complexes. Although the spectra above 1600 cm^{-1} in thymine only has a single peak instead of a dual peak, in the three simulated spectra of thymine-H_2O complexes,

significant differences are observed in the peak intensity ratio of modes 38 and 39 ($\sim$ 1710 and 1720 cm^{-1}) in the three complexes, where the ratio in (B) is much smaller than in (A) and (C). see Figure 4.9. The excited state Cartesian gradients between the three uracil-H_2O (thymine-H_2O) complexes are similar to each other, as shown in Figures 4.7 and 4.10. The PED analysis and cosine similarity showed the unique peak pattern in complex (B) of uracil-H_2O and thymine-H_2O is the result of the sensitivity of C_4-O_{10} bond to the hydrogen bonding environment governed by the explicit water, see Tables 4.3 and 4.4 along with Figures 4.4 and 4.5.

In summary, via the research addressed in this thesis, we gained an improved understanding of the requirements (and limitations) for the computational study of resonance Raman spectra. First, the necessity of utilizing long range corrected functionals for the accurate simulation of the resonance Raman spectra of uracil (and its derivatives) was determined; the best choice of functional for the computation of resonance Raman spectra cannot be determined by vertical excitation energies alone. The test of different functionals for simulating resonance Raman spectra provides a useful tool for the initial screening of methods for performing longer time-scale excited state dynamics. Secondly, the effects of incorporating explicit solvent molecules, i.e., water, on the resulting resonance Raman spectrum of the solute is explored for the first time. The specific solute-solvent interactions are found to be important for simulating the resonance Raman spectra of uracil and thymine. Finally, a powerful procedure is set up to analyze and compare the dimensionless displacements and the resulting resonance Raman spectra for a given species (for different computational protocols) and between similar systems (for a given computational method and/or experimental measurement). To examine the vibrational frequencies and normal modes in the ground state, the PED analysis and cosine similarity provide important tools for understanding the nature of resonance Raman spectra and the differences observed upon substitution or binding with solvent molecules. For the excited state, the vectorial representation of the excited state gradients in Cartesian coordinates provides a visualization of the differences due to computational method for a given species or between different systems (due to substitution or explicit solvation).

5.2 Directions for Future Work

Since in our current simulation approach, the Herzberg-Teller effect, vibrational anharmonicity, and the Duschinsky effect are not fully taken into account, to improve the accuracy of the simulations, and gain better agreement with and understanding of the experimental measurement, one of the goals in the future is to incorporate the effects above into the current simulation package for resonance Raman spectra. This will allow examination of the significance of these effects for specific systems including the nucleobases.

In Chapter 1, we introduced three commonly used approaches, i.e., sum-over-state approach, time dependent approach and transformation theory, to the simulation of resonance Raman spectra. In order to simplify the computation, many approximations are made, which includes the Born Oppenheimer (BO) approximation, Condon approximation, and IMDHO model. In recent years, extensive studies have been focused on improving the current simulation approaches and going beyond the approximations that are made. In this section, the new developments in the resonance Raman spectroscopy simulation methods are used to provide us guidance to the directions of our work in the future.

When deriving Eq 1.15 in Chapter 1, we invoked the Condon approximation, where only the Albrecht A term is kept and the higher order terms (usually known as Albrecht B, C, ... terms) are neglected. The contributions of these higher order terms are known as the Herzberg-Teller effect.[8,9] Recent computational studies, based on the sum-over-state approach[70,211–214] and time-dependent approach,[215] showed that the Herzberg-Teller effect can be significant in the resonance Raman spectra.

When simplifying the FC factor, the IMDHO model is used, where the multidimensional vibrational wavefunction is assumed to be decomposed into $3N-6$ independent harmonic oscillators, see Section 1.1.5 in Chapter 1. Therefore, the vibrational frequencies and corresponding wavefunctions in this model are harmonic, whereas the anharmonic effect is neglected. However, inclusion of anharmonic vibrational frequencies and wavefunctions (hence the evaluation of the overlap of the vibrational states)

can improve the peak positions and peak intensities. Barone et al. determined the vibrational anharmonicity using the VPT2 method,[216–219] and implemented this effect into the simulation of resonance Raman spectra using the sum-over-state approach.[211] This approach has been benchmarked for molecules such as imidazole,[211] pyrene,[211] chlorophyll a1[211] and $[Ru(bpy)_3]^{2+}$.[78] Their studies show that incorporating vibrational anharmonicity into the simulation can provide better agreement (in both peak positions and intensities) to the experimental measurement.

Another approximation made in the present simulations is neglect of the Duschinsky effect when determining the dimensionless normal mode displacements, Δ, see Section 1.1.6 in Chapter 1. In general, the normal mode coordinates of a molecule can change when it is electronically excited. Each normal mode in the excited state can be written as a linear combination of all the ground state normal mode coordinates. This is known as the Duschinsky relation,

$$Q' = \mathbf{J}Q + \mathbf{K}, \tag{5.1}$$

where Q and Q' are the normal mode coordinates on the ground and excited states, respectively; $\mathbf{J}$ and $\mathbf{K}$ account for the rotation and shift of the normal modes on the excited state, respectively. Barone et al.[211–213] and Burova et al.[214] independently included the Duschinsky effect into the sum-over-state approach; Saalfrank et al.[220] and Liang at al.[215] implemented the Duschinsky effect in the time-dependent approach.

Another goal we have in mind is to further explore the effect of solvation on the resonance Raman spectra. As shown in Chapter 4, the interaction between the solvent and solute can significantly change the peak positions and intensities of resonance Raman spectra. Gordon et al.[104] studied the solvent-induced shifts in the electronic spectra of uracil, where 150 water molecules have been included in the simulation using effective fragment potential (EFP) methodology. Our future goal is to further test the capability of the EFP water model in simulating resonance Raman spectra, and find a computationally feasible approach to further study the effect of specific solvation on the resonance Raman spectra.

Bibliography

[1] Long, D. A. *The Raman Effect: A Unified Treatment of the Theory of Raman Scattering by Molecules*; Wiley: New York, 2002.

[2] Myers, A. B.; Mathies, R. A. In *Biological Applications of Raman Spectroscopy*; Spiro, T. G., Ed.; Wiley: New York, 1987; pp 1–58.

[3] Kramers, H. A.; Heisenberg, W. *Z. Phys.* **1925**, *31*, 681–708.

[4] Kramers, H. A.; Heisenberg, W. In *Sources of Quantum Mechanics*; Waerden, B. L. V. D., Ed.; North–Holland Publishing Company: Amsterdam, 1967; pp 223–252.

[5] Dirac, P. A. M. *Proc. R. Soc. London, Ser. A* **1927**, *114*, 243–265.

[6] Schatz, G. C.; Ratner, M. A. *Quantum Mechanics in Chemistry*; Dover: New York, 2002; pp 104–107.

[7] McHale, J. L. *Molecular Spectroscopy*; Prentice Hall: New York, 1998; pp 104–107.

[8] Albrecht, A. C. *J. Chem. Phys.* **1961**, *34*, 1476–1484.

[9] Albrecht, A. C. *J. Chem. Phys.* **1971**, *55*, 4438–4443.

[10] Heller, E. J. *J. Chem. Phys.* **1975**, *62*, 1544–1555.

[11] Lee, S. Y.; Heller, E. J. *J. Chem. Phys.* **1979**, *71*, 4777–4788.

[12] Blazej, D. C.; Peticolas, W. L. *J. Chem. Phys.* **1980**, *72*, 3134–3142.

[13] Page, J. B.; Tonks, D. L. *Chem. Phys. Lett.* **1979**, *66*, 449–453.

[14] Page, J. B.; Tonks, D. L. *J. Chem. Phys.* **1981**, *75*, 5694–5708.

[15] Petrenko, T.; Neese, F. *J. Chem. Phys.* **2007**, *127*, 164319–164333.

[16] Petrenko, T.; Neese, F. *J. Chem. Phys.* **2012**, *137*, 234107.

[17] Valieva, M.; Bylaskaa, E.; Govinda, N.; Kowalskia, K.; Straatsmaa, T.; Dama, H. V.; D. Wanga, J. N.; Aprab, E.; Windusc, T.; de Jonga, W. *Comput. Phys. Commun.* **2010**, *181*, 1477–1489.

[18] Aquino, F. W.; Schatz, G. C. *J. Phys. Chem. A* **2014**, *118*, 517–525.

[19] Jensen, L.; Zhao, L. L.; Autschbach, J.; Schatz, G. C. *J. Chem. Phys.* **2005**, *123*, 174110.

[20] van Gisbergen, S. J. A.; Snijders, J. G.; Baerends, E. J. *Chem. Phys. Lett.* **1996**, *259*, 599–604.

[21] Zhao, L. L.; Jensen, L.; Schatz, G. C. *J. Am. Chem. Soc.* **2006**, *128*, 2911–2919.

[22] van Gisbergen, S. J. A.; Snijders, J. G.; Baerends, E. J. *Comput. Phys. Commun.* **1999**, *118*, 119–138.

[23] Neese, F.; Petrenko, T.; Ganyushin, D.; Olbrich, G. *Coord. Chem. Rev.* **2007**, *251*, 288–327.

[24] Warshel, A.; Dauber, P. *J. Chem. Phys.* **1977**, *66*, 5477–5488.

[25] Myers, A. B. *Chem. Rev.* **1996**, *96*, 911–926.

[26] Heller, E. J.; Sundberg, R. L.; Tannor, D. *J. Phys. Chem.* **1982**, *86*, 1822–1833.

[27] Neugebauer, J.; Hess, B. A. *J. Chem. Phys.* **2004**, *120*, 11564.

[28] Neugebauer, J. Development of Novel Algorithms and Implementations for Efficient Calculations of Infrared, Raman, and Resonance Raman Spectra. Ph.D. thesis, Universität Erlangen-Nuürnberg, 2003.

[29] Manneback, C. *Physica* **1951**, *17*, 1001–1010.

[30] Loppnow, G. R.; Billinghurst, B. E.; Oladepo, S. A. In *Radiation Induced Molecular Phenomena in Nucleic Acids*; Shukla, M. K., Leszczynski, J., Eds.; Springer: Verlag, 2008; pp 237–263.

[31] Benevides, J. M.; Overman, S. A.; Thomas, G. J. *J. Raman Spectosc.* **2005**, *36*, 279–299.

[32] Oladepo, S. A.; Xiong, K.; Hong, Z.; Asher, S. A.; Handen, J.; Lednev, I. K. *Chem. Rev.* **2012**, *112*, 2604–2628.

[33] Robert, B. *Photosynth. Res.* **2009**, *101*, 147–155.

[34] Efremov, E. V.; Ariese, F.; Gooijer, C. *Anal. Chim. Acta* **2008**, *606*, 119–134.

[35] Tsuboi, M.; Nishimura, T.; Hirakawa, A. Y.; Peticolas, W. L. In *Biological Applications of Raman Spectroscopy*; Spiro, T. G., Ed.; Wiley: New York, 1987; pp 109–180.

[36] Peticolas, W. L.; Rush III, T. *J. Comput. Chem.* **1995**, *16*, 1261–1270.

[37] Rush III, T.; Peticolas, W. L. *J. Phys. Chem.* **1995**, *99*, 14647–14658.

[38] Ng, S.; Teimoory, F.; Loppnow, G. R. *J. Phys. Chem. Lett.* **2011**, *2*, 2362–2365.

[39] Sasidharanpillai, S.; Loppnow, G. R. *J. Phys. Chem. A* **2014**, *118*, 4680–4687.

[40] Billinghurst, B. E.; Oladepo, S. A.; Loppnow, G. R. *J. Phys. Chem. B* **2012**, *116*, 10496–10503.

[41] Kundu, L. M.; Loppnow, G. R. *Photochem. Photobiol.* **2007**, *83*, 600–602.

[42] Lagant, P.; Vergoten, G.; Peticolas, W. L. *J. Raman Spectosc.* **1999**, *30*, 1001–1007.

[43] Yarasi, S.; Ng, S.; Loppnow, G. R. *J. Phys. Chem. B* **2009**, *113*, 14336–14342.

[44] Yarasi, S.; Brost, P.; Loppnow, G. R. *J. Phys. Chem. A* **2007**, *111*, 5130–5135, [Additions and Corrections] *J. Phys. Chem. A* **2008**, *112*, 10436-10437.

[45] Billinghurst, B. E.; Loppnow, G. R. *J. Phys. Chem. A* **2006**, *110*, 2353–2359.

[46] Li, M.-J.; Liu, M.-X.; Zhao, Y.-Y.; Pei, K.-M.; Wang, H.-G.; Zheng, X.; Fang, W. H. *J. Phys. Chem. B* **2013**, *117*, 11660–11669.

[47] Blazej, D. C.; Peticolas, W. L. *P. Natl. Acad. Sci. USA* **1977**, *74*, 2639–2643.

[48] Pézolet, M.; Yu, T.-J.; Peticolas, W. L. *J. Raman Spectosc.* **1975**, *3*, 55–64.

[49] Nishimura, Y.; Hirakawa, A. Y.; Tsuboi, M. *Chem. Lett.* **1977**, 907–908.

[50] Fodor, S. P. A.; Rava, R. P.; Hays, T. R.; Spiro, T. G. *J. Am. Chem. Soc.* **1985**, *107*, 1520–1529.

[51] Perno, J. R.; Grygon, C. A.; Spiro, T. G. *J. Phys. Chem.* **1989**, *93*, 5672–5678.

[52] Zhu, X.-M.; Wang, H.-G.; Zheng, X.; Phillips, D. L. *J. Phys. Chem. B* **2008**, *112*, 15828–15836.

[53] Krafft, C.; Benevides, J. M.; Jr, G. J. T. *Nucleic Acids Res.* **2002**, *30*, 3981–3991.

[54] Smulevich, G.; Feis, A. *J. Phys. Chem.* **1986**, *90*, 6388–6392.

[55] Grygon, C. A.; Spiro, T. G. *Biochemistry* **1989**, *28*, 4397–4402.

[56] Kocisova, E.; Chinsky, L.; Miskovsky, P. *J. Biomol. Struct. Dyn.* **1998**, *15*, 1147–1154.

[57] Dobson, C. M.; Šali, A.; Karplus, M. *Angew. Chem. Int. Ed.* **1998**, *37*, 868–893.

[58] Dobson, C. M. *Philos. Trans. R. Soc., B* **2001**, *356*, 133–145.

[59] Asher, S. A.; Ianoul, A.; Mix, G.; Boyden, M. N.; Karnoup, A.; Diem, M.; Schweitzer-Stenner, R. *J. Am. Chem. Soc.* **2001**, *123*, 11775–11781.

[60] Myshakina, N. S.; Ahmed, Z.; Asher, S. A. *J. Phys. Chem. B* **2008**, *112*, 11873–11877.

[61] Chi, Z.; Chen, X. G.; Holtz, J. S. W.; Asher, S. A. *Biochemistry* **1998**, *37*, 2854–2864.

[62] Mikhonin, A. V.; Bykov, S. V.; Myshakina, N. S.; Asher, S. A. *J Phys Chem B* **2006**, *110*, 1928–1943.

[63] Wang, Y.; Purrello, R.; Jordan, T. *J. Am. Chem. Soc.* **1991**, *113*, 6359–6368.

[64] Lednev, I. K.; Karnoup, A. S.; Sparrow, M. C.; Asher, S. A. *J. Am. Chem. Soc.* **2001**, *123*, 2388–2392.

[65] Lednev, I. K.; Karnoup, A. S.; Sparrow, M. C.; Asher, S. A. *J. Am. Chem. Soc.* **1999**, *121*, 4076–4077.

[66] Huang, C.-Y.; Balakrishnan, G.; Spiro, T. G. *Biochemistry* **2005**, *44*, 15734–15742.

[67] Hashimoto, S.; Yabusaki, T.; Takeuchi, H.; Harada, I. *Biospectroscopy* **1995**, *1*, 375–385.

[68] Couling, V. W.; Fischer, P.; Klenerman, D.; Huber, W. *Biophys. J.* **1998**, *75*, 1097–1106.

[69] Sun, S.; Brown, A. *J. Phys. Chem. A* **2014**, *118*, 9228–9238.

[70] Rappoport, D.; Shim, S.; Aspuru-Guzik, A. *J. Phys. Chem. Lett.* **2011**, *2*, 1254–1260.

[71] Ren, H.; Jiang, J.; Mukamel, S. *J. Phys. Chem. B* **2011**, *115*, 13955–13962.

[72] Ren, H.; Lai, Z.; Biggs, J. D.; Wang, J.; Mukamel, S. *Phys. Chem. Chem. Phys.* **2013**, *15*, 19457–19464.

[73] Preketes, N. K.; Biggs, J. D.; Ren, H.; Andricioaei, I.; Mukamel, S. *Chem. Phys.* **2013**, *422*, 63–72.

[74] Wright, P. G.; Stein, P.; Burke, J. M.; Spiro, T. G. *J. Am. Chem. Soc.* **1979**, *101*, 3531–3535.

[75] Fraga, E.; Webb, M. A.; Loppnow, G. R. *J. Phys. Chem.* **1996**, *100*, 3278–3287.

[76] Wootton, J. L.; Zink, J. I. *J. Phys. Chem.* **1995**, *99*, 7251–7257.

[77] Shafaat, H. S.; Weber, K.; Petrenko, T.; Neese, F.; Lubitz, W. *Inorg. Chem.* **2012**, *51*, 11787–11797.

[78] Baiardi, A.; Latouche, C.; Bloino, J.; Barone, V. *Dalton Trans.* **2014**, *43*, 17610–17614.

[79] Silverstein, D. W.; Milojevich, C. B.; Camden, J. P.; Jensen, L. *J. Phys. Chem. C* **2013**, *117*, 20855–20866.

[80] Billinghurst, B. E.; Yeung, R.; Loppnow, G. R. *J. Phys. Chem. A* **2006**, *110*, 6185–6191.

[81] Neese, F. *Wiley Interdiscip. Rev.: Comput. Mol. Sci.* **2012**, *2*, 73–78.

[82] Schmidt, M. W.; Baldridge, K. K.; Boatz, J. A.; Elbert, S. T.; Gordon, M. S.; Jensen, J. H.; Koseki, S.; Matsunaga, N.; Nguyen, K. A.; et al., S. J. S. *J. Comput. Chem.* **1993**, *14*, 1347–1363.

[83] Gordon, M. S.; Schmidt, M. W. In *Theory and Applications of Computational Chemistry, the First Forty Years*; Dykstra, C. E., Frenking, G., Kim, K. S., Scuseria, G. E., Eds.; Elsevier: Amsterdam, 2005; pp 1167–1189.

[84] Frisch, M. J. et al. Gaussian09 Revision D.01. Gaussian Inc. Wallingford CT 2009.

[85] Crespo-Hernández, C. E.; Cohen, B.; Hare, P. M.; Kohler, B. *Chem. Rev.* **2004**, *104*, 1977–2020, PMID: 15080719.

[86] Middleton, C. T.; de La Harpe, K.; Su, C.; Law, Y. K.; Crespo-Hernández, C. E.; Kohler, B. *Ann. Rev. Phys. Chem.* **2009**, *60*, 217–239.

[87] Barbatti, M.; Aquino, A. J. A.; Szymczak, J. J.; Nachtigallová, D.; Hobza, P.; Lischka, H. *Proc. Natl. Acad. Sci. U. S. A.* **2010**, *107*, 21453–21458.

[88] Kistler, K. A.; Matsika, S. In *Multi-Scale Quantum Models for Biocatalysis: Modern Techniques and Applications*; York, D. M., Lee, T., Eds.; Springer: Verlag, 2009; pp 285–239.

[89] Kraemer, K. H. *Proc. Natl. Acad. Sci. U. S. A.* **1997**, *94*, 11–14.

[90] Miller, D. L.; Weinstock, M. A. *J. Am. Acad. Dermatol.* **1994**, *30*, 774–778.

[91] Young, A. R. *Int. J. Clin. Pract., Suppl.* **1997**, *89*, 10–15.

[92] Mukhtart, H.; Elmets, C. A. *Photochem. Photobiol.* **1996**, *63*, 355–357.

[93] Doltsinis, N. L.; Markwick, P. R. L.; Nieber, H.; Langer, H. In *Radiation Induced Molecular Phenomena in Nucleic Acids*; Shukla, M. K., Leszczynski, J., Eds.; Springer: Verlag, 2008; pp 265–299.

[94] El-Yazbi, A. F.; Palech, A.; Loppnow, G. R. *J. Phys. Chem. A* **2011**, *115*, 10445–10451.

[95] Oladepo, S. A.; Loppnow, G. R. *J. Phys. Chem. B* **2011**, *115*, 6149–6156.

[96] Billinghurst, B. E.; Oladepo, S. A.; Loppnow, G. R. *J. Phys. Chem. B* **2009**, *113*, 7392–7397.

[97] Gustavsson, T.; Banyasz, A.; Lazzarotto, E.; Markovitsi, D.; Scalmani, G.; Frisch, M. J.; Barone, V.; Improta, R. *J. Am. Chem. Soc.* **2006**, *128*, 607–619.

[98] Ludwig, V.; Coutinhoa, K.; Canuto, S. *Phys. Chem. Chem. Phys.* **2007**, *9*, 4907–4912.

[99] Ren, H.-S.; Li, Y.-K.; Zhu, Q.; Zhu, J.; Li, X.-Y. *Phys. Chem. Chem. Phys.* **2012**, *14*, 13284–13291.

[100] Olsen, J. M.; Aidas, K.; Mikkelsen, K. V.; Kongsted, J. *J. Chem. Theory Comput.* **2010**, *6*, 249–256.

[101] Improta, R.; Barone, V. *J. Am. Chem. Soc.* **2004**, *126*, 14320–14321.

[102] Zazza, C.; Olsen, J. M.; Kongsted, J. *Comp. Theor. Chem.* **2011**, *974*, 109–116.

[103] Kistler, K. A.; Matsika, S. *J. Phys. Chem. A* **2009**, *113*, 12396–12403.

[104] DeFusco, A.; Ivanic, J.; Schmidt, M. W.; Gordon, M. S. *J. Phys. Chem. A* **2011**, *115*, 4754–4582.

[105] Shukla, M. K.; Leszczynski, J. *J. Phys. Chem. A* **2002**, *106*, 8642–8650.

[106] Herzberg, G.; Teller, E. *Z. Phys. Chem. Abt.* **1933**, *B21*, 410–446.

[107] Shukla, M. K.; Leszczynski, J. *J. Comput. Chem.* **2004**, *25*, 768–778.

[108] Pluta, T.; Kolaski, M.; Medved, M.; Budzk, S. *Chem. Phys. Lett.* **2012**, *546*, 24–29.

[109] Laikov, D.; Matsika, S. *Chem. Phys. Lett.* **2007**, *448*, 132–137.

[110] Lorentzon, J.; Fuelscher, M. P.; Roos, B. O. *J. Am. Chem. Soc.* **1995**, *117*, 9265–73.

[111] Richter, M.; Mai, S.; Marquetand, P.; lez, L. G. x. *Phys. Chem. Chem. Phys.* **2014**, *16*, 24423–24436.

[112] Epifanovsky, E.; Kowalski, K.; Fan, P.-D.; Valiev, M.; Matsika, S.; Krylov, A. I. *J. Phys. Chem. A* **2008**, *112*, 9983–9992.

[113] Zgierski, M. Z.; Patchkovskii, S.; Fujiwara, T.; Lim, E. C. *J. Phys. Chem. A* **2005**, *109*, 9384–9387.

[114] Schreiber, M.; Silva-Junior, M. R.; Sauer, S. P. A.; Thiel, W. *J. Chem. Phys.* **1994**, *128*, 134110–134134.

[115] Matsika, S. *J. Phys. Chem. A* **2004**, *108*, 7584–7590.

[116] Fleig, T.; Knecht, S.; Hättig, C. *J. Phys. Chem. A* **2007**, *111*, 5482–5491.

[117] Yoshikawa, A.; Matsika, S. *Chem. Phys.* **2008**, *347*, 393–404.

[118] Zhang, X.; Herbert, J. M. *J. Phys. Chem. B* **2014**, *118*, 7806–7817.

[119] Adamo, C.; Barone, V. *J. Chem. Phys.* **1999**, *110*, 6158–6169.

[120] Perdew, J. P.; Burke, K.; Ernzerhoff, M. *Phys. Rev. Lett.* **1996**, *77*, 3865–3868, [Erratum] *Phys. Rev. Lett.* **1996**, *78*, 1396.

[121] Becke, A. D. *J. Chem. Phys.* **1993**, *98*, 5648–5652.

[122] Stephens, P. J.; Devlin, F. J.; Chablowski, C. F.; Frisch, M. J. *J. Phys. Chem.* **1994**, *98*, 11623–11627.

[123] Hertwig, R. H.; Koch, W. *Chem. Phys. Lett.* **1997**, *268*, 345–351.

[124] Dunning Jr., T. H. *J. Chem. Phys.* **1990**, *90*, 1007–1023.

[125] Kendall, R. A.; Dunning Jr., T. H.; Harrison, R. J. *J. Chem. Phys.* **1992**, *96*, 6796–6806.

[126] Yanai, T.; Tew, D. P.; Handy, N. C. *Chem. Phys. Lett.* **2004**, *393*, 51 – 57.

[127] Tawada, Y.; Tsuneda, T.; Yanagisawa, S.; Yanai, Y.; Hirao, K. *J. Chem. Phys.* **2004**, *120*, 8425–8433.

[128] Minezawa, N.; Gordon, M. S. *J. Phys. Chem. A* **2009**, *113*, 12749–12753.

[129] Shao, Y.; Head-Gordon, M.; Krylov, A. I. *J. Chem. Phys.* **2003**, *118*, 4807–4818.

[130] McWeeny, R.; Diercksen, G. *J. Chem. Phys.* **1968**, *49*, 4852–4856.

[131] Guest, M. F.; Saunders, V. R. *Mol. Phys.* **1974**, *28*, 819–828.

[132] Binkley, J. S.; Pople, J. A.; Dobosh, P. A. *Mol. Phys.* **1974**, *28*, 1423–1429.

[133] Davidson, E. R. *Chem. Phys. Lett.* **1973**, *21*, 565–567.

[134] Faegri, K.; Manne, R. *Mol. Phys.* **1976**, *31*, 1037–1049.

[135] Hsu, H.; Davidson, E. R.; Pitzer, R. M. *J. Chem. Phys.* **1976**, *65*, 609–613.

[136] Chiba, M.; Tsuneda, T.; Hirao, K. *J. Chem. Phys.* **2006**, *124*, 144106–144116.

[137] Barone, V.; Cossi, M. *J. Phys. Chem. A* **1998**, *102*, 1995–2001.

[138] Cossi, M.; Rega, N.; Scalmani, G.; Barone, V. *J. Comput. Chem.* **2003**, *24*, 669–681.

[139] Cossi, M.; Barone, V. *J. Chem. Phys.* **2001**, *115*, 4708–4717.

[140] Wang, Y.; Li, H. *J. Chem. Phys.* **2009**, *131*, 206101–206102.

[141] Jamróz, M. H. Vibrational Energy Distribution Analysis VEDA4. 2004-2010; Warsaw.

[142] Jamróz, M. H. *Spectrochim. Acta, Part A* **2013**, *114*, 220–230.

[143] Puzzarini, C.; Barone, V. *Phys. Chem. Chem. Phys.* **2011**, *13*, 7189–7197.

[144] Colarusso, P.; Zhang, K.; Guo, B.; Bernath, P. F. *Chem. Phys. Lett.* **1997**, *269*, 39–48.

[145] Szczepaniak, K.; Person, W.; Leszczynski, J.; Kwiatkowski, J. *Pol. J. Chem.* **1998**, *72*, 402–420.

[146] Singh, J. S. *Spectrochim. Acta, Part A* **2013**, *117*, 502–518.

[147] Palafox, M. A.; Tardajos, G.; Guerrero-Martnez, A.; Vats, J. K.; Joe, H.; Rastogi, V. K. *Spectrochim. Acta, Part A* **2010**, *75*, 1261–1269.

[148] Shanmugasundaram, M.; Puranik, M. *J. Raman Spectosc.* **2009**, *40*, 1726–1748.

[149] Peng, C. S.; Jones, K. C.; Tokmakoff, A. *J. Am. Chem. Soc.* **2011**, *133*, 15650–15660.

[150] Palafox, M. A.; Iza, N.; Gil, M. *J. Mol. Struct.: THEOCHEM* **2002**, *585*, 69–92.

[151] Ilich, P.; Hemann, C. F.; Hille, R. *J. Phys. Chem. B* **1997**, *101*, 10923–10932.

[152] Puzzarini, C.; Biczysko, M.; Barone, V. *J. Chem. Theory Comput.* **2011**, *7*, 3702–3710.

[153] Barone, V.; Festa, G.; Grandi, A.; Rega, N.; Sanna, N. *Chem. Phys. Lett.* **2004**, *388*, 279–283.

[154] M. -P. Gaigeot,; Kadri, C.; Ghomi, M. *J. Mol. Struct.* **2001**, *565*, 469–473.

[155] Bencivenni, L.; Ramondo, F.; Pieretti, A.; Sanna, N. *J. Chem. Soc., Perkin Trans. 2* **200**, *2*, 1685–1693.

[156] Szczesniak, M.; Nowak, M. J.; Rostkowska, H.; Szczepaniak, K.; Person, W. B.; Shugar, D. *J. Am. Chem. Soc.* **1983**, *105*, 5969–5976.

[157] Graindourze, M.; Smets, J.; Zeegers-huyskens, T.; Maes, G. *J. Mol. Struct.* **1990**, *222*, 345–364.

[158] Gaigeot, M.-P.; Sprik, M. *J. Phys. Chem. B* **2003**, *107*, 10344–10358.

[159] Gaigeot, M.-P.; Ghomi, M. *J. Phys. Chem. B* **2001**, *105*, 5007–5017.

[160] Laury, L. L.; Boesch, S. E.; Haken, J.; Sinha, P.; Wheeler, R. A.; Wilson, A. K. *J. Comput. Chem.* **2011**, *32*, 2339–2347.

[161] Sinha, P.; Boesch, S. E.; Gu, C.; Wheeler, R. A.; Wilson, A. K. *J. Phys. Chem. A* **2004**, *42*, 9213–9217.

[162] Vogt, N.; Khaikin, L. S.; Grikina, O. E.; Rykov, A. N. *J. Mol. Struct.* **2013**, *1050*, 114–121.

[163] Vaquero, V.; Sanz, M. E.; López, J. C.; Alonso, J. L. *J. Phys. Chem. A* **2007**, *111*, 3343–3445.

[164] Clark, L. B.; Peschel, G. G.; Tinoco Jr., I. *J. Phys. Chem.* **1965**, *69*, 3615–3618.

[165] Peach, M. J. G.; Benfield, P.; Helgaker, T.; Tozer, D. J. *J. Chem. Phys.* **2008**, *128*, 044118.

[166] Zamenhof, S.; Giovanni, R. D.; Greer, S. *Nature* **1958**, *181*, 827–829.

[167] Sugiyama, H.; Tsutsumi, Y.; Saito, I. *J. Am. Chem. Soc.* **1990**, *112*, 6720–6721.

[168] Abdoul-Carime, H.; Huels, M. A.; Illenberger, E.; Sanche, L. *J. Am. Chem. Soc.* **2001**, *123*, 5354–5355.

[169] Schmittgen, T. D.; Danenberg, K. D.; Horikoshi, T.; Lenz, H. J.; Danenberg, P. V. *J. Biol. Chem.* **1994**, *269*, 16269–16275.

[170] Xu, Y.; Tashiro, R.; Sugiyama, H. *Nat. Protoc.* **2007**, *2*, 78–87.

[171] Xu, Y.; Sugiyama, H. *Angew. Chem., Int. Ed. Engl.* **2006**, *45*, 1354–1362.

[172] Morinaga, H.; Kizaki, S.; Takenaka, T.; Kanesato, S.; Sannohe, Y.; Tashiro, R.; Sugiyama, H. *Bioorg. Med. Chem.* **2013**, *21*, 466–469.

[173] Weng, K.-F.; Wang, H.-G.; Zhu, X.-M.; Zheng, X.-M. *Acta Phys.–Chim. Sin.* **2009**, *25*, 1799–1805.

[174] Skinner, K. A.; Dunnington, G.; Silberman, H.; Florentine, B.; Spicer, D.; Formenti, S. C. *Am. J. Surg.* **1997**, *174*, 705–708.

[175] Takeo, I.; Kazuhito, T.; Hisatsugu, Y.; Hiroshi, H.; Sei-ichi, N. *Molecules* **2008**, *13*, 2370–2384.

[176] Yamazaki, S.; Taketsugu, T. *J. Phys. Chem. A* **2012**, *116*, 491–503.

[177] Mercier, Y.; Reguero, M. *Int. J. Quantum Chem.* **2011**, *111*, 3405–3415.

[178] Improta, R.; Barone, V.; Lami, A.; Santoro, F. *J. Phys. Chem. B* **2009**, *113*, 14491–14503.

[179] Santoro, F.; Improta, R.; Barone, V. *Theor. Chem. Acc.* **2009**, *123*, 273–286.

[180] Santoro, F.; Barone, V.; Gustavsson, T.; Improta, R. *J. Am. Chem. Soc.* **2006**, *128*, 16312–16322.

[181] Gustavsson, T.; Sarkar, N.; Lazzarotto, E.; Markovitsi, D.; Barone, V.; Improta, R. *J. Phys. Chem. B* **2006**, *110*, 12843–12847.

[182] Kobyłecka, M.; Migani, A.; Asturiol, D.; Rak, J.; Blancafort, L. *J. Phys. Chem. A* **2009**, *113*, 5489–5495.

[183] Bistafa, C.; Canuto, S. *Theor. Chem. Acc.* **2012**, *132*, 1299–1308.

[184] Ten, G. N.; Burova, T. G.; Baranov, V. I. *J. Appl. Spectrosc.* **2006**, *73*, 492–498.

[185] Furche, F.; Ahlrichs, R. *J. Chem. Phys.* **2002**, *117*, 7433–7447.

[186] Furche, F.; Ahlrichs, R. *J. Chem. Phys.* **2004**, *121*, 12772–12773.

[187] Scalmani, G.; Frisch, M. J.; Mennucci, B.; Tomasi, J.; Cammi, R.; Barone, V. *J. Chem. Phys.* **2006**, *124*, 094107.

[188] Allouche, A.-R. *J. Comput. Chem.* **2011**, *32*, 174–182.

[189] Singh, J. S. *Spectrochim. Acta, Part A* **2011**, *87*, 106–111.

[190] Ortiz, S.; Palafox, M. A.; Rastogi, V. K.; Akitsu, T.; Joe, I. H.; Kumar, S. *Spectrochim. Acta, Part A* **2013**, *110*, 404–418.

[191] Rastogi, V. K.; Palafox, M. A.; Mittal, L.; Peica, N.; Kiefer, W.; Lang, K.; Ojha, S. P. *J. Raman Spectosc.* **2007**, *38*, 1227–1241.

[192] Rastogi, V. K.; Jain, V.; Yadav, R. A.; Singh, C.; Palafox, M. A. *J. Raman Spectosc.* **2000**, *31*, 595–603.

[193] Palafox, M. A.; Rastogi, V. K. *Spectrochim. Acta, Part A* **2002**, *58*, 411–440.

[194] Graindourze, M.; Grootaers, T.; Smets, J.; Zeegers-Huyskens, T.; Maes, G. *J. Mol. Struct.* **1990**, *237*, 389–410.

[195] Dobrowolski, J. C.; Rode, J. E.; Kołos, R.; Jamróz, M. H.; Bajdor, K.; Mazurek, A. P. *J. Phys. Chem. A* **2005**, *109*, 2167–2182.

[196] Shukla, M. K.; Kumar, A.; Mishra, P. C. *J. Mol. Struct.: THEOCHEM* **2001**, *535*, 269–277.

[197] Lohmann, W. *Z. Naturforsch. C* **1974**, *29*, 493–495.

[198] Mercier, Y.; Santoro, F.; Reguero, M.; Improta, R. *J. Phys. Chem. B* **2008**, *112*, 10769–10772.

[199] Etinski, M.; Marian, C. M. *Phys. Chem. Chem. Phys.* **2010**, *12*, 4915–4923.

[200] Kima, S.; Schaefer III, H. F. *J. Chem. Phys.* **2006**, *125*, 144305–144314.

[201] van Mourik, T.; Price, S. L.; Clary, D. C. *J. Phys. Chem. A* **1999**, *103*, 1611–1618.

[202] López, J. C.; Alonso, J. L.; na, I. P.; Vaquero, V. *Phys. Chem. Chem. Phys.* **2010**, *12*, 14128–14134.

[203] Thicoipe, S.; Carbonnière, P.; Pouchan, C. *Phys. Chem. Chem. Phys.* **2013**, *15*, 11646–11652.

[204] Danilov, V. I.; van Mourik, T.; Poltev, V. I. *Chem. Phys. Lett.* **2006**, *429*, 255–260.

[205] Kryachko, E. S.; Nguyen, M. T.; Zeegers-Huyskens, T. *J. Phys. Chem. A* **2001**, *105*, 1934–1943.

[206] van Mourik, T. *Phys. Chem. Chem. Phys.* **2001**, *3*, 2886–2892.

[207] van Mourik, T.; Benoit, D. M.; Price, S. L.; Clary, D. C. *Phys. Chem. Chem. Phys.* **2000**, *2*, 1281–1290.

[208] Graindourze, M.; Grootaers, T.; Smets, J.; Zeegers-Huyskens, T.; Maes, G. *J. Mol. Struct.* **1991**, *243*, 37–60.

[209] Choi, M. Y.; Miller, R. E. *Phys. Chem. Chem. Phys.* **2005**, *7*, 3565–3573.

[210] Chandra, A. K.; Nguyen, M. T.; Zeegers-Huyskens, T. *J. Phys. Chem. A* **1998**, *102*, 6010–6016.

[211] Egidi, F.; Bloino, J.; Cappelli, C.; Barone, V. *J. Chem. Theory Comput.* **2014**, *10*, 346–363.

[212] Avila Ferrer, F. J.; Barone, V.; Cappelli, C.; Santoro, F. *J. Chem. Theory Comput.* **2013**, *9*, 3597–3611.

[213] Santoro, F.; Cappelli, C.; Barone, V. *J. Chem. Theory Comput.* **2011**, *7*, 1824–1839.

[214] Burova, T. G.; Ermolenkov, V. V.; Ten, G. N.; Kadrov, D. M.; Nurlygaianova, M. N.; Baranov, V. I.; Lednev, I. K. *J. Phys. Chem. A* **2013**, *117*, 12734–12748.

[215] Ma, H.; Liu, J.; Liang, W. *J. Chem. Theory Comput.* **2012**, *8*, 4474–4482.

[216] Barone, V. *J. Chem. Phys.* **2005**, *122*, 014108.

[217] Barone, V. *J. Phys. Chem. A* **2004**, *108*, 4146–4150.

[218] Barone, V.; Bloino, J.; Guido, C. A.; Lipparini, F. *Chem. Phys. Lett.* **2010**, *496*, 157–161.

[219] Bloino, J.; Biczysko, M.; Barone, V. *J. Chem. Theory Comput.* **2012**, *8*, 1015–1036.

[220] Banerjee, S.; Kröner, D.; Saalfrank, P. *J. Chem. Phys.* **2012**, *137*, 22A534.

[221] Fallon III, L. *Acta Crystallogr., Sect. B: Struct. Crystallogr. Cryst. Chem.* **1973**, *B29*, 2549–2556.

[222] Sternglanz, H.; Bugg, C. E. *Biochim. Biophys. Acta, Nucleic Acids Protein Synth.* **1975**, *378*, 1–11.

Appendix A

Appendix to Chapter 2

Table A1: *Equilibrium Geometry of Uracil as Determined in the Gas Phase with the PBE0 and B3LYP functionals with the aug-cc-pVTZ Basis Set.*

bond length /Å	PBE0	B3LYP	$\lvert\Delta r\rvert/10^{-3}$[a]	experiment[b]	experiment[c]	experiment[d]
$r(C_6\text{-}C_5)$	1.341477	1.343948	2.471	1.339	1.34496	1.379
$r(C_5\text{-}C_4)$	1.451030	1.455020	3.990	1.454	1.45500	1.451
$r(N_1\text{-}C_6)$	1.364355	1.371226	6.871	1.374	1.37196	1.352
$r(C_2\text{-}N_1)$	1.382518	1.389893	7.375	1.381	1.38175	1.386
$r(N_3\text{-}C_2)$	1.372830	1.379744	6.914	1.379	1.3763	
$r(C_4\text{-}N_3)$	1.399281	1.408310	9.029	1.402	1.39793	
$r(O_8\text{-}C_2)$	1.208501	1.212010	3.509	1.210	1.21025	1.219
$r(O_{10}\text{-}C_4)$	1.210856	1.214559	3.703	1.212	1.21278	1.22
$r(H_{12}\text{-}C_6)$	1.082213	1.080664	1.549	1.079		
$r(H_7\text{-}N_1)$	1.005443	1.006408	0.965	1.005		
$r(H_9\text{-}N_3)$	1.009368	1.010351	0.983	1.009		
$r(H_{11}\text{-}C_5)$	1.078262	1.076957	1.305	1.076		
RMSD	0.002[e]	0.001[f]				
bond angle /°	PBE0	B3LYP	$\lvert\Delta\theta\rvert$[a]			
$\theta(N_1\text{-}C_6\text{-}C_5)$	122.04	121.98	0.06	121.6	121.924	122.3
$\theta(C_2\text{-}N_1\text{-}C_6)$	123.48	123.53	0.05	123.8	123.374	123.0
$\theta(N_3\text{-}C_2\text{-}N_1)$	113.12	113.06	0.06	113.0	113.383	
$\theta(N_3\text{-}C_4\text{-}C_5)$	113.60	113.61	0.01	113.6	113.860	115.4
$\theta(C_4\text{-}N_3\text{-}C_2)$	128.12	127.98	0.14	128.0	127.942	
$\theta(C_4\text{-}C_5\text{-}C_6)$	119.63	119.84	0.21	120.0	119.516	118.8
$\theta(C_5\text{-}C_4\text{-}O_{10})$	126.16	126.17	0.01	126.5	125.768	118.8
$\theta(C_6\text{-}N_1\text{-}H_7)$	121.38	121.27	0.11	121		
$\theta(C_5\text{-}C_6\text{-}H_{12})$	122.53	122.63	0.10	126		
$\theta(O_8\text{-}C_2\text{-}N_1)$	122.71	122.72	0.01	122.6	123.883	122.3
$\theta(O_{10}\text{-}C_4\text{-}N_3)$	120.24	120.22	0.02	119.9		
$\theta(H_{12}\text{-}C_6\text{-}N_1)$	115.43	115.39	0.04			
$\theta(H_7\text{-}N_1\text{-}C_2)$	115.14	115.20	0.06			
$\theta(H_9\text{-}N_3\text{-}C_2)$	115.62	115.71	0.09	114		

θ(H_{11}-C_5-C_6)	121.96	121.92	0.04	122.0		
RMSD	0.44[e]	0.27[f]				
dihedral angle /°	PBE0	B3LYP	$\lvert\Delta\phi\rvert$[a]			
ϕ(C_2-N_1-C_6-C_5)	0.00	0.00	0.00			
ϕ(N_3-C_2-N_1-C_6)	0.00	0.00	0.00			
ϕ(C_4-N_3-C_2-N_1)	0.00	0.00	0.00			
ϕ(O_8-C_2-N_1-C_6)	180.00	180.00	0.00			
ϕ(O_{10}-C_4-N_3-C_2)	180.00	180.00	0.00			
ϕ(H_{12}-C_6-N_1-C_5)	180.00	180.00	0.00			
ϕ(H_7-N_1-C_2-C_6)	180.00	180.00	0.00			
ϕ(H_9-N_3-C_2-C_4)	180.00	180.00	0.00			
ϕ(H_{11}-C_5-C_6-C_4)	180.00	180.00	0.00			

[a] Difference between PBE0/aug-cc-pVTZ and B3LYP/aug-cc-pVTZ.
[b] Ref.162
[c] Ref.143
[d] Ref.163
[e] between PBE0 optimized geometry and experimental data in Ref.162.
[f] between B3LYP optimized geometry and experimental data in Ref.162.

Table A2: *Cartesian Coordinates of Uracil Optimized in the Gas phase at the PBE0/aug-cc-pVTZ Level of Theory.*

N	-1.1685	0.9790	-0.0000
C	-1.2108	-0.4029	0.0000
N	0.0347	-0.9803	0.0000
C	1.2814	-0.3448	-0.0000
C	1.1953	1.1036	0.0000
C	-0.0081	1.6965	-0.0000
H	-2.0652	1.4337	-0.0000
O	-2.2471	-1.0245	0.0000
H	0.0480	-1.9896	0.0000
O	2.2998	-0.9999	-0.0000
H	2.1115	1.6720	0.0000
H	-0.1268	2.7722	-0.0000

Table A3: *Cartesian Coordinates of Uracil Optimized in the Gas Phase at the B3LYP/aug-cc-pVTZ Level of Theory.*

N	-0.4087	-1.7048	0.1049
C	-1.5675	-0.9379	0.0771
N	-1.3180	0.4147	-0.0318
C	-0.0698	1.0620	-0.1121
C	1.0633	0.1501	-0.0720
C	0.8533	-1.1732	0.0329
H	-0.5536	-2.6977	0.1824
O	-2.6761	-1.4235	0.1423
H	-2.1337	1.0104	-0.0562
O	-0.0135	2.2717	-0.2053
H	2.0548	0.5666	-0.1285
H	1.6608	-1.8905	0.0663

Table A4: *Vibrational Frequencies (ω/cm^{-1}) Lower Than 1000 cm^{-1} and Dimensionless Displacements ($|\Delta|$)of Uracil in the Gas Phase for the S_2 Excited State. All Computations use the aug-cc-pVTZ Basis Set.*

modes	6	7	8	9	10	11	12	13	14	15	16
ω(PBE0)	546.38	563.602	579.565	693.735	739.923	781.431	782.669	832.334	979.732	989.199	1000.08
ω(scaled by 0.9776)[b]	534.141	550.978	566.582	678.196	723.349	763.927	765.137	813.69	957.786	967.041	977.679
$\|\Delta\|$(PBE0)	0.087363	0.935912	0.000279	0.000057	0.000009	0.000201	0.811705	0.000079	0.144686	0.000011	0.266069
$\|\Delta\|$(B3LYP)	0.003428	0.799041	0.000230	0.000050	0.000029	0.000255	1.102617	0.000103	0.147868	0.000010	0.159032
$\|\Delta\|$(CAMB3LYP)	0.171446	0.960208	0.000292	0.000069	0.000025	0.000158	0.784303	0.000093	0.242399	0.000007	0.198521
$\|\Delta\|$(LC-BLYP)	0.188104	0.967326	0.000317	0.000040	0.000041	0.000152	0.765938	0.000105	0.299700	0.000021	0.185405
$\|\Delta\|$(BHHLYP)[a]	0.277743	1.326770	0.086000	0.016672	0.021177	0.021631	0.382972	0.010688	0.117934	0.000804	0.265344
ω(B3LYP)	543.147	559.617	573.061	687.073	733.794	768.991	770.933	827.503	963.362	984.946	993.052
ω(scaled by 0.9891)[c]	537.227	553.517	566.815	679.584	725.796	760.609	762.53	818.483	952.861	974.21	982.228
$\|\Delta\|$(PBE0)	0.132020	1.013281	0.001682	0.001149	0.004477	0.505035	0.039416	0.000773	0.055350	0.002319	0.379153
$\|\Delta\|$(B3LYP)	0.032603	0.864644	0.001607	0.001273	0.005895	0.808908	0.065948	0.001238	0.065311	0.001842	0.278671
$\|\Delta\|$(CAMB3LYP)	0.211043	1.039376	0.001897	0.000730	0.003728	0.480741	0.037567	0.000939	0.170791	0.002105	0.313585
$\|\Delta\|$(LC-BLYP)	0.225466	1.046535	0.001335	0.000509	0.002552	0.462497	0.036120	0.000866	0.232719	0.002062	0.304122
$\|\Delta\|$(BHHLYP)[a]	0.340094	1.445337	0.230655	0.022198	0.041682	0.065632	0.011715	0.015256	0.040281	0.010874	0.357910

[a] Determined by SF-TD-DFT using the Tamm Dancoff approximation and numerical gradients.
[b] Ref. 160
[c] Ref. 161

Table A5: *Vibrational Frequencies (ω/cm^{-1}) Higher Than 1000 cm^{-1} and Dimensionless Displacements ($|\Delta|$)of Uracil in the Gas Phase for the S_2 Excited State. All Computations use the aug-cc-pVTZ Basis Set.*

modes	17	18	19	20	21	22	23	24	25	26
ω(PBE0)	1098.76	1211.20	1242.92	1391.36	1419.66	1432.35	1517.87	1695.66	1798.44	1831.32
ω(scaled by 0.9568)[b]	1051.29	1158.87	1189.23	1331.25	1358.34	1370.47	1452.3	1622.41	1720.75	1752.21
$\|\Delta\|$(PBE0)	0.388705	0.335309	0.707331	0.548281	0.103853	0.248493	0.401026	0.766766	0.494443	0.526915
$\|\Delta\|$(B3LYP)	0.435447	0.372100	0.684428	0.522751	0.083451	0.289959	0.441347	0.687390	0.506571	0.627063
$\|\Delta\|$(CAMB3LYP)	0.323122	0.277885	0.788439	0.622701	0.137230	0.200479	0.352604	0.898521	0.546092	0.329532
$\|\Delta\|$(LC-BLYP)	0.307058	0.275179	0.833178	0.656034	0.146073	0.189205	0.295022	0.909734	0.586471	0.322956
$\|\Delta\|$(BHHLYP)[a]	0.003079	0.196268	1.045563	0.73852	0.104367	0.049733	0.341073	0.975498	0.800612	0.264483
ω(B3LYP)	1086.31	1191.50	1226.93	1381.34	1404.29	1421.25	1496.67	1670.17	1758.84	1791.36
ω(scaled by 0.9676)[c]	1051.11	1152.90	1187.19	1336.59	1358.79	1375.21	1448.18	1616.07	1701.86	1733.32
$\|\Delta\|$(PBE0)	0.252215	0.735528	0.539325	0.340603	0.317971	0.330217	0.322337	0.771346	0.467423	0.497980
$\|\Delta\|$(B3LYP)	0.306352	0.759385	0.498852	0.294716	0.353731	0.340241	0.358002	0.688689	0.479184	0.602035
$\|\Delta\|$(CAMB3LYP)	0.166773	0.728102	0.647175	0.433544	0.284458	0.328416	0.279763	0.909407	0.524858	0.294491
$\|\Delta\|$(LC-BLYP)	0.139023	0.748986	0.691298	0.470735	0.275240	0.328995	0.222802	0.921111	0.566863	0.287165
$\|\Delta\|$(BHHLYP)[a]	0.170572	0.808885	0.892861	0.56239	0.248570	0.195733	0.247250	0.979834	0.793935	0.229431

[a] Determined by SF-TD-DFT using the Tamm Dancoff approximation and numerical gradients.
[b] Ref. 160
[c] Ref. 161

Table A6: *Vibrational Frequencies (ω/cm^{-1}) Lower Than 1000 cm^{-1} and Dimensionless Displacements ($|\Delta|$)of Uracil in the Implicit Water for the S_1 Excited State. All Computations use the aug-cc-pVTZ Basis Set.*

modes	6	7	8	9	10	11	12	13	14	15	16
ω(PBE0)	546.38	563.602	579.565	693.735	739.923	781.431	782.669	832.334	979.732	989.199	1000.08
ω(scaled by 0.9776)[b]	534.141	550.978	566.582	678.196	723.349	763.927	765.137	813.69	957.786	967.041	977.679
$\|\Delta\|$(PBE0)	0.146159	0.91435	0.136104	0.010738	0.043847	0.018349	0.763866	0.043113	0.129698	0.013440	0.196380
$\|\Delta\|$(B3LYP)	0.063614	0.783819	0.133009	0.009762	0.042695	0.020893	1.059601	0.041364	0.142885	0.011189	0.092356
$\|\Delta\|$(CAMB3LYP)	0.196065	0.919800	0.136600	0.009110	0.051598	0.019861	0.706915	0.054089	0.201697	0.022553	0.143957
$\|\Delta\|$(LC-BLYP)	0.201992	0.924040	0.141260	0.010372	0.052689	0.019792	0.673838	0.054552	0.256865	0.024173	0.136832
$\|\Delta\|$(BHHLYP)[a]	0.205944	1.345496	0.000338	0.000111	0.000024	0.000107	0.371322	0.000224	0.223651	0.000139	0.323438
ω(B3LYP)	543.147	559.617	573.061	687.073	733.794	768.991	770.933	827.503	963.362	984.946	993.052
ω(scaled by 0.9891)[c]	537.227	553.517	566.815	679.584	725.796	760.609	762.53	818.483	952.861	974.21	982.228
$\|\Delta\|$(PBE0)	0.217771	1.017692	0.264820	0.012500	0.05600	0.450405	0.050261	0.021445	0.054991	0.005047	0.316457
$\|\Delta\|$(B3LYP)	0.126545	0.877122	0.265097	0.012898	0.055085	0.759209	0.079125	0.021353	0.075531	0.005342	0.219535
$\|\Delta\|$(CAMB3LYP)	0.260547	1.022934	0.275816	0.012183	0.060015	0.391592	0.049564	0.028605	0.139238	0.000367	0.262551
$\|\Delta\|$(LC-BLYP)	0.264623	1.027792	0.282998	0.013866	0.060723	0.357192	0.046141	0.027456	0.198337	0.000432	0.259318
$\|\Delta\|$(BHHLYP)[a]	0.243746	1.437928	0.002777	0.000016	0.002611	0.055956	0.000743	0.000254	0.142750	0.002902	0.416476

[a] Determined by SF-TD-DFT using the Tamm Dancoff approximation and numerical gradients.
[b] Ref. 160
[c] Ref. 161

Table A7: *Vibrational Frequencies (ω/cm^{-1}) Higher Than 1000 cm^{-1} and Dimensionless Displacements ($|\Delta|$)of Uracil in the Implicit Water for the S_1 Excited State. All Computations use the aug-cc-pVTZ Basis Set.*

modes	17	18	19	20	21	22	23	24	25	26
ω(PBE0)	1098.76	1211.20	1242.92	1391.36	1419.66	1432.35	1517.87	1695.66	1798.44	1831.32
ω(scaled by 0.9568)[b]	1051.29	1158.87	1189.23	1331.25	1358.34	1370.47	1452.3	1622.41	1720.75	1752.21
$\|\Delta\|$(PBE0)	0.27423	0.173999	0.737523	0.578705	0.090813	0.192717	0.354224	0.868798	0.785196	0.516386
$\|\Delta\|$(B3LYP)	0.319167	0.196722	0.706531	0.552503	0.074100	0.223895	0.379718	0.798802	0.807141	0.593296
$\|\Delta\|$(CAMB3LYP)	0.211588	0.155299	0.844740	0.656272	0.107808	0.173902	0.337909	0.968857	0.835657	0.412577
$\|\Delta\|$(LC-BLYP)	0.191585	0.158285	0.901621	0.693352	0.115630	0.170390	0.289981	0.976556	0.883590	0.427514
$\|\Delta\|$(BHHLYP)[a]	0.143592	0.314089	1.116473	0.792938	0.168581	0.108118	0.362417	1.076174	0.560190	0.151412
ω(B3LYP)	1086.31	1191.50	1226.93	1381.34	1404.29	1421.25	1496.67	1670.17	1758.84	1791.36
ω(scaled by 0.9676)[c]	1051.11	1152.90	1187.19	1336.59	1358.79	1375.21	1448.18	1616.07	1701.86	1733.32
$\|\Delta\|$(PBE0)	0.154192	0.62491	0.639175	0.386636	0.305824	0.264218	0.242962	0.867699	0.777192	0.487194
$\|\Delta\|$(B3LYP)	0.207479	0.629974	0.599022	0.347443	0.330078	0.268715	0.264904	0.794610	0.798545	0.566570
$\|\Delta\|$(CAMB3LYP)	0.070169	0.672566	0.749408	0.459448	0.307190	0.269427	0.224201	0.972727	0.833200	0.381454
$\|\Delta\|$(LC-BLYP)	0.037538	0.706781	0.800835	0.495270	0.306663	0.276206	0.175432	0.980436	0.883537	0.396585
$\|\Delta\|$(BHHLYP)[a]	0.069674	0.944234	0.918472	0.599448	0.256960	0.310762	0.300503	1.086118	0.543420	0.114895

[a] Determined by SF-TD-DFT using the Tamm Dancoff approximation and numerical gradients.
[b] Ref. 160
[c] Ref. 161

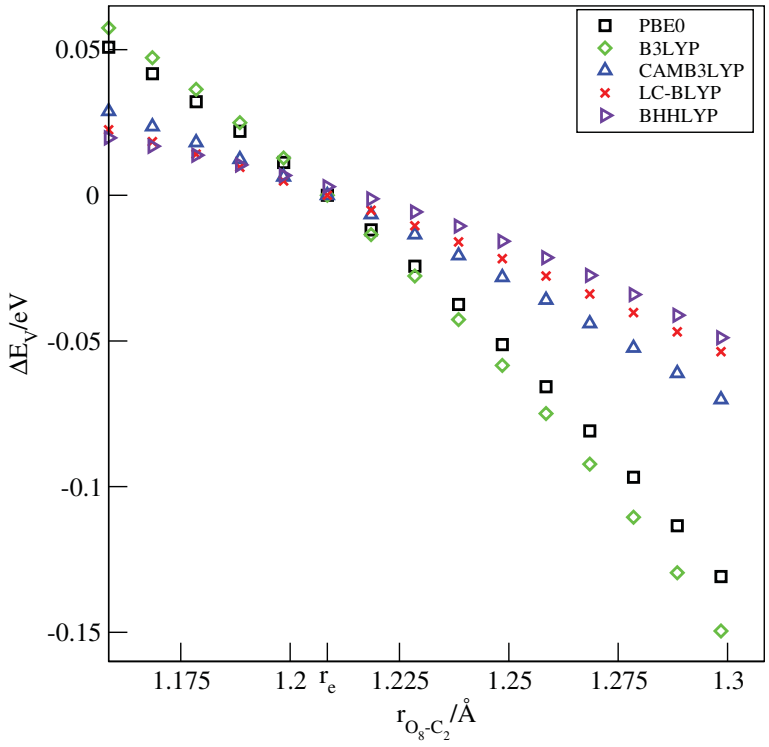

Figure A1: *The relative vertical excitation energy* $\Delta E_V(S_2)$ *along the* O_8-C_2 *bond.* $r_e = 1.208501$Å *indicates the ground state equilibrium bond length of* O_8-C_2.

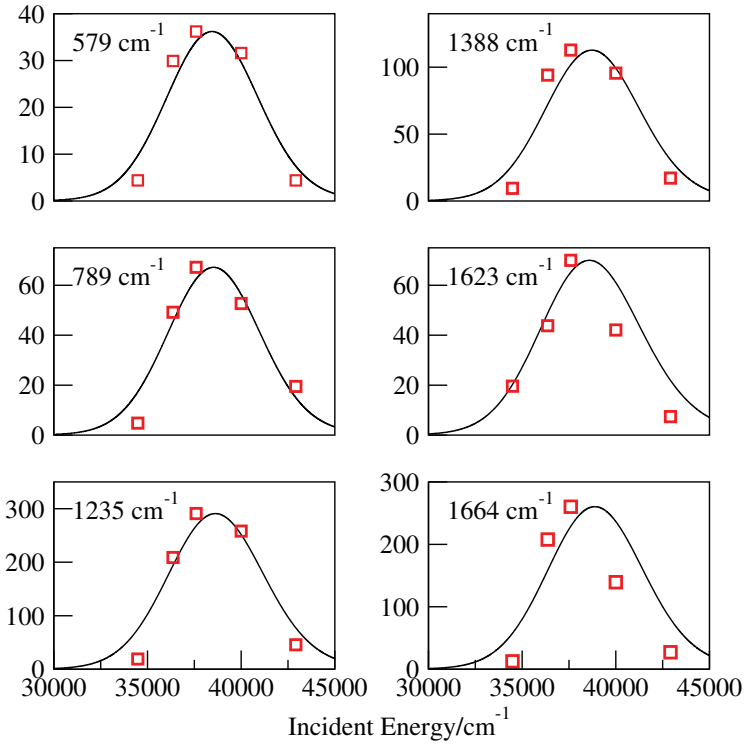

Figure A2: *The theoretical (black line) and experimental[43] (red square) resonance Raman excitation profiles of uracil in the gas phase. The theoretical excitation profile is computed at the PBE0/CAMB3LYP/aug-cc-pVTZ level of theory. The theoretical excitation profiles are scaled such that the maxima are same as experiments.*

Appendix B

Appendix to Chapter 3

Table B1: *Cartesian Coordinates of 5-Halogenated Uracils Optimized in H_2O (C-PCM) at the PBE0/aug-cc-pVTZ Level of Theory.*

	5-fluorouracil		
C	1.19914	0.33679	0.00000
C	1.13808	-1.00145	0.00000
N	-0.06709	-1.63969	0.00000
C	-1.27164	-0.98792	0.00000
N	-1.15726	0.38364	0.00000
C	0.00000	1.14616	0.00000
O	-2.34244	-1.56269	0.00000
O	-0.03403	2.36245	0.00000
H	2.02226	-1.62275	0.00000
H	-0.10265	-2.64640	0.00000
H	-2.02929	0.89401	0.00000
F	2.36650	0.97866	0.00000
	5-chlorouracil		
C	0.00000	0.89771	0.00000
C	-1.29321	0.52604	0.00000
N	-1.65321	-0.78398	0.00000
C	-0.75298	-1.81980	0.00000
N	0.55642	-1.40571	0.00000
C	1.04753	-0.10791	0.00000
O	-1.08261	-2.98836	0.00000
O	2.24425	0.10519	0.00000
H	-2.10297	1.24183	0.00000

H	-2.62868	-1.03764	0.00000
H	1.24794	-2.14239	0.00000
Cl	0.46236	2.55031	0.00000
	5-bromouracil		
C	0.00000	0.35821	0.00000
C	1.34587	0.37934	0.00000
N	2.07257	-0.76806	0.00000
C	1.51364	-2.02199	0.00000
N	0.14106	-2.00796	0.00000
C	-0.70780	-0.90923	0.00000
O	2.17078	-3.04281	0.00000
O	-1.91406	-1.05997	0.00000
H	1.91506	1.29811	0.00000
H	3.07961	-0.72720	0.00000
H	-0.30552	-2.91435	0.00000
Br	-1.00425	1.93599	0.00000

Table B2: *Equilibrium Geometries of 5-Halogenated Uracils as Determined in H_2O (C-PCM) at the PBE0/aug-cc-pVTZ Level of Theory.*

bond length /Å	5-fluorouracil	experiment[d]	5-chlorouracil	experiment[e]	5-bromouracil	experiment[f]	$\lvert\Delta r\rvert$[b]	$\lvert\Delta r\rvert$[c]
$r(C_5\text{-}C_6)$	1.3396	1.35	1.3456	1.370	1.3460	1.355	0.0060	0.0064
$r(C_5\text{-}C_4)$	1.4467	1.46	1.4521	1.432	1.4517	1.443	0.0054	0.0050
$r(C_5\text{-}X_{11})$[a]	1.3322	1.36	1.7161	1.715	1.8703	1.867	0.3839	0.5381
$r(C_6\text{-}N_1)$	1.3637	1.39	1.3586	1.374	1.3582	1.372	0.0051	0.0055
$r(C_6\text{-}H_{12})$	1.0806		1.0808	0.96	1.0808	0.96	0.0002	0.0002
$r(N_1\text{-}C_2)$	1.3696	1.40	1.3723	1.363	1.3729	1.358	0.0027	0.0033
$r(N_1\text{-}H_7)$	1.0073		1.0079	1.03	1.0079	0.81	0.0006	0.0006
$r(C_2\text{-}N_3)$	1.3763	1.40	1.3733	1.359	1.3726	1.372	0.0030	0.0037
$r(C_2\text{-}O_8)$	1.2153	1.20	1.2142	1.227	1.214	1.224	0.0011	0.0013
$r(N_3\text{-}C_4)$	1.3859	1.39	1.3876	1.386	1.3884	1.389	0.0017	0.0025
$r(N_3\text{-}H_9)$	1.0104		1.0104	0.85	1.0104	0.94	0.0000	0.0000
$r(C_4\text{-}O_{10})$	1.2168	1.24	1.2155	1.238	1.2156	1.231	0.0013	0.0012
RMSD		0.01		0.02		0.003		
bond angle /°	5-fluorouracil	experiment[d]	5-chlorouracil	experiment[e]	5-bromouracil	experiment[f]	$\lvert\Delta\theta\rvert$[b]	$\lvert\Delta\theta\rvert$[c]
$\theta(C_6\text{-}C_5\text{-}C_4)$	121.4057	125	120.1343	120.6	120.0803	120.4	1.2714	1.3254
$\theta(C_6\text{-}C_5\text{-}X_{11})$[a]	121.4162	122	121.6652	120.6	121.5771	120.4	0.2490	0.1609
$\theta(C_4\text{-}C_5\text{-}X_{11})$[a]	117.1781	113	118.2005	118.8	118.3426	119.2	1.0224	1.1645
$\theta(C_5\text{-}C_6\text{-}N_1)$	120.5172	118	121.4007	119.3	121.4485	120.4	0.8835	0.9313
$\theta(C_5\text{-}C_6\text{-}H_{12})$	122.4832		122.4897		122.6778		0.0065	0.1946
$\theta(N_1\text{-}C_6\text{-}H_{12})$	116.9996		116.1096		115.8737		0.8900	1.1259
$\theta(C_6\text{-}N_1\text{-}C_2)$	123.6777	122	123.6403	123.4	123.6275	123.3	0.0374	0.0502
$\theta(C_6\text{-}N_1\text{-}H_7)$	119.9282		119.9418		120.0245		0.0136	0.0963
$\theta(C_2\text{-}N_1\text{-}H_7)$	116.3941		116.4179		116.348		0.0238	0.0461
$\theta(N_1\text{-}C_2\text{-}N_3)$	113.6501	116	113.4447	115.4	113.4389	115.2	0.2054	0.2112
$\theta(N_1\text{-}C_2\text{-}O_8)$	123.3571	121	123.2533	122.2	123.2038	122.8	0.1038	0.1533
$\theta(N_3\text{-}C_2\text{-}O_8)$	122.9928	123	123.302	122.5	123.3573	122.0	0.3092	0.3645
$\theta(C_2\text{-}N_3\text{-}C_4)$	128.1482	127	128.2766	126.4	128.2746	126.6	0.1284	0.1264
$\theta(C_2\text{-}N_3\text{-}H_9)$	115.5719		115.6395		115.6436		0.0676	0.0717
$\theta(C_4\text{-}N_3\text{-}H_9)$	116.2799		116.0839		116.0818		0.1960	0.1981
$\theta(C_5\text{-}C_4\text{-}N_3)$	112.6011	112	113.1034	114.9	113.1302	114.1	0.5023	0.5291
$\theta(C_5\text{-}C_4\text{-}O_{10})$	125.6207	126	126.0723	125.7	126.3039	125.8	0.4516	0.6832

θ(N_3-C_4-O_{10})	121.7781	122	120.8243	119.4	120.5659	120.1	0.9538	1.2122
RMSD		3.59		1.06		0.86		
dihedral angle /°	5-fluorouracil		5-chlorouracil		5-bromouracil		$\lvert\Delta\phi\rvert$[b]	$\lvert\Delta\phi\rvert$[c]
ϕ(C_4-C_5-C_6-N_1)	0.0		0.0		0.0		0	0
ϕ(C_4-C_5-C_6-H_{12})	180.0		180.0		180.0		0	0
ϕ(X_{11}-C_5-C_6-N_1)[a]	180.0		180.0		180.0		0	0
ϕ(X_{11}-C_5-C_6-H_{12})[a]	0.0		0.0		0.0		0	0
ϕ(C_6-C_5-C_4-N_3)	0.0		0.0		0.0		0	0
ϕ(C_6-C_5-C_4-O_{10})	180.0		180.0		180.0		0	0
ϕ(X_{11}-C_5-C_4-N_3)[a]	180.0		180.0		180.0		0	0
ϕ(X_{11}-C_5-C_4-O_{10})[a]	0.0		0.0		0.0		0	0
ϕ(C_5-C_6-N_1-C_2)	0.0		0.0		0.0		0	0
ϕ(C_5-C_6-N_1-H_7)	180.0		180.0		180.0		0	0
ϕ(H_{12}-C_6-N_1-C_2)	180.0		180.0		180.0		0	0
ϕ(H_{12}-C_6-N_1-H_7)	0.0		0.0		0.0		0	0
ϕ(C_6-N_1-C_2-N_3)	0.0		0.0		0.0		0	0
ϕ(C_6-N_1-C_2-O_8)	180.0		180.0		180.0		0	0
ϕ(H_7-N_1-C_2-N_3)	180.0		180.0		180.0		0	0
ϕ(H_7-N_1-C_2-O_8)	0.0		0.0		0.0		0	0
ϕ(N_1-C_2-N_3-C_4)	0.0		0.0		0.0		0	0
ϕ(N_1-C_2-N_3-H_9)	180.0		180.0		180.0		0	0
ϕ(O_8-C_2-N_3-C_4)	180.0		180.0		180.0		0	0
ϕ(O_8-C_2-N_3-H_9)	0.0		0.0		0.0		0	0
ϕ(C_2-N_3-C_4-C_5)	0.0		0.0		0.0		0	0
ϕ(C_2-N_3-C_4-O_{10})	180.0		180.0		180.0		0	0
ϕ(H_9-N_3-C_4-C_5)	180.0		180.0		180.0		0	0
ϕ(H_9-N_3-C_4-O_{10})	0.0		0.0		0.0		0	0

[a] X=F, Cl, Br.
[b] Difference between 5-chlorouracil and 5-fluorouracil.
[c] Difference between 5-bromouracil and 5-fluorouracil.
[d] Crystal structure of 5-fluorouracil in Ref. 221.
[e] Crystal structure of 5-chlorouracil in Ref. 222.
[f] Crystal structure of 5-bromouracil in Ref. 222.

Table B3: *Potential Energy Distribution Analysis and Vibrational Frequencies (ω/cm^{-1}) of Ground State Normal Modes of 5-Fluorouracil at the PBE0/aug-cc-pVTZ level of theory in H_2O (C-PCM).*

mode	ω	PED
8	545	+stretch(O_8C_2)[2%]+stretch($O_{10}C_4$)[1%]+stretch(C_5C_6)[2%]+stretch(N_1C_6)[1%]
		+stretch(N_3C_2)[7%]+stretch(N_3C_4)[13%]+stretch($F_{11}C_5$)[1%]+bend($C_4N_3C_2$)[1%]
		-bend($H_9N_3C_4$)[1%]-bend($H_{12}C_6C_5$)[1%]-bend($O_8C_2N_3$)[1%]+bend($O_{10}C_4N_3$)[25%]
		+bend($C_5C_6N_1$)[5%]-bend($C_6N_1C_2$)[16%]-bend($N_3C_2N_1$)[22%]+bend($F_{11}C_5C_4$)[1%]
9	585	+torsion($H_7N_1C_6C_5$)[94%]+torsion($H_9N_3C_4C_5$)[4%]-out-of-plane($O_{10}N_3C_5C_4$)[2%]
10	637	-stretch($O_{10}C_4$)[1%]-stretch(C_5C_6)[5%]+stretch(N_1C_2)[4%]-stretch(N_3C_2)[1%]
		-bend($C_4N_3C_2$)[12%]-bend($H_7N_1C_6$)[1%]+bend($H_9N_3C_4$)[2%]-bend($O_8C_2N_3$)[27%]
		+bend($O_{10}C_4N_3$)[15%]-bend($C_5C_6N_1$)[1%]+bend($C_6N_1C_2$)[1%]-bend($N_3C_2N_1$)[1%]
		+bend($F_{11}C_5C_4$)[28%]
11	662	-torsion($H_7N_1C_6C_5$)[4%]+torsion($H_9N_3C_4C_5$)[90%]+torsion($H_{12}C_6C_5C_4$)[2%]
		-torsion($C_5C_6N_1C_2$)[1%]+torsion($N_3C_2N_1C_6$)[2%]-out-of-plane($O_8N_1N_3C_2$)[1%]
		-out-of-plane($F_{11}C_6C_4C_5$)[1%]
12	762	+stretch($O_{10}C_4$)[2%]+stretch(C_5C_6)[1%]+stretch(N_1C_6)[8%]+stretch(N_1C_2)[17%]
		+stretch(N_3C_2)[9%]+stretch(N_3C_4)[2%]+stretch($F_{11}C_5$)[7%]-bend($C_4N_3C_2$)[12%]
		+bend($H_9N_3C_4$)[1%]-bend($O_8C_2N_3$)[2%]-bend($C_5C_6N_1$)[10%]+bend($C_6N_1C_2$)[5%]
		+bend($N_3C_2N_1$)[22%]-bend($F_{11}C_5C_4$)[1%]
13	772	+torsion($H_9N_3C_4C_5$)[1%]+torsion($C_5C_6N_1C_2$)[3%]-torsion($N_3C_2N_1C_6$)[5%]
		+torsion($C_4N_3C_2N_1$)[3%]+out-of-plane($O_8N_1N_3C_2$)[90%]
14	789	+torsion($H_7N_1C_6C_5$)[1%]-torsion($H_9N_3C_4C_5$)[1%]-torsion($H_{12}C_6C_5C_4$)[3%]

		+torsion($C_5C_6N_1C_2$)[1%]+out-of-plane($O_{10}N_3C_5C_4$)[80%]+out-of-plane($F_{11}C_6C_4C_5$)[15%]
15	826	-stretch(O_8C_2)[8%]-stretch($O_{10}C_4$)[2%]+stretch(C_5C_6)[3%]-stretch(N_1C_6)[1%] -stretch(N_1C_2)[8%]-stretch(N_3C_2)[6%]-stretch(N_3C_4)[2%]+stretch($F_{11}C_5$)[19%] -bend($C_4N_3C_2$)[11%]+bend($H_7N_1C_6$)[2%]+bend($H_9N_3C_4$)[2%]-bend($H_{12}C_6C_5$)[1%] -bend($O_8C_2N_3$)[1%]+bend($O_{10}C_4N_3$)[2%]+bend($C_5C_6N_1$)[25%]-bend($C_6N_1C_2$)[1%] +bend($N_3C_2N_1$)[6%]+bend($F_{11}C_5C_4$)[1%]
16	942	+torsion($H_{12}C_6C_5C_4$)[75%]+torsion($C_5C_6N_1C_2$)[11%]-torsion($N_3C_2N_1C_6$)[4%] -torsion($C_4N_3C_2N_1$)[1%]+out-of-plane($F_{11}C_6C_4C_5$)[8%]
17	995	-stretch($O_{10}C_4$)[2%]+stretch(N_1C_6)[1%]+stretch(N_1C_2)[21%]+stretch(N_3C_2)[12%] -stretch(N_3C_4)[1%]-bend($C_4N_3C_2$)[12%]+bend($H_7N_1C_6$)[1%]-bend($H_9N_3C_4$)[6%] -bend($H_{12}C_6C_5$)[10%]+bend($O_8C_2N_3$)[1%]-bend($O_{10}C_4N_3$)[6%]+bend($C_5C_6N_1$)[5%] -bend($C_6N_1C_2$)[17%]+bend($N_3C_2N_1$)[4%]
18	1185	-stretch(C_5C_6)[1%]-stretch(N_1C_6)[26%]+stretch(N_1C_2)[3%]+stretch(N_3C_2)[3%] +stretch(N_3C_4)[6%]-stretch($F_{11}C_5$)[5%]-bend($H_7N_1C_6$)[23%]+bend($H_{12}C_6C_5$)[13%] -bend($O_8C_2N_3$)[3%]-bend($O_{10}C_4N_3$)[4%]+bend($C_5C_6N_1$)[10%]-bend($F_{11}C_5C_4$)[2%]
19	1227	+stretch(N_1C_2)[1%]-stretch(N_3C_2)[18%]+stretch(N_3C_4)[34%]-stretch($F_{11}C_5$)[4%] -bend($C_4N_3C_2$)[1%]+bend($H_7N_1C_6$)[3%]+bend($H_9N_3C_4$)[11%]-bend($H_{12}C_6C_5$)[18%] -bend($O_{10}C_4N_3$)[4%]+bend($C_5C_6N_1$)[1%]-bend($C_6N_1C_2$)[1%]+bend($N_3C_2N_1$)[2%] -bend($F_{11}C_5C_4$)[2%]
20	1278	+stretch(C_5C_6)[1%]-stretch(N_1C_6)[27%]+stretch(N_1C_2)[3%]-stretch(N_3C_2)[8%] +stretch(N_3C_4)[1%]+stretch($F_{11}C_5$)[39%]+bend($C_4N_3C_2$)[2%]-bend($H_7N_1C_6$)[2%] -bend($C_5C_6N_1$)[8%]+bend($C_6N_1C_2$)[3%]-bend($N_3C_2N_1$)[5%]
21	1370	+stretch(C_5C_6)[16%]+stretch(N_1C_6)[1%]+stretch(N_1C_2)[2%]-stretch(N_3C_2)[9%]

		+stretch(N_3C_4)[4%]-stretch($F_{11}C_5$)[3%]+bend($C_4N_3C_2$)[1%]+bend($H_7N_1C_6$)[8%]
		-bend($H_9N_3C_4$)[2%]+bend($H_{12}C_6C_5$)[39%]+bend($O_8C_2N_3$)[1%]-bend($C_5C_6N_1$)[1%]
		-bend($C_6N_1C_2$)[6%]+bend($N_3C_2N_1$)[3%]+bend($F_{11}C_5C_4$)[5%]
22	1415	+stretch(O_8C_2)[6%]-stretch($O_{10}C_4$)[8%]+stretch(N_1C_6)[1%]+stretch(N_1C_2)[2%]
		+stretch(N_3C_2)[1%]-stretch(N_3C_4)[7%]+bend($C_4N_3C_2$)[2%]-bend($H_7N_1C_6$)[4%]
		+bend($H_9N_3C_4$)[59%]+bend($H_{12}C_6C_5$)[3%]+bend($O_8C_2N_3$)[5%]-bend($C_6N_1C_2$)[1%]
23	1454	+stretch(O_8C_2)[5%]-stretch($O_{10}C_4$)[3%]-stretch(N_1C_6)[5%]-stretch(N_1C_2)[12%]
		+stretch(N_3C_2)[10%]+stretch(N_3C_4)[4%]+stretch($F_{11}C_5$)[4%]-bend($C_4N_3C_2$)[8%]
		+bend($H_7N_1C_6$)[25%]+bend($H_9N_3C_4$)[3%]+bend($H_{12}C_6C_5$)[1%]-bend($O_8C_2N_3$)[7%]
		-bend($O_{10}C_4N_3$)[5%]-bend($C_5C_6N_1$)[3%]+bend($C_6N_1C_2$)[4%]+bend($N_3C_2N_1$)[1%]
24	1533	-stretch(O_8C_2)[7%]-stretch($O_{10}C_4$)[2%]+stretch(C_5C_6)[1%]+stretch(N_1C_6)[8%]
		-stretch(N_1C_2)[18%]+stretch(N_3C_4)[10%]+stretch($F_{11}C_5$)[2%]-bend($C_4N_3C_2$)[3%]
		-bend($H_7N_1C_6$)[23%]+bend($H_{12}C_6C_5$)[1%]-bend($O_{10}C_4N_3$)[2%]-bend($C_5C_6N_1$)[15%]
		+bend($C_6N_1C_2$)[5%]+bend($N_3C_2N_1$)[2%]
25	1730	-stretch(O_8C_2)[4%]+stretch($O_{10}C_4$)[15%]+stretch(C_5C_6)[47%]-stretch(N_1C_6)[3%]
		-stretch(N_3C_4)[2%]-stretch($F_{11}C_5$)[3%]-bend($C_4N_3C_2$)[2%]-bend($H_7N_1C_6$)[1%]
		+bend($H_9N_3C_4$)[4%]-bend($H_{12}C_6C_5$)[6%]-bend($C_5C_6N_1$)[1%]+bend($C_6N_1C_2$)[3%]
		-bend($N_3C_2N_1$)[4%]+bend($F_{11}C_5C_4$)[3%]
26	1740	-stretch(O_8C_2)[16%]+stretch($O_{10}C_4$)[40%]-stretch(C_5C_6)[18%]+stretch(N_1C_6)[2%]
		-stretch(N_3C_4)[1%]+stretch($F_{11}C_5$)[3%]+bend($H_7N_1C_6$)[4%]+bend($H_9N_3C_4$)[6%]
		+bend($H_{12}C_6C_5$)[4%]+bend($O_8C_2N_3$)[1%]-bend($O_{10}C_4N_3$)[2%]-bend($C_6N_1C_2$)[1%]
		-bend($N_3C_2N_1$)[3%]
27	1782	+stretch(O_8C_2)[49%]+stretch($O_{10}C_4$)[22%]-stretch(N_1C_2)[7%]-stretch(N_3C_2)[3%]

-bend($C_4N_3C_2$)[6%]-bend($H_7N_1C_6$)[3%]-bend($C_6N_1C_2$)[3%]+bend($N_3C_2N_1$)[5%]

Table B4: *Potential Energy Distribution Analysis and Vibrational Frequencies (ω/cm^{-1}) of Ground State Normal Modes of 5-Chlorouracil at the PBE0/aug-cc-pVTZ level of theory in H_2O (C-PCM).*

mode	ω	PED
8	549	+stretch(O_8C_2)[1%]+stretch($O_{10}C_4$)[2%]+stretch(C_5C_6)[2%]+stretch(N_3C_2)[12%]
		+stretch(N_3C_4)[14%]+stretch($Cl_{11}C_5$)[2%]+bend($C_4N_3C_2$)[9%]-bend($H_{12}C_6C_5$)[1%]
		-bend($O_8C_2N_3$)[2%]+bend($O_{10}C_4N_3$)[28%]+bend($C_5C_6N_1$)[1%]-bend($C_6N_1C_2$)[17%]
		-bend($N_3C_2N_1$)[7%]
9	611	+torsion($H_7N_1C_6C_5$)[89%]+torsion($H_9N_3C_4C_5$)[7%]-out-of-plane($O_{10}N_3C_5C_4$)[3%]
10	613	+stretch($O_{10}C_4$)[1%]+stretch(C_5C_6)[2%]-stretch(N_1C_6)[1%]-stretch(N_1C_2)[2%]
		+stretch(N_3C_2)[2%]+stretch($Cl_{11}C_5$)[1%]+bend($C_4N_3C_2$)[13%]+bend($H_7N_1C_6$)[2%]
		-bend($H_9N_3C_4$)[1%]+bend($O_8C_2N_3$)[27%]-bend($O_{10}C_4N_3$)[17%]+bend($C_5C_6N_1$)[2%]
		-bend($C_6N_1C_2$)[4%]+bend($N_3C_2N_1$)[8%]-bend($Cl_{11}C_5C_4$)[16%]
11	675	-torsion($H_7N_1C_6C_5$)[7%]+torsion($H_9N_3C_4C_5$)[87%]+torsion($H_{12}C_6C_5C_4$)[1%]
		-torsion($C_5C_6N_1C_2$)[1%]+torsion($N_3C_2N_1C_6$)[2%]-out-of-plane($O_8N_1N_3C_2$)[1%]
12	676	-stretch(O_8C_2)[1%]+stretch(C_5C_6)[1%]+stretch(N_1C_6)[1%]+stretch(N_1C_2)[3%]
		+stretch(N_3C_2)[1%]+stretch($Cl_{11}C_5$)[27%]-bend($C_4N_3C_2$)[10%]+bend($H_9N_3C_4$)[2%]
		-bend($O_8C_2N_3$)[4%]+bend($O_{10}C_4N_3$)[3%]-bend($C_5C_6N_1$)[6%]-bend($C_6N_1C_2$)[7%]
		+bend($N_3C_2N_1$)[33%]
13	773	-torsion($H_7N_1C_6C_5$)[1%]+torsion($H_9N_3C_4C_5$)[1%]+torsion($C_5C_6N_1C_2$)[2%]
		-torsion($N_3C_2N_1C_6$)[4%]+torsion($C_4N_3C_2N_1$)[2%]+out-of-plane($O_8N_1N_3C_2$)[88%]
		-out-of-plane($O_{10}N_3C_5C_4$)[3%]-out-of-plane($Cl_{11}C_6C_4C_5$)[1%]
14	787	+torsion($H_7N_1C_6C_5$)[1%]-torsion($H_{12}C_6C_5C_4$)[2%]+torsion($C_5C_6N_1C_2$)[3%]

		-torsion($N_3C_2N_1C_6$)[1%]+torsion($C_4N_3C_2N_1$)[2%]+out-of-plane($O_8N_1N_3C_2$)[3%]
		+out-of-plane($O_{10}N_3C_5C_4$)[79%]+out-of-plane($Cl_{11}C_6C_4C_5$)[9%]
15	797	+stretch(O_8C_2)[5%]+stretch($O_{10}C_4$)[3%]+stretch(C_5C_6)[1%]+stretch(N_1C_6)[4%]
		+stretch(N_1C_2)[24%]+stretch(N_3C_2)[12%]+stretch(N_3C_4)[5%]-stretch($Cl_{11}C_5$)[3%]
		+bend($C_4N_3C_2$)[5%]-bend($H_7N_1C_6$)[1%]-bend($O_{10}C_4N_3$)[1%]
		-bend($C_5C_6N_1$)[2%]+bend($C_6N_1C_2$)[19%]-bend($N_3C_2N_1$)[14%]
16	958	+torsion($H_{12}C_6C_5C_4$)[78%]+torsion($C_5C_6N_1C_2$)[12%]-torsion($N_3C_2N_1C_6$)[5%]
		-torsion($C_4N_3C_2N_1$)[1%]+out-of-plane($Cl_{11}C_6C_4C_5$)[5%]
17	999	+stretch($O_{10}C_4$)[1%]-stretch(N_1C_6)[1%]-stretch(N_1C_2)[21%]-stretch(N_3C_2)[12%]
		+stretch(N_3C_4)[1%]+bend($C_4N_3C_2$)[12%]-bend($H_7N_1C_6$)[1%]+bend($H_9N_3C_4$)[6%]
		+bend($H_{12}C_6C_5$)[9%]-bend($O_8C_2N_3$)[1%]+bend($O_{10}C_4N_3$)[6%]-bend($C_5C_6N_1$)[7%]
		+bend($C_6N_1C_2$)[17%]-bend($N_3C_2N_1$)[4%]
18	1102	-stretch(O_8C_2)[1%]+stretch(N_1C_6)[2%]-stretch(N_1C_2)[1%]+stretch(N_3C_4)[5%]
		-stretch($Cl_{11}C_5$)[23%]-bend($C_4N_3C_2$)[4%]+bend($H_9N_3C_4$)[4%]-bend($O_8C_2N_3$)[1%]
		-bend($O_{10}C_4N_3$)[1%]+bend($C_5C_6N_1$)[38%]-bend($C_6N_1C_2$)[8%]+bend($N_3C_2N_1$)[11%]
19	1207	+stretch(C_5C_6)[2%]+stretch(N_1C_6)[51%]-stretch(N_1C_2)[2%]-stretch(N_3C_2)[1%]
		-stretch(N_3C_4)[4%]-stretch($Cl_{11}C_5$)[3%]+bend($C_4N_3C_2$)[1%]+bend($H_7N_1C_6$)[24%]
		-bend($H_{12}C_6C_5$)[6%]+bend($O_8C_2N_3$)[1%]+bend($O_{10}C_4N_3$)[2%]-bend($C_6N_1C_2$)[1%]
		+bend($N_3C_2N_1$)[1%]+bend($Cl_{11}C_5C_4$)[2%]
20	1233	-stretch(N_1C_6)[1%]-stretch(N_3C_2)[25%]+stretch(N_3C_4)[35%]+bend($H_7N_1C_6$)[3%]
		+bend($H_9N_3C_4$)[8%]-bend($H_{12}C_6C_5$)[19%]-bend($O_{10}C_4N_3$)[2%]-bend($C_5C_6N_1$)[1%]
		-bend($C_6N_1C_2$)[2%]+bend($N_3C_2N_1$)[2%]-bend($Cl_{11}C_5C_4$)[1%]
21	1360	+stretch(C_5C_6)[23%]+stretch(N_1C_2)[2%]-stretch(N_3C_2)[10%]+stretch(N_3C_4)[2%]

		+bend($C_4N_3C_2$)[2%]+bend($H_7N_1C_6$)[4%]-bend($H_9N_3C_4$)[2%]+bend($H_{12}C_6C_5$)[44%]
		+bend($O_8C_2N_3$)[1%]-bend($C_5C_6N_1$)[2%]-bend($C_6N_1C_2$)[4%]+bend($N_3C_2N_1$)[1%]
		+bend($Cl_{11}C_5C_4$)[2%]
22	1419	+stretch(O_8C_2)[6%]-stretch($O_{10}C_4$)[7%]+stretch(N_1C_6)[1%]+stretch(N_1C_2)[1%]
		+stretch(N_3C_2)[1%]-stretch(N_3C_4)[8%]+bend($C_4N_3C_2$)[1%]-bend($H_7N_1C_6$)[5%]
		+bend($H_9N_3C_4$)[62%]+bend($H_{12}C_6C_5$)[2%]+bend($O_8C_2N_3$)[5%]-bend($C_6N_1C_2$)[1%]
23	1442	-stretch(O_8C_2)[3%]+stretch($O_{10}C_4$)[3%]+stretch(N_1C_2)[19%]-stretch(N_3C_2)[12%]
		-stretch(N_3C_4)[7%]-stretch($Cl_{11}C_5$)[1%]+bend($C_4N_3C_2$)[9%]-bend($H_7N_1C_6$)[15%]
		-bend($H_9N_3C_4$)[3%]-bend($H_{12}C_6C_5$)[4%]+bend($O_8C_2N_3$)[7%]+bend($O_{10}C_4N_3$)[7%]
		+bend($C_5C_6N_1$)[5%]-bend($C_6N_1C_2$)[3%]-bend($N_3C_2N_1$)[3%]
24	1522	+stretch(O_8C_2)[9%]-stretch(N_1C_6)[15%]+stretch(N_1C_2)[12%]-stretch(N_3C_4)[8%]
		+bend($C_4N_3C_2$)[1%]+bend($H_7N_1C_6$)[36%]+bend($O_{10}C_4N_3$)[1%]+bend($C_5C_6N_1$)[13%]
		-bend($C_6N_1C_2$)[2%]-bend($N_3C_2N_1$)[2%]
25	1688	+stretch(C_5C_6)[64%]-stretch(N_1C_6)[7%]-stretch(N_1C_2)[2%]+stretch(N_3C_2)[1%]
		-stretch(N_3C_4)[1%]-stretch($Cl_{11}C_5$)[2%]-bend($C_4N_3C_2$)[1%]-bend($H_7N_1C_6$)[3%]
		+bend($H_9N_3C_4$)[1%]-bend($H_{12}C_6C_5$)[13%]-bend($C_5C_6N_1$)[2%]+bend($C_6N_1C_2$)[1%]
		-bend($N_3C_2N_1$)[1%]+bend($Cl_{11}C_5C_4$)[1%]
26	1738	-stretch(O_8C_2)[13%]+stretch($O_{10}C_4$)[65%]+stretch(N_1C_2)[1%]+stretch(N_3C_2)[1%]
		-stretch(N_3C_4)[1%]-bend($C_4N_3C_2$)[2%]+bend($H_7N_1C_6$)[1%]+bend($H_9N_3C_4$)[9%]
		-bend($O_{10}C_4N_3$)[1%]+bend($C_6N_1C_2$)[1%]-bend($N_3C_2N_1$)[4%]
27	1782	+stretch(O_8C_2)[60%]+stretch($O_{10}C_4$)[16%]-stretch(N_1C_2)[6%]-stretch(N_3C_2)[4%]
		-bend($C_4N_3C_2$)[5%]-bend($H_7N_1C_6$)[4%]-bend($C_6N_1C_2$)[2%]+bend($N_3C_2N_1$)[3%]

Table B5: *Potential Energy Distribution Analysis and Vibrational Frequencies (ω/cm^{-1}) of Ground State Normal Modes of 5-Bromouracil at the PBE0/aug-cc-pVTZ level of theory in H_2O (C-PCM).*

mode	ω	PED
8	547	+stretch(O_8C_2)[1%]+stretch($O_{10}C_4$)[2%]+stretch(C_5C_6)[2%]+stretch(N_3C_2)[13%]
		+stretch(N_3C_4)[11%]+stretch($Br_{11}C_5$)[3%]+bend($C_4N_3C_2$)[13%]-bend($H_{12}C_6C_5$)[1%]
		-bend($O_8C_2N_3$)[2%]+bend($O_{10}C_4N_3$)[28%]+bend($C_5C_6N_1$)[3%]-bend($C_6N_1C_2$)[17%]
		-bend($N_3C_2N_1$)[2%]-bend($Br_{11}C_5C_4$)[1%]
9	605	+stretch(O_8C_2)[1%]-stretch($O_{10}C_4$)[2%]-stretch(C_5C_6)[1%]+stretch(N_1C_6)[2%]
		+stretch(N_1C_2)[1%]-stretch(N_3C_2)[2%]-stretch($Br_{11}C_5$)[2%]-bend($C_4N_3C_2$)[9%]
		-bend($H_7N_1C_6$)[2%]+bend($H_9N_3C_4$)[1%]-bend($O_8C_2N_3$)[25%]+bend($O_{10}C_4N_3$)[16%]
		+bend($C_6N_1C_2$)[5%]-bend($N_3C_2N_1$)[18%]+bend($Br_{11}C_5C_4$)[13%]
10	609	+torsion($H_7N_1C_6C_5$)[90%]+torsion($H_9N_3C_4C_5$)[6%]-out-of-plane($O_{10}N_3C_5C_4$)[3%]
11	639	-stretch(O_8C_2)[2%]+stretch(N_1C_2)[2%]-stretch(N_3C_4)[1%]+stretch($Br_{11}C_5$)[24%]
		-bend($C_4N_3C_2$)[8%]+bend($H_9N_3C_4$)[3%]-bend($O_8C_2N_3$)[10%]+bend($O_{10}C_4N_3$)[7%]
		-bend($C_5C_6N_1$)[4%]-bend($C_6N_1C_2$)[6%]+bend($N_3C_2N_1$)[31%]-bend($Br_{11}C_5C_4$)[1%]
12	676	-torsion($H_7N_1C_6C_5$)[6%]+torsion($H_9N_3C_4C_5$)[88%]+torsion($H_{12}C_6C_5C_4$)[1%]
		-torsion($C_5C_6N_1C_2$)[1%]+torsion($N_3C_2N_1C_6$)[2%]-out-of-plane($O_8N_1N_3C_2$)[1%]
13	774	-torsion($H_7N_1C_6C_5$)[1%]+torsion($H_9N_3C_4C_5$)[1%]+torsion($C_5C_6N_1C_2$)[2%]
		-torsion($N_3C_2N_1C_6$)[4%]+torsion($C_4N_3C_2N_1$)[2%]+out-of-plane($O_8N_1N_3C_2$)[87%]
		-out-of-plane($O_{10}N_3C_5C_4$)[5%]-out-of-plane($Br_{11}C_6C_4C_5$)[1%]
14	787	+torsion($H_7N_1C_6C_5$)[1%]-torsion($H_{12}C_6C_5C_4$)[1%]+torsion($C_5C_6N_1C_2$)[4%]
		-torsion($N_3C_2N_1C_6$)[2%]+torsion($C_4N_3C_2N_1$)[3%]+out-of-plane($O_8N_1N_3C_2$)[6%]

		+out-of-plane($O_{10}N_3C_5C_4$)[77%]+out-of-plane($Br_{11}C_6C_4C_5$)[7%]
15	794	+stretch(O_8C_2)[4%]+stretch($O_{10}C_4$)[3%]+stretch(C_5C_6)[1%]+stretch(N_1C_6)[5%] +stretch(N_1C_2)[25%]+stretch(N_3C_2)[12%]+stretch(N_3C_4)[5%]-stretch($Br_{11}C_5$)[2%] +bend($C_4N_3C_2$)[4%]-bend($C_5C_6N_1$)[5%]+bend($C_6N_1C_2$)[21%]-bend($N_3C_2N_1$)[12%]
16	961	+torsion($H_{12}C_6C_5C_4$)[78%]+torsion($C_5C_6N_1C_2$)[12%]-torsion($N_3C_2N_1C_6$)[5%] -torsion($C_4N_3C_2N_1$)[1%]+out-of-plane($Br_{11}C_6C_4C_5$)[3%]
17	1001	-stretch($O_{10}C_4$)[1%]+stretch(N_1C_6)[1%]+stretch(N_1C_2)[21%]+stretch(N_3C_2)[12%] -stretch(N_3C_4)[1%]-bend($C_4N_3C_2$)[13%]+bend($H_7N_1C_6$)[1%]-bend($H_9N_3C_4$)[6%] -bend($H_{12}C_6C_5$)[8%]+bend($O_8C_2N_3$)[1%]-bend($O_{10}C_4N_3$)[6%]+bend($C_5C_6N_1$)[6%] -bend($C_6N_1C_2$)[17%]+bend($N_3C_2N_1$)[3%]
18	1074	-stretch(O_8C_2)[1%]+stretch(N_1C_6)[3%]-stretch(N_1C_2)[2%]+stretch(N_3C_4)[3%] -stretch($Br_{11}C_5$)[16%]-bend($C_4N_3C_2$)[4%]+bend($H_9N_3C_4$)[4%]-bend($H_{12}C_6C_5$)[1%] -bend($O_8C_2N_3$)[1%]-bend($O_{10}C_4N_3$)[1%]+bend($C_5C_6N_1$)[40%]-bend($C_6N_1C_2$)[10%] +bend($N_3C_2N_1$)[13%]
19	1204	+stretch(C_5C_6)[2%]+stretch(N_1C_6)[51%]-stretch(N_1C_2)[3%]-stretch(N_3C_4)[10%] -stretch($Br_{11}C_5$)[2%]+bend($C_4N_3C_2$)[1%]+bend($H_7N_1C_6$)[21%]-bend($H_9N_3C_4$)[1%] -bend($H_{12}C_6C_5$)[2%]+bend($O_8C_2N_3$)[1%]+bend($O_{10}C_4N_3$)[3%]-bend($C_5C_6N_1$)[1%] -bend($C_6N_1C_2$)[1%]+bend($N_3C_2N_1$)[1%]+bend($Br_{11}C_5C_4$)[2%]
20	1235	+stretch(N_1C_2)[1%]-stretch(N_3C_2)[26%]+stretch(N_3C_4)[29%]+bend($H_7N_1C_6$)[7%] +bend($H_9N_3C_4$)[7%]-bend($H_{12}C_6C_5$)[20%]-bend($O_{10}C_4N_3$)[1%]-bend($C_5C_6N_1$)[2%] -bend($C_6N_1C_2$)[2%]+bend($N_3C_2N_1$)[3%]
21	1361	+stretch(C_5C_6)[24%]+stretch(N_1C_2)[2%]-stretch(N_3C_2)[10%]+stretch(N_3C_4)[2%] +bend($C_4N_3C_2$)[2%]+bend($H_7N_1C_6$)[3%]-bend($H_9N_3C_4$)[2%]+bend($H_{12}C_6C_5$)[47%]

		+bend($O_8C_2N_3$)[1%]-bend($C_5C_6N_1$)[1%]-bend($C_6N_1C_2$)[3%]+bend($N_3C_2N_1$)[1%]
		+bend($Br_{11}C_5C_4$)[2%]
22	1418	+stretch(O_8C_2)[5%]-stretch($O_{10}C_4$)[7%]+stretch(N_1C_6)[1%]+stretch(N_1C_2)[2%]
		+stretch(N_3C_2)[1%]-stretch(N_3C_4)[8%]+bend($C_4N_3C_2$)[2%]-bend($H_7N_1C_6$)[6%]
		+bend($H_9N_3C_4$)[61%]+bend($H_{12}C_6C_5$)[2%]+bend($O_8C_2N_3$)[5%]-bend($C_6N_1C_2$)[1%]
23	1438	+stretch(O_8C_2)[3%]-stretch($O_{10}C_4$)[3%]+stretch(N_1C_6)[1%]-stretch(N_1C_2)[19%]
		+stretch(N_3C_2)[12%]+stretch(N_3C_4)[7%]-bend($C_4N_3C_2$)[10%]+bend($H_7N_1C_6$)[14%]
		+bend($H_9N_3C_4$)[4%]+bend($H_{12}C_6C_5$)[4%]-bend($O_8C_2N_3$)[7%]-bend($O_{10}C_4N_3$)[7%]
		-bend($C_5C_6N_1$)[4%]+bend($C_6N_1C_2$)[3%]+bend($N_3C_2N_1$)[3%]
24	1518	+stretch(O_8C_2)[9%]-stretch(N_1C_6)[16%]+stretch(N_1C_2)[12%]-stretch(N_3C_4)[8%]
		+bend($C_4N_3C_2$)[1%]+bend($H_7N_1C_6$)[37%]-bend($H_{12}C_6C_5$)[1%]+bend($O_{10}C_4N_3$)[1%]
		+bend($C_5C_6N_1$)[11%]-bend($C_6N_1C_2$)[2%]-bend($N_3C_2N_1$)[1%]
25	1681	+stretch(C_5C_6)[63%]-stretch(N_1C_6)[7%]-stretch(N_1C_2)[2%]+stretch(N_3C_2)[1%]
		-stretch(N_3C_4)[1%]-stretch($Br_{11}C_5$)[1%]-bend($C_4N_3C_2$)[1%]-bend($H_7N_1C_6$)[3%]
		+bend($H_9N_3C_4$)[1%]-bend($H_{12}C_6C_5$)[13%]-bend($O_8C_2N_3$)[1%]-bend($C_5C_6N_1$)[2%]
		+bend($C_6N_1C_2$)[2%]-bend($N_3C_2N_1$)[1%]+bend($Br_{11}C_5C_4$)[1%]
26	1736	-stretch(O_8C_2)[10%]+stretch($O_{10}C_4$)[68%]+stretch(N_1C_2)[1%]+stretch(N_3C_2)[1%]
		-stretch(N_3C_4)[1%]-bend($C_4N_3C_2$)[3%]+bend($H_7N_1C_6$)[1%]+bend($H_9N_3C_4$)[9%]
		-bend($O_{10}C_4N_3$)[1%]+bend($C_6N_1C_2$)[1%]-bend($N_3C_2N_1$)[4%]
27	1782	+stretch(O_8C_2)[62%]+stretch($O_{10}C_4$)[14%]-stretch(N_1C_2)[6%]-stretch(N_3C_2)[4%]
		-bend($C_4N_3C_2$)[5%]-bend($H_7N_1C_6$)[4%]-bend($C_6N_1C_2$)[2%]+bend($N_3C_2N_1$)[2%]

Table B6: *Vibrational Frequencies (ω/cm^{-1}) and Dimensionless Displacements ($|\Delta|$) for the S_1 Excited State of 5-Halogenated Uracils at the CAMB3LYP/aug-cc-pVTZ level of theory with the ground state equilibrium geometry determined using PBE0/aug-cc-pVTZ in H_2O (C-PCM).*

	modes	8	9	10	11	12	13	14	15	16	17	18	19
5-fluorouracil	ω	545	585	637	662	762	772	789	826	942	995	1185	1227
	$\|\Delta\|$	0.7051	0.0000	0.3025	0.0000	0.6311	0.0000	0.0000	0.5241	0.0000	0.0457	0.0253	0.5852
	modes	20	21	22	23	24	25	26	27				
	ω	1278	1370	1415	1454	1533	1730	1740	1782				
	$\|\Delta\|$	0.5348	0.9796	0.2126	0.0775	0.3863	1.1035	0.1935	0.2688				
	modes	8	9	10	11	12	13	14	15	16	17	18	19
5-chlorouracil	ω	549	611	613	675	676	773	787	797	958	999	1102	1207
	$\|\Delta\|$	0.5591	0.0000	0.4572	0.0000	0.2412	0.0000	0.0000	0.8020	0.0000	0.0733	0.0312	0.0216
	modes	20	21	22	23	24	25	26	27				
	ω	1233	1360	1419	1442	1522	1688	1738	1782				
	$\|\Delta\|$	0.6093	0.9867	0.2054	0.1840	0.3436	1.0617	0.2603	0.2945				
	modes	8	9	10	11	12	13	14	15	16	17	18	19
5-bromouracil	ω	547	605	609	639	676	774	787	794	961	1001	1074	1204
	$\|\Delta\|$	0.4571	0.4802	0.0000	0.1282	0.0000	0.0000	0.0000	0.8029	0.0000	0.1084	0.0243	0.0202
	modes	20	21	22	23	24	25	26	27				
	ω	1235	1361	1418	1438	1518	1681	1736	1782				
	$\|\Delta\|$	0.6261	0.9782	0.1603	0.1928	0.3367	1.0354	0.2775	0.2893				

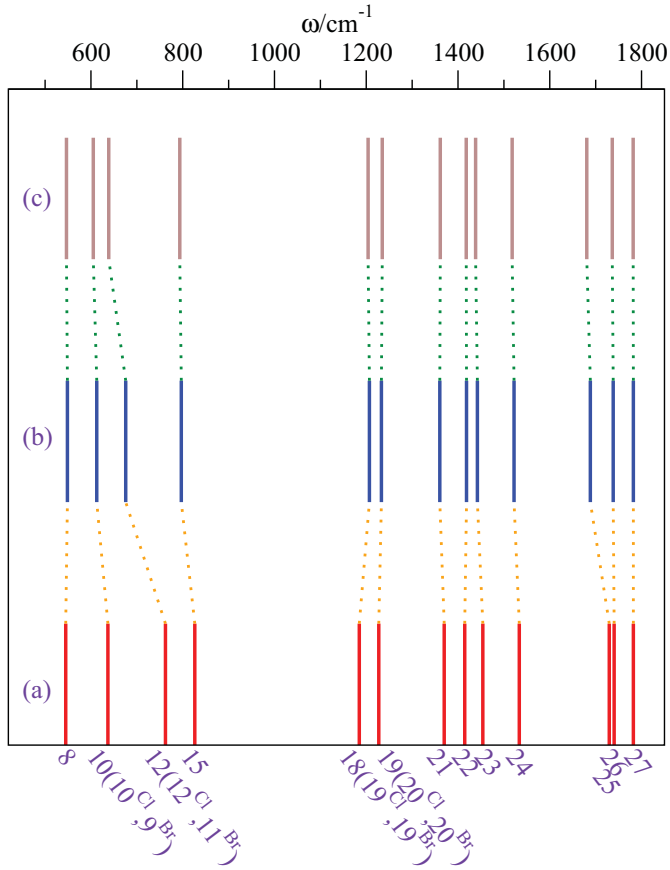

Figure B1: *Comparison between the ground state vibrational frequencies of (a) 5-fluorouracil (b) 5-chlorouracil and (c) 5-bromouracil. x-axis is vibrational mode numbered according to 5-fluorouracil, unless indicated otherwise, i.e.,* N^{Cl}, N^{Br}.

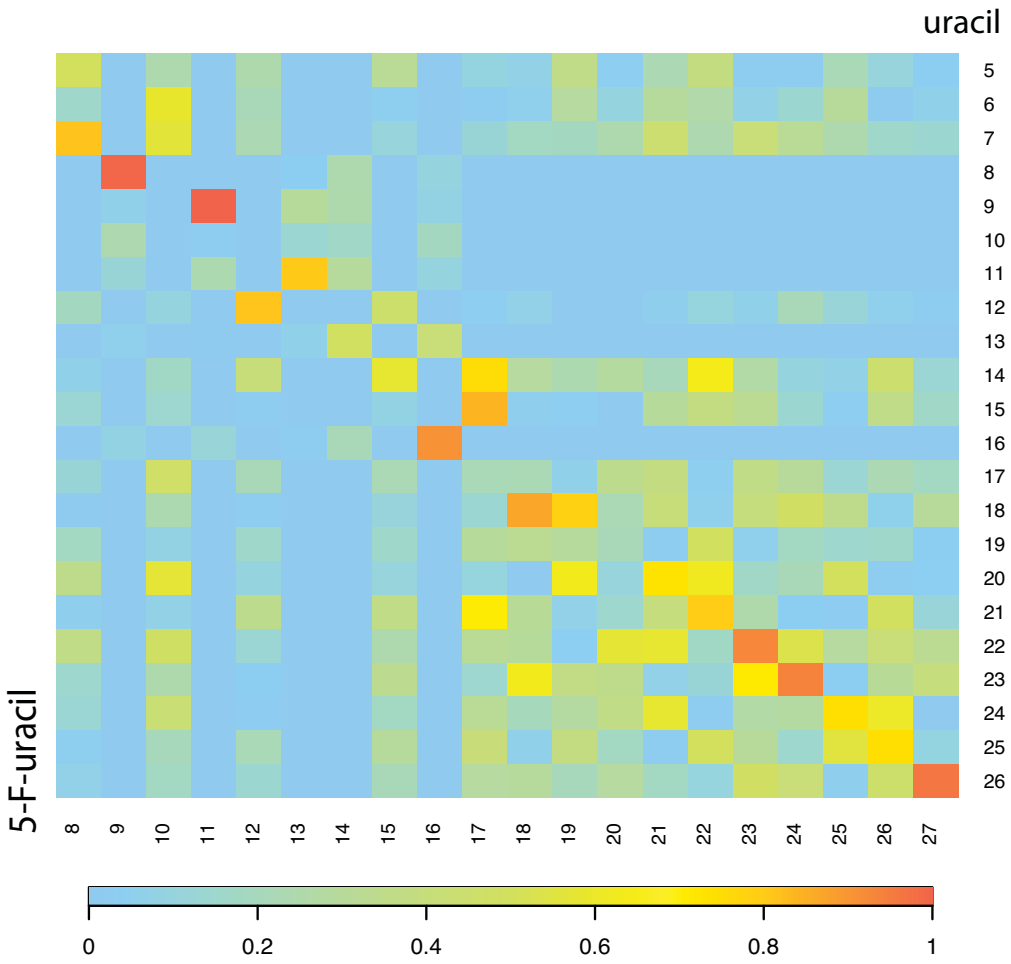

Figure B2: *The cosine similarity for the normal modes of 5-fluorouracil vs. uracil. x- and y-axes are corresponding vibrational mode numbering.*

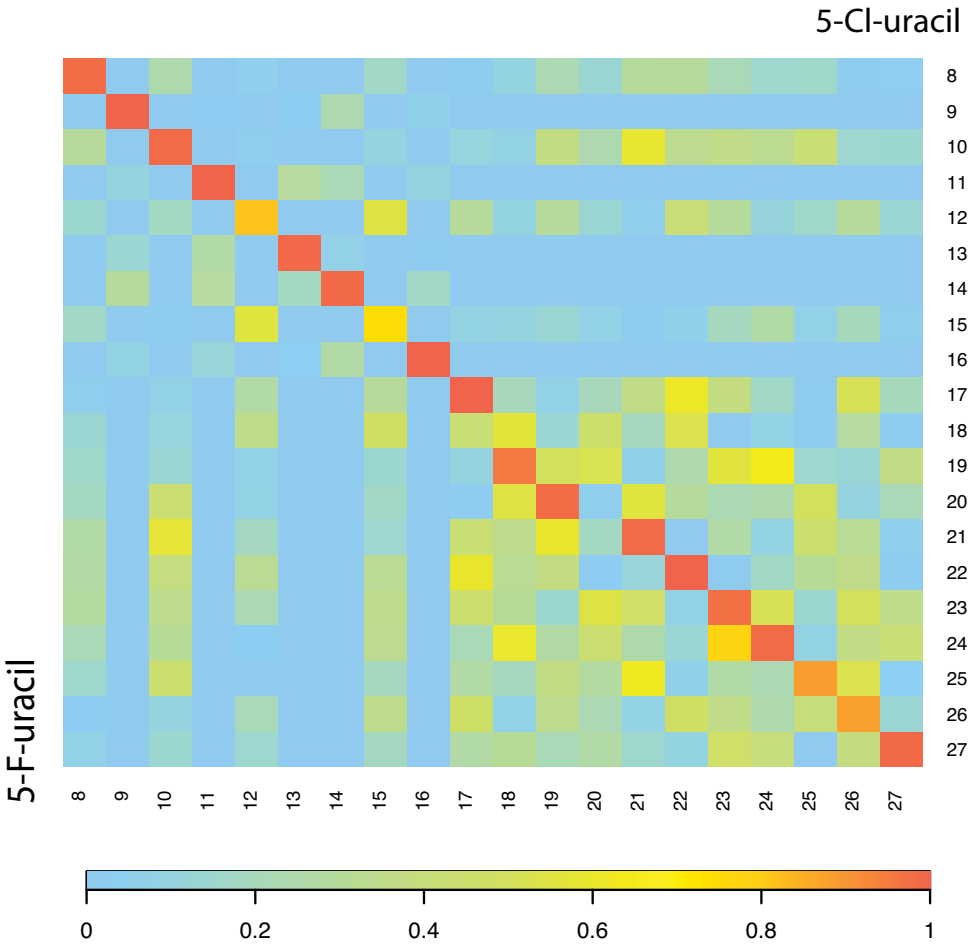

Figure B3: *The cosine similarity for the normal modes of 5-fluorouracil vs. 5-chlorouracil. x- and y-axes are corresponding vibrational mode numbering.*

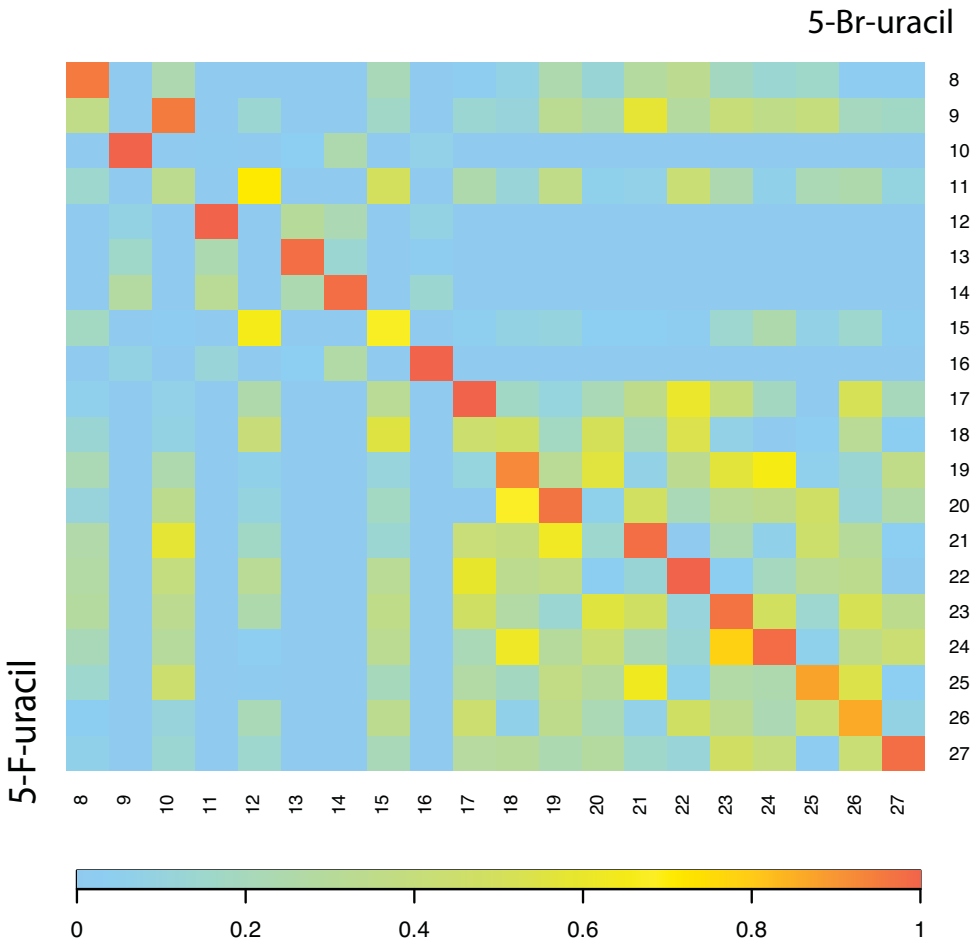

Figure B4: *The cosine similarity for the normal modes of 5-fluorouracil vs. 5-bromouracil. x- and y-axes are corresponding vibrational mode numbering.*

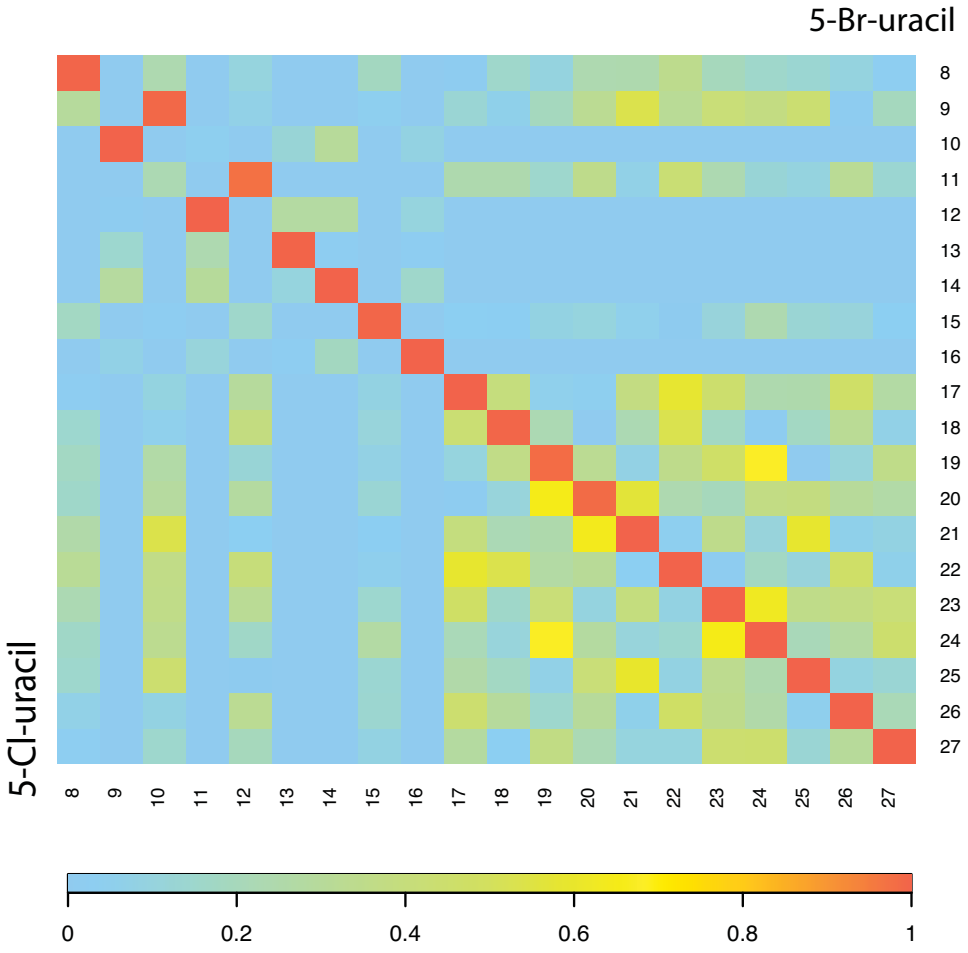

Figure B5: *The cosine similarity for the normal modes of 5-chlorouracil vs. 5-bromouracil. x- and y-axes are corresponding vibrational mode numbering.*

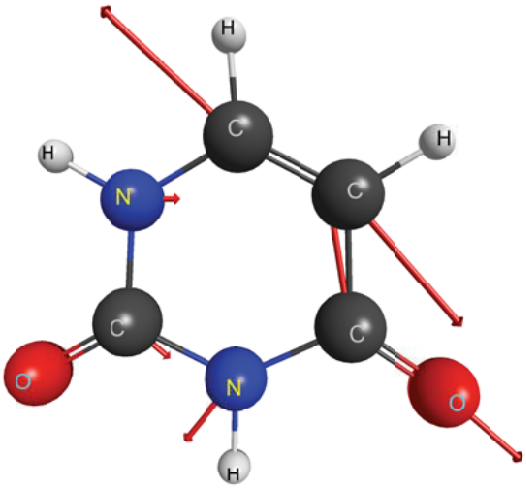

Figure B6: *Vectors illustrating the Cartesian gradients for each atom of uracil using TD-CAMB3LYP/aug-cc-pVTZ in H_2O (C-PCM) for the S_1 excited state.*

Appendix C

Appendix to Chapter 4

Table C1: *Equilibrium Geometries of Uracil in the Gas Phase, Implicit Water and with One Explicit Water Plus C-PCM as Determined using PBE0/aug-cc-pVTZ. See Figure 4.2 in the Main Text for the Corresponding Structures.*

bond length/Å	gas	implicit water	(A)	(B)	(C)
$r(C_2\text{-}N_3)$	1.3728	1.3713	1.3661	1.3706	1.3653
$r(C_2\text{-}O_8)$	1.2085	1.2162	1.2252	1.2159	1.2251
$r(C_4\text{-}C_5)$	1.4510	1.4418	1.4410	1.4370	1.4428
$r(C_4\text{-}O_{10})$	1.2109	1.2213	1.2209	1.2308	1.2212
$r(C_5\text{-}C_6)$	1.3414	1.3449	1.3459	1.3462	1.3442
$r(C_5\text{-}H_{11})$	1.0782	1.0783	1.0784	1.0782	1.0784
$r(C_6\text{-}H_{12})$	1.0822	1.0812	1.0814	1.0813	1.081
$r(N_1\text{-}C_2)$	1.3825	1.3726	1.3667	1.374	1.3672
$r(N_1\text{-}C_6)$	1.3644	1.3606	1.3594	1.3585	1.3621
$r(N_1\text{-}H_7)$	1.0054	1.0073	1.0194	1.0076	1.0074
$r(N_3\text{-}C_4)$	1.3993	1.3921	1.394	1.3847	1.3914
$r(N_3\text{-}H_9)$	1.0093	1.0100	1.0102	1.0197	1.0196
$r(O_{13}\text{-}H_{14})$			0.9601	0.9766	0.9736
$r(O_{13}\text{-}H_{15})$			0.9734	0.9599	0.96
bond angle/°	gas	implicit water	(A)	(B)	(C)
$\theta(C_2\text{-}N_1\text{-}C_6)$	123.48	123.3098	122.8347	123.3478	122.9683
$\theta(C_2\text{-}N_1\text{-}H_7)$	115.14	116.202	115.1733	116.2214	116.4522
$\theta(C_2\text{-}N_3\text{-}C_4)$	128.12	127.6366	127.2321	127.1096	127.0971
$\theta(C_2\text{-}N_3\text{-}H_9)$	115.62	115.7069	116.0215	116.8825	114.8826
$\theta(C_4\text{-}C_5\text{-}C_6)$	119.63	119.4371	119.4569	119.0647	119.4962
$\theta(C_4\text{-}C_5\text{-}H_{11})$	118.41	119.0727	118.9957	119.2961	119.0622
$\theta(C_4\text{-}N_3\text{-}H_9)$	116.25	116.6565	116.7464	116.0073	118.0198
$\theta(C_5\text{-}C_4\text{-}O_{10})$	126.16	126.1179	126.2991	125.3154	125.9521
$\theta(C_5\text{-}C_6\text{-}H_{12})$	122.53	122.6911	122.5998	122.7103	122.8181
$\theta(C_6\text{-}C_5\text{-}H_{11})$	121.96	121.4902	121.5474	121.6392	121.4416
$\theta(C_6\text{-}N_1\text{-}H_7)$	121.38	120.4882	121.9909	120.4308	120.5795
$\theta(N_1\text{-}C_2\text{-}N_3)$	113.12	113.6126	114.4397	113.7287	114.4757

θ(N_1-C_2-O_8)	122.71	123.0704	122.8451	122.9309	122.4293
θ(N_1-C_6-C_5)	122.04	121.9626	122.0716	121.8582	121.8059
θ(N_1-C_6-H_{12})	115.43	115.3463	115.3287	115.4315	115.376
θ(N_3-C_2-O_8)	124.17	123.317	122.7151	123.3404	123.095
θ(N_3-C_4-C_5)	113.60	114.0412	113.965	114.8909	114.1568
θ(N_3-C_4-O_{10})	120.24	119.8409	119.7359	119.7937	119.8911
θ(H_{14}-O_{13}-H_{15})			105.6669	105.675	105.5946
dihedral angle/°	gas	implicit water	(A)	(B)	(C)
ϕ(C_2-N_1-C_6-C_5)	0.0	0.0	0.0624	0.0342	-0.0343
ϕ(C_2-N_1-C_6-H_{12})	180.0	180.0	179.9498	179.9655	179.9685
ϕ(C_2-N_3-C_4-C_5)	0.0	0.0	0.0186	0.0196	0.0793
ϕ(C_2-N_3-C_4-O_{10})	180.0	180.0	179.9862	179.9898	179.9212
ϕ(C_4-C_5-C_6-H_{12})	180.0	180.0	179.9748	179.9679	179.9844
ϕ(C_4-N_3-C_2-O_8)	180.0	180.0	179.9774	179.9298	179.9825
ϕ(C_5-C_4-N_3-H_9)	180.0	180.0	179.9902	179.7292	179.8073
ϕ(C_5-C_6-N_1-H_7)	180.0	180.0	179.6826	179.9856	179.978
ϕ(C_6-C_5-C_4-O_{10})	180.0	180.0	179.995	179.9295	179.9373
ϕ(C_6-N_1-C_2-O_8)	180.0	180.0	179.9821	179.9234	179.957
ϕ(H_7-N_1-C_2-O_8)	0.0	0.0	0.338	0.0299	0.0112
ϕ(H_7-N_1-C_6-H_{12})	0.0	0.0	0.3296	0.0141	0.0248
ϕ(H_9-N_3-C_4-O_{10})	0.0	0.0	0.0146	0.3006	0.1932
ϕ(H_{11}-C_5-C_6-H_{12})	0.0	0.0	0.0165	0.0057	0.0025
ϕ(N_1-C_2-N_3-C_4)	0.0	0.0	0.0015	0.0789	0.0377
ϕ(N_1-C_2-N_3-H_9)	180.0	180.0	179.9703	179.7862	179.7729
ϕ(N_1-C_6-C_5-C_4)	0.0	0.0	0.0383	0.0324	0.0126
ϕ(N_1-C_6-C_5-H_{11})	180.0	180.0	179.9704	179.9946	179.9945
ϕ(N_3-C_2-N_1-C_6)	0.0	0.0	0.042	0.0852	0.0229
ϕ(N_3-C_2-N_1-H_7)	180.0	180.0	179.6861	179.9616	179.9688
ϕ(N_3-C_4-C_5-C_6)	0.0	0.0	0.0002	0.0387	0.0632
ϕ(N_3-C_4-C_5-H_{11})	180.0	180.0	179.9913	179.9981	179.9545
ϕ(O_8-C_2-N_3-H_9)	0.0	0.0	0.0057	0.2224	0.2473
ϕ(O_{10}-C_4-C_5-H_{11})	0.0	0.0	0.0035	0.0336	0.045

Table C2: *Equilibrium Geometries of Thymine in the Gas Phase, Implicit Water and with One Explicit Water Plus C-PCM Determined using PBE0/aug-cc-pVTZ. See Figure 4.3 in the Main Text for the Corresponding Structures.*

bond length/Å	gas	implicit water	(A)	(B)	(C)
r(C_2-N_3)	1.374	1.3712	1.3658	1.3706	1.3653
r(C_2-O_8)	1.2097	1.2181	1.2275	1.2178	1.2273
r(C_4-C_5)	1.4595	1.4511	1.4502	1.4462	1.4521
r(C_4-O_{10})	1.2127	1.2219	1.2214	1.2314	1.2217
r(C_5-C_6)	1.3436	1.3467	1.3475	1.3481	1.3461
r(C_5-C_{11})	1.489	1.4897	1.4897	1.4899	1.4894
r(C_6-H_{12})	1.083	1.0821	1.082	1.0819	1.0818
r(C_{11}-H_{13})	1.092	1.0922	1.0923	1.0922	1.0922
r(C_{11}-H_{14})	1.092	1.0922	1.0923	1.0922	1.0922
r(C_{11}-C_{15})	1.0903	1.0894	1.0895	1.0894	1.0895
r(N_1-C_2)	1.377	1.3672	1.3614	1.3686	1.3616

$r(N_1\text{-}C_6)$	1.3692	1.3656	1.3644	1.3634	1.367
$r(N_1\text{-}H_7)$	1.0053	1.0069	1.0182	1.0072	1.0073
$r(N_3\text{-}C_4)$	1.3944	1.389	1.391	1.382	1.3885
$r(N_3\text{-}H_9)$	1.0093	1.0099	1.0101	1.0194	1.0191
$r(O_{16}\text{-}H_{17})$			0.96	0.9599	0.9599
$r(O_{16}\text{-}H_{18})$			0.9746	0.9767	0.9747
bond angle/°	gas	implicit water	(A)	(B)	(C)
$\theta(C_2\text{-}N_1\text{-}C_6)$	123.6891	123.5259	123.0068	123.5487	123.1515
$\theta(C_2\text{-}N_1\text{-}H_7)$	115.2235	116.2481	115.3461	116.2632	116.5693
$\theta(C_2\text{-}N_3\text{-}C_4)$	128.0591	127.6468	127.2431	127.1235	127.1155
$\theta(C_2\text{-}N_3\text{-}H_9)$	115.6852	115.8141	116.1225	116.9277	115.0355
$\theta(C_4\text{-}C_5\text{-}C_6)$	117.8622	117.6737	117.6946	117.3076	117.7394
$\theta(C_4\text{-}C_5\text{-}C_{11})$	118.1046	118.8207	118.8108	119.1028	118.8473
$\theta(C_4\text{-}N_3\text{-}H_9)$	116.2557	116.5392	116.6344	115.9482	117.8485
$\theta(C_5\text{-}C_4\text{-}O_{10})$	124.9894	125.153	125.3195	124.3597	125.0102
$\theta(C_5\text{-}C_6\text{-}H_{12})$	121.9845	122.2428	122.1033	122.1997	122.3269
$\theta(C_5\text{-}C_{11}\text{-}H_{13})$	110.767	110.972	110.97	110.9756	110.9318
$\theta(C_5\text{-}C_{11}\text{-}H_{14})$	110.7669	110.972	110.9713	110.9757	110.9329
$\theta(C_5\text{-}C_{11}\text{-}C_{15})$	111.139	110.8137	110.8049	110.7897	110.8149
$\theta(C_6\text{-}C_5\text{-}C_{11})$	124.0332	123.5056	123.4946	123.5895	123.4132
$\theta(C_6\text{-}N_1\text{-}H_7)$	121.0874	120.226	121.6464	120.1881	120.2791
$\theta(H_{13}\text{-}C_{11}\text{-}H_{14})$	106.4931	106.9458	106.9515	106.9936	106.9527
$\theta(H_{13}\text{-}C_{11}\text{-}C_{15})$	108.766	108.5032	108.5064	108.4889	108.5395
$\theta(H_{14}\text{-}C_{11}\text{-}C_{15})$	108.766	108.5031	108.5063	108.4879	108.5413
$\theta(N_1\text{-}C_2\text{-}N_3)$	112.7943	113.2687	114.1179	113.3853	114.148
$\theta(N_1\text{-}C_2\text{-}O_8)$	123.1791	123.4669	123.2293	123.3282	122.8281
$\theta(N_1\text{-}C_6\text{-}C_5)$	122.8719	122.8156	122.9567	122.7309	122.6887
$\theta(N_1\text{-}C_6\text{-}H_{12})$	115.1435	114.9416	114.9399	115.0694	114.9844
$\theta(N_3\text{-}C_2\text{-}O_8)$	124.0267	123.2643	122.6528	123.2865	123.0239
$\theta(N_3\text{-}C_4\text{-}C_5)$	114.7234	115.0693	114.9808	115.9039	115.1569
$\theta(N_3\text{-}C_4\text{-}O_{10})$	120.2873	119.7777	119.6997	119.7364	119.8329
$\theta(H_{17}\text{-}O_{16}\text{-}H_{18})$			105.6592	105.6719	105.5939
dihedral angle/°	gas	implicit water	(A)	(B)	(C)
$\phi(C_2\text{-}N_1\text{-}C_6\text{-}C_5)$	0.0007	0.0	0.0515	0.0258	0.0335
$\phi(C_2\text{-}N_1\text{-}C_6\text{-}H_{12})$	-179.9994	180.0	-179.9639	-179.9729	-179.9649
$\phi(C_2\text{-}N_3\text{-}C_4\text{-}C_5)$	-0.0004	0.0001	0.0271	-0.0282	0.0782
$\phi(C_2\text{-}N_3\text{-}C_4\text{-}O_{10})$	179.9996	-180.0004	-179.9769	-179.9971	-179.9232
$\phi(C_4\text{-}C_5\text{-}C_6\text{-}H_{12})$	179.9998	-179.9997	179.9818	-179.9672	-179.9875
$\phi(C_4\text{-}C_5\text{-}C_{11}\text{-}H_{13})$	58.9697	59.3808	-59.3752	59.4164	-59.3575
$\phi(C_4\text{-}C_5\text{-}C_{11}\text{-}H_{14})$	-58.9686	-59.3838	59.3948	-59.4127	59.3644
$\phi(C_4\text{-}C_5\text{-}C_{11}\text{-}C_{15})$	180.0005	179.9985	-179.9898	-179.9976	-179.9951
$\phi(C_4\text{-}N_3\text{-}C_2\text{-}O_8)$	-179.9993	-180.0004	179.9619	-179.9244	179.9887
$\phi(C_5\text{-}C_4\text{-}N_3\text{-}H_9)$	-179.9996	-179.9999	179.9832	-179.7428	179.797
$\phi(C_5\text{-}C_6\text{-}N_1\text{-}H_7)$	179.9994	-179.9998	179.721	179.9898	179.9649
$\phi(C_6\text{-}C_5\text{-}C_4\text{-}O_{10})$	180.0001	180.0002	-179.998	179.9345	179.9377
$\phi(C_6\text{-}C_5\text{-}C_{11}\text{-}H_{13})$	-121.0305	-120.6191	120.618	-120.5496	120.6578
$\phi(C_6\text{-}C_5\text{-}C_{11}\text{-}H_{14})$	121.0313	120.6163	-120.6121	120.6212	-120.6203
$\phi(C_6\text{-}C_5\text{-}C_{11}\text{-}C_{15})$	0.0004	-0.0014	0.0033	0.0364	0.0203
$\phi(C_6\text{-}N_1\text{-}C_2\text{-}O_8)$	179.9992	-179.9997	179.9988	179.9268	179.9523
$\phi(C_{11}\text{-}C_5\text{-}C_6\text{-}H_{12})$	0.0	0.0002	-0.0114	-0.0005	-0.0027

ϕ(H_7-N_1-C_2-O_8)	0.0004	0.0002	0.3101	-0.0385	0.0186
ϕ(H_7-N_1-C_6-H_{12})	-0.0006	0.0002	-0.2944	-0.009	-0.0335
ϕ(H_9-N_3-C_4-O_{10})	0.0004	-0.0004	-0.0207	0.2884	-0.2044
ϕ(N_1-C_2-N_3-C_4)	0.0007	0.0001	-0.0136	0.082	-0.0345
ϕ(N_1-C_2-N_3-H_9)	-180.0001	180.0001	-179.9699	179.7942	-179.7601
ϕ(N_1-C_6-C_5-C_4)	-0.0002	0.0003	-0.0346	0.0342	0.0142
ϕ(N_1-C_6-C_5-C_{11})	179.9999	-179.9998	179.9721	-179.9992	179.999
ϕ(N_3-C_2-N_1-C_6)	-0.0009	-0.0002	-0.0258	-0.0796	-0.0245
ϕ(N_3-C_2-N_1-H_7)	-179.9997	179.9996	-179.7145	179.9551	-179.9582
ϕ(N_3-C_4-C_5-C_6)	0.0001	-0.0003	-0.0022	-0.0327	-0.0638
ϕ(N_3-C_4-C_5-C_{11})	180.0	179.9997	179.9914	179.9991	179.9507
ϕ(O_8-C_2-N_3-H_9)	-0.0001	-0.0004	0.0056	-0.2122	0.2631
ϕ(O_{10}-C_4-C_5-C_{11})	0.0	0.0002	-0.0045	-0.0336	-0.0478

Table C3: *Intermolecular Equilibrium Geometries of Uracil- and Thymine-H_2O as Determined using PBE0/aug-cc-pVTZ in H_2O (C-PCM). See Figure 4.2 and 4.3 in the Main Text for the Corresponding Structures.*

uracil-H_2O(A)		uracil-H_2O(B)		uracil-H_2O(C)	
r(H_7-O_{13})	1.9611	r(H_9-O_{13})	2.0209	r(H_9-O_{13})	2.0283
r(O_8-H_{15})	1.8982	r(O_{10}-H_{15})	1.834	r(O_8-H_{15})	1.879
θ(N_1-H_7-O_{13})	144.1502	θ(N_3-H_9-O_{13})	142.709	θ(N_3-H_9-O_{13})	143.0742
θ(O_8-H_{15}-O_{13})	149.7555	θ(O_{10}-H_{15}-O_{13})	154.724	θ(O_8-H_{15}-O_{13})	152.2778
θ(H_7-O_{13}-H_{14})	118.7964	θ(H_9-O_{13}-H_{14})	118.467	θ(H_9-O_{13}-H_{14})	118.6066
θ(C_2-O_8-H_{15})	108.0004	θ(C_4-O_{10}-H_{15})	110.5115	θ(C_2-O_8-H_{15})	108.7737
θ(H_7-O_{13}-H_{15})	79.4733	θ(H_9-O_{13}-H_{15})	75.6689	θ(H_9-O_{13}-H_{15})	77.2831
thymine-H_2O(A)		thymine-H_2O(B)		thymine-H_2O(C)	
r(O_8-H_{18})	1.8723	r(O_{10}-H_{18})	1.8315	r(O_8-H_{18})	1.858
r(H_7-O_{16})	1.987	r(H_9-O_{16})	2.01137	r(H_9-O_{16})	2.0453
θ(C_2-O_8-H_{18})	107.8265	θ(C_4-O_{10}-H_{18})	110.6205	θ(C_2-O_8-H_{18})	108.8602
θ(N_1-H_7-O_{16})	142.9592	θ(N_3-H_9-O_{16})	143.032	θ(N_3-H_9-O_{16})	142.3025
θ(O_8-H_{18}-O_{16})	151.7236	θ(O_{10}-H_{18}-O_{16})	155.0345	θ(O_8-H_{18}-O_{16})	153.7905
θ(H_7-O_{16}-H_{18})	78.615	θ(H_9-O_{16}-H_{18})	75.879	θ(H_9-O_{16}-H_{18})	76.4024

Table C4: *Vibrational Frequencies (ω/cm^{-1}) and Frequency Shifts ($\Delta\omega/\mathrm{cm}^{-1}$) of Uracil When Forming a 1:1 Complex with Water. Results are Determined at the PBE0/aug-cc-pVTZ Level of Theory in Implicit Water (C-PCM). See Figure 4.2 in the Main Text for the Corresponding Structures.*

(A)	modes	12	17	24	25	26	27	28	29	31	32	33
	ω	579	794	1243	1254	1404	1424	1462	1542	1685	1723	1763
(B)	modes	12	17	24	25	26	28	27	29	31	32	33
	ω	574	798	1230	1265	1407	1450	1447	1532	1683	1711	1772
	$\Delta\omega$[a]	-5	4	-13	11	3	26	-15	-10	-2	-12	9
(C)	modes	12	17	24	25	26	27	28	29	31	32	33
	ω	574	795	1224	1261	1414	1445	1458	1523	1690	1724	1758
	$\Delta\omega$[b]	-5	1	-19	7	10	21	-4	-19	5	1	-5
H_2O (C-PCM)	modes	7	12	18	19	20	21	22	23	24	25	26
	ω	568	791	1220	1251	1396	1424	1441	1524	1686	1724	1775
	$\Delta\omega$[c]	-11	-3	-23	-3	-8	0	-21	-18	1	1	12

[a] $\Delta\omega = \omega(\mathrm{B}) - \omega(\mathrm{A})$.
[b] $\Delta\omega = \omega(\mathrm{C}) - \omega(\mathrm{A})$.
[c] $\Delta\omega = \omega(\mathrm{H_2O\ (C\text{-}PCM)}) - \omega(\mathrm{A})$.

Table C5: *Vibrational Frequencies (ω/cm^{-1}) and Frequency Shifts ($\Delta\omega/\mathrm{cm}^{-1}$) of Thymine When Forming a 1:1 Complex with Water. Results are Determined at the PBE0/aug-cc-pVTZ Level of Theory in Implicit Water (C-PCM). See Figure 4.3 in the Main Text for the Corresponding Structures.*

(A)	modes	14	15	19	22	27	28	29	30	31	32	36	38	39	40
	ω	562	618	757	818	1188	1238	1266	1387	1410	1413	1538	1711	1719	1755
(B)	modes	14	15	18	21	27	28	29	30	31	32	36	38	39	40
	ω	559	621	764	821	1190	1238	1266	1385	1410	1448	1533	1701	1713	1767
	$\Delta\omega$[a]	-3	3	7	3	2	0	0	-2	0	35	-5	-10	-6	12
(C)	modes	14	16	18	21 (22)	27	28	29	30	31	32	36	38	39	40
	ω	561	618	760	819 (821)	1185	1232	1269	1390	1409	1446	1526	1715	1720	1752
	$\Delta\omega$[b]	-1	0	3	1(3)	-3	-6	3	3	-1	33	-12	4	1	-3
H_2O (C-PCM)	modes	9	11	13	16	21	22	23	24	25	26	30	31	32	33
	ω	556	612	753	818	1182	1223	1261	1384	1409	1414	1525	1712	1719	1769
	$\Delta\omega$[c]	-6	-6	-4	0	-6	-15	-5	-3	-1	1	-13	1	0	14

[a] $\Delta\omega = \omega(\mathrm{B}) - \omega(\mathrm{A})$.
[b] $\Delta\omega = \omega(\mathrm{C}) - \omega(\mathrm{A})$.
[c] $\Delta\omega = \omega(\mathrm{H_2O\ (C\text{-}PCM)}) - \omega(\mathrm{A})$.

Table C6: *Potential Energy Distribution Analysis and Vibrational Frequencies (ω/cm^{-1}) of Ground State Normal Modes of Uracil-H_2O (A) Plus Implicit Water (C-PCM). See Figure 4.2 in the Main Text for the Corresponding Structure.*

mode	ω	PED
10	528	-stretch(C_2N_3)[15%]+bend($C_2N_1C_6$)[23%]-bend($N_1C_2N_3$)[17%]-bend($C_2N_3C_4$)[14%]
11	557	+bend($N_1C_6C_5$)[12%]+bend($C_5C_4O_{10}$)[14%]+bend($N_3C_2O_8$)[28%]+bend($C_2N_3C_4$)[18%]
12	579	-stretch(N_3C_4)[9%]+bend($C_5C_4O_{10}$)[24%]+bend($N_3C_2O_8$)[13%]+bend($N_1C_2N_3$)[30%]
13	668	+bend($O_8H_{15}O_{13}$)[37%]-bend($C_2O_8H_{15}$)[32%]
14	677	+torsion($C_5C_4N_3H_9$)[90%]
15	731	-torsion($C_5C_6N_1H_7$)[8%]+torsion($N_3C_4C_5H_{11}$)[41%]+out-of-plane($C_4C_5N_3O_{10}$)[28%]-out-of-plane($C_2N_3N_1O_8$)[18%]
16	783	+torsion($C_5C_6N_1H_7$)[25%]+torsion($N_3C_4C_5H_{11}$)[12%]+out-of-plane($C_2N_3N_1O_8$)[49%]
17	794	+stretch(N_1C_2)[25%]+stretch(C_2N_3)[11%]-bend($N_1C_6C_5$)[9%]+bend($C_2N_1C_6$)[23%]
18	801	+torsion($C_5C_6N_1H_7$)[51%]-out-of-plane($C_2N_3N_1O_8$)[25%]
19	833	-torsion($C_5C_6N_1H_7$)[8%]+torsion($C_4C_5C_6H_{12}$)[13%]+torsion($N_3C_4C_5H_{11}$)[26%]-out-of-plane($C_4C_5N_3O_{10}$)[49%]
20	997	+bend($N_1C_6C_5$)[33%]-bend($C_2N_1C_6$)[12%]+bend($N_1C_2N_3$)[17%]-bend($C_2N_3C_4$)[8%]
21	1007	+torsion($C_4C_5C_6H_{12}$)[63%]-torsion($N_3C_4C_5H_{11}$)[15%]+torsion($C_2N_1C_6C_5$)[14%]
22	1009	-stretch(N_1C_2)[22%]-stretch(C_2N_3)[10%]+bend($C_5C_6H_{12}$)[8%]+bend($C_2N_1C_6$)[15%]+bend($C_2N_3C_4$)[20%]
23	1112	-stretch(C_5C_6)[16%]-stretch(N_1C_6)[24%]+bend($C_4C_5H_{11}$)[33%]
24	1243	-stretch(N_1C_6)[10%]+stretch(C_2N_3)[19%]-stretch(N_3C_4)[11%]-bend($C_6N_1H_7$)[13%]+bend($C_5C_6H_{12}$)[28%]
25	1254	-stretch(N_1C_6)[17%]-stretch(C_2N_3)[9%]+stretch(N_3C_4)[21%]-bend($C_4C_5H_{11}$)[25%]
26	1404	+stretch(C_2N_3)[11%]+bend($C_4N_3H_9$)[42%]-bend($C_4C_5H_{11}$)[9%]
27	1424	-stretch(C_4O_{10})[9%]+stretch(C_2O_8)[8%]+bend($C_4N_3H_9$)[21%]+bend($C_5C_6H_{12}$)[28%]+bend($C_4C_5H_{11}$)[16%]
28	1462	-stretch(N_1C_2)[23%]+stretch(N_3C_4)[10%]+bend($C_6N_1H_7$)[12%]-bend($N_3C_2O_8$)[9%]-bend($C_2N_3C_4$)[16%]
29	1542	+stretch(C_2O_8)[15%]-stretch(N_1C_6)[17%]+bend($C_6N_1H_7$)[43%]+bend($N_1C_6C_5$)[8%]

30	1621	+bend($H_{14}O_{13}H_{15}$)[89%]
31	1685	+stretch(C_5C_6)[58%]-stretch(N_1C_6)[8%]-bend($C_5C_6H_{12}$)[12%]
32	1723	+stretch(C_4O_{10})[51%]-stretch(C_2O_8)[16%]+bend($C_4N_3H_9$)[11%]
33	1763	+stretch(C_4O_{10})[21%]+stretch(C_2O_8)[40%]-bend($C_6N_1H_7$)[8%]

Table C7: *Potential Energy Distribution Analysis and Vibrational Frequencies (ω/cm^{-1}) of Ground State Normal Modes of Uracil-H_2O (B) Plus Implicit Water (C-PCM). See Figure 4.2 in the Main Text for the Corresponding Structure.*

mode	ω	PED
10	535	+stretch(C_2N_3)[16%]-bend($C_2N_1C_6$)[21%]+bend($N_1C_2N_3$)[17%]+bend($C_2N_3C_4$)[21%]
11	562	+bend($N_1C_6C_5$)[18%]+bend($N_3C_2O_8$)[28%]+bend($C_5C_4O_{10}$)[14%]+bend($C_2N_3C_4$)[15%]
12	574	+bend($N_3C_2O_8$)[15%]+bend($C_5C_4O_{10}$)[30%]+bend($N_1C_2N_3$)[30%]
13	620	+torsion($C_5C_6N_1H_7$)[92%]
14	721	+bend($O_{10}H_{15}O_{13}$)[39%]-bend($C_4O_{10}H_{15}$)[34%]
15	742	+torsion($N_3C_4C_5H_{11}$)[51%]-out-of-plane($C_2N_3N_1O_8$)[13%]+out-of-plane($C_4C_5N_3O_{10}$)[24%]
16	778	-torsion($C_5C_4N_3H_9$)[20%]+out-of-plane($C_2N_3N_1O_8$)[65%]
17	798	+stretch(N_1C_2)[28%]+stretch(C_2N_3)[10%]+bend($C_2N_1C_6$)[25%]
18	812	+torsion($C_5C_4N_3H_9$)[57%]+torsion($N_3C_4C_5H_{11}$)[15%]+out-of-plane($C_2N_3N_1O_8$)[16%]
19	839	+torsion($C_5C_4N_3H_9$)[14%]-torsion($C_4C_5C_6H_{12}$)[8%]-torsion($N_3C_4C_5H_{11}$)[14%]+out-of-plane($C_4C_5N_3O_{10}$)[53%]
20	1003	+stretch(N_1C_2)[16%]+bend($N_1C_6C_5$)[28%]-bend($C_2N_1C_6$)[12%]+bend($N_1C_2N_3$)[10%]-bend($C_2N_3C_4$)[13%]
21	1007	+torsion($C_4C_5C_6H_{12}$)[65%]-torsion($N_3C_4C_5H_{11}$)[14%]+torsion($C_2N_1C_6C_5$)[14%]
22	1018	+stretch(N_3C_4)[9%]+bend($N_1C_6C_5$)[9%]+bend($C_4N_3H_9$)[10%]- bend($N_3C_2O_8$)[8%]+bend($C_2N_1C_6$)[16%]+bend($N_1C_2N_3$)[17%]
23	1109	-stretch(C_5C_6)[16%]-stretch(N_1C_6)[28%]+bend($C_4C_5H_{11}$)[32%]
24	1230	+stretch(N_1C_6)[18%]+bend($C_6N_1H_7$)[23%]-bend($C_5C_6H_{12}$)[31%]+bend($C_4C_5H_{11}$)[10%]
25	1265	-stretch(C_2N_3)[27%]+stretch(N_3C_4)[32%]-bend($C_4C_5H_{11}$)[14%]
26	1407	+stretch(C_5C_6)[9%]+bend($C_6N_1H_7$)[9%]+bend($C_5C_6H_{12}$)[32%]+bend($C_4C_5H_{11}$)[24%]
27	1447	-stretch(N_1C_2)[15%]+bend($C_6N_1H_7$)[15%]-bend($C_2N_3C_4$)[15%]
28	1450	-stretch(C_4O_{10})[13%]+bend($C_4N_3H_9$)[52%]

29	1532	+stretch(C_2O_8)[9%]-stretch(N_1C_6)[16%]+stretch(N_1C_2)[12%]- stretch(N_3C_4)[10%]+bend($N_1C_6C_5$)[10%]+bend($C_6N_1H_7$)[27%]
30	1625	+bend($H_{14}O_{13}H_{15}$)[85%]
31	1683	-stretch(C_4O_{10})[13%]+stretch(C_5C_6)[52%]-stretch(N_1C_6)[8%]-bend($C_5C_6H_{12}$)[13%]
32	1711	+stretch(C_4O_{10})[47%]+stretch(C_5C_6)[8%]+bend($C_4N_3H_9$)[14%]
33	1772	+stretch(C_2O_8)[69%]

Table C8: *Potential Energy Distribution Analysis and Vibrational Frequencies (ω/cm^{-1}) of Ground State Normal Modes of Uracil-H_2O (C) Plus Implicit Water (C-PCM). See Figure 4.2 in the Main Text for the Corresponding Structure.*

mode	ω	PED
10	535	+stretch(C_2N_3)[15%]-bend($C_2N_1C_6$)[19%]+bend($N_1C_2N_3$)[19%]+bend($C_2N_3C_4$)[21%]
11	556	+stretch(N_3C_4)[11%]+bend($N_1C_6C_5$)[14%]+bend($C_5C_4O_{10}$)[9%]+bend($N_3C_2O_8$)[27%]+bend($C_2N_3C_4$)[19%]
12	574	+bend($C_5C_4O_{10}$)[29%]+bend($N_3C_2O_8$)[20%]+bend($N_1C_2N_3$)[24%]
13	617	+torsion($C_5C_6N_1H_7$)[92%]
14	674	+bend($O_8H_{15}O_{13}$)[39%]-bend($C_2O_8H_{15}$)[34%]-torsion($C_2O_8H_{15}O_{13}$)[9%]
15	741	+torsion($N_3C_4C_5H_{11}$)[50%]+out-of-plane($C_4C_5N_3O_{10}$)[26%]-out-of-plane($C_2N_3N_1O_8$)[15%]
16	776	-torsion($C_5C_4N_3H_9$)[31%]+out-of-plane($C_2N_3N_1O_8$)[53%]
17	795	+stretch(N_1C_6)[8%]+stretch(N_1C_2)[26%]+stretch(C_2N_3)[11%]+bend($C_2N_1C_6$)[22%]
18	817	+torsion($C_5C_4N_3H_9$)[51%]+out-of-plane($C_2N_3N_1O_8$)[24%]
19	836	+torsion($C_5C_4N_3H_9$)[10%]-torsion($C_4C_5C_6H_{12}$)[12%]-torsion($N_3C_4C_5H_{11}$)[19%]+out-of-plane($C_4C_5N_3O_{10}$)[50%]
20	999	+bend($N_1C_6C_5$)[37%]-bend($C_2N_1C_6$)[17%]+bend($N_1C_2N_3$)[21%]
21	1006	+torsion($C_4C_5C_6H_{12}$)[64%]-torsion($N_3C_4C_5H_{11}$)[16%]+torsion($C_2N_1C_6C_5$)[14%]
22	1021	-stretch(N_1C_2)[16%]-stretch(C_2N_3)[10%]+bend($C_5C_6H_{12}$)[8%]+bend($C_2N_1C_6$)[20%]+bend($C_2N_3C_4$)[13%]
23	1108	-stretch(C_5C_6)[15%]-stretch(N_1C_6)[29%]+bend($C_4C_5H_{11}$)[29%]
24	1224	-stretch(N_1C_6)[16%]-bend($C_6N_1H_7$)[24%]+bend($C_5C_6H_{12}$)[31%]-bend($C_4C_5H_{11}$)[12%]
25	1261	-stretch(C_2N_3)[22%]+stretch(N_3C_4)[31%]-bend($C_4C_5H_{11}$)[17%]
26	1414	+stretch(C_5C_6)[10%]+bend($C_6N_1H_7$)[11%]+bend($C_5C_6H_{12}$)[32%]+bend($C_4C_5H_{11}$)[21%]
27	1445	-stretch(C_4O_{10})[10%]+stretch(C_2O_8)[13%]+bend($C_4N_3H_9$)[33%]+bend($C_5C_6H_{12}$)[8%]
28	1458	-stretch(N_1C_2)[12%]+stretch(N_3C_4)[10%]+bend($C_6N_1H_7$)[15%]-bend($C_4N_3H_9$)[23%]-bend($N_3C_2O_8$)[11%]-bend($C_2N_3C_4$)[12%]

29	1523	+stretch(C_2O_8)[12%]-stretch(N_1C_6)[17%]+stretch(N_1C_2)[11%]-stretch(N_3C_4)[9%]+bend($N_1C_6C_5$)[10%]+bend($C_6N_1H_7$)[26%]
30	1624	+bend($H_{14}O_{13}H_{15}$)[89%]
31	1690	+stretch(C_5C_6)[58%]-bend($C_5C_6H_{12}$)[11%]
32	1724	+stretch(C_4O_{10})[50%]-stretch(C_2O_8)[14%]+bend($C_4N_3H_9$)[14%]
33	1758	+stretch(C_4O_{10})[21%]+stretch(C_2O_8)[44%]

Table C9: *Potential Energy Distribution Analysis and Vibrational Frequencies (ω/cm^{-1}) of Ground State Normal Modes of Thymine-H_2O (A) Plus Implicit Water (C-PCM). See Figure 4.3 in the Main Text for the Corresponding Structure.*

mode	ω	PED
14	562	-stretch(N_3C_4)[12%]-bend($N_3C_4O_{10}$)[24%]+bend($C_2N_1C_6$)[15%]+bend($N_1C_2N_3$)[11%]
15	618	-bend($N_3C_4O_{10}$)[17%]-bend($N_1C_2O_8$)[33%]+bend($C_2N_3C_4$)[15%]-bend($C_4C_5C_{11}$)[14%]
16	680	+torsion($C_5C_4N_3H_9$)[81%]
17	689	-bend($C_2O_8H_{18}$)[30%]+torsion($C_2O_8H_{18}O_{16}$)[30%]
18	754	+torsion($N_1H_7O_{16}H_{17}$)[16%]-torsion($C_5C_6N_1H_7$)[13%]+out-of-plane($C_4C_5N_3O_{10}$)[12%]+out-of-plane($C_2N_1N_3O_8$)[41%]
19	757	+stretch(N_1C_2)[13%]+stretch(C_5C_{11})[12%]-bend($N_1C_6C_5$)[9%]+bend($N_1C_2N_3$)[27%]-bend($C_2N_3C_4$)[14%]
20	791	+torsion($N_1H_7O_{16}H_{17}$)[11%]-torsion($C_5C_6N_1H_7$)[8%]-torsion($N_1C_2O_8H_{18}$)[8%]+out-of-plane($C_4C_5N_3O_{10}$)[9%]-out-of-plane($C_2N_1N_3O_8$)[44%]
21	798	+torsion($N_1H_7O_{16}H_{17}$)[9%]-torsion($C_5C_6N_1H_7$)[8%]-out-of-plane($C_4C_5N_3O_{10}$)[55%]
22	818	+stretch(N_1C_2)[12%]-stretch(C_5C_{11})[15%]-bend($N_1C_6C_5$)[14%]+bend($C_2N_1C_6$)[11%]-bend($N_1C_2N_3$)[8%]+bend($C_2N_3C_4$)[10%]
23	946	-torsion($C_{11}C_5C_6H_{12}$)[77%]
24	991	-stretch(N_1C_2)[8%]-bend($H_{13}C_{11}H_{14}$)[8%]+bend($C_2N_1C_6$)[8%]+torsion($C_6C_5C_{11}H_{13}$)[17%]-torsion($C_6C_5C_{11}H_{14}$)[17%]
25	1035	+stretch(N_1C_2)[13%]+stretch(C_2N_3)[8%]-bend($C_2N_3C_4$)[8%]+torsion($C_6C_5C_{11}H_{13}$)[15%]-torsion($C_6C_5C_{11}H_{14}$)[15%]
26	1069	-bend($H_{13}C_{11}H_{15}$)[12%]+bend($H_{14}C_{11}H_{15}$)[12%]-torsion($C_{11}C_5C_6H_{12}$)[19%]+torsion($C_6C_5C_{11}H_{15}$)[51%]
27	1188	+stretch(N_3C_4)[29%]-stretch(C_5C_{11})[14%]+bend($N_1C_6C_5$)[9%]-bend($N_3C_4O_{10}$)[8%]
28	1238	+stretch(N_1C_6)[29%]-stretch(C_2N_3)[11%]+bend($C_6N_1H_7$)[17%]+bend($N_1C_6H_{12}$)[18%]
29	1266	-stretch(N_1C_6)[20%]-stretch(C_2N_3)[14%]+stretch(N_3C_4)[11%]+stretch(C_5C_{11})[20%]-bend($N_1C_6C_5$)[8%]+bend($N_1C_6H_{12}$)[15%]
30	1387	-stretch(C_5C_6)[17%]+stretch(C_2N_3)[9%]+bend($N_1C_6H_{12}$)[34%]
31	1410	+bend($H_{13}C_{11}H_{15}$)[25%]+bend($H_{13}C_{11}H_{14}$)[35%]+bend($H_{14}C_{11}H_{15}$)[25%]

32	1413	-stretch(C_4O_{10})[9%]+stretch(C_2O_8)[12%]+bend($C_4N_3H_9$)[58%]
33	1454	-bend($H_{13}C_{11}H_{15}$)[40%]+bend($H_{14}C_{11}H_{15}$)[40%]+torsion($C_6C_5C_{11}H_{15}$)[12%]
34	1476	-stretch(N_1C_2)[13%]+bend($H_{13}C_{11}H_{15}$)[8%]-bend($H_{13}C_{11}H_{14}$)[27%]+bend($H_{14}C_{11}H_{15}$)[8%]
35	1477	+stretch(N_1C_2)[12%]-bend($C_6N_1H_7$)[15%]-bend($H_{13}C_{11}H_{14}$)[17%]
36	1538	+stretch(C_2O_8)[13%]-stretch(N_1C_6)[8%]+stretch(N_1C_2)[10%]+bend($N_1C_6C_5$)[13%]+bend($C_6N_1H_7$)[37%]
37	1623	+bend($O_8H_{18}O_{16}$)[9%]+bend($H_{17}O_{16}H_{18}$)[72%]-torsion($C_2O_8H_{18}O_{16}$)[9%]
38	1711	+stretch(C_4O_{10})[11%]+stretch(C_5C_6)[46%]+bend($N_1C_6H_{12}$)[8%]
39	1719	+stretch(C_4O_{10})[47%]-stretch(C_5C_6)[17%]
40	1755	+stretch(C_4O_{10})[19%]+stretch(C_2O_8)[42%]-stretch(N_1C_2)[8%]-bend($C_6N_1H_7$)[9%]

Table C10: *Potential Energy Distribution Analysis and Vibrational Frequencies (ω/cm^{-1}) of Ground State Normal Modes of Thymine-H_2O (B) Plus Implicit Water (C-PCM). See Figure 4.3 in the Main Text for the Corresponding Structure.*

mode	ω	PED
14	559	+stretch(C_2N_3)[10%]+stretch(N_3C_4)[13%]+bend($N_3C_4O_{10}$)[27%]-bend($C_2N_1C_6$)[17%]-bend($N_1C_2N_3$)[15%]
15	621	+bend($N_1C_2O_8$)[15%]+bend($N_3C_4O_{10}$)[9%]-bend($C_2N_3C_4$)[9%]-torsion($C_5C_6N_1H_7$)[45%]
16	622	+bend($N_1C_2O_8$)[13%]+bend($N_3C_4O_{10}$)[8%]-bend($C_2N_3C_4$)[8%]+torsion($C_5C_6N_1H_7$)[50%]
17	726	+bend($O_{10}H_{18}O_{16}$)[14%]-bend($C_4O_{10}H_{18}$)[27%]+torsion($C_4O_{10}H_{18}O_{16}$)[33%]
18	764	-stretch(N_1C_2)[13%]-stretch(C_5C_{11})[11%]+bend($N_1C_6C_5$)[9%]-bend($N_1C_2N_3$)[28%]+bend($C_2N_3C_4$)[12%]
19	774	-out-of-plane($C_2N_1N_3O_8$)[82%]
20	785	+out-of-plane($C_5C_4C_6C_{11}$)[9%]+out-of-plane($C_4C_5N_3O_{10}$)[54%]
21	821	+stretch(N_1C_2)[11%]-stretch(C_5C_{11})[16%]-bend($N_1C_6C_5$)[14%]+bend($C_2N_1C_6$)[11%]-bend($N_1C_2N_3$)[9%]+bend($C_2N_3C_4$)[10%]
22	827	+torsion($N_3H_9O_{16}H_{17}$)[33%]+torsion($C_5C_4N_3H_9$)[14%]-out-of-plane($C_2N_1N_3O_8$)[9%]+out-of-plane($C_4C_5N_3O_{10}$)[10%]
23	948	-torsion($C_{11}C_5C_6H_{12}$)[75%]-torsion($C_2N_1C_6C_5$)[9%]
24	996	-bend($H_{13}C_{11}H_{14}$)[9%]+bend($C_2N_1C_6$)[8%]+torsion($C_6C_5C_{11}H_{13}$)[20%]-torsion($C_6C_5C_{11}H_{14}$)[20%]
25	1032	-stretch(N_1C_2)[15%]-stretch(C_2N_3)[8%]+bend($C_2N_1C_6$)[9%]-torsion($C_6C_5C_{11}H_{13}$)[14%]+torsion($C_6C_5C_{11}H_{14}$)[14%]
26	1068	-bend($H_{13}C_{11}H_{15}$)[13%]+bend($H_{14}C_{11}H_{15}$)[13%]-torsion($C_{11}C_5C_6H_{12}$)[19%]+torsion($C_6C_5C_{11}H_{15}$)[51%]
27	1190	-stretch(N_1C_6)[18%]+stretch(N_3C_4)[10%]+bend($N_1C_6C_5$)[9%]-bend($C_6N_1H_7$)[17%]-bend($N_1C_6H_{12}$)[16%]
28	1238	-stretch(N_1C_6)[18%]+stretch(C_2N_3)[9%]-stretch(N_3C_4)[18%]+stretch(C_5C_{11})[19%]-bend($C_6N_1H_7$)[12%]
29	1266	+stretch(N_1C_6)[20%]+stretch(C_2N_3)[21%]-stretch(N_3C_4)[18%]-stretch(C_5C_{11})[13%]-bend($N_1C_6H_{12}$)[13%]
30	1385	-stretch(C_5C_6)[17%]+bend($N_1C_6H_{12}$)[38%]
31	1410	+stretch(C_5C_{11})[8%]+bend($H_{13}C_{11}H_{15}$)[24%]+bend($H_{13}C_{11}H_{14}$)[37%]+bend($H_{14}C_{11}H_{15}$)[25%]

32	1448	-stretch(C_4O_{10})[11%]-bend($C_6N_1H_7$)[13%]+bend($C_4N_3H_9$)[53%]
33	1455	-bend($H_{13}C_{11}H_{15}$)[40%]+bend($H_{14}C_{11}H_{15}$)[39%]+torsion($C_6C_5C_{11}H_{15}$)[12%]
34	1459	-stretch(N_1C_2)[13%]+stretch(C_2N_3)[12%]+bend($C_6N_1H_7$)[17%]
35	1477	-bend($H_{13}C_{11}H_{15}$)[13%]+bend($H_{13}C_{11}H_{14}$)[40%]-bend($H_{14}C_{11}H_{15}$)[13%]-torsion($C_6C_5C_{11}H_{13}$)[12%]+torsion($C_6C_5C_{11}H_{14}$)[12%]
36	1533	+stretch(C_2O_8)[8%]+stretch(N_1C_2)[16%]-stretch(N_3C_4)[12%]+bend($N_1C_6C_5$)[18%]+bend($C_6N_1H_7$)[23%]
37	1623	+bend($H_{17}O_{16}H_{18}$)[73%]-torsion($C_4O_{10}H_{18}O_{16}$)[10%]
38	1701	+stretch(C_4O_{10})[60%]-bend($H_{17}O_{16}H_{18}$)[8%]+bend($C_4N_3H_9$)[17%]
39	1713	+stretch(C_5C_6)[63%]+bend($N_1C_6H_{12}$)[14%]
40	1767	+stretch(C_2O_8)[69%]

Table C11: *Potential Energy Distribution Analysis and Vibrational Frequencies (ω/cm^{-1}) of Ground State Normal Modes of Thymine-H_2O (C) Plus Implicit Water (C-PCM). See Figure 4.3 in the Main Text for the Corresponding Structure.*

mode	ω	PED
14	561	+stretch(C_2N_3)[9%]+stretch(N_3C_4)[13%]+bend($N_3C_4O_{10}$)[25%]-bend($C_2N_1C_6$)[19%]-bend($N_1C_2N_3$)[12%]
15	611	+torsion($C_5C_6N_1H_7$)[95%]
16	618	-bend($N_3C_4O_{10}$)[16%]-bend($N_1C_2O_8$)[33%]+bend($C_2N_3C_4$)[15%]-bend($C_4C_5C_{11}$)[14%]
17	688	+bend($O_8H_{18}O_{16}$)[36%]-bend($C_2O_8H_{18}$)[32%]+torsion($C_2O_8H_{18}O_{16}$)[9%]
18	760	+stretch(N_1C_2)[12%]+stretch(C_5C_{11})[12%]-bend($N_1C_6C_5$)[10%]+bend($N_1C_2N_3$)[28%]-bend($C_2N_3C_4$)[13%]
19	771	+torsion($C_5C_4N_3H_9$)[18%]+out-of-plane($C_2N_1N_3O_8$)[73%]
20	785	+torsion($C_5C_4N_3H_9$)[19%]-out-of-plane($C_4C_5N_3O_{10}$)[53%]
21	819	-stretch(C_5C_{11})[8%]+torsion($C_5C_4N_3H_9$)[25%]+out-of-plane($C_4C_5N_3O_{10}$)[9%]
22	821	+torsion($C_5C_4N_3H_9$)[32%]+out-of-plane($C_4C_5N_3O_{10}$)[10%]
23	940	-torsion($C_{11}C_5C_6H_{12}$)[76%]-torsion($C_2N_1C_6C_5$)[8%]
24	997	+bend($H_{13}C_{11}H_{14}$)[11%]-torsion($C_6C_5C_{11}H_{14}$)[22%]+torsion($C_6C_5C_{11}H_{13}$)[22%]
25	1039	+stretch(N_1C_2)[18%]+stretch(C_2N_3)[11%]-bend($C_2N_1C_6$)[11%]-bend($C_2N_3C_4$)[10%]+torsion($C_6C_5C_{11}H_{14}$)[10%]-torsion($C_6C_5C_{11}H_{13}$)[10%]
26	1068	-bend($H_{14}C_{11}H_{15}$)[13%]+bend($H_{13}C_{11}H_{15}$)[13%]-torsion($C_{11}C_5C_6H_{12}$)[18%]+torsion($C_6C_5C_{11}H_{15}$)[51%]
27	1185	-stretch(N_1C_6)[14%]+stretch(N_3C_4)[19%]-stretch(C_5C_{11})[8%]+bend($N_1C_6C_5$)[9%]-bend($C_6N_1H_7$)[11%]-bend($N_1C_6H_{12}$)[9%]
28	1232	+stretch(N_1C_6)[25%]-stretch(C_2N_3)[10%]+stretch(N_3C_4)[13%]-stretch(C_5C_{11})[15%]+bend($C_6N_1H_7$)[18%]+bend($N_1C_6H_{12}$)[9%]
29	1269	-stretch(N_1C_6)[16%]-stretch(C_2N_3)[17%]+stretch(N_3C_4)[15%]+stretch(C_5C_{11})[16%]+bend($N_1C_6H_{12}$)[18%]
30	1390	-stretch(C_5C_6)[17%]+bend($N_1C_6H_{12}$)[40%]

31	1409	+stretch(C_5C_{11})[8%]+bend($H_{14}C_{11}H_{15}$)[26%]+bend($H_{13}C_{11}H_{14}$)[36%]+bend($H_{13}C_{11}H_{15}$)[26%]
32	1446	-stretch(C_4O_{10})[10%]+stretch(C_2O_8)[14%]+bend($C_4N_3H_9$)[62%]
33	1454	-bend($H_{14}C_{11}H_{15}$)[40%]+bend($H_{13}C_{11}H_{15}$)[40%]+torsion($C_6C_5C_{11}H_{15}$)[12%]
34	1464	-stretch(N_1C_2)[14%]+stretch(C_2N_3)[11%]+bend($C_6N_1H_7$)[31%]+bend($N_1C_2O_8$)[10%]-bend($C_2N_3C_4$)[8%]
35	1476	-bend($H_{14}C_{11}H_{15}$)[13%]+bend($H_{13}C_{11}H_{14}$)[41%]-bend($H_{13}C_{11}H_{15}$)[13%]-torsion($C_6C_5C_{11}H_{14}$)[11%]+torsion($C_6C_5C_{11}H_{13}$)[11%]
36	1526	+stretch(C_2O_8)[9%]+stretch(N_1C_2)[18%]-stretch(N_3C_4)[10%]+bend($N_1C_6C_5$)[18%]+bend($C_6N_1H_7$)[22%]
37	1624	+bend($H_{17}O_{16}H_{18}$)[88%]
38	1715	+stretch(C_4O_{10})[20%]+stretch(C_5C_6)[37%]+bend($C_4N_3H_9$)[9%]
39	1720	+stretch(C_4O_{10})[39%]-stretch(C_5C_6)[27%]
40	1752	+stretch(C_4O_{10})[18%]+stretch(C_2O_8)[47%]-stretch(N_1C_2)[8%]

Table C12: *Vibrational Frequencies (ω/cm^{-1}) and Dimensionless Displacements ($|\Delta|$) of Isolated Uracil in H_2O (C-PCM) and Uracil-H_2O in the (A), (B) and (C) Conformers for the Bright Excited State.*

H_2O (C-PCM)	modes	5	6	7	8	9	10	11	12	13	14	15	16
	ω	527	552	568	599	680	740	783	791	830	995	1003	1004
	$\|\Delta\|$	0.1440	0.1262	0.8935	0.0000	0.0000	0.0000	0.0000	0.8168	0.0000	0.2054	0.0530	0.0000
	modes	17	18	19	20	21	22	23	24	25	26		
	ω	1106	1220	1251	1396	1424	1441	1524	1686	1724	1775		
	$\|\Delta\|$	0.3034	0.1458	0.8846	0.6841	0.0728	0.1747	0.2312	0.9235	0.5791	0.4008		
(A)	modes	10	11	12	13	14	15	16	17	18	19	20	21
	ω	528	557	579	668	677	731	783	794	801	833	997	1007
	$\|\Delta\|$	0.1487	0.1231	0.8510	0.3444	0.0444	0.0145	0.0331	0.8286	0.0371	0.0004	0.2153	0.0085
	modes	22	23	24	25	26	27	28	29	30	31	32	33
	ω	1009	1112	1243	1254	1404	1424	1462	1542	1621	1685	1723	1763
	$\|\Delta\|$	0.1438	0.3248	0.3376	0.8329	0.6589	0.2494	0.1325	0.1099	0.0505	0.9030	0.4914	0.4692
(B)	modes	10	11	12	13	14	15	16	17	18	19	20	21
	ω	535	562	574	620	721	742	778	798	812	839	1003	1007
	$\|\Delta\|$	0.1947	0.3329	0.8765	0.0112	0.0741	0.0257	0.0288	0.9226	0.0894	0.0159	0.0793	0.0009
	modes	22	23	24	25	26	27	28	29	30	31	32	33
	ω	1018	1109	1230	1265	1407	1447	1450	1532	1625	1683	1711	1772
	$\|\Delta\|$	0.1238	0.3588	0.0385	0.9123	0.5734	0.1034	0.2661	0.3193	0.2774	0.6984	0.7207	0.2875
(C)	modes	10	11	12	13	14	15	16	17	18	19	20	21
	ω	535	556	574	617	674	741	776	795	817	836	999	1006
	$\|\Delta\|$	0.0692	0.2610	0.8975	0.0047	0.1446	0.0059	0.0042	0.7962	0.0075	0.0044	0.2151	0.0074
	modes	22	23	24	25	26	27	28	29	30	31	32	33
	ω	1021	1108	1224	1261	1414	1445	1458	1523	1624	1690	1724	1758
	$\|\Delta\|$	0.1888	0.3011	0.0992	0.9143	0.6843	0.1612	0.1625	0.2155	0.0491	0.9404	0.5237	0.4912

Table C13: *Vibrational Frequencies (ω/cm^{-1}) and Dimensionless Displacements ($|\Delta|$) of Uracil-$(H_2O)_2$ in the (AB), (BB) and (BC) Conformers for the Bright Excited State.*

(AB)	modes	15	16	17	18	19	20	21	22	23	24	25	26
	ω	535	566	583	668	718	732	783	797	801	826	842	1003
	$\|\Delta\|$	0.2039	0.3848	0.7604	0.4483	0.0282	0.0099	0.0711	0.0177	0.9141	0.0027	0.0113	0.0517
	modes	27	28	29	30	31	32	33	34	35	36	37	38
	ω	1011	1023	1116	1245	1269	1416	1447	1469	1545	1619	1625	1681
	$\|\Delta\|$	0.0093	0.1759	0.3465	0.0270	0.8964	0.6316	0.2240	0.2551	0.1855	0.1751	0.1815	0.6962
	modes	39	40										
	ω	1712	1756										
	$\|\Delta\|$	0.6705	0.3467										
(BB)	modes	15	16	17	18	19	20	21	22	23	24	25	26
	ω	539	561	573	620	668	743	785	799	831	877	942	1002
	$\|\Delta\|$	0.1964	0.4039	0.8708	0.0019	0.0271	0.0358	0.0127	0.8615	0.0274	0.0620	0.0214	0.1414
	modes	27	28	29	30	31	32	33	34	35	36	37	38
	ω	1008	1027	1112	1225	1271	1409	1447	1496	1538	1635	1648	1685
	$\|\Delta\|$	0.0133	0.1177	0.3528	0.0042	0.9306	0.5022	0.1104	0.2021	0.4075	0.1104	0.1842	0.6561
	modes	39	40										
	ω	1707	1770										
	$\|\Delta\|$	0.7182	0.2499										
(BC)	modes	15	16	17	18	19	20	21	22	23	24	25	26
	ω	538	560	577	612	650	669	742	778	801	826	841	1002
	$\|\Delta\|$	0.2106	0.4406	0.8567	0.0094	0.1404	0.0987	0.0197	0.0001	0.8384	0.0023	0.0155	0.1740
	modes	27	28	29	30	31	32	33	34	35	36	37	38
	ω	1010	1025	1110	1224	1270	1413	1448	1462	1528	1620	1640	168
	$\|\Delta\|$	0.0035	0.1354	0.3119	0.0664	0.9110	0.6589	0.1304	0.1936	0.2872	0.0359	0.0655	0.7635
	modes	39	40										
	ω	1710	1760										
	$\|\Delta\|$	0.7001	0.3344										

Table C14: *Vibrational Frequencies (ω/cm^{-1}) and Dimensionless Displacements ($|\Delta|$) of Isolated Thymine in H_2O (C-PCM) and Thymine-H_2O in the (A), (B) and (C) Conformers for the Bright Excited State.*

H_2O (C-PCM)	modes	9	10	11	12	13	14	15	16	17	18	19	20
	ω	556	596	612	684	753	775	793	818	946	987	1029	1068
	$\|\Delta\|$	0.6292	0.0000	0.4427	0.0000	0.5643	0.0001	0.0001	0.4864	0.0000	0.3925	0.2694	0.0002
	modes	21	22	23	24	25	26	27	28	29	30	31	32
	ω	1182	1223	1261	1384	1409	1414	1453	1455	1476	1525	1712	1719
	$\|\Delta\|$	0.2748	0.3424	0.5878	0.9806	0.0463	0.1630	0.0520	0.0000	0.0272	0.3012	1.0710	0.2310
	modes	33											
	ω	1769											
	$\|\Delta\|$	0.2867											
(A)	modes	14	15	16	17	18	19	20	21	22	23	24	25
	ω	562	618	680	689	754	757	791	798	818	946	991	1035
	$\|\Delta\|$	0.6096	0.4768	0.1535	0.3504	0.1382	0.5389	0.0173	0.0029	0.4785	0.0051	0.3663	0.1960
	modes	26	27	28	29	30	31	32	33	34	35	36	37
	ω	1069	1188	1238	1266	1387	1410	1413	1454	1476	1477	1538	1623
	$\|\Delta\|$	0.0039	0.3965	0.1812	0.5576	1.0026	0.0506	0.1965	0.0001	0.0423	0.0434	0.2068	0.0438
	modes	38	39	40									
	ω	1711	1719	1755									
	$\|\Delta\|$	1.0723	0.1694	0.3671									
(B)	modes	14	15	16	17	18	19	20	21	22	23	24	25
	ω	559	621	622	726	764	774	785	821	827	948	996	1032
	$\|\Delta\|$	0.5768	0.5022	0.1604	0.0421	0.6897	0.0945	0.0135	0.4701	0.0868	0.0007	0.3737	0.2598
	modes	26	27	28	29	30	31	32	33	34	35	36	37

	ω	1068	1190	1238	1266	1385	1410	1448	1455	1459	1477	1533	1623
	$\|\Delta\|$	0.0027	0.1342	0.3514	0.6907	0.9355	0.0626	0.3386	0.0011	0.0235	0.0552	0.3335	0.2424
	modes	38	39	40									
	ω	1701	1713	1767									
	$\|\Delta\|$	0.4660	0.8895	0.1996									
	modes	14	15	16	17	18	19	20	21	22	23	24	25
	ω	561	611	618	688	760	771	785	819	821	940	997	1039
	$\|\Delta\|$	0.5664	0.0032	0.5199	0.2965	0.4699	0.0029	0.0157	0.3318	0.3140	0.0046	0.4169	0.1237
(C)	modes	26	27	28	29	30	31	32	33	34	35	36	37
	ω	1068	1185	1232	1269	1390	1409	1446	1454	1464	1476	1526	1624
	$\|\Delta\|$	0.0047	0.2951	0.2579	0.6385	1.0068	0.0207	0.3255	0.0003	0.0362	0.0631	0.2598	0.0517
	modes	38	39	40									
	ω	1715	1720	1752									
	$\|\Delta\|$	1.0589	0.3588	0.3407									

Table C15: *Vibrational Frequencies (ω/cm^{-1}) and Dimensionless Displacements ($|\Delta|$) of Thymine-$(H_2O)_2$ in the (AB), (BB) and (BC) Conformers for the Bright Excited State.*

(AB)	modes	19	20	21	22	23	24	25	26	27	28	29	30
	ω	564	626	683	719	758	768	782	804	820	838	952	1000
	$\|\Delta\|$	0.4878	0.5520	0.3472	0.0497	0.0659	0.6405	0.0827	0.0360	0.5002	0.0033	0.0049	0.4050
	modes	31	32	33	34	35	36	37	38	39	40	41	42
	ω	1037	1069	1201	1246	1270	1386	1411	1449	1456	1478	1480	1543
	$\|\Delta\|$	0.1558	0.0010	0.2724	0.2035	0.6482	0.9674	0.0106	0.3424	0.0015	0.0379	0.0672	0.2386
	modes	43	44	45	46	47							
	ω	1620	1626	1703	1710	1750							
	$\|\Delta\|$	0.1383	0.1598	0.3257	0.9153	0.2307							
(BB)	modes	19	20	21	22	23	24	25	26	27	28	29	30
	ω	557	616	621	668	763	776	794	821	878	938	947	999
	$\|\Delta\|$	0.5579	0.0036	0.5138	0.1519	0.6483	0.0026	0.0275	0.4845	0.0672	0.0096	0.0161	0.3534
	modes	31	32	33	34	35	36	37	38	39	40	41	42
	ω	1035	1068	1191	1243	1267	1383	1410	1455	1456	1477	1495	1537
	$\|\Delta\|$	0.1699	0.0142	0.1323	0.2654	0.7506	0.8916	0.0061	0.0102	0.0821	0.0686	0.2752	0.4463
	modes	43	44	45	46	47							
	ω	1634	1648	1698	1715	1765							
	$\|\Delta\|$	0.1234	0.2237	0.3909	0.8783	0.1806							
(BC)	modes	19	20	21	22	23	24	25	26	27	28	29	30
	ω	560	622	624	660	670	764	773	787	821	836	944	999
	$\|\Delta\|$	0.6138	0.4734	0.1608	0.0271	0.3275	0.5455	0.0394	0.0058	0.5071	0.0417	0.0051	0.3752
	modes	31	32	33	34	35	36	37	38	39	40	41	42

ω	1039	1069	1189	1236	1271	1387	1410	1452	1455	1463	1476	1531
$\|\Delta\|$	0.1049	0.0034	0.1370	0.2536	0.6633	0.9551	0.0666	0.3420	0.0006	0.0485	0.0488	0.3142

modes	43	44	45	46	47
ω	1621	1640	1701	1715	1754
$\|\Delta\|$	0.0552	0.0711	0.6120	0.8667	0.2232

Table C16: *Cartesian Coordinates of Uracil-H_2O at the PBE0/aug-cc-pVTZ Level of Theory in H_2O (C-PCM).*

(A)

C	0.28317000	1.62272900	-0.00347900
N	-0.72039600	0.70570500	-0.00674500
C	-0.49282700	-0.64194300	-0.00377900
N	0.82758900	-0.99216100	0.00183300
C	1.92734800	-0.13561100	0.00475300
C	1.58001500	1.26287000	0.00170900
O	-1.39711900	-1.46855400	-0.00639900
O	3.05653200	-0.59989700	0.00954900
H	-1.70227000	0.97964300	-0.00588400
H	1.02322600	-1.98322800	0.00365200
H	2.36943200	1.99757500	0.00379500
H	-0.03464700	2.65639500	-0.00555200
O	-3.54130200	0.30327600	-0.08511800
H	-4.08915000	0.35980300	0.70132000
H	-3.04806900	-0.53186900	-0.00241900

(B)

C	1.96869300	-1.04046100	0.00785200
N	2.00844300	0.31745700	0.00456200
C	0.88330200	1.10600000	-0.00092400
N	-0.28846200	0.39502900	-0.00464900
C	-0.42991000	-0.98247200	-0.00190300
C	0.80499000	-1.71726300	0.00524900
O	0.92771500	2.32106200	-0.00247700
O	-1.55490800	-1.48174400	-0.00612400
H	2.89176200	0.80215500	0.00683000
H	-1.15446100	0.93344100	-0.00539000
H	0.77756100	-2.79508400	0.00778900
H	2.93118900	-1.53316200	0.01267600
O	-3.16479900	0.74485700	-0.08908300
H	-2.83906400	-0.17236600	-0.00969000
H	-3.67337200	0.90939100	0.70822500

(C)

C	-1.99475400	-0.99603400	0.00735300
N	-0.78167500	-1.61549100	0.00448000

C	0.40253800	-0.93231200	-0.00172900
N	0.27155300	0.42667200	-0.00433700
C	-0.91363900	1.15558800	-0.00063700
C	-2.10619000	0.34356900	0.00491000
O	1.48831700	-1.49970600	-0.00504300
O	-0.87739400	2.37623700	-0.00222600
H	-0.71967000	-2.62096100	0.00605500
H	1.15109600	0.94244900	-0.00530200
H	-3.06972200	0.82789700	0.00729600
H	-2.85153300	-1.65520400	0.01174500
O	3.16467100	0.71390900	-0.08977900
H	2.84820600	-0.20306100	-0.00627100
H	3.67999500	0.88222500	0.70247200

Table C17: *Cartesian Coordinates of Thymine-H_2O at the PBE0/aug-cc-pVTZ Level of Theory in H_2O (C-PCM).*

(A)

C	0.28728	1.34073	-0.00382
N	-0.89582	0.66107	-0.00587
C	-0.97019	-0.69832	-0.00277
N	0.24401	-1.32365	0.00202
C	1.49942	-0.72464	0.00369
C	1.48608	0.72549	0.00044
O	-2.03216	-1.31388	-0.00458
O	2.50248	-1.42159	0.00769
H	-1.79084	1.14658	-0.00488
H	0.22415	-2.33353	0.00395
H	0.19419	2.41870	-0.00614
O	-3.75437	0.85331	-0.08675
H	-4.27738	1.00978	0.70293
H	-3.42193	-0.05922	-0.00556
C	2.78472	1.45538	0.00212
H	3.37783	1.19592	0.88187
H	3.38215	1.19232	-0.87362
H	2.62307	2.53282	-0.00049

(B)

C	1.93075	0.54073	0.00585

N	1.17198	1.67343	0.00416
C	-0.19655	1.66703	-0.00036
N	-0.73464	0.40652	-0.00480
C	-0.04867	-0.79323	-0.00349
C	1.39424	-0.69599	0.00268
O	-0.87040	2.68139	-0.00056
O	-0.67373	-1.85422	-0.00807
H	1.61341	2.57870	0.00682
H	-1.75179	0.33877	-0.00503
H	3.00002	0.70526	0.00997
O	-3.28080	-0.98917	-0.08864
H	-2.47804	-1.53986	-0.00958
H	-3.78658	-1.15182	0.71079
C	2.20477	-1.94610	0.00447
H	1.97839	-2.55758	0.88063
H	1.98579	-2.55528	-0.87517
H	3.26969	-1.71646	0.00927

(C)

C	1.40861900	1.35878400	-0.00635100
N	0.10515900	1.77075700	-0.00409700
C	-0.94839500	0.90816100	0.00230700
N	-0.59131600	-0.40963500	0.00577500
C	0.69651600	-0.92877400	0.00279000
C	1.76040600	0.05945700	-0.00306800
O	-2.11653300	1.28463400	0.00515700
O	0.86397100	-2.13889900	0.00516400
H	-0.11697900	2.75328600	-0.00616700
H	-1.36970400	-1.06734800	0.00671200
H	2.13978700	2.15604400	-0.01095600
C	3.17480800	-0.40733300	-0.00547000
H	3.38477200	-1.02071200	0.87351400
H	3.38009000	-1.02592600	-0.88190500
H	3.86158600	0.43838000	-0.00979300
O	-3.41138500	-1.15839000	0.08712700
H	-3.22754200	-0.20462600	0.00644200
H	-3.88906800	-1.39748200	-0.71042600

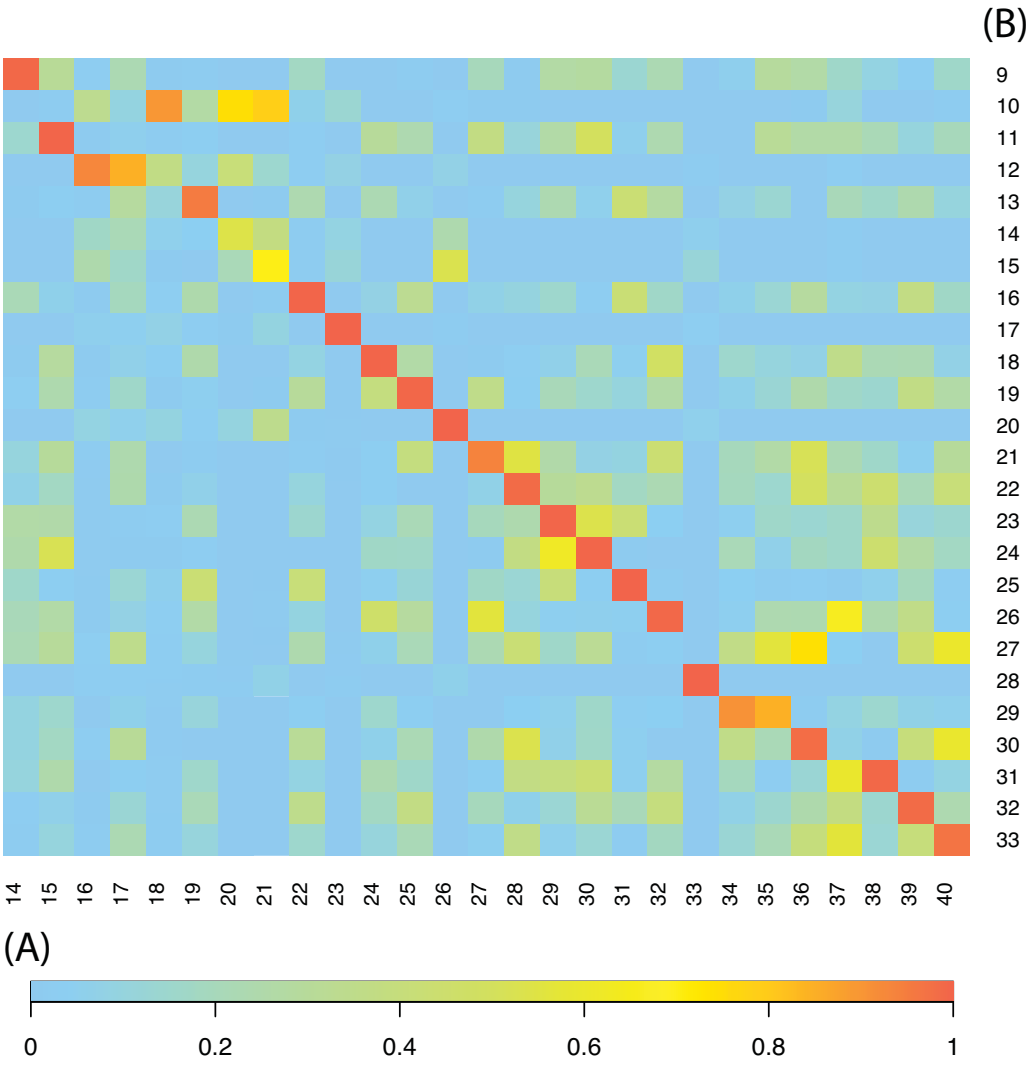

Figure C1: *The cosine similarity of (A) vs. (B) for uracil.*

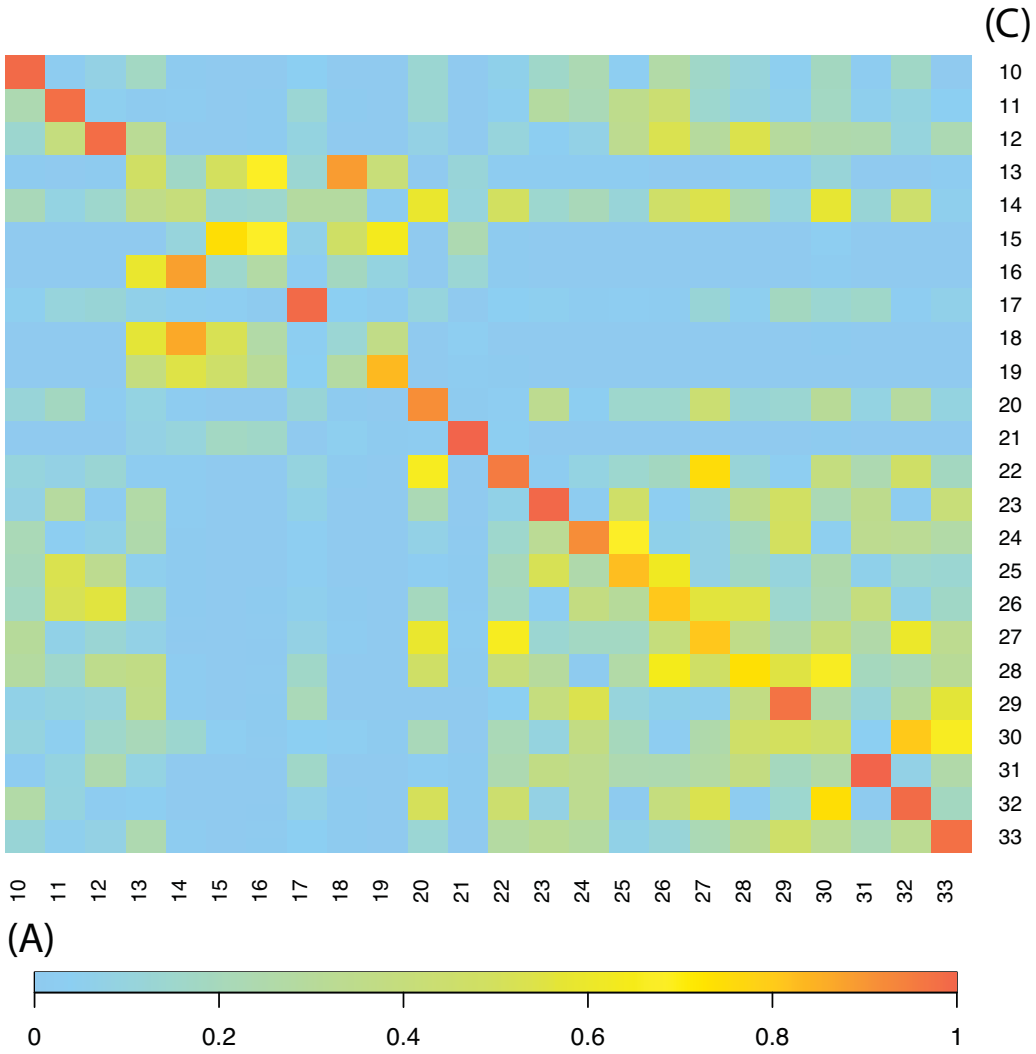

Figure C2: *The cosine similarity of (A) vs. (C) for uracil.*

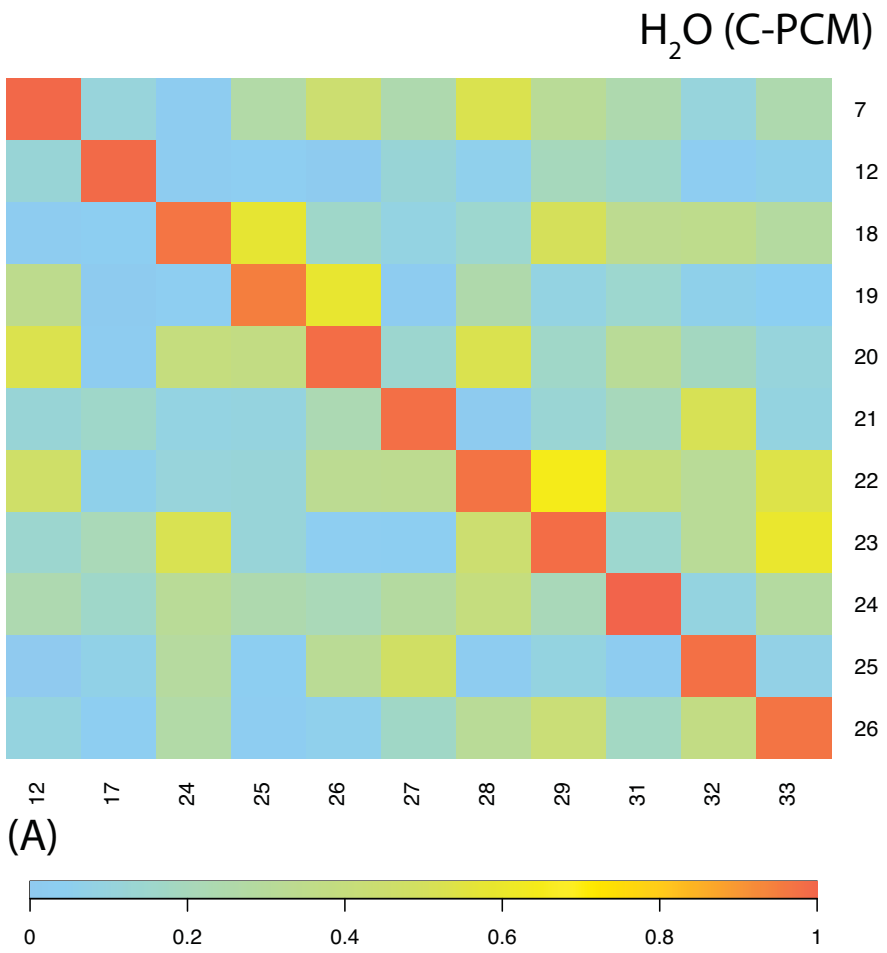

Figure C3: *The cosine similarity of uracil-H_2O (A) vs. isolated uracil in H_2O (C-CPM).*

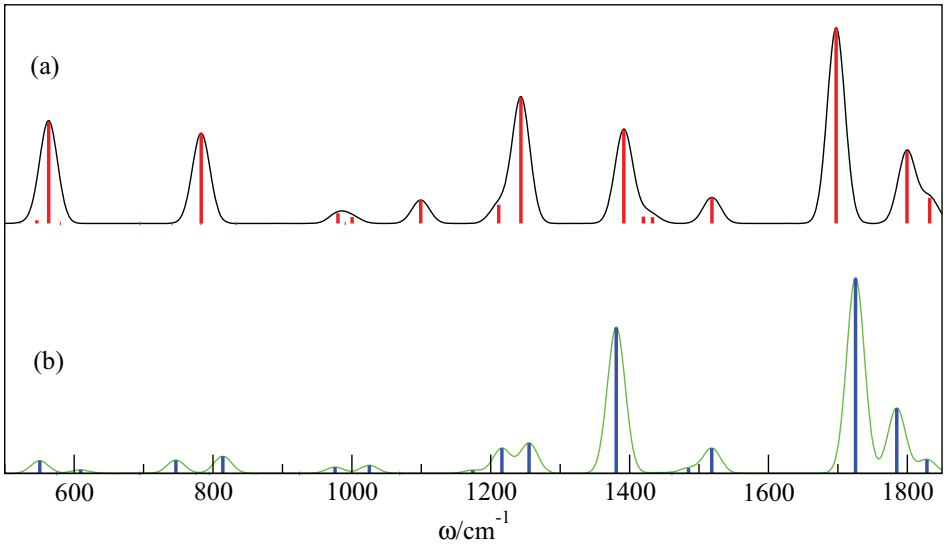

Figure C4: *Resonance Raman spectra of (a) uracil and (b) thymine in the gas phase. Ground and excited state determined at the PBE0/aug-cc-pVTZ and TD-CAMB3LYP/aug-cc-pVTZ levels of theory, respectively. fwhm used in the simulation is 30 cm^{-1}.*

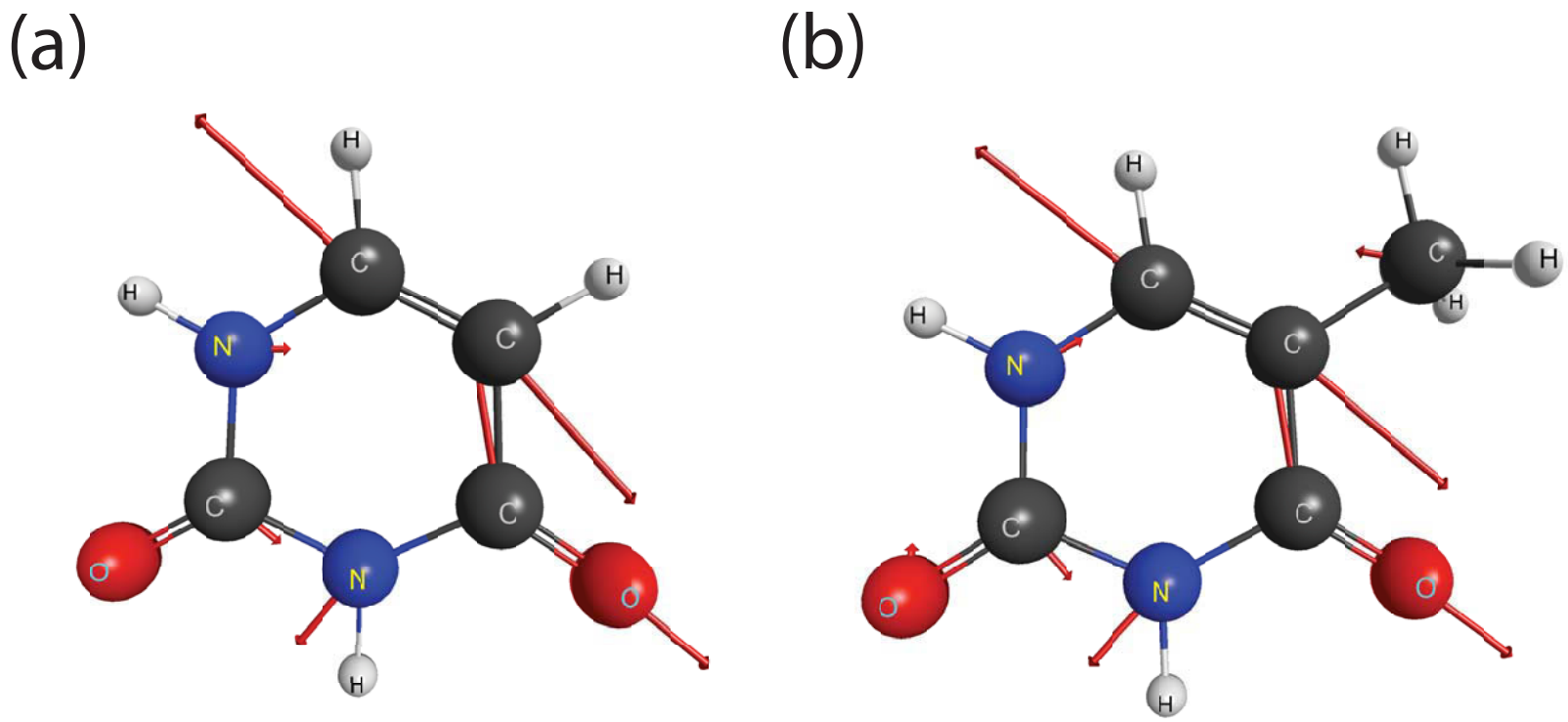

Figure C5: *Vectors illustrating the Cartesian gradients for each atom of (a) isolated uracil in implicit water (C-PCM) and (b) isolated thymine in implicit water (C-PCM) for the S_1 excited state as determined at the TD-CAMB3LYP/aug-cc-pVTZ level of theory.*

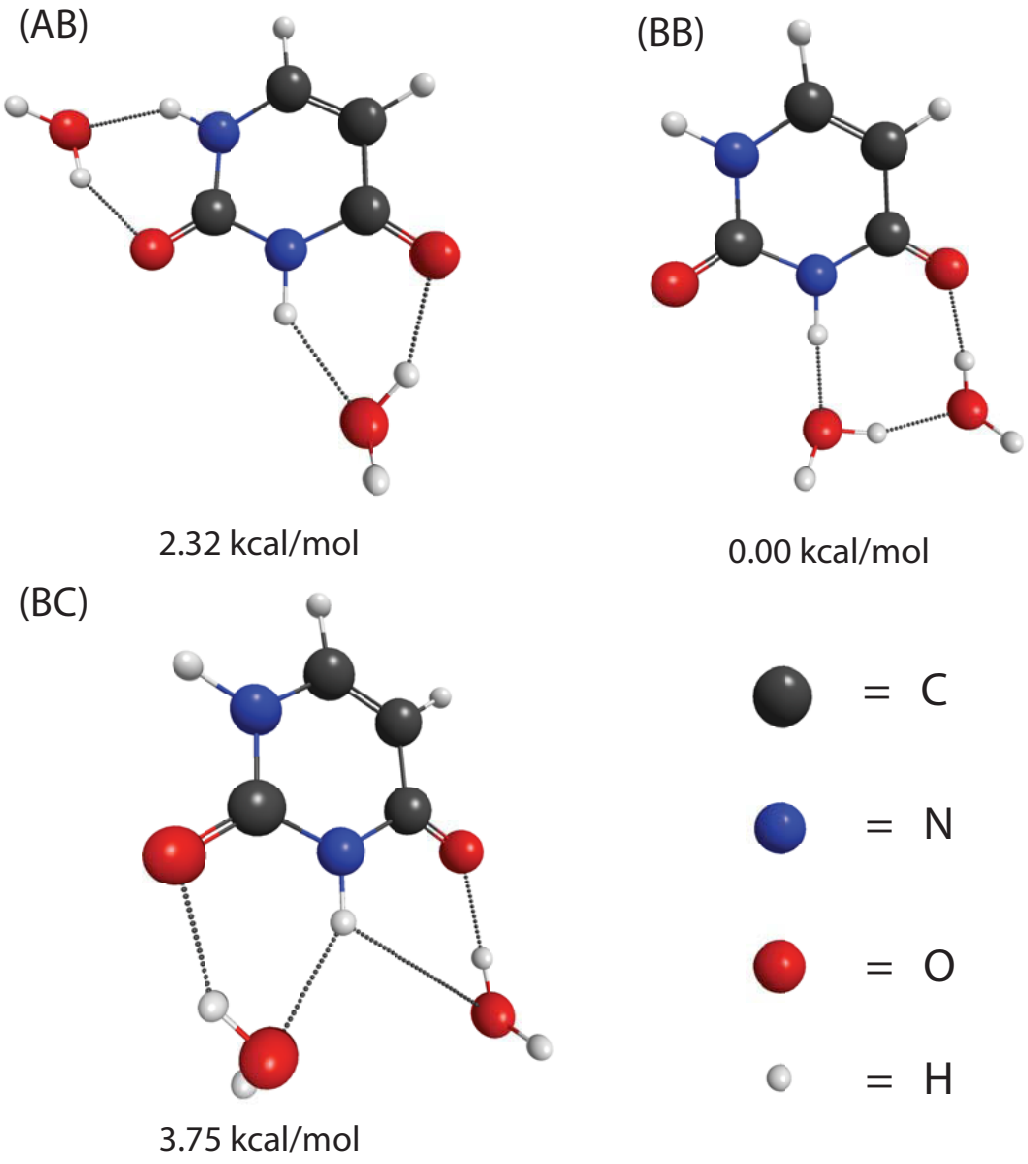

Figure C6: *The geometries and relative energies (kcal/mol) of uracil-$(H_2O)_2$ determined at the PBE0/aug-cc-pVTZ level of theory in H_2O (C-PCM).*

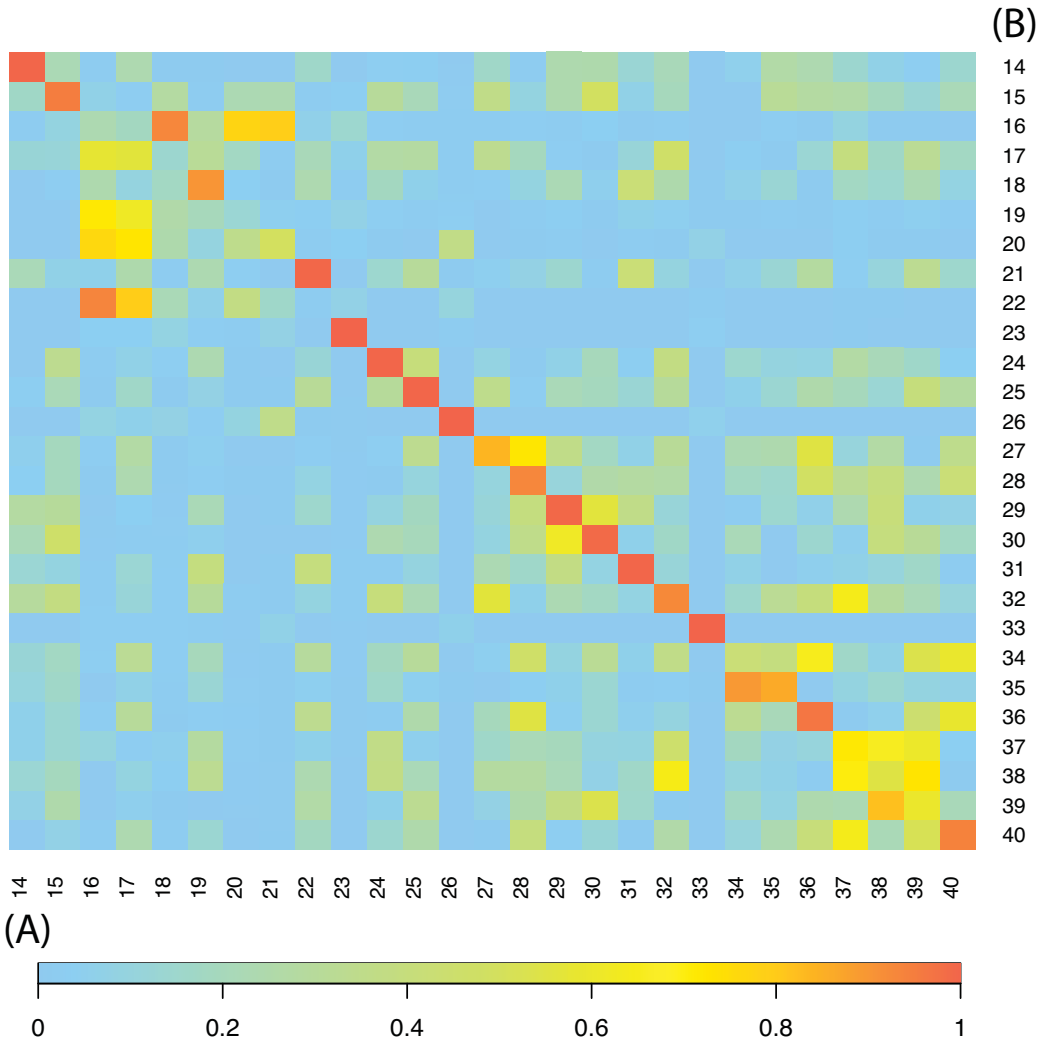

Figure C7: *The cosine similarity of (A) vs. (B) for thymine.*

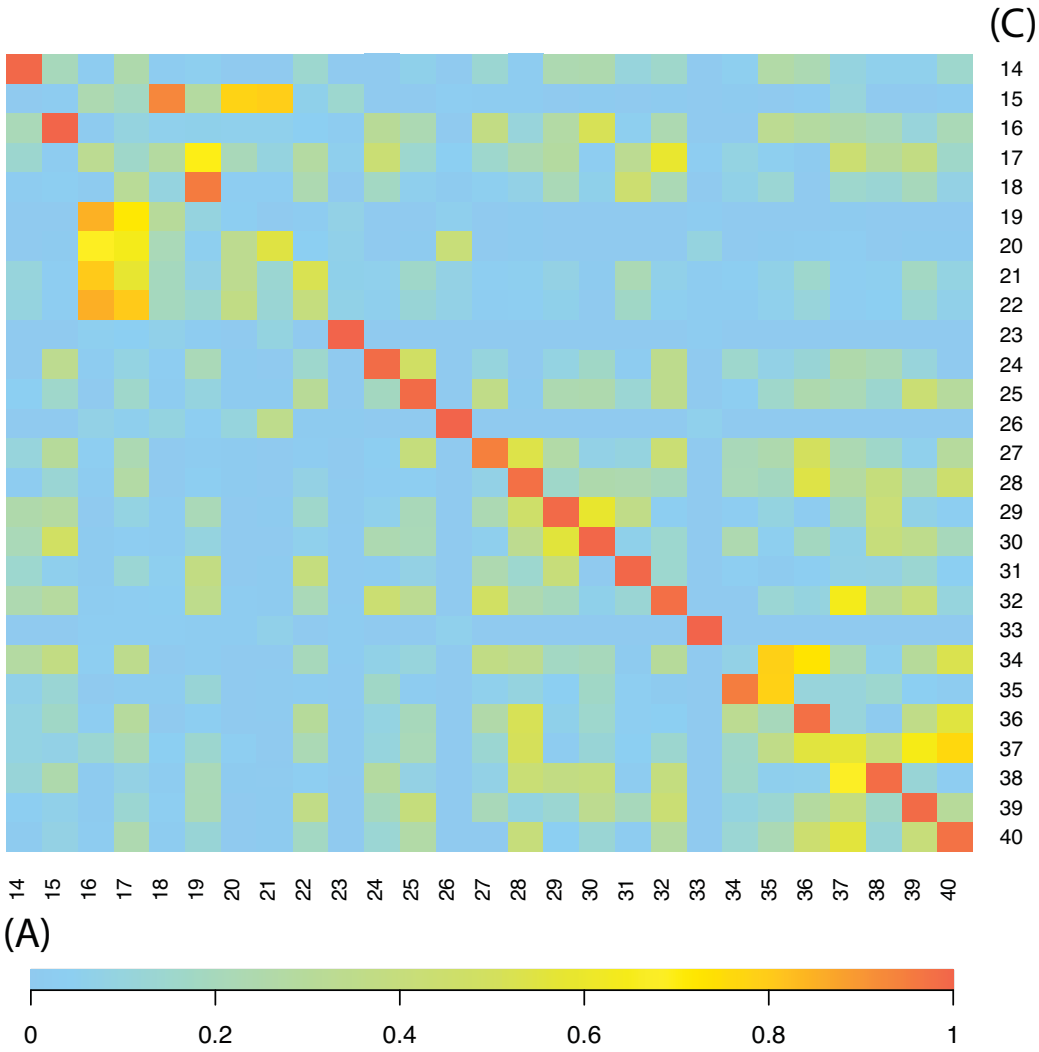

Figure C8: *The cosine similarity of (A) vs. (C) for thymine.*

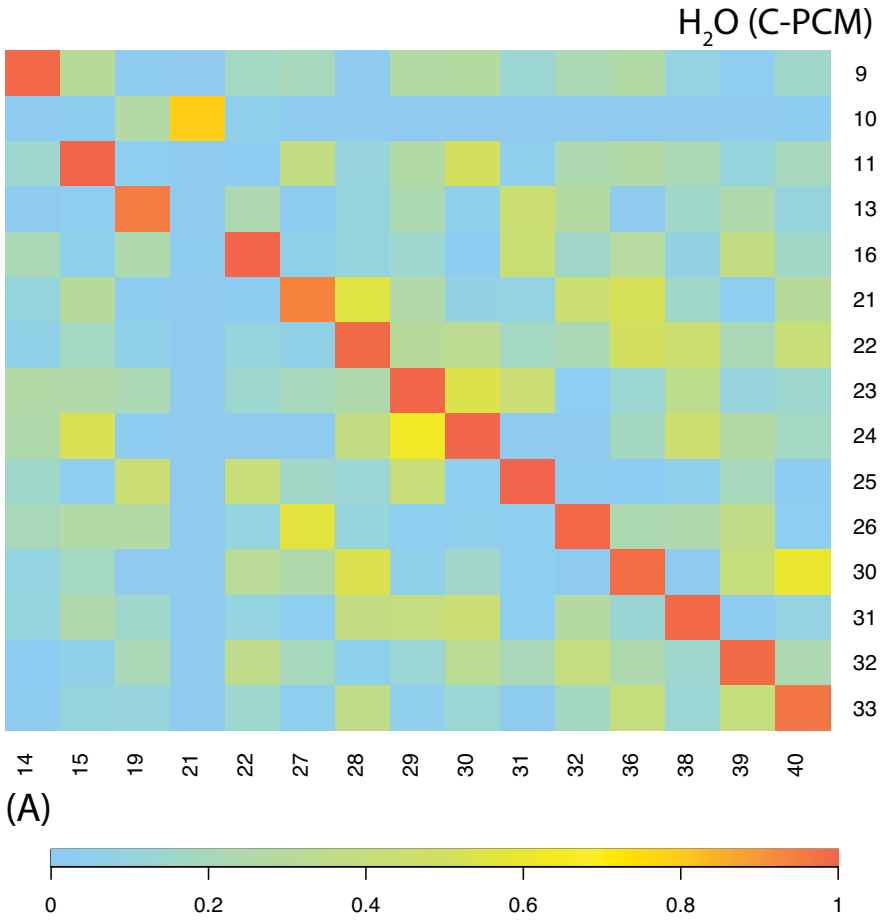

Figure C9: *The cosine similarity of thymine-H_2O(A) vs. isolated thymine in H_2O (C-CPM).*

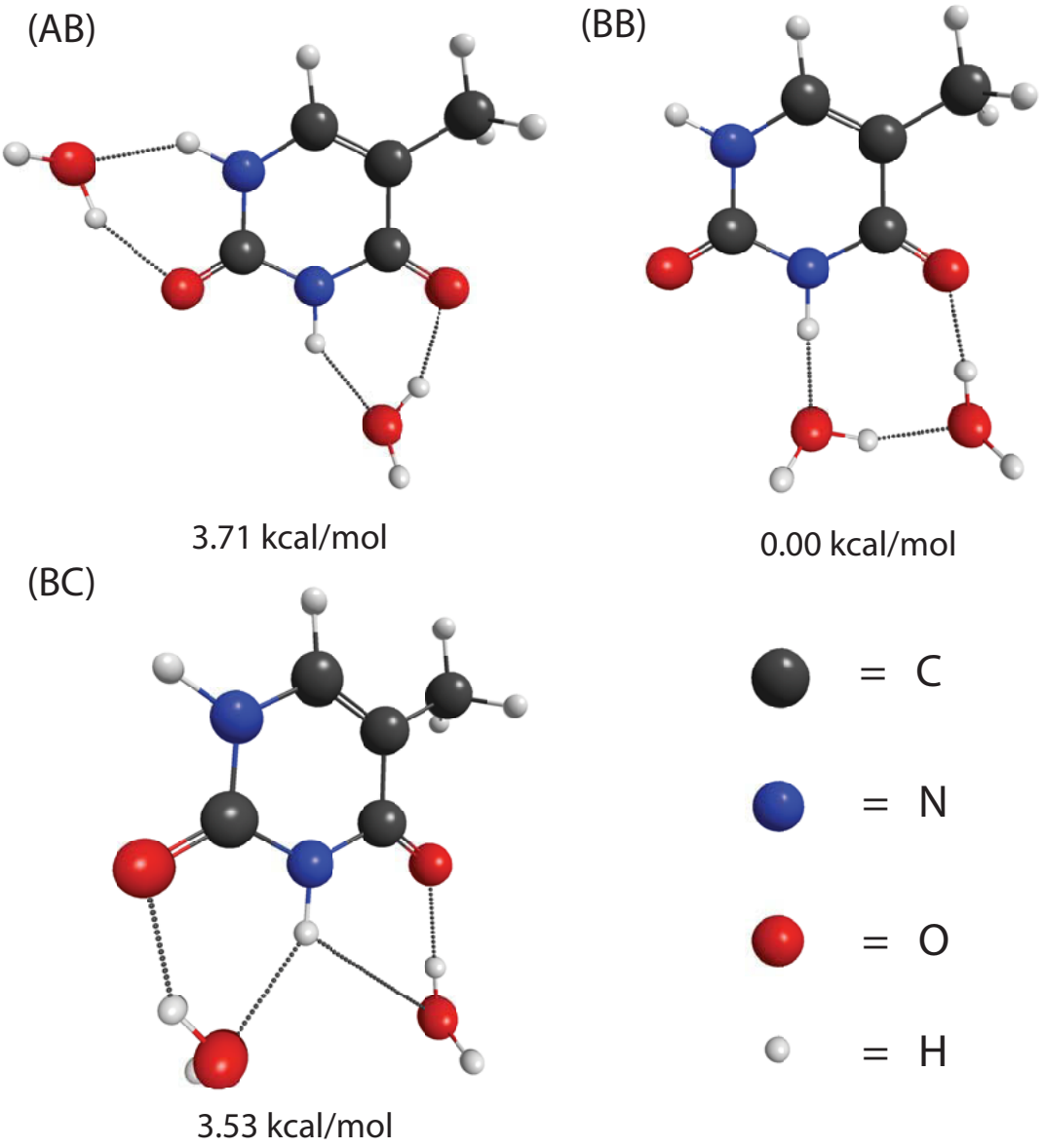

Figure C10: *The geometries and relative energies (kcal/mol) of thymine-$(H_2O)_2$ determined at the PBE0/aug-cc-pVTZ level of theory in H_2O (C-PCM).*